



UNIL | Université de Lausanne

Unicentre
CH-1015 Lausanne
<http://serval.unil.ch>

Year : 2021

Assessment of the arterial wall and lumen with spectral computed tomography

ROTZINGER David Christian

Rotzinger David Christian, 2021, Assessment of the arterial wall and lumen with spectral
computed tomography

Originally published at : Thesis, University of Lausanne

Posted at the University of Lausanne Open Archive <http://serval.unil.ch>
Document URN : urn:nbn:ch:serval:BIB_5FB7106E2E91

Droits d'auteur

L'Université de Lausanne attire expressément l'attention des utilisateurs sur le fait que tous les documents publiés dans l'Archive SERVAL sont protégés par le droit d'auteur, conformément à la loi fédérale sur le droit d'auteur et les droits voisins (LDA). A ce titre, il est indispensable d'obtenir le consentement préalable de l'auteur et/ou de l'éditeur avant toute utilisation d'une oeuvre ou d'une partie d'une oeuvre ne relevant pas d'une utilisation à des fins personnelles au sens de la LDA (art. 19, al. 1 lettre a). A défaut, tout contrevenant s'expose aux sanctions prévues par cette loi. Nous déclinons toute responsabilité en la matière.

Copyright

The University of Lausanne expressly draws the attention of users to the fact that all documents published in the SERVAL Archive are protected by copyright in accordance with federal law on copyright and similar rights (LDA). Accordingly it is indispensable to obtain prior consent from the author and/or publisher before any use of a work or part of a work for purposes other than personal use within the meaning of LDA (art. 19, para. 1 letter a). Failure to do so will expose offenders to the sanctions laid down by this law. We accept no liability in this respect.



UNIL | Université de Lausanne

Faculté de biologie
et de médecine

Département de Radiologie Médicale (DRM) CHUV

Service de Radiodiagnostic et Radiologie Interventionnelle

Assessment of the arterial wall and lumen with spectral computed tomography

Thèse de doctorat ès sciences de la vie (PhD)

présentée à la
Faculté de Biologie et de Médecine de l'Université de Lausanne

par

David Christian ROTZINGER

Médecin diplômé de la Confédération Suisse, Université de Lausanne

Docteur en médecine (MD), Université de Lausanne

Prof. Etienne Pruvot, Président
Prof. Reto A. Meuli, Directeur de thèse
Prof. Philippe C. Douek (HCL-UdL, Lyon, France), Co-directeur de thèse
Prof. Salah D. Qanadli, Co-directeur de thèse
Prof. Francis R. Verdun, Expert
Prof. Jean-Paul Vallée, Expert

Lausanne
2021



UNIL | Université de Lausanne

Faculté de biologie
et de médecine

Département de Radiologie Médicale (DRM) CHUV

Service de Radiodiagnostic et Radiologie Interventionnelle

Assessment of the arterial wall and lumen with spectral computed tomography

Thèse de doctorat ès sciences de la vie (PhD)

présentée à la
Faculté de Biologie et de Médecine de l'Université de Lausanne

par

David Christian ROTZINGER

Médecin diplômé de la Confédération Suisse, Université de Lausanne

Docteur en médecine (MD), Université de Lausanne

Prof. Etienne Pruvot, Président
Prof. Reto A. Meuli, Directeur de thèse
Prof. Philippe C. Douek (HCL-UdL, Lyon, France), Co-directeur de thèse
Prof. Salah D. Qanadli, Co-directeur de thèse
Prof. Francis R. Verdun, Expert
Prof. Jean-Paul Vallée, Expert

Lausanne
2021



UNIL | Université de Lausanne

Faculté de biologie
et de médecine

Ecole Doctorale

Doctorat ès sciences de la vie

Imprimatur

Vu le rapport présenté par le jury d'examen, composé de

Président·e	Monsieur	Prof.	Etienne	Pruvot
Directeur·trice de thèse	Monsieur	Prof.	Reto A.	Meuli
Co-directeur·trice·s	Monsieur	Prof.	Philippe C.	Douek
	Monsieur	Prof.	Salah D.	Qanadli
Expert·e·s	Monsieur	Prof.	Francis R.	Verdun
	Monsieur	Prof.	Jean-Paul	Vallée

le Conseil de Faculté autorise l'impression de la thèse de

Monsieur David Christian Rotzinger

Doctorat en médecine, Université de Lausanne

intitulée

**Assessment of the arterial wall and lumen
with spectral computed tomography**

Date de l'examen : 24 novembre 2021

Date d'émission de l'imprimatur : Lausanne, le 16 décembre 2021.

pour le Doyen
de la Faculté de biologie et de médecine

Prof. Niko GELDNER
Directeur de l'Ecole Doctorale

Affiliation

Thesis directors/supervision

Prof. Reto A. Meuli, Department of diagnostic and interventional radiology, Lausanne University Hospital (CHUV). Faculty of Biology and Medicine, University of Lausanne (UNIL), Switzerland.

Prof. Philippe C. Douek, Radiology Department, Lyon University Hospital (HCL). University Claude Bernard Lyon 1, CREATIS, CNRS UMR 5220, INSERM U1206, INSA-Lyon, Lyon, France.

Prof. Salah D. Qanadli, Department of diagnostic and interventional radiology, Lausanne University Hospital (CHUV). Faculty of Biology and Medicine, University of Lausanne (UNIL), Switzerland.

Experts

Prof. Francis R. Verdun, Institute of Radiation Physics (IRA), Lausanne University Hospital

(CHUV). Faculty of Biology and Medicine,
University of Lausanne (UNIL), Switzerland.

Prof. Jean-Paul Vallée, Service of Radiology,
Department of Radiology and Medical
Informatics, University Hospital of Geneva
(HUG). Faculty of Medicine, University of
Geneva (UNIGE), Switzerland.

President

Prof. Etienne Pruvot, Heart and Vessel
Department, Service of Cardiology, Lausanne
University Hospital (CHUV). Faculty of Biology
and Medicine, University of Lausanne (UNIL),
Switzerland.

No matter what accomplishments you make, somebody helped you.

Althea Gibson

Acknowledgments

This work derives its richness and innovative approach from multiple collaborations between universities and industry, but above all, between people I have had the joy of meeting along this journey. First and foremost, I would like to thank my thesis directors, Prof. Meuli, Prof. Douek, and Prof. Qanadli, who each in their way, not only conveyed to me their enthusiasm for medical imaging and research, but also knew to get essential values across, including rigor, openness, responsibility, and fairness. By being steadily available and providing support when needed, they also offered me a great deal of autonomy in carrying out the project. Furthermore, I would like to thank the people, doctors, physicists, medical radiology technicians who have helped me shape, step by step, the scientific work published or in progress. I'm thinking of so many people located in France, Switzerland, Germany, and Israel, too many to list them all one by one. Nevertheless, the experience of meeting these creative and pleasant persons marked my mind for the rest of my career.

I extend particular gratitude to my parents, Yvonne and François, for their encouraging attitude and support since my childhood, without whom I would never have embraced academic education. Special thanks go to my wife Aurélie, who has stoically sustained the highs and lows along the route, taking care of the growing family and even prompting me to embark on a doctoral thesis.

This work was partially funded by a grant from the Leenaards Foundation, Lausanne, Switzerland, to whom I am grateful for the trust they placed in me and ultimately made the whole project happen.

Table of content

1. Abstract.....	14
2. List of acronyms.....	17
3. Introduction	20
4.1 Background.....	20
4.2 Iodine in X-ray imaging.....	20
4.3 The advent of dual-energy CT.....	21
4.3.1 Advantages and limitations of dual-energy CT.....	26
4.3.2 Dual-energy CT data processing and image types	27
4.3.3 Clinical applications.....	29
4.3.4 Clinical examples of dual-energy CT.....	31
4.4 Photon-counting CT	38
4.4.1 Advantages and limitations	40
4.4.2 Clinical applications.....	41
4.4.3 Clinical examples of photon-counting CT	43
4.5 Aims of the thesis	47
4. Thesis milestones	50
5.1 Building a collaborative project.....	50
5.2 Importance of experimental approaches	51
5.2.1 Assessing image quality in CT	51

5.2.2. Experimental assessment of tissue characteristics	56
5.2.3. Experimental assessment of spatial resolution performance	57
5.3 Clinical studies and approaches	59
6 Achieved results.....	63
6.1 Radiation and iodine dose	63
6.1.1 Virtual versus true non-contrast dual-energy CT imaging for the diagnosis of aortic intramural hematoma [94]	63
6.1.2 Reduced-iodine-dose dual-energy coronary CT angiography: qualitative and quantitative comparison between virtual monochromatic and polychromatic images [109].....	73
6.2 Tissue contrast and characterization	85
6.2.1 Effect of contrast material injection protocol on first-pass myocardial perfusion assessed by dual-energy CT	85
6.2.2 “Dark-blood” dual-energy computed tomography angiography for thoracic aortic wall imaging [111].....	116
6.1.3 Identification and quantification of monosodium urate crystals in coronary atheroma “COROGOUT”	124
6.3 Spatial resolution, noise and detection performance	138
6.3.1 Feasibility of spectral photon-counting coronary CT angiography and comparison with energy-integrating-detector CT: objective assessment with model observer	138

7. Excerpts from related publications leveraging spectral CT	174
7.1 Quantitative imaging with spectral CT helps understand COVID-19 [119]	174
7.2 Application of spectral CT in COVID-19-related vascular involvement [120].....	178
7.4 Emerging role of spectral CT chronic thromboembolic pulmonary hypertension diagnosis [125]	187
8. Discussion and future directions	194
9. Conclusion	200
8. References.....	201
Conference proceedings	217
Curriculum vitae.....	220

1. Abstract

Computed tomography (CT) has deeply affected the approach to diagnosis in medical practice and is heavily relied on for numerous therapeutic decisions. Meanwhile, diagnostic imaging and CT in particular remains at the core of medical innovation, not least due to remarkable developments on the imaging chain. After three decades of conventional CT – intrinsically disregarding energy-dependency of X-ray attenuation – spectral CT became available clinically, fostering research and improvement of patient management. Spectral CT is regarded as a disruptive technology that can affect workflow, patient safety, and diagnostic accuracy but needs validation. With this in mind, we sought to explore the potential benefits of spectral CT for evaluating cardiovascular disease.

To provide a thorough assessment of spectral CT in evaluating vascular lumen and wall, we designed several phantom experiments to assess the feasibility of dedicated tasks and expanded our research to clinical studies for validation. To this end, we used both clinically available dual-energy CT (DECT) and pre-clinical multi-energy (spectral photon-counting detector CT [SPCCT]) platforms.

We confirmed that DECT can save radiation dose thanks to virtual non-contrast reconstructions, reduce iodine doses considerably for coronary artery imaging, and task-oriented material decomposition reconstructions improve aortic wall conspicuity, notably in aortic intramural hematoma. We also showed that SPCCT coronary angiography outperforms DECT in terms of noise, spatial resolution, and diagnostic performance. These findings advance both patient safety and the clinical value of spectral CT in cardiovascular imaging.

Résumé

La tomodensitométrie (TDM) a profondément affecté l'approche diagnostique et thérapeutique pour nombre de pathologies. Parallèlement, l'imagerie diagnostique et la TDM en particulier restent au cœur de l'innovation médicale, notamment grâce aux progrès technologiques. Après trois décennies de TDM conventionnelle ignorant l'atténuation différentielle des rayons X en fonction de leur énergie, la TDM spectrale est apparue, favorisant la recherche et l'optimisation de la prise en charge des patients. La TDM spectrale peut affecter le flux de travail, la sécurité des patients et la précision du diagnostic, mais nécessite d'être validée. Nous avons donc exploré les avantages potentiels de la TDM spectrale pour l'évaluation des maladies cardiovasculaires. Pour étudier la TDM spectrale dans l'évaluation de la lumière et de la paroi vasculaires, nous avons conçu plusieurs expériences de faisabilité sur fantômes et avons ensuite étendu notre recherche à des études cliniques, en utilisant à la fois des plateformes TDM à double énergie (« DECT ») disponibles en clinique et des plateformes multi-énergies précliniques (détecteurs à comptage de photons spectraux [« SPCCT »]).

Nous avons confirmé que le DECT permet de réduire l'irradiation grâce aux reconstructions virtuellement sans contraste, que les doses d'iode peuvent être considérablement réduites pour l'imagerie des artères coronaires, et que les reconstructions en décomposition matériaux peuvent améliorer la visibilité de la paroi aortique. Nous avons également montré que l'imagerie des coronaires en SPCCT surpasse le DECT en termes de bruit, de résolution spatiale et de performances diagnostiques. Ces résultats font progresser à la fois la sécurité des patients et la valeur clinique de la tomodensitométrie spectrale en imagerie cardiovasculaire.

Résumé public

En un demi-siècle d'existence, la tomodesitométrie (TDM) – communément appelée « scanner » – a révolutionné le diagnostic et la prise en charge médicale, en permettant d'obtenir des images de l'intérieur du corps humain sous formes de coupes consécutives détaillant l'intégralité de l'anatomie en trois dimensions. La technique de la TDM repose sur le principe de la mesure de l'absorption du faisceau de rayons X ; celui-ci traverse le corps humain et subit une atténuation plus ou moins forte en fonction de la composition des tissus et de l'épaisseur traversée. Cette mesure d'atténuation se fait en continu au cours d'un balayage qui consiste à faire tourner un couple tube à rayons X - récepteurs autour du patient, et les données brutes ainsi obtenues sont transférées à un ordinateur. Un traitement informatique des données brutes permet de reconstruire des images 2 dimensions des tissus humains, et des vues en 3 dimensions d'organes ou de lésions. Toutefois, les équipements de TDM conventionnels ne prennent pas en compte le fait que le faisceau de rayons est composé d'un mélange de photons X d'énergie très variable, alors même que l'atténuation des rayons X dépend directement de leur énergie. La TDM multi-énergie (spectrale) exploite cette propriété physique et permet de reconstituer, dans une certaine mesure, la composition chimique des tissus scannés. La TDM spectrale est une innovation relativement récente, et il est essentiel d'étudier ses avantages et inconvénients avant de l'appliquer sur l'être humain. Le but de cette thèse est de mettre en lumière certains bénéfices de la TDM spectrale en imagerie cardiovasculaire. Nous montrons notamment que la TDM spectrale permet de réduire la dose de produit de contraste injecté et la dose d'irradiation, tout en apportant des informations diagnostiques additionnelles.

2. List of acronyms

ASIC	Application-Specific Integrated Circuit
CdZnTe	Cadmium Zinc Telluride
CM	Contrast Medium
CNR	Contrast-to-Noise Ratio
CT	Computed Tomography
CTA	Computed Tomography Angiography
CCTA	Coronary Computed Tomography Angiography
CPP	Calcium Pyrophosphate
CURML	Centre Universitaire Romand de Médecine Légale
DECT	Dual-Energy Computed Tomography
DER	Dual-Energy Ratio
DLIR	Deep Learning Image Reconstruction
ECG	Electrocardiogram
EID	Energy-Integrating Detector
HA	Hydroxyapatite
HU	Hounsfield Units

IMH	Intramural Hematoma
GBPCI	Grating-Based Phase Contrast Imaging
keV	Kiloelectron-Volt
MSU	Monosodium Urate
MTF	Modulation Transfer Function
NIST	National Institute of Standards and Technology
NPS	Noise Power Spectrum
PCD	Photon-Counting Detector
PCCT	Photon-Counting Computed Tomography
ROI	Region Of Interest
Si	Silicon
TTF	Target Transfer Function
TNC	True Non-Contrast
UA	Uric Acid
VMI	Virtual Monochromatic Image
VNC	Virtual Non-Contrast
Zeff	Effective Atomic Number

3. Introduction

4.1 Background

Computed tomography (CT) for medical purposes was first reported in 1973 [1, 2] and became more widely available in the 80s. CT was an instant success in the medical field, being the first imaging technique to render 3-dimensional images of the human body, casting aside the limitations of projectional imaging. The new imaging area CT established has profoundly altered diagnostic approaches over the last four decades, disrupting both the diagnostic workup and treatment strategies. Despite astonishing technological improvements made to the initial so-called “EMI CT scanner,” the system Godfrey Hounsfield and his team developed [3], CT is far from reaching its foreseeable fundamental physical limits. This thesis is about leveraging the latest available CT technology by transposing innovative techniques into clinical applications.

CT uses X-ray beams consisting of a continuous spectrum of photon energies that undergo absorption when traveling through tissue and interacting with matter. Photons reaching the detector located on the opposite side of the X-ray tube are quantified at multiple 2-dimensional angular projections to recover the 3-dimensional internal structure of the subject being scanned [4]. Until recently, photon detection occurred by so-called “conventional CT detectors,” referred to as “energy integrating,” because they sum up all the photons reaching the detector regardless of their energy.

4.2 Iodine in X-ray imaging

Iodinated contrast medium (CM) has been used for angiography since 1920, and nowadays, an estimated 75 million procedures are performed per year [5]. In CT, first

reports describing the use of iodinated were published very soon, i.e. two years after the introduction of CT [6]. Since the early 1920s, CM safety has improved dramatically, leading to much lower toxicity, better tolerability, and improved angiographic contrast. Nevertheless, adverse reactions still occur in 1-3% of procedures, and as a result, the use of CM cannot be considered harmless [6]. Because some adverse reactions to CM are dose-dependent, including post-injection heart failure, acute pulmonary edema, and nephrotoxicity, limiting the volume of CM is a relevant approach [7].

Furthermore, it has been shown that the DNA damage resulting from ionizing radiation is adversely affected by the use of iodine, further supporting CM dose reduction [8]. Finally, the use of CM comes at a cost, and a potential decrease of the financial burden can be achieved by reducing the total volume used per procedure. Nevertheless, over one hundred years after its introduction, iodinated CM remains a unique tool to image patients, make accurate diagnoses, and support decision-making. This is especially true for cardiovascular imaging, where CM helps identify both the vascular lumen and its wall. Computed tomography angiography (CTA) has quickly established itself as the principal imaging technique for large vessels and has also become a key player in cardiac radiology. In recent years, coronary CTA has become the most widely used method for the non-invasive assessment of coronary artery disease, of course, thanks to lumen enhancement with iodine.

4.3 The advent of dual-energy CT

X-ray absorption from interaction with tissue mainly depends on two effects in the clinical energy range: photoelectric absorption and Compton scattering [4, 9]. Conventional CT systems measure the X-ray attenuation and can extract the linear attenuation coefficient

of each voxel. When the latter is normalized against water, we obtain the voxels' CT number, which is expressed in Hounsfield Units [HU] and primarily depends on the energy of the polychromatic X-ray spectrum, the materials' mass density, and effective atomic number (Z_{eff}). Compton scattering is predominant at high energy and mainly driven by the electron density (ρ), providing most of the soft tissue contrast while interacting with low-atomic number elements (i.e., oxygen, $Z=8$; nitrogen, $Z=7$; carbon, $Z=6$; hydrogen, $Z=1$). On the other hand, photoelectric absorption is more likely to occur at low energy and is proportional to the cube of atomic number. Conventional CT systems do not use pulse detection but integrate the overall energy deposited in the detector during a projection; this is why they are commonly referred to as energy integrating detectors (EID). To translate X-rays into a digital signal, EID first converts X-ray photons to visible light sensed by a photodiode and undergoes analog-to-digital conversion (Fig. 1). The output signal of EIDs is proportional to the energy deposited by the sum of incident photons, which means that the higher energy photons bearing the least contrast information generate a stronger output, overriding valuable information from low-energy photons.

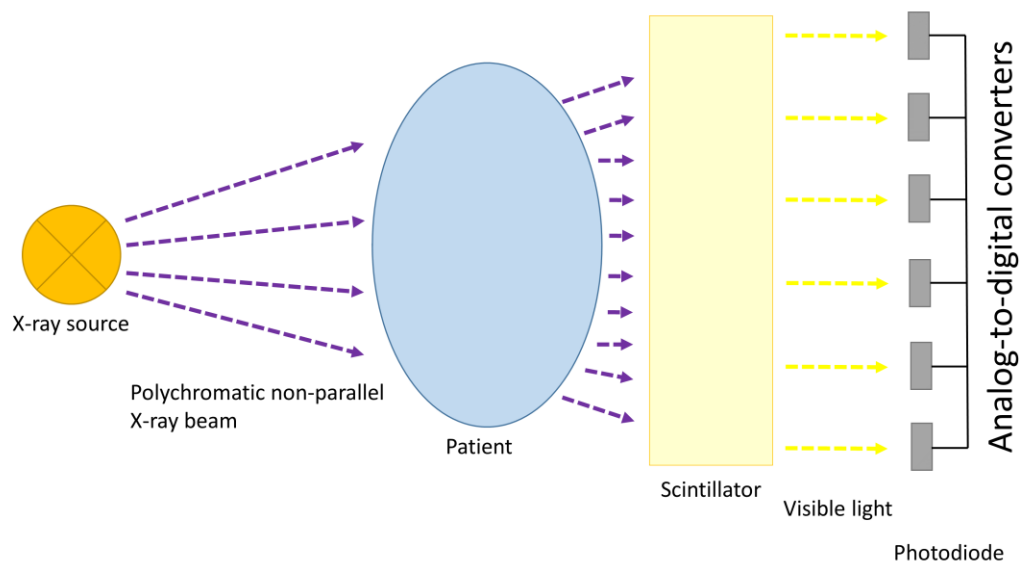


Fig. 1 Scintillator-photodiode detector (indirect X-ray detector). Photodiodes provide an analog signal that is processed by analog-to-digital (A/D) converters.

When CT images are reconstructed, algorithms mathematically assume that a parallel monoenergetic X-ray beam traverses the patient, which is not the case in reality since (a) the beam is fan-shaped and (b) its composition is polyenergetic. Notably, the type and magnitude of photon/material interaction and the resulting beam absorption strongly depend on the energy level of the photons, which is not accounted for in conventional CT systems. At conventional CT, samples with different elemental composition can still exhibit similar mass densities [10] and identical CT numbers, making the materials difficult or impossible to classify [11]. One way to overcome the often-overlapping nature of attenuation coefficients and extract information related to the materials' mass attenuation is to collect absorption data in two or more different energy bands. The energy-

dependency of X-ray attenuation was highlighted quickly after implementing the first CT system in medicine, and physical characterization of the material being scanned – including density and atomic number – had already been recognized and was reported at the very beginning of CT [12, 13]. Additionally, pioneering DECT experiments assessing tissue characterization, bone mineralization quantification, and computation of Z_{eff} and electron density have taken place in the 70s [13-15]. Despite these early insights into the physics of CT, the industrial implementation of spectral CT occurred more than three decades later, and clinical CT systems offering X-ray energy quantification were not available until recently. Reasons for the prolonged time until DECT hit the market are related to technical challenges at this time, including unstable CT numbers, longer scan duration, and limited current at low tube potential [16].

This has changed with the introduction of dual-energy CT (DECT) systems about 15 years ago [17, 18], which can distinguish two (often overlapping) energy bands. Spectral CT detectors are generally referred to as "energy resolving" because they measure not only the transmitted X-ray intensity but can, to a certain extent, measure the spectral composition of X-rays exiting the object or subject being scanned [19]. An ideal DECT system requires the use of two monochromatic X-ray beams with the same photon fluence rate to measure tissue absorption in each band at the same time. Currently, such a design is not suitable for clinical application; hence DECT systems still use less-than-perfect polychromatic beams. CT manufacturers developed various techniques to collect absorption data in two different energy bands. Table 1 summarizes the most widespread approaches, all of which are emission-based except the dual-layer detector design that

operates with standard beam composition and shaping, discriminating two energy bands at the detector level.

Table 1. Commercially available DECT implementations

Type	Manufacturer	X-ray tube	Detectors	kVp range
Dual-source	Siemens	Two tubes with or without beam filtration	Two arrays of energy-integrating detectors	70-150 kVp
Rapid kV-switching	General Electric	Single X-ray tube with ultrafast voltage switching between low and high kVp	One array of energy-integrating detectors with fast scintillator speed	80 and 140 kVp
Dual-layer detector	Philips	Single X-ray tube	One array of dual-layer energy-resolving detectors	120 or 140 kVp
Twin-beam	Siemens	Single X-ray tube with filter splitting the beam in the Z-direction	One array of energy-integrating detectors	120 kVp (with additional Au and Sn filtration)
Sequential dual scans	Canon	Single X-ray tube; first rotation at low kVp, second rotation at high kVp	One array of energy-integrating detectors	80-140 kVp

4.3.1 Advantages and limitations of dual-energy CT

Single-energy CT has a fundamental limitation in differentiating soft tissue because the CT number depends entirely on the linear attenuation coefficient (μ), which is strongly overlapping between body tissues [20]. Only a handful of heavier elements, such as calcium or iodine, exhibiting strong photoelectric absorption can be classified relatively easily. DECT is a significant step forward with respect to soft tissue differentiation due to its ability to measure materials' differential attenuation as a function of photon energy. Compared with conventional single-energy scanning, DECT has the advantage of incorporating both lower (usually 70-80 kVp) and higher (usually 140-150 kVp) energy images simultaneously, providing a new layer of information enabling the extraction of optimized image features for various clinical scenarios. Practically, DECT can serve the purpose of improving image quality itself, but also to save radiation dose and contrast medium. In vascular radiology, DECT can improve diagnostic accuracy and even reduce interpretation times [21].

On the other hand, DECT systems suffer from several fundamental limitations, including a considerable overlap of energy spectra, the absence of notable improvement in spatial resolution compared with single-energy CT, and high electronic noise precluding major dose savings. Except for the detector-based DECT implementation, current DECT systems also suffer from spatial and/or temporal misalignment of spectral data because the high and low energy data are not acquired at the same location and at the exact same moment. Moreover, DECT samples only have two spectral datapoints, limiting multi-material decomposition. A typical example is the iodine density map (iodine versus water material decomposition), which cannot reliably classify calcium as non-iodine material

because calcium exhibits a substantial probability of photoelectric effect and will show up as iodine. Furthermore, some systems have specific limitations directly depending on engineering challenges. For instance, dual-source DECT systems, operating with two distinct sets of tubes and detectors, have a partial spectral field-of-view coverage, which can limit the use of bone subtraction or interpretation of liver lesions in large patients. Such systems – whose strengths include a superior temporal resolution for cardiac imaging – also need to cut back temporal resolution when used in DECT mode because each tube/detector pair will be required to acquire data in a specific energy band.

One more critical point to address when considering DECT for routine use is the impact on workflow: DECT can be time-saving or time-consuming. While spectral reconstructions can speed up CT interpretation, e.g., by allowing a confident distinction between calcium and iodine, and may avoid an additional late-phase acquisition, the implementation of DECT in clinical workflows comes with additional image series. In cardiovascular imaging, these usually include virtual non-contrast (VNC), low/high keV VMI, and iodine density maps, all of which will be discussed later. Spectral image series take time to reconstruct, transfer to PACS, and may interrupt the radiologist's usual workflow.

4.3.2 Dual-energy CT data processing and image types

DECT systems and spectral CT systems in general provide qualitative and quantitative information about tissue composition, offering a range of established and emerging clinical applications. On the whole, spectral CT imaging can be divided into material-specific and material-non-specific applications. The first includes effective atomic mapping (Z_{eff}), electron density mapping, and material decomposition, which can serve to detect, quantify or suppress materials from reconstructed images [22]. The second

comprises virtual monochromatic imaging (VMI), which provides images whose voxels express CT numbers (in HU) as on single-energy images. Still, the energy level at which CT numbers are represented can be selected freely, usually between 40 and 200 keV. This can be useful, for instance, to optimize lesion contrast-to-noise ratio (CNR), to reduce the radiation or iodine dose [23]. VMI is sometimes referred to as “pseudo-monochromatic” because it is a simplified version of true monochromatic imaging utilizing a synchrotron. In VMI, the materials’ energy-dependent CT number is linearly extrapolated from a limited number of data points – two in DECT – and does not represent real-world measurements [24]. VNC images are a particular form of material-non-specific reconstruction that simulates non-contrast CT derived from contrast-enhanced DECT datasets. VNC makes use of the photon-absorption variation at two energy levels of high atomic number elements, i.e., iodine, exhibiting a higher photoelectric to Compton ratio, to selectively remove the contribution of iodine from reconstructed images [25].

Spectral CT post-processing can be done in the projection or the image domain. Projection-based post-processing algorithms operate before the images are reconstructed and yield lower beam-hardening artifacts. On the other hand, they require high spatial and temporal registration of the acquired sinograms, which is only possible with detector-based or fast kV-switching spectral CT [26]. In DECT data analysis, it became apparent that one can decompose spectral CT datasets comprising attenuation data of N energy bands into a set of N basis materials using a mathematical operation called "material decomposition." Material decomposition algorithms assume that the entire sample is composed of N preselected materials and that voxels contain a volume fraction of each material in variable amounts. This means that mathematically, the sum of

volume fractions must always be equal to 1. The fractional composition of a voxel can then be computed based on (a) the measured CT number at each energy level and (b) the energy-dependent attenuation of each material in pure form. The latter is a physical constant that can be obtained from the National Institute of Standards and Technology (NIST), among others. The concept of two-material decomposition (when $N=2$) has translated from research into clinical routine with DECT systems, one of the most popular material pairs being water-iodine (iodine density map), allowing iodine quantification [27]. Though, in theory, any material pair can be reconstructed using these algorithms, depending on the materials present in the sample of interest (e.g., bone, fat, iodine) and the clinical task [28, 29].

4.3.3 Clinical applications

Once DECT became clinically available, research groups have enthusiastically geared up to find out where this technology could add value. Despite remarkable efforts from institutions and researchers worldwide, the widespread use and integration of DECT in clinical routine have occurred at a slow pace, likely due to concerns regarding healthcare costs and radiation dose [30]. Meanwhile, the role of DECT in clinical care is continuously developed and emphasized. In cardiovascular imaging, in particular, DECT has shown the potential to improve patient safety (by reducing radiation and iodine doses) and improve disease detection and classification. Iodine dose reduction in large-vessel examinations has been demonstrated [31] by using low-energy (40 keV) VMI. Still, the same spectral imaging type also helped improve vessel opacification in cases of suboptimal enhancement in pulmonary CT angiography [32]. Other studies confirmed radiation dose saving potential with virtual non-contrast reconstruction for aortic endograft

surveillance [33], a very specific clinical application whose promising results call for broader concept validation. While dual-energy pulmonary CT angiography failed to prove superior to single-energy for detecting pulmonary embolism [30], its use can provide additional prognostic value derived from semi-quantitative perfusion beyond clot burden quantification, with no additional contrast medium or radiation dose exposure [34, 35]. Thanks to its ability to optimize lesion-to-background contrast with VMI and iodine density maps (iodine versus water material decomposition), DECT also offers advantages in the characterization of myocardial ischemia [36] and the discrimination of left atrial appendage thrombus from slow flow [37]. Furthermore, DECT enables accurate myocardial late enhancement evaluation compared to late gadolinium enhancement, the current gold standard [38], paving the way for the so-called “one-stop-shop” acute chest pain imaging workup with the possibility to detect myocarditis using DECT [39]. Preliminary research also highlights the value of DECT to increase the conspicuity of acute bowel ischemia in small cohorts. However, the optimal VMI energy level to use is still debated [40, 41]. Finally, DECT has been proved efficient in reducing metal artifacts that are highly prevalent in cardiovascular imaging due to the frequent presence of electronic devices, leads, coils, and grafts containing metallic components [42].

Apart from these benefits directly related to cardiovascular medicine, DECT offers a diverse spectrum of clinical applications in other fields such as musculoskeletal radiology, neuroradiology, emergency radiology, to name only a few, extending even to forensic imaging [43].

4.3.4 Clinical examples of dual-energy CT

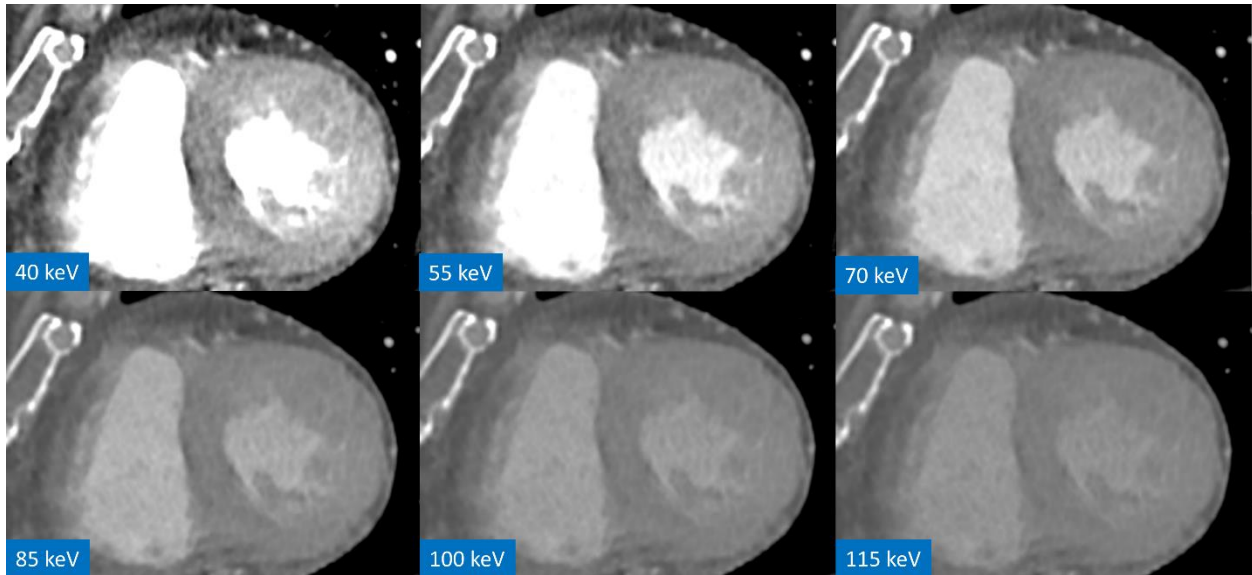


Fig. 2 Small-axis multiplanar reformats of the heart from a pulmonary CTA acquired on a fast kV-switching DECT without ECG-gating. VMI at six different energy levels show the dramatic increase in heart chamber attenuation at lower energies (40 and 55 keV) and attenuation decrease at higher energies (85, 100, and 115 keV). The 70 keV image can be considered equivalent to conventional CT. Note the increase in myocardial tissue contrast, demonstrating heterogeneity at 40 keV.

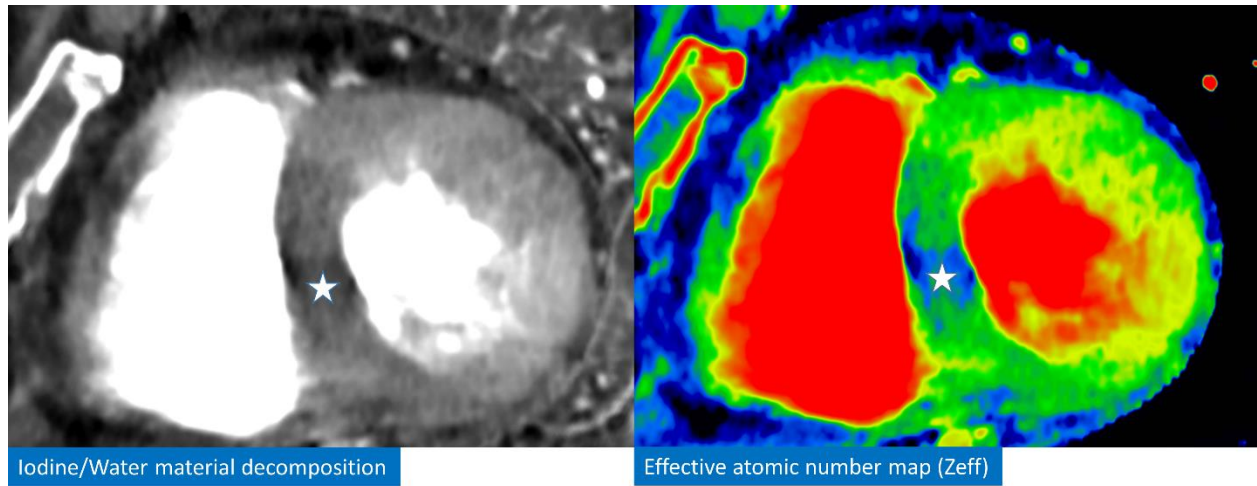


Fig. 3 Same pulmonary CTA examination as in Fig. 2 shows two other spectral reconstructions highlighting acute myocardial ischemia in the septal wall (white star), in the form of decreased iodine concentration on the Iodine/Water material decomposition, and the form of a decreased Z_{eff} .

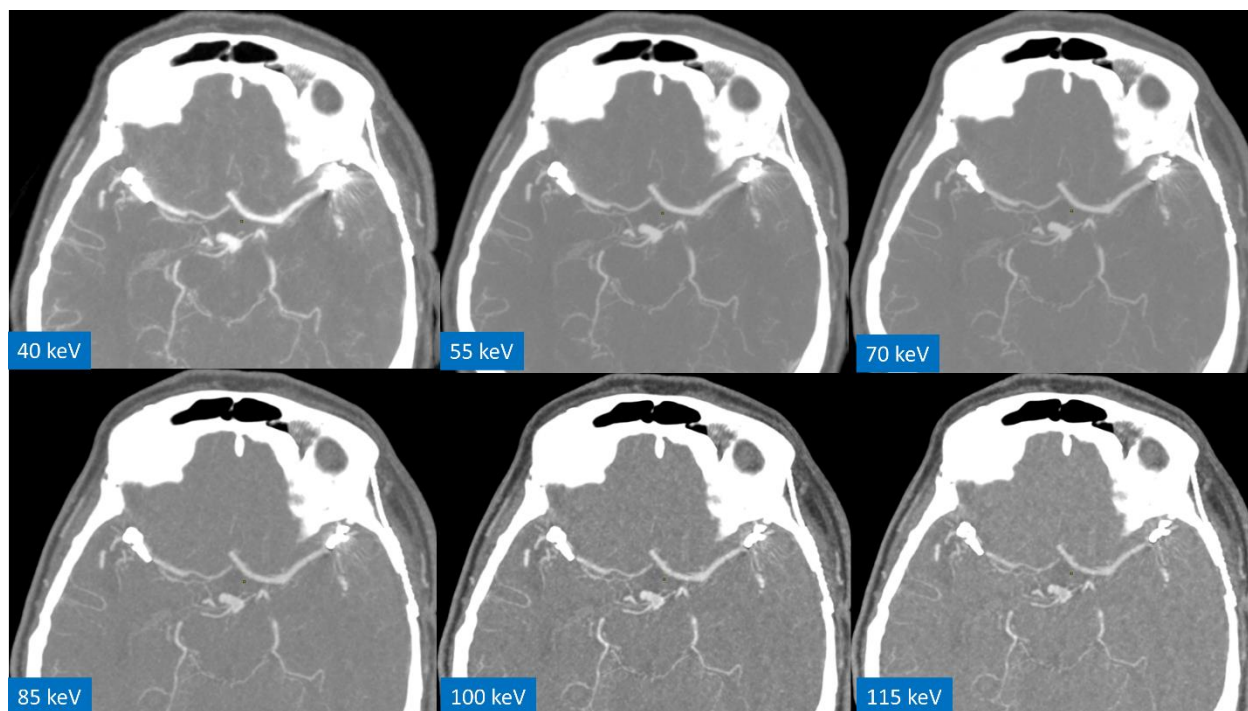


Fig. 4 Cerebral imaging in a patient with bilateral intracranial aneurysm clipping causing beam hardening artifacts. The CTA was acquired on a fast kV-switching DECT system and reconstructed as VMI at different energy levels. The strong beam hardening artifacts hampering image analysis on the 40 keV VMI increasingly vanish with higher VMI energies.

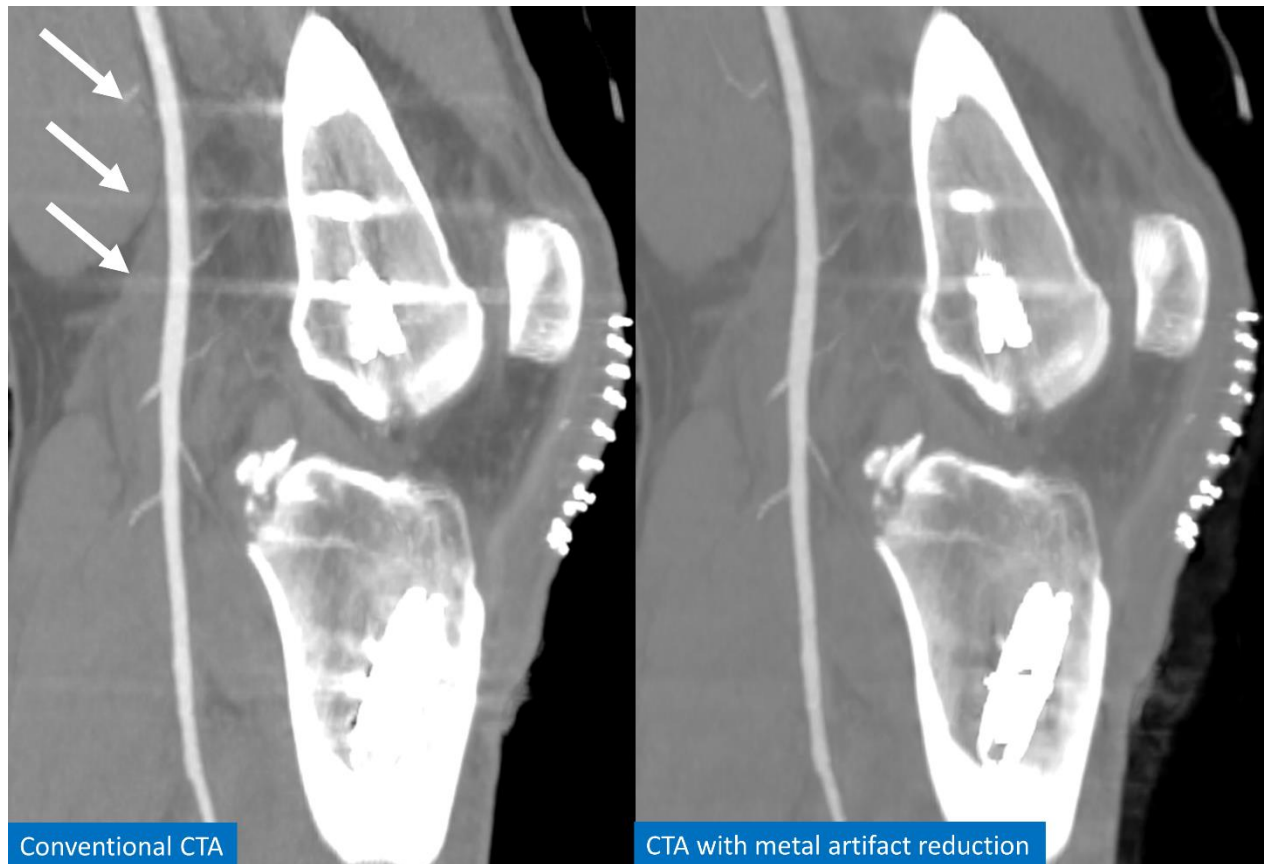


Fig. 5 Lower extremity CTA acquired on a fast kV-switching system without and with the vendor's proprietary metal artifact reduction software (MARS). This software segments and corrects metal artifacts based on CT number thresholds [44]. Note the significant reduction of streak artifacts (white arrows) due to metallic osteosynthesis material of the femur on the MARS reconstruction.

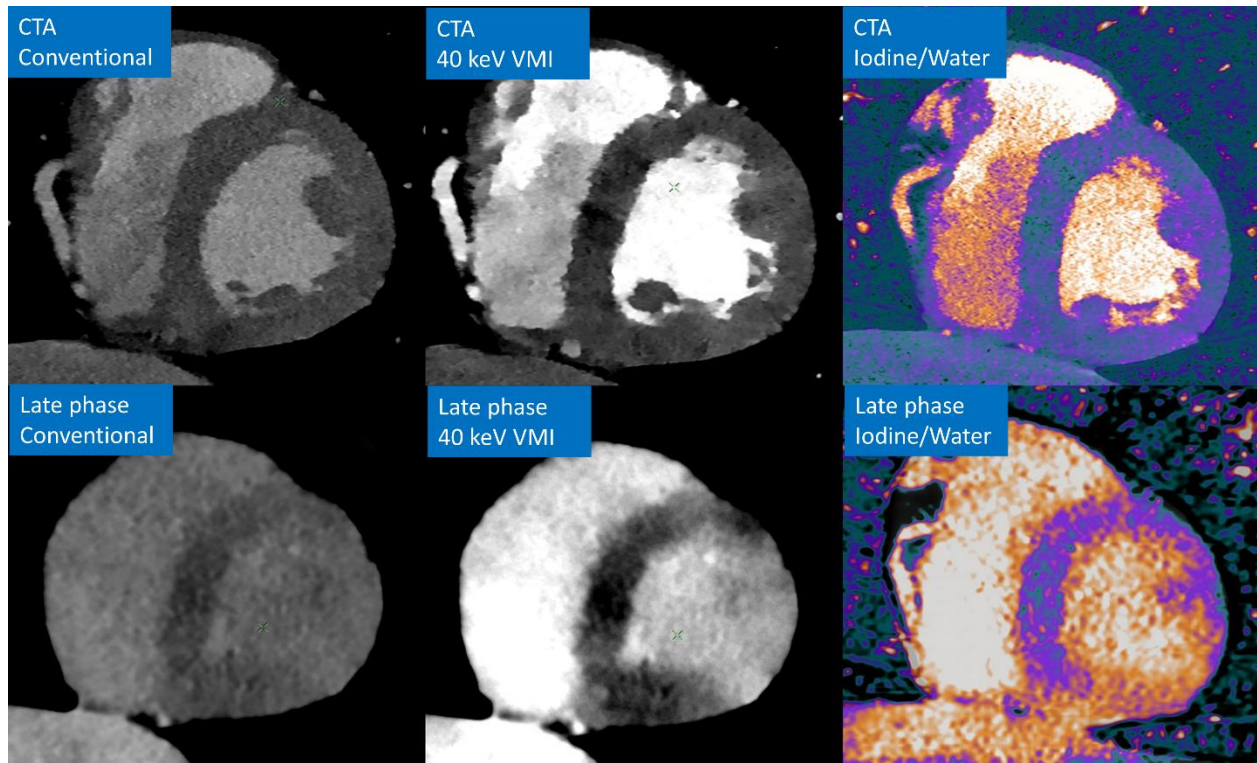


Fig. 6 Cardiac CTA acquired on a dual-layer spectral detector system in a patient with acute chest pain. Coronary CTA was unremarkable, and no perfusion abnormality was seen on first-pass static perfusion (upper row), whether on conventional, low-energy VMI or iodine vs. water material decomposition. On the other hand, late phase (late iodine enhancement) images showed almost transmurular enhancement of the lateral myocardial wall, better depicted on low-energy VMI and iodine vs. water images, consistent with acute myocarditis [39].

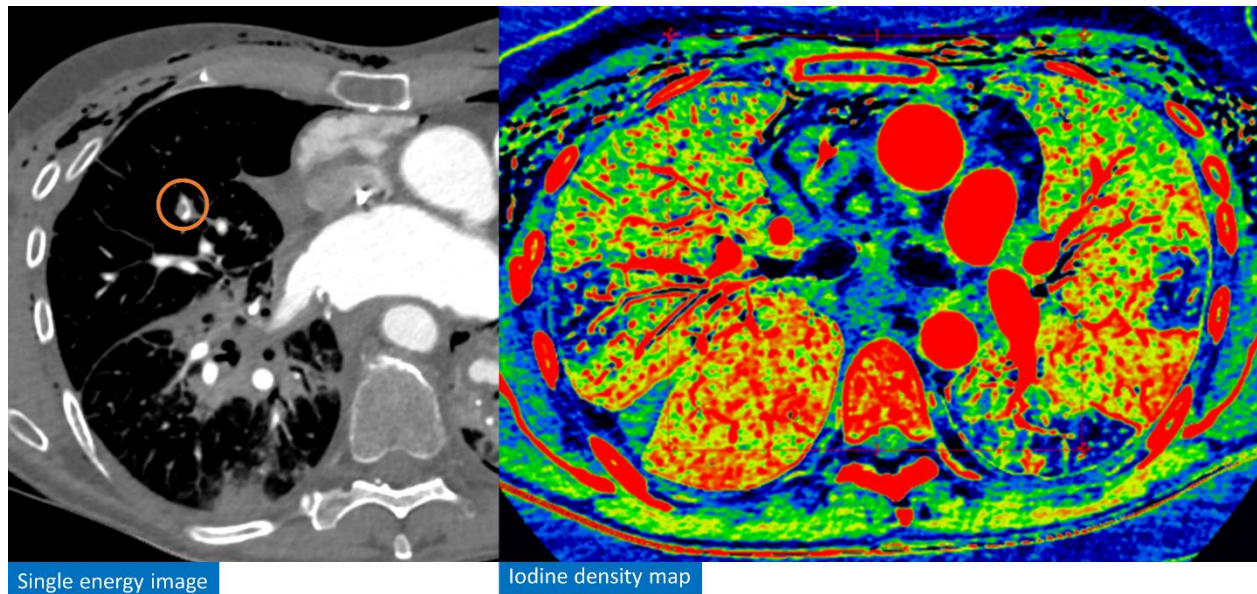


Fig. 7 Pulmonary CTA in a patient with post lung transplantation (day 5) dyspnea. While HU images depicted right middle lobe sub segmental pulmonary embolism (orange circle), iodine basis images (“iodine density maps”) representing iodine distribution (blue, no iodine, red maximum iodine concentration) help diagnose multiple bilateral peripheral perfusion defects throughout the lungs (not all defects are shown in the Figure), consistent with additional occlusive pulmonary emboli.

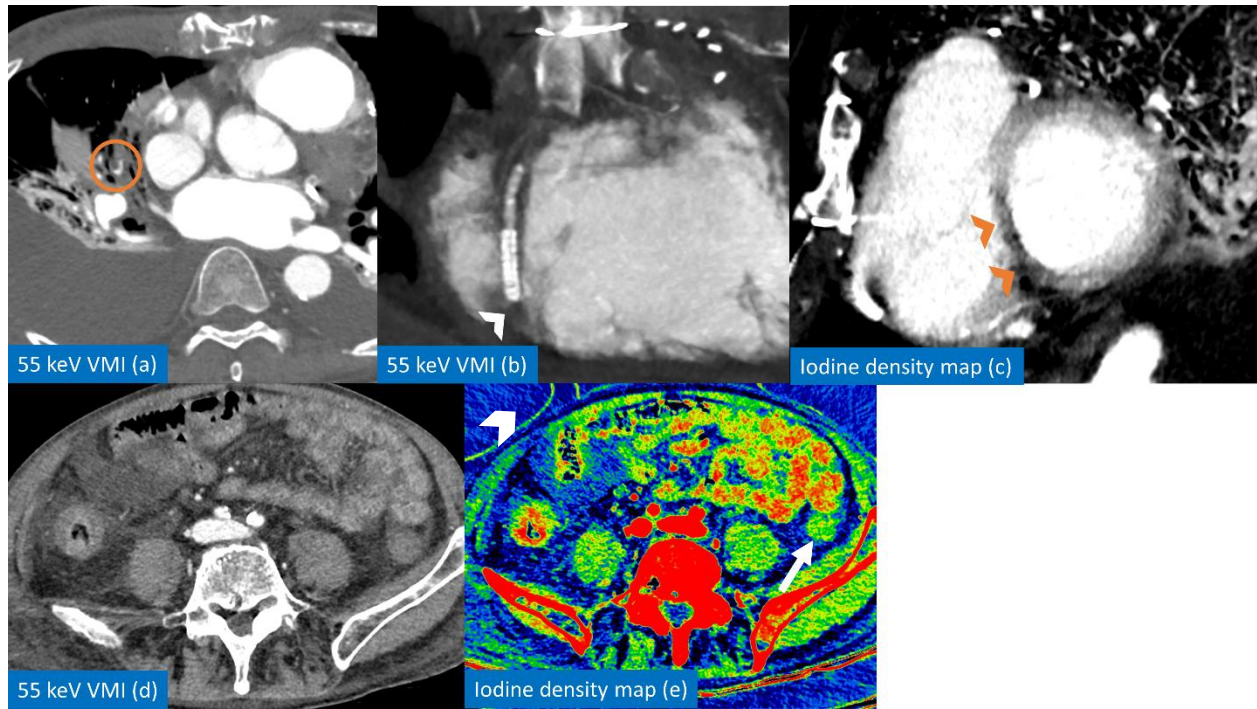


Fig. 8 Thoracic-abdominal CTA in a hemodynamically unstable patient presenting with acute abdominal pain and beta blocker overdose. Questions asked to the emergency department's radiologist included: acute aortic syndrome, acute pulmonary embolism, and mesenteric ischemia. In this case, spectral CTA addresses all questions in a single acquisition; thoracic 55 keV VMIs show right middle lobe segmental acute pulmonary embolism (a, orange circle), and the absence of distal right coronary artery opacification (b, white arrowhead), indicating stent occlusion, causing mid cavity septal hypoperfusion as demonstrated on the iodine density map (c, orange arrowheads). The same acquisition covering the abdomen (d) confirmed colon ischemia likely due to the overall compromised hemodynamics, better visible on the colored iodine density map where the left colon (e, white arrow) appears to be less perfused than its right portion or the small bowel.

4.4 Photon-counting CT

More recently, spectral photon-counting CT (PCCT) systems have been developed and are currently undergoing prototype testing by medical researchers [45, 46]. Such systems provide improved energy resolution over DECT, being able to classify photon energies according to three or more energy bands with less overlap [46, 47]. PCCT is one of the most advanced spectral CT techniques currently under investigation. Photon counting detectors' (PCD)'s principle is to use semi-conductor detector materials operating without the need of generating visible light inside detector elements, thereby getting rid of the challenges related to scintillators and associated electronic noise while providing a refined spectral analysis (Fig. 9). Incident X-ray photons create hole pairs in the semiconductor material that travel to the anode under the influence of the (high) bias voltage applied across the semiconductor and create directly measurable electric signals, whose pulse amplitude is proportional to the photon's energy; for this reason, PCD are considered direct-conversion detectors. Each detector channel is equipped with an application-specific integrated circuit (ASIC) that reads out the electric pulse and discriminates its amplitude according to discrete thresholds called "energy bins." The number of energy bins is given by the ASIC's design. PCD can reject electronic noise almost entirely by using a threshold high enough to be above the noise floor and discriminate real photon counts from noise.

Contrary to conventional energy-integrating detectors (EID) that measure the total energy deposited in the detector and may corrupt part of the attenuation data due to electronic noise, PCDs quantify the energy of each individual incident photon according to two or more energy bins which are user-selectable energy sub-ranges that can be adjusted

according to the clinical task. This results in a much better spectral sampling of X-ray transmission. The scintillators used in EIDs suffer from reduced dose efficiency due to the septa that isolate detector elements from each other; because PCDs do not require a physical separation inside the detector material, they can be produced with a much smaller detector element size to increase spatial resolution (150 μm). For these reasons, PCCT is expected to address major limitations of EID-based DECT [48].

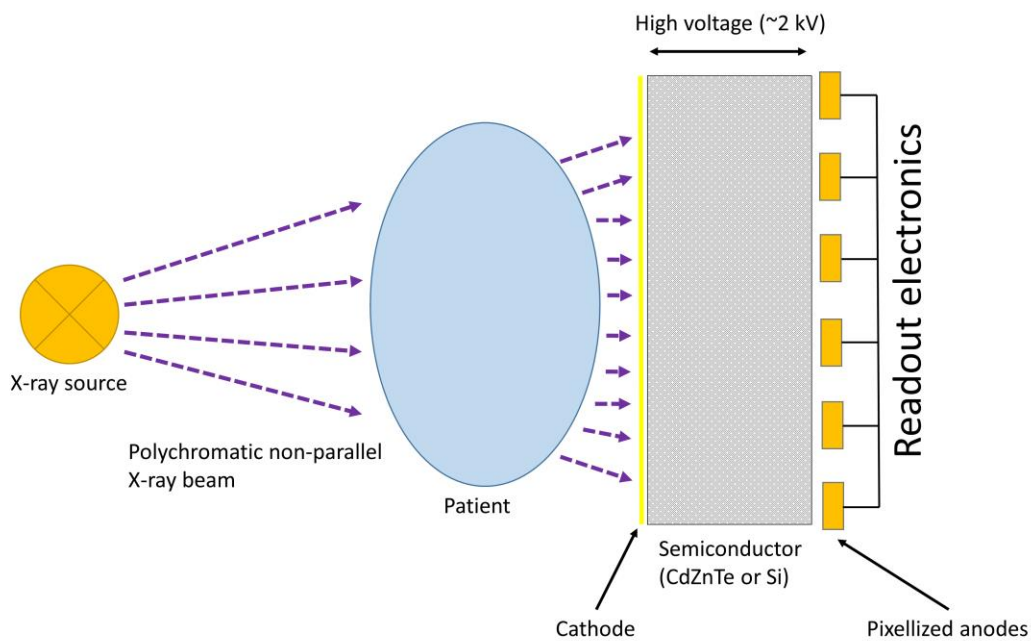


Fig. 9 Photon counting (direct conversion) detector. Currently evaluated detector materials for CT are Cadmium Zinc Telluride (CdZnTe) and Silicon (Si). Ideally, each X-ray photon is detected separately and assigned to an energy category.

The first large field-of-view PCCT ran cadmium zinc telluride (CdZnTe) detectors and was tested for carotid CTA in 2007 [49]. At the time of writing, several more PCCT systems

were being evaluated, most of which used Cd-based detectors, i.e., CdZnTe or Cadmium Telluride (CdTe) [50-52]. Of note, one silicon-based (Si) PCCT system was being tested as well [53, 54]. CdZnTe, CdTe, and Si detectors have their own advantages and limitations. A hallmark of CdZnTe and CdTe is their high X-ray stopping power; less than 2 mm are enough to stop 95% of photons at 120 kVp after traveling through 30 cm of water, while Si detectors have a lower atomic number and need 55 mm of thickness to achieve the same absorption [47]. Another difference between Cd-based and Si detectors is the predominance of different types of photon interaction within the semiconductor material itself; the first will exhibit more photoelectric effect, while the latter has a much higher probability of Compton scattering. Also, Cd-based detectors have a higher amount of material imperfections, which can degrade detector performance [55]. Last but not least, Cd is a highly toxic element [56], which should be taken into account when speaking about the widespread production and handling of Cd-based PCDs.

4.4.1 Advantages and limitations

Apart from the strengths mentioned above – higher spatial resolution and severely reduced electronic noise – PCD offers further versatility depending on the number of energy bins available. Theoretically, a PCCT system should allow distinguishing more than two materials in a non-contrast examination, which can be helpful in specific clinical scenarios, such as imaging the vulnerable atherosclerotic plaque [57]. Because the PCD's energy bands are user-configurable, it is possible to collect data just above and below a material's K-edge, enabling "K-edge imaging" and introducing simultaneous imaging of multiple CMs and potentially molecular imaging [58, 59]. This is true for materials whose K-edge lies within the clinical energy range. Moreover, PCCT eliminates any spatial or

temporal misregistration thanks to its detector-based nature, offering full-field-of-view capability and can operate at various tube potentials. Finally, PCDs have no scintillator afterglow, which can introduce measurement errors in EIDs.

Despite significant advantages, PCDs come with a number of limitations, including pulse pile-up, K-escape, and charge sharing, some of which have been preventing PCCT from becoming clinically useful until now. PCDs have been in use in nuclear medicine from the beginning. Still, the much more tough challenge of the high count rate encountered in X-ray CT prevented the technology from being clinically useful until recently [60]. The major challenge for manufacturers has been to design a detector and readout electronic chain capable of handling the high photon flux and exposure (X-ray fluence rates can be up to $10^9 \text{ mm}^{-2} \text{ s}^{-1}$). Each photon must be separated and registered; otherwise, two pulses can accidentally be read a single pulse, a condition referred to as “pulse pile-up,” causing spectral resolution decrease. Another drawback is pulse sharing, which refers to the distribution of the charge cluster produced by one incident photon into multiple detector elements, misleading the system into counting several lower-energy photons. Finally, K-escape happens when the characteristic fluorescence photon generated inside the detector escapes and cannot contribute to the pulse amplitude. All those issues deteriorate noise performance, spatial and spectral resolution [61].

4.4.2 Clinical applications

The rapid technological innovations currently serving the medical field are astonishing, and by overcoming many of today’s challenges of conventional CT, PCCT will have a profound impact on patient management. Currently, prototype systems operating with

PCD have restricted availability but drive a worldwide enthusiasm, and some pre-clinical and even early clinical studies are available.

One of the most direct clinical benefits of PCCT – with radiation hazards in mind – is to save dose, which is easily achieved thanks to the low noise characteristics of PCDs. Because PCDs reject electronic noise, the X-ray dose can be reduced substantially while preserving diagnostic information [50, 62, 63]. Children who are extra sensitive to ionizing radiation but whose clinical management still relies on CT will be prime beneficiaries of the drastic dose savings PCCT can achieve [64]. Furthermore, improved CNR owing to a selective weighting of lower-energy photons brings a broad range of clinical applications, some of which have already been assessed in initial studies. These include lung nodule assessment in asymptomatic volunteers [45] or improved visualization of blood vessels and enhancing tumors [65]. The CNR improvement will be even more marked for heavier elements like iodine or gadolinium since the attenuation due to the photoelectric effect is proportional to the atomic number [66]. Better energy information and improved CNR can be utilized either to achieve higher lesion conspicuity or can be translated into X-ray dose reduction.

The intrinsically higher spatial resolution offered by PCCT may benefit lung, musculoskeletal, inner ear, but above all cardiac imaging, although only phantom and ex-vivo studies are currently available [67-69]. PCCT also showed promise for metal artifact reduction in phantom studies [70], beam-hardening artifact reduction in cadaveric studies [62], and nanoparticle-based blood pool imaging [71]. Radiomics, a promising research field aiming to extract a large number of quantitative features from CT images, currently

depends on acquisition parameters, thereby hampering widespread applicability. Quantitative PCCT-derived maps have the potential to mitigate this limitation.

That being said, with the combination of high spatial resolution, low-noise, and versatile multi-energy capabilities offered by PCCT, imaging will become increasingly task-driven. One might go so far as to imagine patient-dependent energy bin configuration to optimize detection or quantification tasks – and further improvements are ahead of us, especially once the technology comes into the hands of radiologists and clinicians.

4.4.3 Clinical examples of photon-counting CT

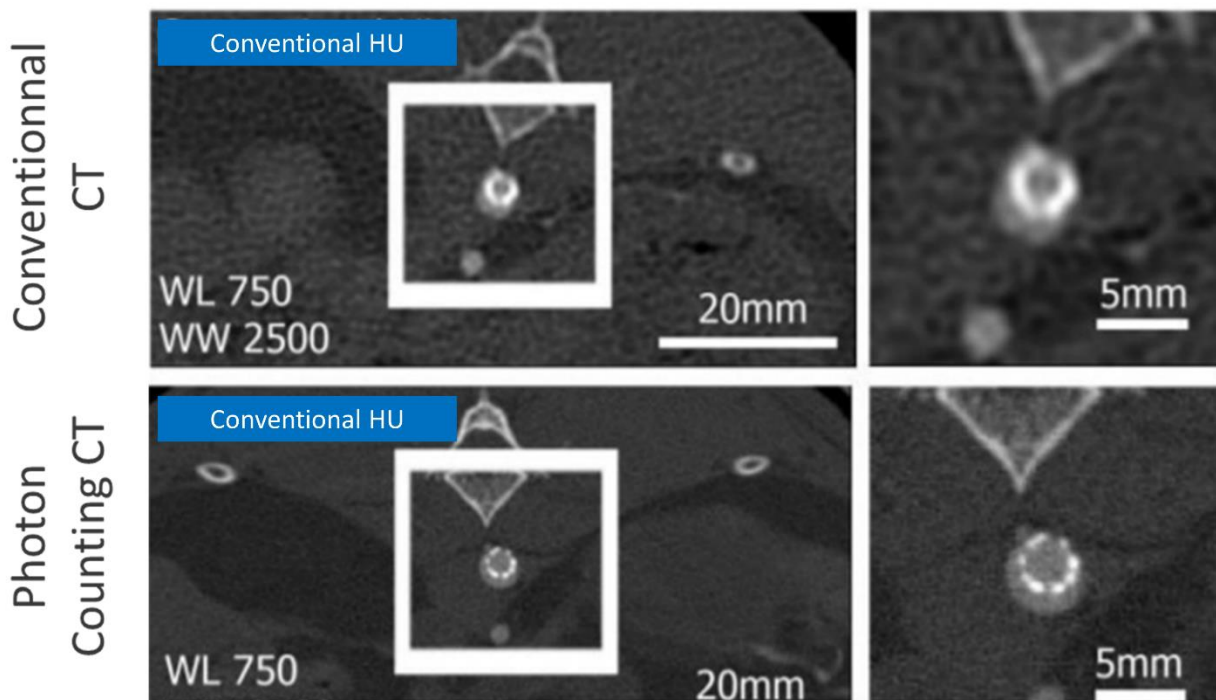


Fig. 10 Comparison of photon-counting and conventional CT for in vivo stent assessment in a rabbit. Ultra-High Spatial Resolution images from PCCT (lower row) show a significantly improved visualization of the rabbit aorta (about 4 mm diameter) compared with conventional CT (upper

row). In particular, the stent and intrastent lumen can better be visualized—courtesy of Dr. M. Sigovan, CREATIS Laboratory, Lyon University, France.

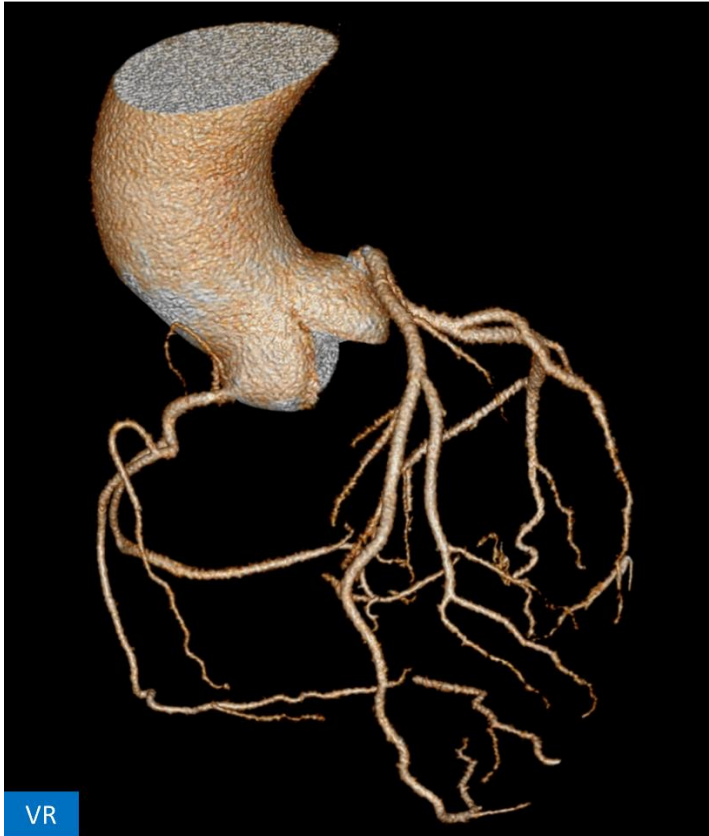




Fig. 11 Cardiac images of a 48-year-old woman with chest pain, acquired on a single source CT prototype with a photon-counting detector, after the injection of 45 mL of iodine (400 mg/mL) at a rate of 4 mL/sec. Data acquisition: ECG gated helical mode with 64 x 0.27 mm collimation, 0.33 s rotation time, CT Image reconstruction: sharp reconstruction kernel, 1024 x 1024 image matrix, 0.25 mm slice thickness. Excellent visualization of the coronary arteries, including small branches in volume rendering (VR) and subtle peri-coronary fat infiltration consistent with inflammation on short-axis multiplanar reformat (MPR) of the left circumflex (LCx) artery. Courtesy of Prof. Douek, Hospices Civils de Lyon, France.

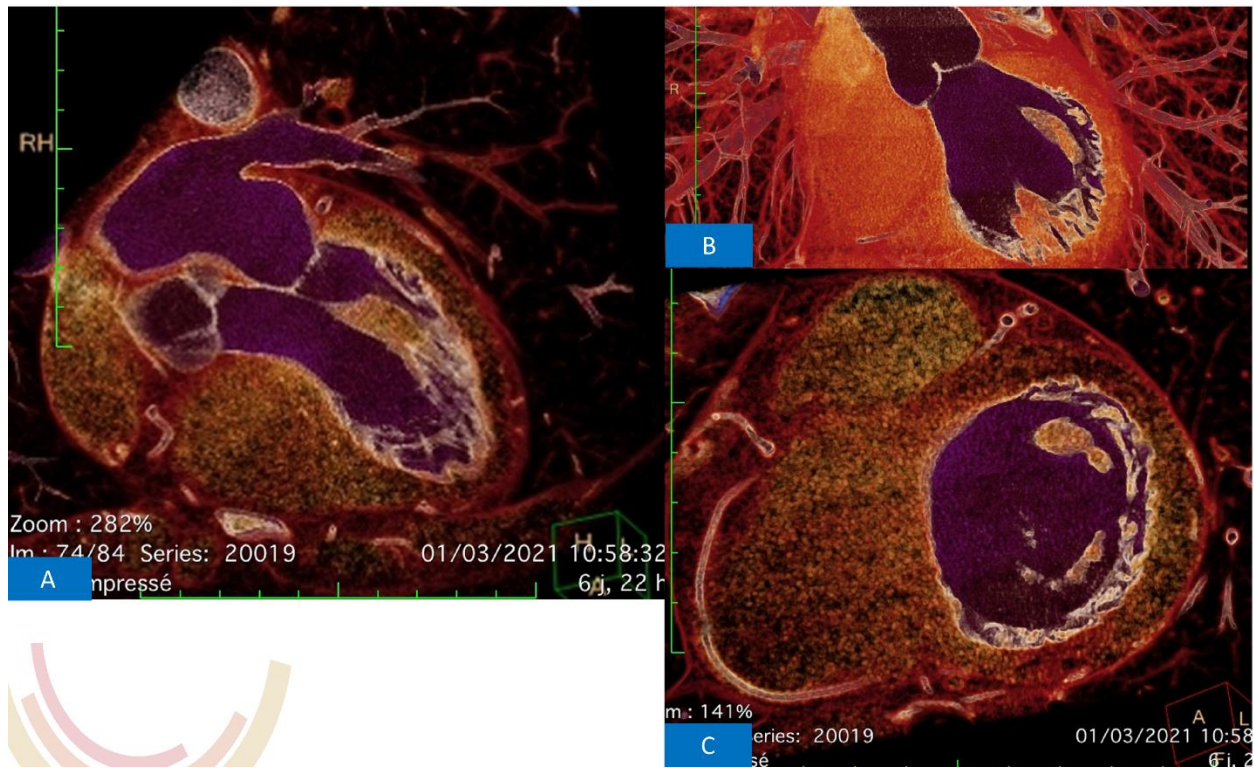


Fig. 12 Cardiac PCCT reconstructed in volume rendering showing anatomical details of the mitral valve an papillary muscle, and the aortic valve on 3-chamber (A), left ventricular outflow tract (LVOT) 2 (B), and left ventricular short axis (C). Courtesy of Prof. Douek, Hospices Civils de Lyon, France.

4.5 Aims of the thesis

Despite significant efforts made to deliver improved patient care with the help of spectral CT, a number of which are discussed above, numerous open questions remain regarding both DECT and PCCT systems. While some advantages in using spectral CT have been clearly identified, the rapid expansion of spectral CT systems for clinical practice must happen with all due caution because inappropriate use of new technologies can harm the diagnostic performance in clinical routine. Consequently, both new roles and limitations of spectral CT have to be assessed thoroughly before clinical implementation. This is especially true because the continuing efforts granted by the manufacturers result in gradually improving technology; as a consequence, early concerns related to artifacts, excessive radiation dose, or workflow issues do not necessarily hold true with more modern systems hitting the market [72-74].

Patient security undergoing CT has been continuously improving. However, ionizing radiation and iodinated contrast media exposure remain potential drawbacks to unrestricted use of CT. The first is especially concerning for children and young adults whose tissues are highly radiosensitive [75]. The latter is problematic for the elderly at higher risk of cardiac or renal adverse reactions [76]. Strategies to reduce both ionizing radiation and contrast media exposure will be explored.

Disease detection is usually the first task involved in radiological evaluation; a diagnostic test with inappropriate detection performance is useless. Spectral capability redefines CT imaging in many ways, and detection rates are expected to improve, as suggested by preliminary DECT studies [27, 77]. We will assess lesion detectability with spectral CT in

the field of cardiovascular imaging, such as atherosclerotic plaque and lipid core detection.

Following lesion detection on CT, a second and often a third task that characterizes and quantifies the disease is required to provide relevant information to drive therapeutic decisions. Because spectral CT offers insights into tissue composition, striking advances in lesion characterization are anticipated. Initial studies support this hypothesis, both using DECT [78] and SPCCT [79]. In this respect, we will evaluate the potential roles of spectral CT in improving the accuracy of quantitative tasks.

With this in mind, the goal of this thesis is to highlight the added value of spectral CT compared with conventional to assess the vascular lumen (stenosis quantification) and disease of the vascular wall (wall conspicuity, atheroma plaque size, and composition), using the latest systems available clinically and pre-clinically. Expected benefits for patient care are twofold: (a) to potentially reduce the ionizing radiation dose and/or intravenous iodine dose associated with a CT examination; (b) to improve the detection, characterization, and quantification of disease. The first set of benefits relates to patient safety when undergoing a CT examination. The latter aims to provide higher diagnostic accuracy by extracting more relevant information from X-ray imaging to drive therapeutic decisions.

The practical approach to the project's scientific part involves designing several phantom experiments to address specific issues and evaluate the feasibility of spectral CT techniques. When adequate evidence from phantom works and available peer-reviewed

literature is gathered, the experimental approach translates into clinical studies that are also part of the thesis. An overview is provided in section 5 of the dissertation.

4. Thesis milestones

5.1 Building a collaborative project

The two mainstays (expected benefits) defined above are the thesis' framework. Several projects – including experimental and clinical studies – are designed to expand the current understanding of cardiovascular spectral CT. To succeed in such a complex field, the whole project had to rely on multiple international collaborations illustrated in Fig. 13. First and foremost, a solid collaborative relationship between the University Hospitals and Universities of Lausanne (UNIL/CHUV) and Lyon (UdL/HCL) constituted the project's base. The UdL hosts a clinical DECT system and is one of the rare institutions to have a pre-clinical prototype PCCT system. This privileged situation of UdL/HCL is the result of a tight collaboration with an industrial partner (Philips Healthcare and Philips Research), successful fundraising with H2020, and the launch of a multinational consortium aiming to advance the science and technology of PCCT [80]. The UNIL/CHUV also hosts clinical DECT systems and benefits from an expert Radiation Physics Institute developing leading-edge image quality metrics in CT. Methods developed by the CHUV's Radiation Physics Institute can leverage the impact of novel technology, both in the form of prototypes still under development or fully approved commercial products. The center for biomedical imaging (CIBM), a partnership between the Universities of Lausanne, Geneva, and the Swiss Federal Institute of Technology in Lausanne (EPFL), supported phantom analyses conducted as part of this thesis. Needless to say, the industrial partners (Philips Medical Systems, Haifa, Israel, and Philips Research Europe, Hamburg, Germany), in charge of developing DECT and PCCT technology, were involved in the project and provided technical support. Thanks to the long-lasting and reliable relationship between

academic and industrial entities, the research was conducted smoothly, except for the coronavirus disease 2019 (COVID-19) pandemic, which delayed critical sections of the project (COROGOUT project, please refer to section 6.1.3).

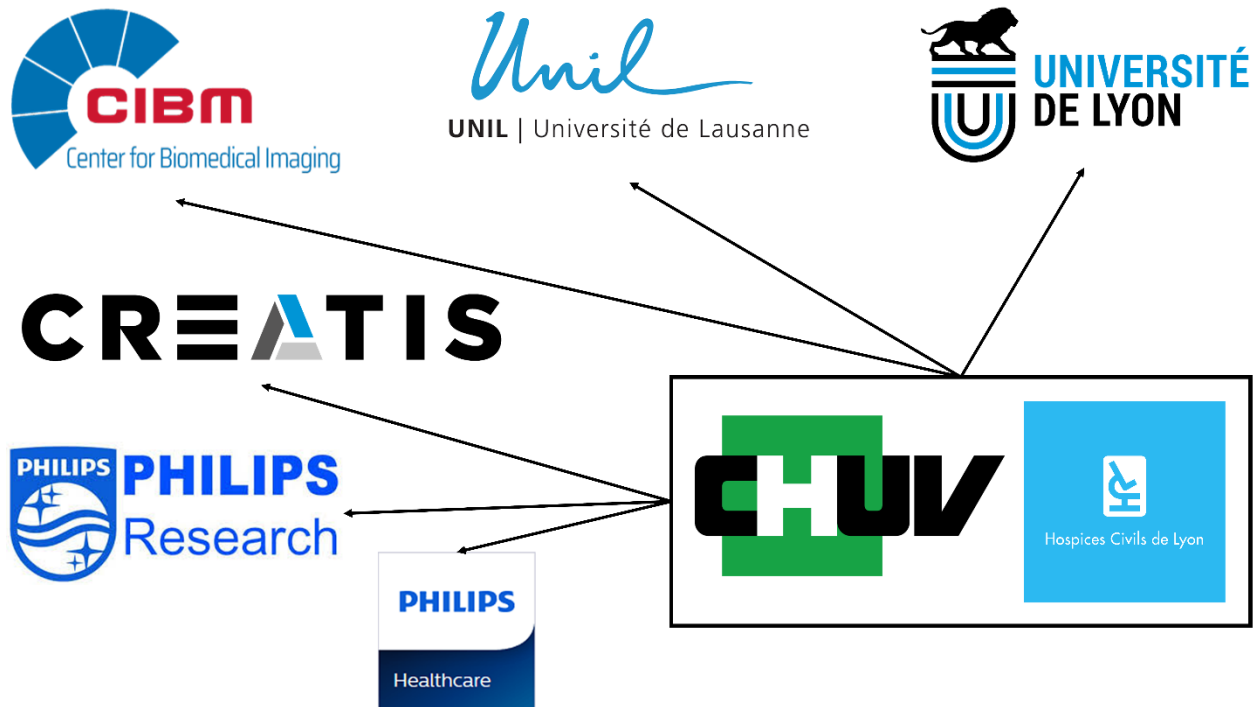


Fig. 13 Institutions and companies constituting an extensive international collaboration made the thesis project possible.

5.2 Importance of experimental approaches

5.2.1 Assessing image quality in CT

The decision to implement new technology in medicine relies on two main pillars: it should improve diagnostic accuracy and outcomes. Incidentally, its cost should be reasonable, and the economic burden put on the community must be seriously counterbalanced by apparent public health benefits [81]. Therefore, techniques and methods to assess the

diagnostic performance of CT play a crucial role in ensuring a certain consistency in system performance and highlighting advancements in imaging technology in the medical field. Because technological innovation has been CT's daily bread, continuing efforts have been undertaken to put into practice the latest CT systems in medical care. However, CT research, in general, has received criticism because producing a visually adequate image of the human body may be an essential step but does not necessarily translate into better outcomes, and the reporting of radiology studies was sometimes lacking [82]. What really matters is the diagnostic information an imaging examination can grasp, and the doctor in charge can recover. Only clinically relevant information can alter the decision-making process, and ultimately, patient outcomes [83]. Despite this, much of the literature has focused on describing new technology, especially in the early days of CT [84]. Radiology research has since gone a long way, the scientific rigor and methodological robustness of studies have improved steadily, and quality/safety research is now part of the landscape in radiology [85].

Meanwhile, more than ever, technological advances in CT are underway, and previously designed methods to quantitatively assess image quality in CT are no longer suitable. This is especially true with the introduction of modern image reconstruction algorithms, whose non-linear behavior threatens the interpretation and conclusions drawn from classical image quality metrics [86]. In this context, spatial resolution in CT has classically been evaluated using the modulation transfer function (MTF) [87]. The MTF is usually obtained by scanning a thin tungsten wire surrounded by air; in other words, a high object-to-background contrast situation with low noise. Because such conditions are not representative of clinical tasks, medical physicists have developed a more advanced

target transfer function (TTF) technique. The TTF can measure the CT system's performance at lower contrast and higher noise (using water filtration) to approximate specific clinical tasks [88, 89]. Likewise, image noise in CT is often assessed by measuring the standard deviation of CT numbers in a region-of-interest taken in a homogenous part of the object or patient. While this kind of metric can broadly approximate the overall noise magnitude, it disregards a critical noise characterization component: noise texture [90]. With constant noise texture, a lesion's detectability is well correlated to its contrast-to-noise ratio (CNR), as shown in Fig. 14.

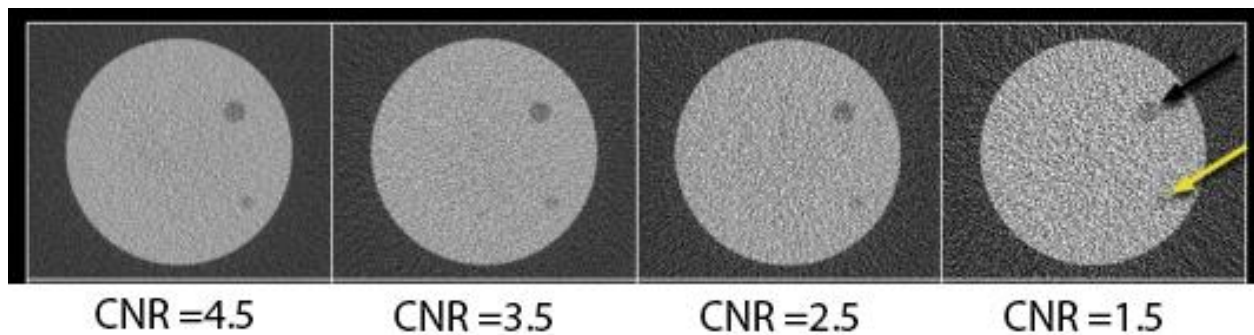


Fig. 14 With increasing noise but constant texture, lesion detectability and contrast-to-noise ratio (CNR) are correlated. Courtesy of Prof. Francis R. Verdun.

On the other hand, when noise texture changes – which is the case with modern CT reconstruction – despite a constant CNR, lesion detectability can vary dramatically. In other words, lesion detectability and CNR are no longer correlated, as shown in Fig. 15.

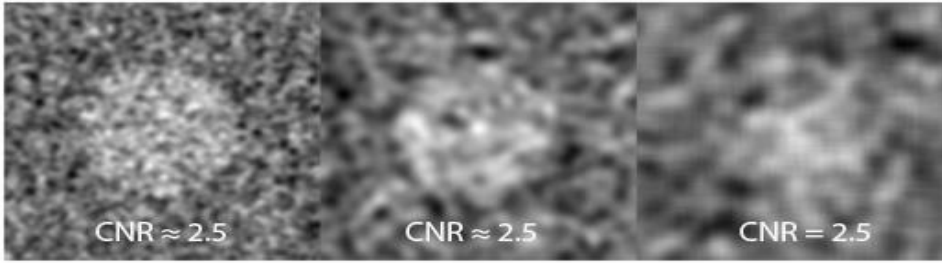


Fig. 15 With noise texture deviation, lesion detectability and contrast-to-noise ratio (CNR) are no longer correlated. Courtesy of Prof. Francis R. Verdun.

To overcome this limitation and account for noise texture, the recommended noise measurement technique is the noise power spectrum (NPS). NPS allows for complete noise characterization by decomposing it according to its spatial frequency components, thereby indicating noise texture [88]. Fig. 16 Schematically represents the effect of increasing noise magnitude with constant texture on the NPS.

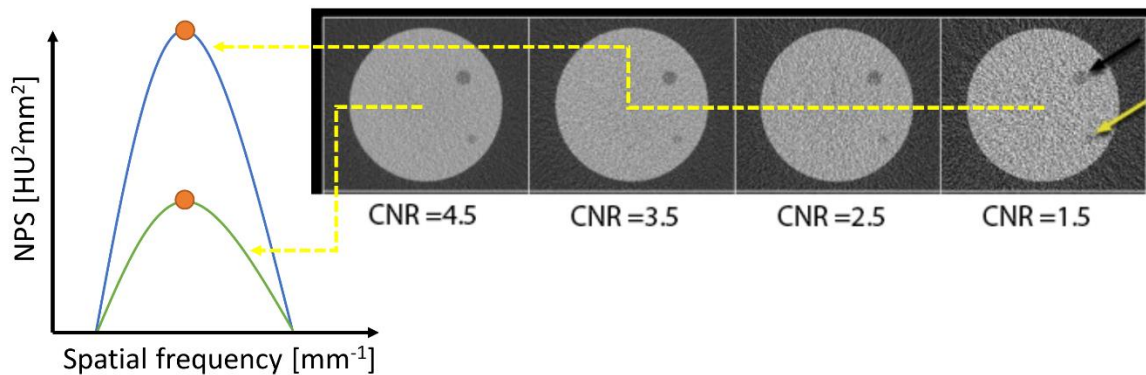


Fig. 16 Schematic representation of the NPS for a low (green curve) and a high noise environment (blue curve). The noise magnitude peak spatial frequency is constant, as indicated by the orange dots.

On the other hand, the effect of noise texture deviation is illustrated in Fig 17; despite constant noise magnitude, the lesion detectability is profoundly altered when the noise texture is shifted towards lower spatial frequencies.

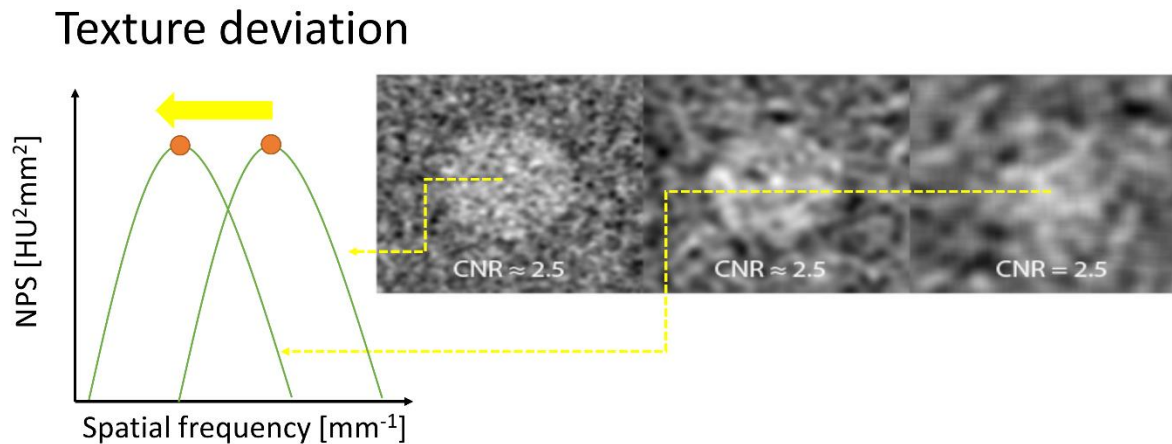


Fig. 17 Schematic representation of the NPS under constant noise magnitude conditions, but texture deviation. When the peak spatial frequency is shifted towards lower spatial frequencies (towards the left of the graph), as indicated by the orange dots, the lesion detectability decreases despite constant noise magnitude (area under the curve) and CNR.

To account for combined effects of contrast-dependent spatial resolution and noise characteristics, various mathematical model observers have been validated to provide the missing link between physical metrics and the feasibility of a diagnostic task [86]. Such model observers can simulate a lesion (by its size, shape, and object-to-background contrast) and determine whether the lesion can be detected or not on a CT image under specific radiation dose conditions [91].

Using such state-of-the-art physical metrics (NPS, TTF, model observers) is not feasible with any study design. Still, it is strongly encouraged when a thorough assessment of image characteristics is needed, such as when a disruptive technology hits the market, as is the case with PCCT. This is why we conducted a phantom study using these metrics on a prototype PCCT.

5.2.2. Experimental assessment of tissue characteristics

One straightforward clinical application of DECT in cardiovascular medicine is the use of virtual non-contrast (VNC) images. Such reconstructions can be derived from contrast-enhanced CT and simulate non-contrast images by subtracting the attenuation attributable to iodine, thereby offering the possibility to save the ionizing radiation from acquiring true non-contrast images. Non-contrast CT provides value in many clinical scenarios, of which aortic intramural hematoma (IMH) suspicion is typical. Acute IMH classically appears as a spontaneously hyperdense eccentric regular aortic wall thickening that can be obscured on contrast-enhanced images [92, 93]. In work co-authored with Si-Mohamed S, Dupuis N, Tatard-Leitman V, Boccalini S, Dion M, Vlassenbroek A, Coulon P, Yagil Y, Shapira N, Douek P, Boussel L [94], we designed a phantom model of IMH using porcine bowel, clotted and heparinized blood and demonstrated the ability of VNC to depict the above-mentioned hyperdense wall thickening. This finding led the team to proceed with a clinical study [94].

Further use of DECT, receiving much attention from the rheumatological sphere, is detecting and characterizing gout crystals in peripheral joints and other organs [95-97]. Several studies have shown that gout is a risk factor for the development of atherosclerotic coronary artery disease and major cardiovascular events [98-103].

Besides, it has been shown that monosodium urate (MSU) crystals can be demonstrated ex vivo in coronary atherosclerotic plaques in hyperuricemic patients [104]. To date, no study has been able to detect coronary deposits of MSU in vivo appropriately. Spectral CT may be able to meet this challenge, and a project we refer to as “COROGOUT” is part of this. COROGOUT is designed to evaluate the capability of spectral CT to detect coronary MSU deposits in vitro and contribute to addressing the aims of better detecting and characterizing the disease. To this end, precision phantoms were designed and scanned both on a clinical DECT and pre-clinical PCCT systems. This project was still underway at the time of writing, so no manuscript is available, but an abstract using one of the phantoms was accepted by the Radiological Society of North America (RNSA) annual meeting 2021. Furthermore, preliminary results are provided in section 6.

5.2.3. Experimental assessment of spatial resolution performance

A further application of DECT aiming to reduce the probability of unwanted side-effects related to intravenous iodinated CM is to take advantage of virtual monochromatic images (VMI). Because iodine exhibits a relatively strong photoelectric effect in the lower range of energy clinically available with DECT (i.e., 40-60 keV), reading CTA studies with low-energy VMI comes with remarkably higher CT numbers in opacified or enhanced structures, which can be translated into CM reduction. While some studies attempted to look into the advantage of using VMI in CCTA [105-108], spatial resolution properties of VMI had not been assessed before proceeding to clinical studies. This led us to develop a high-precision phantom to prove that VMI does not deteriorate the vessels' cross-sectional area quantification accuracy with CCTA in both regular and reduced iodine dose settings. Instead, reduced CM DECT improved the vessel's cross-sectional quantification

compared with standard CM dose conventional CT, advocating the implementation of dual-layer DECT with VMI reconstruction in clinical routine. This work was co-authored with Si-Mohamed SA, Yerly J, Boccalini S, Becce F, Bousset L, Meuli RA, Qanadli SD, Douek PC [109].

Spatial resolution is of utmost importance in CCTA because coronary arteries are small and exhibit complex anatomy requiring small isotropic voxels to resolve lumen, wall, atherosclerotic plaques, and composition thereof [110]. On top of that, coronary arteries are constantly moving, further challenging non-invasive imaging, requiring techniques that can freeze motion thanks to high temporal resolution. For these reasons, CCTA exploits CT systems at the edge of their technical capabilities and immediately integrates any technological advance in image resolution, noise, or acquisition speed. Therefore, it is self-evident that PCCT can bring numerous advances for CCTA at once. This includes intrinsically lower noise, markedly higher spatial resolution, and the ability to provide spectral images, including VNC (to obviate non-contrast CT) and VMI (to enable iodine dose reduction or increase tissue contrast). Since no human data regarding photon-counting coronary CT angiography currently exists, we sought to objectively evaluate photon-counting-detector (PCD) CCTA in vitro and investigate its image quality characteristics compared with a clinical energy-integrating-detector (EID) CT system. To this end, we used a semi-anthropomorphic phantom simulating various patient sizes. Objective image quality analysis was performed using state-of-the-art physical metrics (noise power spectrum, target transfer function, model observer). Its encouraging results are written up in a manuscript co-authored with Damien Racine, Fabio Becce, Elias Lahoud, Klaus Erhard, Salim A. Si-Mohamed, Joël Greffier, Anaïs Viry, Loïc Bousset,

Reto A. Meuli, Yoad Yagil, Pascal Monnin, and Philippe C. Douek, under consideration for publication in a peer-reviewed journal at time of writing.

5.3 Clinical studies and approaches

The various potential applications of DECT led us to design clinical studies tackling either patient safety issues or diagnostic benefits and consolidating findings from experimental studies.

First, we evaluated patients with confirmed aortic intramural hematoma, who underwent both true non-contrast and contrast-enhanced DECT of the aorta. Arterial phase DECT images were reconstructed as VNC and compared with true non-contrast regarding diagnostic confidence and CNR. Results indicate that a single arterial-phase DECT-angiography with VNC image reconstruction can replace the true non-contrast acquisition. This study contributes to addressing the purpose of saving ionizing radiation avoiding the true non-contrast acquisition. Furthermore, the implementation of such a protocol would reduce the examination time. The manuscript, co-authored with Si-Mohamed S, Dupuis N, Tatard-Leitman V, Boccalini S, Dion M, Vlassenbroek A, Coulon P, Yagil Y, Shapira N, Douek P, and Boussel L, was published in a peer-reviewed scientific journal [94].

Having established VNC as a clinical standard to evaluate the aortic wall in the setting of acute IMH, we sought to develop the technique further and optimize the use of contrast information gathered in DECT datasets. Since DECT allows for material decomposition (see section 4.3.2) of a pair of arbitrary materials, we concretized the idea of performing a patient-oriented material decomposition to void the aortic lumen's attenuation beyond

the appearance of a non-contrast CT. To do this, we selected a region-of-interest in the ascending aorta of patients referred to CTA for suspected acute aortic syndrome, and defined the ROI's content as a material to be decomposed with water as would be done with classic material decomposition. The water basis images obtained present a hypodense aortic lumen, recalling the so-called "dark-blood" or "black-blood" MRI sequences. The result is a stronger contrast between the aortic lumen and wall. We assessed dark-blood CT images for aortic wall conspicuity in patients presenting with acute IMH and control subjects. This work, co-authored with Si-Mohamed SA, Shapira N, Douek PC, Meuli RA, and Boussel L, was published in a peer-reviewed scientific journal [111].

An equally important facet of cardiovascular DECT is the readily available VMI that can provide, to some extent, a layer of "lower-energy" information. As mentioned earlier, low-energy photons convey more contrast information than their higher energy counterparts, and separating them is relevant, especially in CM-enhanced examinations. VMI are synthetic images extrapolated from DECT datasets and represent voxels whose CT number is computed as if the X-ray beam was monochromatic and can be obtained down to 40 keV on most systems, close to the K-absorption edge ("K-edge") of iodine. The K-edge describes a discrete energy level found just above the k-shell's electron binding energy, associated with an abrupt increase of the photoelectric effect of incident X-ray photons. In X-ray computed tomography, this physical property can be used to gain tissue contrast by reconstruction VMI as closely as possible to a material's K-edge or even to perform specific imaging of a material whose K-edge falls within the available energy range of a PCCT system. Iodine's ($Z = 53$) K-edge is at 33.2 keV, somewhat lower than

the minimum energy level of 40 keV that can be reconstructed on most DECT systems, yet 40 keV will provide much higher CT numbers than single energy CT. Higher CT numbers can obviously be translated into lower iodine CM doses in CTA; however, the extent of CM reduction and ideal VMI energy is still debated in the literature. Our paper entitled “Reduced-iodine-dose dual-energy coronary CT angiography: qualitative and quantitative comparison between virtual monochromatic and conventional CT images” co-authored with Si-Mohamed SA, Yerly J, Boccalini S, Becce F, Boussel L, Meuli RA, Qanadli SD, and Douek PC [109] addresses these questions by providing VMI image analysis across an energy range from 40 to 130 keV, with quantitative and qualitative image quality markers. Of note, we demonstrate that with a 40% CM dose reduction, 55 keV VMI provide non-inferior diagnostic quality compared with regular CM single energy CT, and 40 keV’s strong boost of iodine CT number should be used carefully to avoid obscuring calcified plaque.

Along the same lines, VMI and also iodine basis images (iodine versus water material decomposition maps) can be used to assess static first-pass myocardial perfusion in any CCTA performed with spectral CT. DECT can quantify the concentration of materials and, therefore, is supposed to add relevant information regarding myocardial perfusion. However, the impact of the injection protocol on the absolute iodine concentration measured on first-pass DECT-myocardial perfusion may lead to variability and has never been explored. The purpose of this clinical study was twofold: (a) to demonstrate the effect of contrast material injection rate on the iodine distribution in healthy myocardium during first-pass perfusion; (b) to evaluate the impact of virtual monochromatic images (VMI) on image noise, signal-to-noise ratio, and contrast-to-noise ratio. This work raises awareness

of the critical dependency of myocardial iodine content on contrast media injection rate and dose; this is relevant and undermines the clinical applicability of previous studies attempting at determining a normal range of iodine concentration measured on iodine basis images [112, 113], but the tremendous effect of the injection protocol was disregarded, at least until now. We even found that higher CM doses lead to increased iodine inhomogeneity, potentially hampering perfusion and ischemia analysis. In other words, this study provides another strong argument in favor of using DECT and reduced CM doses for cardiac CT. Furthermore, the study's secondary endpoints show a marked contrast-to-noise improvement achieved with spectral CT. This work, co-authored with Boccalini S, Si-Mohamed S, Matzuzzi M, Tillier M, Revel D, Bousset L, and Douek P, was under review at the time of writing.

6 Achieved results

6.1 Radiation and iodine dose

6.1.1 Virtual versus true non-contrast dual-energy CT imaging for the diagnosis of aortic intramural hematoma [94]

Implications for patient care

DECT allows skipping the non-contrast acquisition usually performed as part of aortic CTA. This saves radiation dose and examination time.

Author contribution

Co-author; participated in the phantom experiments, CT image assessment of the clinical part of the study, and manuscript editing.



Virtual versus true non-contrast dual-energy CT imaging for the diagnosis of aortic intramural hematoma

Salim Si-Mohamed^{1,2} · Nicolas Dupuis^{1,2,3} · Valérie Tatard-Leitman¹ · David Rotzinger⁴ · Sara Boccalini² · Matthias Dion^{1,2,3} · Alain Vlassenbroek⁵ · Philippe Coulon⁶ · Yoad Yagil⁷ · Nadav Shapira⁷ · Philippe Douek^{1,2} · Loïc Bousset^{1,2}

Received: 11 February 2019 / Revised: 24 May 2019 / Accepted: 11 June 2019
© European Society of Radiology 2019

Abstract

Purpose To assess whether virtual non-contrast (VNC) images derived from contrast dual-layer dual-energy computed tomography (DL-DECT) images could replace true non-contrast (TNC) images for aortic intramural hematoma (IMH) diagnosis in acute aortic syndrome (AAS) imaging protocols by performing quantitative as well as qualitative phantom and clinical studies.

Materials and methods Patients with confirmed IMH were included retrospectively in two centers. For in vitro imaging, a custom-made phantom of IMH was placed in a semi-anthropomorphic thorax phantom (QRM GmbH) and imaged on a DL-DECT at 120 kVp under various conditions of patient size, radiation exposure, and reconstruction modes. For in vivo imaging, 21 patients (70 ± 13 years) who underwent AAS imaging protocols at 120 kVp were included. In both studies, contrast-to-noise ratio (CNR) between hematoma and lumen was compared using a paired *t* test. Diagnostic confidence (1 = non-diagnostic, 4 = exemplary) for VNC and TNC images was rated by two radiologists and compared. Effective radiation doses for each acquisition were calculated.

Results In both the phantom and clinical studies, we observed that the CNRs were similar between the VNC and TNC images. Moreover, both methods allowed differentiating the hyper-attenuation within the hematoma from the blood. Finally, we obtained equivalent high diagnostic confidence with both VNC and TNC images (VNC = 3.2 ± 0.7, TNC = 3.1 ± 0.7; *p* = 0.3). Finally, by suppressing TNC acquisition and using VNC, the mean effective dose reduction would be 40%.

Conclusion DL-DECT offers similar performances with VNC and TNC images for IMH diagnosis without compromise in diagnostic image quality.

Key Points

- Dual-layer dual-energy CT enables virtual non-contrast imaging from a contrast-enhanced acquisition.
- Virtual non-contrast imaging with dual-layer dual-energy CT reduces the number of acquisitions and radiation exposure in acute aortic syndrome imaging protocol.
- Dual-layer dual-energy CT has the potential to become a suitable imaging tool for acute aortic syndrome.

Salim Si-Mohamed and Nicolas Dupuis contributed equally to this work.

Electronic supplementary material The online version of this article (<https://doi.org/10.1007/s00330-019-06322-5>) contains supplementary material, which is available to authorized users.

✉ Salim Si-Mohamed
salimaymeric@gmail.com; salim.si-mohamed@chu-lyon.fr

¹ Univ Lyon, INSA-Lyon, Université Claude Bernard Lyon 1, UJM-Saint Etienne, CNRS, Insem, CREATIS UMR 5220, U1206, F-69621 Lyon, France

² Radiology Department, Hospices Civils de Lyon, CHU Louis Pradel, 59 Boulevard Pinel, 69500 Bron, France

³ Anatomy Lab, Rockefeller Faculty, Lyon Est, Lyon, France

⁴ Department of Diagnostic and Interventional Radiology, Lausanne University Hospital, Lausanne, Switzerland

⁵ CT Clinical Science, Best, Netherlands

⁶ CT Clinical Science, Philips, Suresnes, France

⁷ Global Advanced Technologies, CT, Philips, Haifa, Israel

Keywords Tomography, x-ray computed · Humans · In vitro · Acute disease · Aorta

Abbreviations

AAS	Acute aortic syndrome
CNR	Contrast-to-noise ratio
CTA	CT angiography
CTDI _{vol}	Volume CT dose index
DL-DECT	Dual-layer dual-energy computed tomography
DLP	Dose-length product
DS-DECT	Dual-source dual-energy computed tomography
IMH	Intramural hematoma
ROI	Regions of interest
SD	Standard deviations
TNC	True non-contrast
VNC	virtual non-contrast
WED	Water-equivalent diameter

Introduction

Aortic intramural hematoma (IMH) is a life-threatening condition that belongs to the spectrum of acute aortic syndrome (AAS). It is caused by micro-intimal tear or rupture of the vasa vasorum that creates a hemorrhage into the aortic media and thickens the aortic wall. Between 16% and 47% of IMH will progress to dissection often leading to patient's death [1]. Therefore, it is essential to promptly diagnose IMH in order to perform emergency surgery when necessary [2].

Today, dual-phase CT angiography (CTA) is considered the best tool available for IMH diagnosis [3, 4]. Indeed, while IMH appears as a circumference of hyperattenuation on non-contrast CT images, it is undetectable on contrast CT images due to the masking effect of iodine [1, 5–7]. Therefore, dual-phase CTA requires a non-contrast scan for the detection of aortic IMH and a contrast scan during the arterial phase for the detection of intimal tears, extension of an aortic disease, contrast leakage, and visceral ischemia [2, 4, 8, 9]. However, a disadvantage of dual-phase CTA is the higher radiation dose [10, 11]. To decrease the dose, Knollman et al have proposed to replace the non-contrast phase using a threshold to differentiate the IMH from the aortic lumen [12]. Unfortunately, this method highly depends on attenuation levels, which are affected by various factors such as tube voltage, patient size, or beam-hardening effects that make the diagnosis of thin IMH particularly difficult due to the high concentration of iodine within the blood pool [13].

Dual-energy CT (DECT), comparing two different energy levels, discriminates materials of different effective atomic numbers [14–18]. Post-processing can create

virtual non-contrast images (VNC) that simulate true non-contrast images (TNC) by subtracting the attenuation due to iodine from the contrast-enhanced images [19, 20]. However, the comparability of VNC with TNC images depends on the accuracy of iodine quantification. For example, in the study of Hua et al [19], iodine accuracy is within 0.3 mg/mL (median) with a maximal deviation of 0.5 mg/mL. This translates into variation of up to 10–15 HU, in line with the results of previous studies [19, 21–26]. Therefore, since VNC is only an approximation of TNC, it is important to check the usefulness of VNC within specific clinical situations [20, 21, 25, 27, 28]. The rationale of replacing TNC by VNC images is to reduce radiation exposure by waiving the non-enhanced acquisition. It serves also when the non-contrast acquisition was erroneously omitted.

In the absence of previous demonstration in the literature, we conducted this study to assess whether VNC images could replace TNC images for aortic IMH diagnosis in AAS imaging protocols, by performing phantom and clinical experiments.

Material and methods

Study design

This work consisted of an in vitro phantom study performed in an academic hospital (Hôpital Louis Pradel, Lyon) and an in vivo clinical study carried out in two academic hospitals (Hôpital Louis Pradel, Lyon, and Clinique Universitaire UCL, Brussels) and approved by the Institutional Review Board of both institutions. The patients were included retrospectively; their data were anonymized and no informed consent was required.

Dual-layer dual-energy CT

This study was carried out on a single source dual-layer spectral CT (IQon, Philips Healthcare) equipped with two separate scintillator layers. The top layer absorbs the low-energy photons and the bottom layer the high-energy ones. Therefore, both acquisitions are perfectly simultaneous and the spectral separation is not compromised by any motion. An original feature of this technology is that it allows processing spectral data without having to select a dual-energy protocol prior to an examination and delivers the same dose as a conventional single-source CT [19, 22].

Phantom study

IMH phantom

To compare the TNC and VNC image quality, a custom IMH phantom was built using animal tissue and blood (Fig. 1). Experimental details are provided in the [Supplemental data](#).

Image acquisition and reconstruction

The acquisition was carried out using a non-ECG gating aortic protocol (Table 1). The acquisitions were performed at three different CTDI_{vol} (2.5, 5, and 10 mGy) without automatic current modulation in order to keep the dose constant between different phantoms. These exposure levels were chosen to match clinical AAS imaging protocols and correspond to a dose right index at 15, 21, 27 and 6, 12, 18 for the small and large phantoms, respectively. Each acquisition was repeated three times and the standard deviations and ranges of the averaged attenuation values were calculated. Conventional TNC images of the non-contrast phantoms, VNC images of the contrast phantoms, and “iodine no water” images were reconstructed using the proprietary iDose/Spectral iterative reconstruction algorithm at levels 0 and 3 and obtained directly from commercial software (Spectral Philips IntelliSpace Portal 9.0). To obtain the VNC images, the reconstruction algorithm subtracts the respective iodine component from each of the base components and creates a monoenergetic 70 keV from the resulting base components [19]. Level 0 corresponds closely to an FBP reconstruction with a minimum of additional iterative post-processing.

Image analysis

Images were analyzed on a clinical workstation with commercial software (Spectral Philips IntelliSpace Portal 9.0). Regions of interest (ROIs) of 0.8 to 2.0 cm² were drawn within the hematoma, blood, and fat by a radiologist with 6 years of experience in cardiovascular imaging (SSM) to measure the

mean attenuation values and standard deviations (SD). After carefully matching each set of acquisition in the z-direction, the ROIs were copied/pasted on the corresponding slice. The absolute mean attenuation difference between TNC and VNC attenuation values was calculated. The contrast-to-noise ratio (CNR) between blood and hematoma on both images was calculated for each conditions using the formula below:

$$\text{CNR} = \frac{[\text{Mean HU (hematoma)} - \text{Mean HU (blood)}]}{\text{SD (fat)}}$$

The SD of the fat attenuation surrounding the IMH model was chosen to assess image noise because of the homogeneity of this tissue. The water-equivalent diameters (WED) of the phantoms and the patients were calculated using custom software.

Clinical study

Patient characteristics

We retrospectively reviewed clinical and imaging data for patients who were suspected of having an acute aortic syndrome and who underwent a CTA between April 2017 and November 2018. The inclusion criterion was the presence of an isolated intramural hematoma confirmed by the surgery. When surgery had been declined, the diagnosis was based on a final consensus between the clinical signs and the imaging findings on CTA. Patients who underwent a single-phase CTA examination were excluded from the study. Taken together, 21 patients were included. The information about the population included in the study is shown in Table 2.

Image acquisition and reconstruction

All patients underwent a dual-phase CT according to the European Society of Cardiology 2014 guidelines on the diagnosis and treatment of aortic disease [9] (Table 1). For the arterial phase, bolus tracking and retrospective ECG gating were used following intravenous administration of 60–



Fig. 1 Representation of the aortic intramural hematoma (a) and anthropomorphic (b, c) phantoms. The false and inner lumen were filled with blood with extra iodinated contrast media for the inner

lumen to target an attenuation value of 80 HU and 350 HU, respectively. Obese patients were simulated by adding an outer extension ring (b)

Table 1 Acquisition and reconstruction parameters for phantom and clinical studies

	Parameters	Phantom study	Clinical study
Acquisition	Tube potential (kVp)	120	120
	Detector collimation	64 × 0.625	64 × 0.625
	Pitch	1.234	1.234
	Rotation time (s)	0.27	0.27
	Exposure control	None	3D modulation
Reconstruction	Filter	B	B
	Section thickness (mm)	1.5	1.5
	Field of view (mm)	300	300

80 mL of iodinated contrast medium (3–3.5 mL/s) followed by 25 mL of physiologic saline solution. The image reconstructions for all patient included TNC, VNC, and “iodine no water” images, at iDose/Spectral level range 3.

Quantitative analysis

The images were analyzed similarly to what has been performed for the *in vitro* study. For each patient, a stack of 3 contiguous slices of 1.5 mm width was drawn at different positions separated by 15 mm depending on the IMH size. Measurements were performed within three different tissues: hematoma, blood, and peri-aortic or peri-abdominal fat. The CNRs were calculated as described above.

Qualitative analysis

Two radiologists (SSM, DR) with 6 years of experience in cardiovascular imaging as well as respectively 4 years (SSM) and no experience (DR) in dual-layer dual-energy CT (DL-DECT) images read the patients' cases. The readers were

not blinded to the type of images and scored them for each patient at 4 different levels. The readers could change settings and window according to their personal preferences. The readers were asked to score the diagnostic confidence of the hyper-attenuation of the aortic wall relative to the blood pool based on a scale from 1 to 4: 1 = non-diagnostic, 2 = limited, 3 = diagnostic, and 4 = exemplary (Fig. 2) [29].

Radiation dose

The dose-length product (DLP) and volumic CT dose index (CTDI_{vol}) for the non-contrast and contrast acquisitions were recorded. The effective dose (ED) was calculated as follows: ED = DLP × 0.014 (Thorax conversion factor) [30].

Statistical analysis

Statistical analyses were performed using the software R (R Foundation for Statistical Computing) [31]. All data are given as mean ± SD (1st quartile; 3rd quartile). Attenuation and CNR values were compared using a paired *t* test as the

Table 2 Patient characteristics (population, clinical data, radiation dose data). Data are represented with mean values ± standard deviation (1st quartile–3rd quartile)

	Criteria	Population
Population	Patients (<i>n</i>)	21
	Age (years)	70.2 ± 12.8 (63.7–78.3)
	Gender	8M, 13F
	BMI (m/kg ²)	24.8 ± 4.9 (21.3–29.1)
	WED (cm)	25.8 ± 5.0 (21.2–30.4)
Clinical data	IMH type (Stanford)	14A, 7B
	IMH thickness (mm)	7.0 ± 3.4 (5.0–8.6)
	Surgery	13
	Delay between CT and onset of AAS (days)	13.4 ± 38.2 (0.0–9.0)
Radiation dose data	CTDI _{TNC} (mGy)	8.3 ± 6.1 (6.1–9.3)
	CTDI _{VNC} (mGy)	11.3 ± 6.1 (7.1–13.5)
	mAs _{TNC}	110.1 ± 67.5 (67.0–113.0)
	mAs _{VNC}	135.1 ± 67.9 (83.0–180.0)
	Overall DLP (mGy cm)	101.6 ± 753.7 (682.0–1130.1)
	Effective dose (mSv)	14.2 ± 10.6 (9.5–15.8)

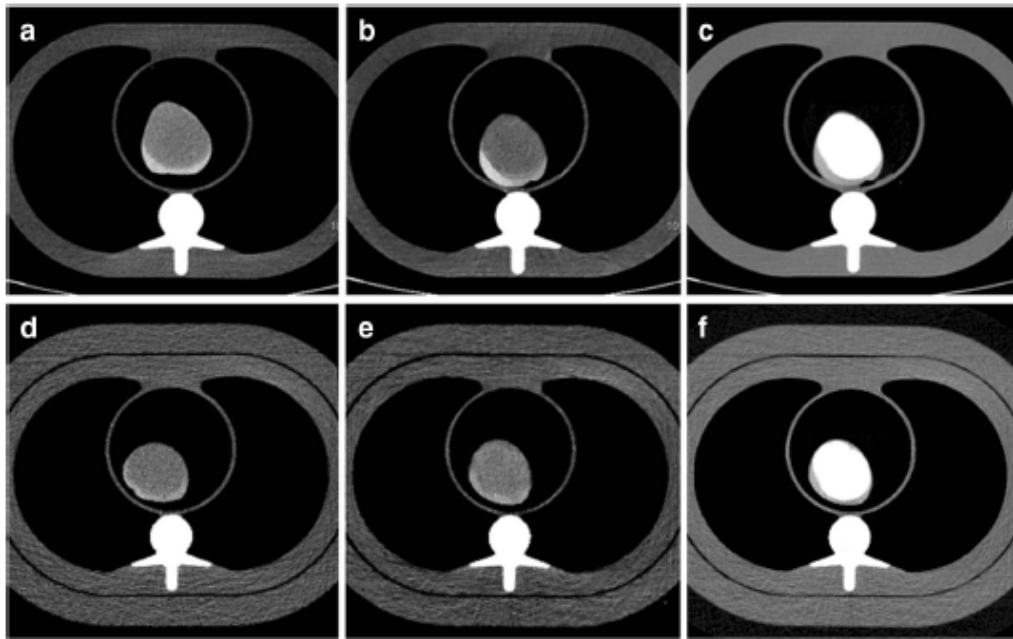


Fig. 3 CT scan of the in vitro IMH: the aortic wall hyper-attenuation in the phantom could be observed on the TNC (a, d) and VNC (b, e) images but not on the contrast images (c, f) for the small (a–c) as well as the large (d–f) phantoms (WL, 100; WW, 350)

Diagnostic confidence

The diagnostic confidence scores were close to exemplary for both the TNC and VNC images and were not significantly different between the two (TNC = 3.13 ± 0.74 ; VNC = 3.22 ± 0.73 , $p > 0.30$). The inter-radiologists agreement was high for both images with TNC = 96.51%, $k = 0.87$; VNC = 93.80%, $k = 0.76$, as well as for the intra-radiologist reliability with TNC = 98.07%, $k = 0.87$; VNC = 96.74%, $k = 0.90$.

Radiation dose

The calculated effective doses (mSv) were 5.5 ± 3.7 (3.7; 6.3) and 8.8 ± 7.2 (4.3; 11.0), respectively, for non-contrast and contrast scans leading to an overall dose of 14.2 ± 10.6 (9.5–15.8) (Table 2). By suppressing TNC acquisition and using VNC, mean effective dose reduction would be $39.9 \pm 10.8\%$ (33.1; 44.0).

Discussion

In the present study, we demonstrated that using a DL-DECT system, it is possible to replace TNC images with VNC images and obtain reliable aortic IMH diagnosis while delivering lower doses of radiation than a typically dual-phase CT AAS protocol. The CNRs were comparable in both images between the hematoma and the blood allowing for the visualization of the relative hyper-attenuation of the hematoma in clinical study and also for every experimental condition of the in vitro study despite WED variations, CTDI_{vol} differences, and iDose level choices.

In both studies, the attenuation values in the VNC images were slightly different than in the TNC images (up to ~ 10 HU). Such differences are expected since the VNC images mimic a monoenergetic image at 70 keV of non-contrast acquisition while TNC values are derived from conventional polychromatic images. HU values of conventional images are impacted by the beam-hardening effect: tube kVp, post-tube

Table 3 Hematoma and blood attenuation values for the small phantom in TNC and VNC images with conditions closest to clinical settings (similar WED than clinical study), CTDI_{vol} 10 and iDose 3

Phantom	Images	Attenuation _{hematoma} (HU)	Attenuation _{blood} (HU)	<i>p</i>
Small	TNC	88.8 ± 0.8 (88.3–88.8)	56.4 ± 0.33 (79.3–79.5)	0.0001
	VNC	79.4 ± 0.3 (79.3–79.5)	47.6 ± 0.2 (47.6–47.7)	0.0002
Large	TNC	83.5 ± 0.66 (83.1–83.9)	55.8 ± 2.8 (53.8–57.6)	0.0002
	VNC	80.9 ± 1.2 (80.5–81.3)	52.1 ± 0.6 (51.8–52.5)	0.0001

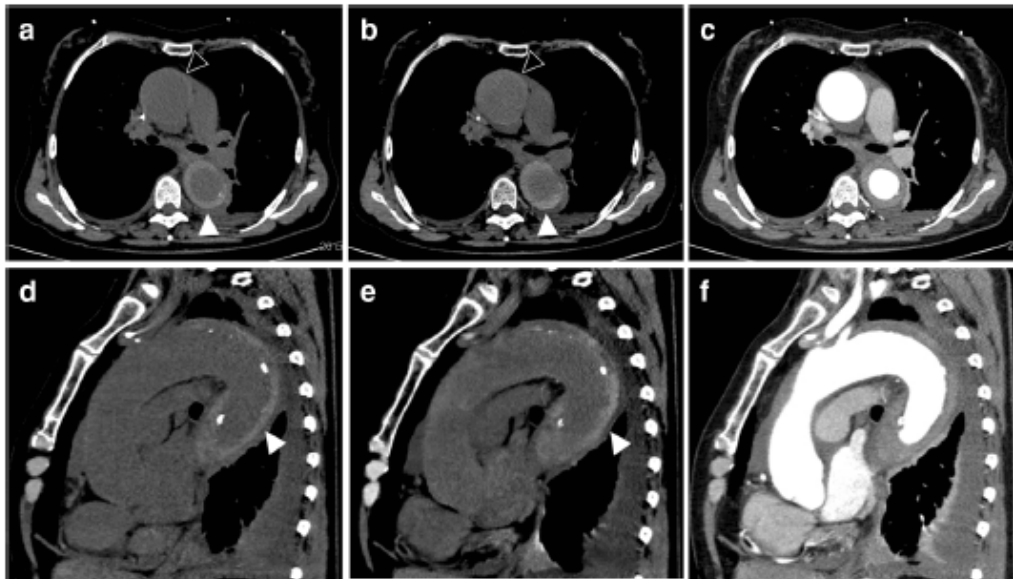


Fig. 4 CT scan of a 64-year-old patient diagnosed with aortic IMH (full arrowheads) on the TNC (a, d) and VNC (b, e) images, which was hardly visible at the level of the ascending aorta (empty arrowheads), especially

on the contrast images (c, f), where its presence was later confirmed during the surgery (WL, 100; WW, 350)

filtration, and patient size. By definition, monoenergetic images are virtually free from such beam-hardening effects. Indeed, the VNC attenuation values in the two different phantom sizes are more consistent compared with the conventional TNC values.

In the phantom study, the attenuation values in the VNC images were lower than in the TNC images. This difference was accentuated at low-dose levels and phantom size, in agreement with previous studies [19, 22]. This could be explained by two factors. First, in DECT, the VNC images are derived from the water components based on a material decomposition between two components (water-iodine) in which any deviation from water-like attenuation is interpreted as non-zero iodine component [19, 22]. Therefore, their attenuation values end up being decreased. For example, as for bones, the calcifications are interpreted as a mixture of water-like and iodine-like materials, and the VNC algorithm does not separate the bone from iodine, explaining that the attenuation value of bone or calcification in VNC images is roughly half of their value in the original 70-keV image.

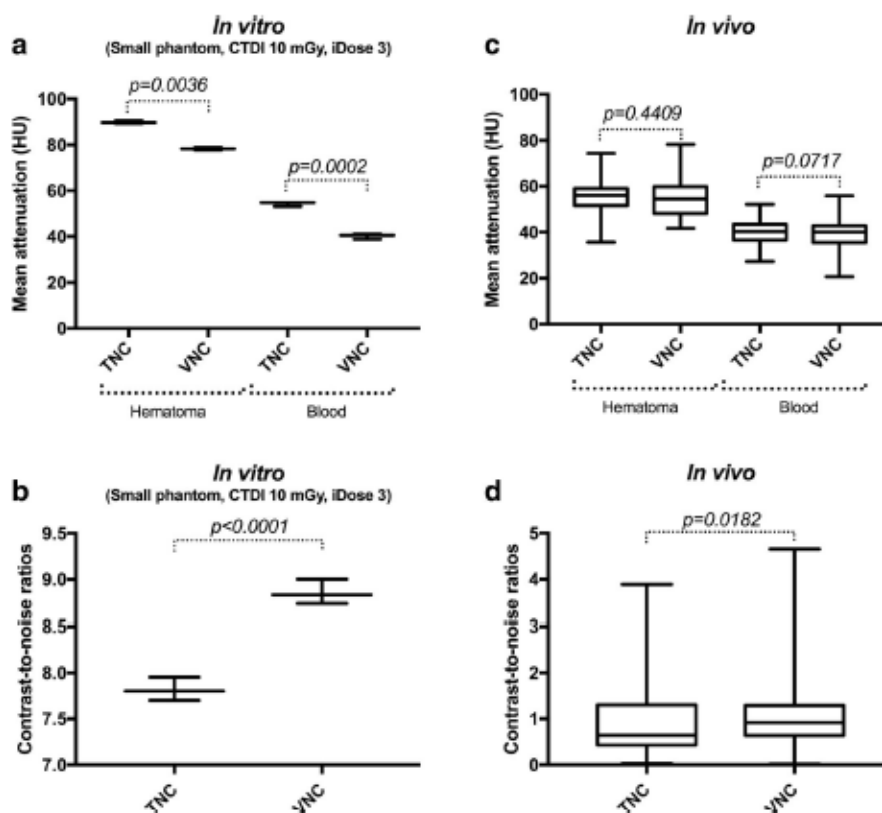
Similarly, the elevated protein, iron, and hemoglobin content in the hematoma and blood, which increases the x-ray attenuation [32], is interpreted as a mixture of water-like and iodine-like material. Hence, the iodine content is overestimated which leads to an underestimation of the hematoma and blood attenuation in the VNC image. Second, in low-dose conditions (obese patients, low CTDI_{vol}), the accuracy of iodine quantification is biased which, as demonstrated in several studies, also results in inaccurate attenuation values [22, 33]. However, in such cases, we found similar CNR probably explained by the noise suppression algorithms included in spectral reconstructions which take advantage of known statistical properties of the noise (anti-correlation between the two base images) to target it and reduce it [22, 34].

In the clinical study, we found slightly different results in comparison with the phantom study due to the difficulties mimicking perfectly the hematoma composition, as well as the heterogeneity of hematoma attenuation between patients. Firstly, the attenuation values were closer between VNC and TNC images in vivo, probably explained by the lower

Table 4 Attenuation and noise values in HU. Data are represented with mean values ± standard deviation (1st quartile–3rd quartile). Mean absolute differences were calculated between TNC and VNC images

Criteria	TNC	VNC	<i>p</i>
Attenuation _{hematoma} (HU)	54.8 ± 7.4 (50.9–59.5)	55.2 ± 8.5 (49.1–60.2)	0.440
Attenuation _{blood} (HU)	40.3 ± 5.9 (36.5–43.6)	39.2 ± 7.0 (35.9–43.7)	0.071
Mean absolute difference _{hematoma} (HU)	5.0 ± 4.2		NA
Mean absolute difference _{blood} (HU)	4.7 ± 3.9		NA
Noise (HU)	19.6 ± 6.0 (16.2–23.5)	18.1 ± 6.3 (13.2–22.2)	0.041

Fig. 5 Distribution of the in vitro (a, b) and in vivo (c, d) mean CT attenuation values and contrast-to-noise ratios shown as boxplots. The lower and upper margins of each box indicate the 25th and 75th percentile. Median is marked by the line in the box, and outliers indicate the minimal and maximal values



concentrations of hemoglobin, protein, and iron. Indeed, the mean attenuations for hematoma and blood were lower in vivo than in vitro. This decreased the overestimation of the iodine content, as confirmed by the lower iodine concentrations present in the hematoma, which led to a greater estimation of hematoma attenuations in the VNC images. Secondly, the percentages of absolute differences measurements of less than 5, 10, and 15 HU were found in more than 70, 92, and 98% of the cases, respectively, in line with recent studies [24, 35]. Finally, there was a significant difference in CNR between VNC and TNC images. This result was most likely due to the different doses of radiation that were used between the non-contrast and contrast acquisitions.

An important result of our work is the similar diagnostic confidence for the hyper-attenuation of the aortic wall relative to the blood pool on VNC compared with TNC images, independently from the experience of the readers to DL-DECT images. This finding, combined with the enhanced CTA, would then end up with a similar diagnostic performance of IMH to a standard CT protocol with two acquisitions. We also observed good and excellent inter-rater agreement for the VNC and TNC images, respectively. This contrasts with previous studies that demonstrated inhomogeneous subtraction of iodine in VNC images [20, 36, 37]. We can explain our results by a better correction of the beam hardening and management

of the high iodine concentrations. Indeed, we took advantage of a recent software update of the DL-DECT system that improves image quality.

Altogether, our data appear to be consistent with previous studies from other fields that reported comparable quality between VNC and TNC images [20, 21, 23, 28]. However, it is the first study to evaluate VNC images obtained from clinically acquired examinations in an acute condition setting. In addition, AAS have variable clinical presentations that may overlap with other acute cardiovascular events (e.g., myocardial infarction, pericarditis) that are more frequent and only require enhanced CT to be diagnosed. Unfortunately, IMH can be diagnosed only if an unenhanced CT has been done first. Therefore, when a radiologist is unexpectedly confronted to a thickened aortic wall on an enhanced CT, it is not possible to reliably diagnose IMH. On the contrary, using DL-DECT, it would be possible to use VNC images a posteriori and look for hyper-attenuation relative to the blood pool to diagnose IMH. This protocol also has the advantage of substantially decreasing the radiation dose as shown here as well as in other studies [20, 36].

Our work has some limitations such as static blood in the phantom aortic lumen led to a greater heterogeneity of the attenuation values. Secondly, our phantom, by the high

attenuation found in the hematoma, was not reflecting the full range attenuations of IMH. However, the acute ones were well reflected. Finally, while the patients included in the study represented a heterogeneous panel of the population with a great diversity of WEDs and CTDI_{vol}, there were still only 21 subjects.

In conclusion, we demonstrate in the present study that it is possible to use VNC images from DECT to diagnose IMH while potentially decreasing the dose of radiation delivered to the patients.

Acknowledgments We thank Pr. Emmanuel Coche, Dr. Begum Demirler, and Dr. Matteo Pozzi for helping with the clinical study.

Funding This work has not received any funding.

Compliance with ethical standards

Guarantor The scientific guarantor of this publication is Professor Loic Boussel.

Conflict of interest Philippe Coulon, Yoav Yagil, and Nadav Shapira are employees of Philips Healthcare, the manufacturer of the scanner.

Statistics and biometry Prof. Loic Boussel provided statistical advice for this manuscript.

Informed consent Written informed consent was waived by the Institutional Review Board.

Ethical approval Institutional Review Board approval was not required.

Methodology

- Retrospective
- Observational
- Multicenter study

References

1. Mussa FF, Horton JD, Moridzadeh R, Nicholson J, Trimarchi S, Eagle KA (2016) Acute aortic dissection and intramural hematoma: a systematic review. *JAMA* 316:754–763
2. Hiratzka LF, Bakris GL, Beckman JA et al (2010) 2010 ACCF/AHA/AATS/ACR/ASA/SCA/SCAI/SIR/STS/SVM guidelines for the diagnosis and management of patients with Thoracic Aortic Disease: a report of the American College of Cardiology Foundation/American Heart Association Task Force on Practice Guidelines, American Association for Thoracic Surgery, American College of Radiology, American Stroke Association, Society of Cardiovascular Anesthesiologists, Society for Cardiovascular Angiography and Interventions, Society of Interventional Radiology, Society of Thoracic Surgeons, and Society for Vascular Medicine. *Circulation* 121:e266–e369
3. Bhalla S, West OC (2005) CT of nontraumatic thoracic aortic emergencies. *Semin Ultrasound CT MR* 26:281–304
4. Romano L, Pinto A, Gagliardi N (2007) Multidetector-row CT evaluation of nontraumatic acute thoracic aortic syndromes. *Radiol Med* 112:1–20
5. Song JK (2011) Aortic intramural hematoma: aspects of pathogenesis 2011. *Herz* 36:488–497
6. Vilacosta I, San Román JA, Ferreirós J et al (1997) Natural history and serial morphology of aortic intramural hematoma: a novel variant of aortic dissection. *Am Heart J* 134:495–507
7. Manghat NE, Morgan-Hughes GJ, Roobottom CA (2005) Multidetector row computed tomography: imaging in acute aortic syndrome. *Clin Radiol* 60:1256–1267
8. Vardhanabhuti V, Nicol E, Morgan-Hughes G et al (2016) Recommendations for accurate CT diagnosis of suspected acute aortic syndrome (AAS)—on behalf of the British Society of Cardiovascular Imaging (BSCI)/British Society of Cardiovascular CT (BSCCT). *Br J Radiol* 89:20150705
9. Erbel R, Aboyans V, Boileau C et al (2014) ESC guidelines on the diagnosis and treatment of aortic diseases: document covering acute and chronic aortic diseases of the thoracic and abdominal aorta of the adult. The task force for the diagnosis and treatment of aortic diseases of the European Society of Cardiology (ESC). *Eur Heart J* 35:2873–2926
10. Sodickson A, Baeyens PF, Andriole KP et al (2009) Recurrent CT, cumulative radiation exposure, and associated radiation-induced cancer risks from CT of adults. *Radiology* 251:175–184
11. Brenner DJ, Hall EJ (2007) Computed tomography—an increasing source of radiation exposure. *N Engl J Med* 357:2277–2284
12. Knollmann FD, Lacomis JM, Oakl I, Gleason T (2013) The role of aortic wall CT attenuation measurements for the diagnosis of acute aortic syndromes. *Eur J Radiol* 82:2392–2398
13. Godwin JD, Breiman RS, Speckman JM (1982) Problems and pitfalls in the evaluation of thoracic aortic dissection by computed tomography. *J Comput Assist Tomogr* 6:750–756
14. McCollough CH, Leng S, Yu L, Fletcher JG (2015) Dual- and multi-energy CT: principles, technical approaches, and clinical applications. *Radiology* 276:637–653
15. Altman A, Carmi R (2009) A double-layer detector, dual-energy CT — principles, advantages and applications. *Med Phys* 36:2750
16. Fleischmann D, Boas FE (2011) Computed tomography—old ideas and new technology. *Eur Radiol* 21:510–517
17. Sclerker T, Noël PB, Patino M et al (2018) Dual-energy CT: a phantom comparison of different platforms for abdominal imaging. *Eur Radiol* 28:2745–2755
18. Qin L, Gu S, Chen C et al (2019) Initial exploration of coronary stent image subtraction using dual-layer spectral CT. *Eur Radiol*. <https://doi.org/10.1007/s00330-018-5990-1>
19. Hua CH, Shapira N, Merchant TE, Klahr P, Yagil Y (2018) Accuracy of electron density, effective atomic number, and iodine concentration determination with a dual-layer dual-energy computed tomography system. *Med Phys* 45:2486–2497
20. Sauter AP, Muenzel D, Dangelmaier J et al (2018) Dual-layer spectral computed tomography: virtual non-contrast in comparison to true non-contrast images. *Eur J Radiol* 104:108–114
21. Graser A, Johnson TR, Hecht EM et al (2009) Dual-energy CT in patients suspected of having renal masses: can virtual nonenhanced images replace true nonenhanced images? *Radiology* 252:433–440
22. Ehn S, Sclerker T, Muenzel D et al (2018) Assessment of quantification accuracy and image quality of a full-body dual-layer spectral CT system. *J Appl Clin Med Phys* 19:204–217
23. Lehti L, Söderberg M, Höglund P, Nyman U, Gottsäter A, Wassélius J (2018) Reliability of virtual non-contrast computed tomography angiography: comparing it with the real deal. *Acta Radiol Open* 7:2058460118790115
24. Toepker M, Moritz T, Krauss B et al (2012) Virtual non-contrast in second-generation, dual-energy computed tomography: reliability of attenuation values. *Eur J Radiol* 81:e398–e405
25. Cha D, Kim CK, Park JJ, Park BK (2016) Evaluation of hyperdense renal lesions incidentally detected on single-phase post-contrast CT using dual-energy CT. *Br J Radiol* 89:1062

26. Yoo SY, Kim Y, Cho HH et al (2013) Dual-energy CT in the assessment of mediastinal lymph nodes: comparative study of virtual non-contrast and true non-contrast images. *Korean J Radiol* 14: 532–539
27. Aran S, Daftari Besheli L, Karcaaltincaba M, Gupta R, Flores EJ, Abujudh HH (2014) Applications of dual-energy CT in emergency radiology. *AJR Am J Roentgenol* 202:W314–W324
28. Tijssen MPM, Hofman PA, Stadler AAR et al (2014) The role of dual energy CT in differentiating between brain haemorrhage and contrast medium after mechanical revascularisation in acute ischaemic stroke. *Eur Radiol* 24:834–840
29. European guidelines on quality criteria for computed tomography. Available via <http://drs.dk/guidelines/ct/quality/mainindex.htm>. Last accessed 24 May 2019
30. Si-Mohamed S, Greffier J, Bobbia X et al (2017) Diagnostic performance of a low dose triple rule-out CT angiography using SAFIRE in emergency department. *Diagn Interv Imaging* 98:881–891
31. R Core Team (2018). R: A language and environment for statistical computing. R Foundation for Statistical Computing, Vienna, Austria
32. New PF, Aronow S (1976) Attenuation measurements of whole blood and blood fractions in computed tomography. *Radiology* 121:635–640
33. Kim H, Goo JM, Kang CK, Chae KJ, Park CM (2018) Comparison of iodine density measurement among dual-energy computed tomography scanners from 3 vendors. *Invest Radiol* 53:321–327
34. Park KK, Oh CH, Akay M (2011) Image enhancement by spectral-error correction for dual-energy computed tomography. *Conf Proc IEEE Eng Med Biol Soc* 2011:8491–8494
35. Ananthakrishnan L, Rajiah P, Ahn R et al (2017) Spectral detector CT-derived virtual non-contrast images: comparison of attenuation values with unenhanced CT. *Abdom Radiol (N Y)* 42:702–709
36. Sahni VA, Shinagare AB, Silverman SG (2013) Virtual unenhanced CT images acquired from dual-energy CT urography: accuracy of attenuation values and variation with contrast material phase. *Clin Radiol* 68:264–271
37. De Cecco CN, Buffa V, Fedeli S et al (2010) Dual energy CT (DECT) of the liver: conventional versus virtual unenhanced images. *Eur Radiol* 20:2870–2875

Publisher's note Springer Nature remains neutral with regard to jurisdictional claims in published maps and institutional affiliations.

6.1.2 Reduced-iodine-dose dual-energy coronary CT angiography: qualitative and quantitative comparison between virtual monochromatic and polychromatic images [109]

Implications for patient care

First, DECT with standard and reduced iodine concentrations was evaluated in a high-precision coronary artery phantom. This in vitro study demonstrated that reduced-iodine DECT not only preserves but also improves cross-sectional area quantification accuracy compared with conventional standard-dose CT. Cross-sectional area quantification is a crucial figure of merit in coronary CTA because patient management directly depends on stenosis assessment, which is derived from vessel diameter and section area.

Second, in a clinical study, the iodine reduction potential of coronary DECT angiography was demonstrated. In other words, DECT allows for substantial iodine dose reductions without cutting back on qualitative and quantitative image quality.

Author contribution

Lead author; designed the study, explored and implemented the non-inferiority strategy, performed phantom acquisitions, quantitative clinical CT analysis, statistical analysis, literature review, manuscript drafting, and editing.



Reduced-iodine-dose dual-energy coronary CT angiography: qualitative and quantitative comparison between virtual monochromatic and polychromatic CT images

David C. Rotzinger^{1,2} · Salim A. Si-Mohamed^{3,4} · Jérôme Yerly^{2,5} · Sara Boccalini^{3,4} · Fabio Becce^{2,6} · Loïc Boussel^{3,4} · Reto A. Meuli^{2,6} · Salah D. Qanadli^{1,2} · Philippe C. Douek^{3,4}

Received: 1 October 2020 / Revised: 6 January 2021 / Accepted: 17 February 2021
© The Author(s) 2021

Abstract

Objectives To quantitatively evaluate the impact of virtual monochromatic images (VMI) on reduced-iodine-dose dual-energy coronary computed tomography angiography (CCTA) in terms of coronary lumen segmentation in vitro, and secondly to assess the image quality in vivo, compared with conventional CT obtained with regular iodine dose.

Materials and methods A phantom simulating regular and reduced iodine injection was used to determine the accuracy and precision of lumen area segmentation for various VMI energy levels. We retrospectively included 203 patients from December 2017 to August 2018 (mean age, 51.7 ± 16.8 years) who underwent CCTA using either standard (group A, $n = 103$) or reduced (group B, $n = 100$) iodine doses. Conventional images (group A) were qualitatively and quantitatively compared with 55-keV VMI (group B). We recorded the location of venous catheters.

Results In vitro, VMI outperformed conventional CT, with a segmentation accuracy of 0.998 vs. 1.684 mm², respectively ($p < 0.001$), and a precision of 0.982 vs. 1.229 mm², respectively ($p < 0.001$), in simulated overweight adult subjects. In vivo, the rate of diagnostic CCTA in groups A and B was 88.4% ($n = 91/103$) vs. 89% ($n = 89/100$), respectively, and noninferiority of protocol B was inferred. Contrast-to-noise ratios (CNR) of lumen versus fat and muscle were higher in group B ($p < 0.001$) and comparable for lumen versus calcium ($p = 0.423$). Venous catheters were more often placed on the forearm or hand in group B ($p < 0.001$).

Conclusion In vitro, low-keV VMI improve vessel area segmentation. In vivo, low-keV VMI allows for a 40% iodine dose and injection rate reduction while maintaining diagnostic image quality and improves the CNR between lumen versus fat and muscle.

Key Points

- Dual-energy coronary CT angiography is becoming increasingly available and might help improve patient management.
- Compared with regular-iodine-dose coronary CT angiography, reduced-iodine-dose dual-energy CT with low-keV monochromatic image reconstructions performed better in phantom-based vessel cross-sectional segmentation and proved to be noninferior in vivo.
- Patients receiving reduced-iodine-dose dual-energy coronary CT angiography often had the venous catheter placed on the forearm or wrist without compromising image quality.

✉ David C. Rotzinger
david.rotzinger@chuv.ch

¹ Department of Diagnostic and Interventional Radiology, Division of Cardiothoracic and Vascular Imaging, Lausanne University Hospital (CHUV), Rue du Bugnon 46, 1011 Lausanne, Switzerland

² Faculty of Biology and Medicine (FBM), University of Lausanne (UNIL), Lausanne, Switzerland

³ Radiology Department, Hospices Civils de Lyon, 59 Boulevard Pinel, 69500 Bron, France

⁴ University Claude Bernard Lyon 1, CREATIS, CNRS UMR 5220, INSERM U1206, INSA-Lyon, Lyon, France

⁵ Department of Diagnostic and Interventional Radiology, Center for Biomedical Imaging (CIBM), Lausanne University Hospital (CHUV), Lausanne, Switzerland

⁶ Department of Diagnostic and Interventional Radiology, Lausanne University Hospital (CHUV), Rue du Bugnon 46, 1011 Lausanne, Switzerland

Keywords Coronary vessels · Computed tomography angiography · Iodine · Phantoms, imaging · Dimensional measurement accuracy

Abbreviations

CCTA	Coronary computed tomography angiography
CM	Contrast medium
CNR	Contrast-to-noise ratio
LAD	Left anterior descending
LCx	Left circumflex
LM	Left main
RCA	Right coronary artery
ROI	Region of interest
VMI	Virtual monochromatic image

Introduction

Coronary computed tomography angiography (CCTA) has become the most widely used method for non-invasive assessment of coronary artery disease [1]. To minimize adverse effects from contrast medium (CM) injection, iodine dose reduction should be a continuing effort, especially for patients with impaired kidney function or cardiopulmonary decompensation [2], but also in general, since lower iodine usage can reduce CT-induced DNA damage [3] and save costs. Furthermore, using lower injection rates could help manage patients with poor vein integrity when the catheter is inserted in the forearm or the hand [4]. Then again, efforts to save iodinated CM should be implemented with care in clinical routine to maintain CT examinations' diagnostic performance and ultimately patient outcomes.

Lately, dual-energy CT and virtual monochromatic images (VMI) have shown promise in reducing CM dose in phantoms [5] and small patient cohorts, using fast kV switching [6, 7] or dual-layer spectral detector [8, 9] technology. However, these initial studies failed to perform a sample size calculation and did not apply appropriate noninferiority statistics to prove the similarity between conventional CCTA and reduced-CM-dose dual-energy CCTA [10]. Furthermore, data regarding the impact of VMI on image quality, especially vessel diameter accuracy and precision, are still limited. Previous research has attempted to assess the accuracy and precision of vessel lumen area measurements with conventional CT [11], but no data exist regarding dual-energy/spectral image reconstructions. Some studies recommend various low- or mid-energy VMI for CCTA [12–14], but to our knowledge, segmentation reliability for vessel lumen area quantification has not been evaluated yet. VMI have different contrast and noise characteristics than conventional CT images; since spatial resolution strongly depends on contrast and noise [15, 16], increased image noise may be a concern for vessel lumen quantification tasks.

In the absence of previous demonstration, we used quantitative metrics to evaluate the impact of VMI on the accuracy and precision of coronary lumen segmentation in a high-precision phantom. Secondly, we aimed to assess the image quality of reduced-CM-dose dual-energy coronary CCTA compared with conventional CT obtained with regular CM delivery rate and volume in a large patient cohort.

Materials and methods

Study design

This study consisted of a phantom experiment simulating coronary arteries with high-precision vessel lumen areas and clinical research, including patients referred for CCTA. The phantom analyses were performed in an academic cardiovascular imaging laboratory (Lausanne University Hospital and Center for Biomedical Imaging, Switzerland). The clinical work was a single-center retrospective observational study approved by the local ethics committee, performed in an expert tertiary center (Hôpital Louis Pradel, Hospices Civils de Lyon, France), in which patients who received regular (range 50–90 mL) CM delivery rate and volume were assigned to group A, and those who had a reduced-CM-dose protocol (range 30–40 mL) constituted group B. Supplementary Figure A presents the study flow diagram.

Phantom study

A previously described custom-designed resolution module [17] inserted in the center of an anthropomorphic chest phantom (QRM) simulating a normal (70 kg) or an overweight (120 kg) adult patient was used (Supplementary Figure B). The module consisted of a 2-cm-thick polymethyl methacrylate (PMMA) slab drilled with 110 holes whose diameters matched human coronary arteries, ranging from 3.00 ± 0.004 to 3.42 ± 0.004 mm [18], in 22 steps of 0.02 mm, repeated five times at different locations in the PMMA slab. The choice of PMMA was related to the ultra-high drilling precision required to serve as a reliable ground truth. The holes were homogeneously filled with two different iodinated CM concentrations (Iomeron 400, Bracco) mixed with saline. To build an experimental model recreating the lumen enhancement observed *in vivo* as closely as possible, we prepared Iomeprol 400/saline mixtures that exhibit similar CT numbers (at 120 kVp) as patients had *in vivo* (i.e., ~400 HU in group A, and ~242 HU in group B). This has brought us to use 18.5 mg I/mL to simulate regular injection and 10.5 mg I/mL to simulate a

reduced CM protocol. These concentrations were adjusted to simulate lumen-to-epicardial fat contrast obtained in patients from group A (18.5 mg/mL, 400 HU) and group B (10.5 mg/mL, 242 HU). The phantom was scanned using the same parameters as in the clinical study, and the resulting DICOM images were automatically processed using a Matlab routine (MathWorks). This routine automatically segmented the vessel lumen area based on the full-width at half maximum method to outline the lumen interface and compute vessel area [19]. The difference between the known and measured vessel area was assessed on single-energy/conventional CT images (18.5 mg/mL) and 40–130-keV VMI (10.5 mg/mL), in 15 keV increments to derive segmentation accuracy and precision. The segmentation accuracy was defined as the mean area's difference from the ground truth (drilled area), whereas the segmentation precision was defined as the standard deviation of the area measurements [19].

Clinical study

We enrolled 203 consecutive patients referred for clinically indicated CCTA from December 2017 to August 2018. Exclusion criteria were as follows: age < 18 years, known severe allergy to iodinated CM, renal insufficiency with eGFR < 30 mL/min, coronary artery calcium score > 400. Patient characteristics and univariate comparisons between groups A and B are detailed in Table 1.

Contrast medium injection protocol

Iomeprol 400 mg I/mL (Iomeron®, Bracco) was the only CM used, warmed beforehand, and injected through an 18-G catheter using a dual-head power injector. The best venous catheter insertion site was used, ideally in the right antecubital fossa. Depending on the quality of venous access (catheter

location and saline test injection), the radiologist determined the CM injection rate according to the American College of Radiology Manual On Contrast Media's recommendations [4]. The total injected CM volume was individualized based on patient weight. The injection protocols were as follows: group A ($n = 103$): volume, 1 mL/kg (maximum 90 mL); iodine delivery rate, 2 g/s; flow rate, 5 mL/s; group B ($n = 100$): volume, 0.5 mL/kg (maximum 45 mL); iodine delivery rate, 1 g/s; flow rate, 2.5 mL/s. The injection duration was 18 s in both groups and followed by a 20 mL saline flush.

Coronary CT angiography protocols and image reconstruction

All examinations were performed on a dual-layer spectral detector CT system (IQon, Philips Healthcare), with patients lying supine, arms above the head, in a single breath-hold. If necessary, patients received intravenous beta-blockers to achieve a pre-scan heart rate no higher than 65 bpm. Helical mode CCTA with retrospective ECG-gating was performed. Detailed CCTA parameters were as follows: tube potential, 120 kVp; tube load, maximum 220 mAs; gantry revolution time, 0.27 s; automatic exposure control (angular and longitudinal), combined xyz-axis; beam collimation geometry, 64×0.625 mm. Bolus tracking was used, with a region of interest (ROI) placed in the descending aorta, and acquisition was triggered when an attenuation threshold of 130 HU was reached. The occurrence of allergic reactions was recorded. Volume CT dose indexes and dose-length products were retrieved from the radiation-dose structured reports. Conventional- and spectral-based images were reconstructed using a standard kernel, iterative reconstruction (iDose 3, Philips Healthcare), and section thickness of 0.9 mm.

Table 1 Patient characteristics of the study population and univariate comparisons

	Overall	Group A, 5 mL/s	Group B, 2.5 mL/s	<i>p</i> value
<i>n</i>	203	103	100	
Age [year]	53 [23] (18–87)	50 [21.5] (18–86)	54.5 [22] (18–87)	0.362
Female sex	87 (42.8)	44 (42.7)	42 (42.0)	0.967
Height [cm]	169.3 ± 15.2 (146–198)	169.8 ± 9.1 (150–192)	168.7 ± 19.6 (146–198)	0.445
Weight [kg]	73 [21.3] (41–164)	73.5 [23.8] (47–112)	74 [18] (41–124)	0.653
Body mass index [kg/m ²]	25 [5.7]	25 [6.1]	25.5 [5.8]	0.863
Obesity (BMI > 30 kg/m ²)	36 (17.6)	19 (18.3)	17 (17.0)	0.957
Current or past smoking	63 (31)	37 (35.9)	26 (26.0)	0.184
Hypertension	53 (26.1)	20 (19.4)	33 (33.0)	0.037
Diabetes	21 (10.3)	10 (9.7)	11 (11.0)	0.924
Dyslipidemia	38 (18.7)	19 (18.5)	19 (19.0)	0.581
Family history of CAD	46 (22.7)	18 (17.5)	28 (28.0)	0.097

Data are means ± standard deviation or median [IQR], and (range)

BMI body mass index, CAD coronary artery disease

Images were reviewed offline utilizing the manufacturer's workstation (IntelliSpace Portal 10.0, Philips Healthcare).

Quantitative image analysis

A cardiothoracic radiologist (D.C.R.) with 7 years of experience performed all measurements. In group A, only conventional CCTA images were analyzed, whereas in group B, measurements were performed on VMI reconstructions ranging between 40 and 130 keV in 15 keV increments. Circular ROIs spanning at least 2 mm² were drawn in the proximal and distal segments of the right coronary artery (RCA), left main (LM), left anterior descending (LAD), and left circumflex (LCx), to measure lumen attenuation, and special care was taken to avoid any partial volume effect. These measurements served to identify the VMI energy level providing the closest attenuation to conventional CT images. Likewise, circular ROIs of at least 2 cm² were drawn in homogeneous areas of the ascending aorta, epicardial fat adjacent to the proximal RCA, trabecular bone in the center of a vertebra chosen in the mid-thoracic region, and adjacent paravertebral muscles. We selected a 2-cm² area to keep the noise-dependency of values to a minimum. Contrast-to-noise ratios (CNR) were calculated using the following formula:

$$\text{CNR} = \frac{|\text{mean CT number}_{\text{lumen}} - \text{mean CT number}_{\text{tissue}}|}{\sqrt{\frac{1}{2} (\text{SD}_{\text{lumen}}^2 + \text{SD}_{\text{tissue}}^2)}}$$

CNR was calculated between the lumen and various tissues to approximate several physiological or pathological clinical scenarios: CNR between the lumen and fat to assess the vessel in its normal environment, between lumen and muscle to approximate a non-calcified plaque, and between lumen and trabecular bone to approximate a calcified plaque. In the phantom, CNR between the vessel and surrounding background material was computed.

Qualitative image analysis

Two radiologists (P.C.D. and S.S.-M.), with 25 and 7 years of experience in cardiovascular imaging, respectively, independently analyzed all CCTA images and could choose the best temporal phase in the cardiac cycle and the optimal grayscale windowing. Both were fully blinded to the CM injection protocol (patient groups) and clinical characteristics. In group A, the analysis was performed on conventional/single-energy images solely, whereas in group B the VMI exhibiting the closest lumen attenuation compared with group A were used. Inter-rater agreement was calculated based on the first 100 patients. The 18 coronary segments of the Society of Cardiovascular Computed Tomography model were analyzed using a 4-point Likert scale as previously published (9): excellent (no

artifacts; score = 4), good (minor artifacts, good diagnostic quality; score = 3), adequate (moderate artifacts, acceptable for routine clinical diagnosis; score = 2), or poor (severe artifacts impairing accurate evaluation, segment classified as non-evaluable; score = 1). A segment was deemed assessable if scored ≥ 2 , and each non-assessable segment was categorized as insufficiently enhanced or artifact-related (motion or streak). Arteries with a diameter smaller than 1.5 mm were excluded from the analysis.

Statistical analysis

Sample size was calculated for 80% power and a type-one error rate of 5%, based on a noninferiority margin of 10% [20, 21]. To meet these requirements, we had to enroll at least 182 patients (91 in each group), assuming a 92% rate of patients with a diagnostic CCTA [21]. Results were expressed as number of subjects (percentage), as mean (\pm SD), or median (IQR) for non-normally distributed data, unless otherwise specified. Bivariate statistical analysis was conducted using chi-squared, Wilcoxon two-sample, or Student's *t* test where appropriate. Variables with multiple levels were compared using the Kruskal-Wallis test with post hoc testing, and *p*-values were adjusted using the Holm method. Interobserver agreement for qualitative ratings was evaluated using weighted kappa coefficients, and interpreted as follows: ≤ 0 , poor; 0.01–0.20, slight; 0.21–0.40, fair; 0.41–0.60, moderate; 0.61–0.80, substantial; ≥ 0.81 , excellent. *p* values < 0.05 were considered statistically significant.

Results

Phantom study

For both iodine doses (18.5 mg/L and 10.5 mg/L), the algorithm achieved visually adequate segmentation of cross-sectional areas on conventional images and VMI up to 85 keV (Supplementary Figures C and D). The 55-keV VMI reconstructions (at 10.5 mg/L iodine) approximating group B patients performed better than the conventional images (at 18.5 mg/L iodine) mimicking group A patients, for accuracy (0.601 mm² vs. 0.342 mm², respectively, $p < 0.001$), but not for precision (0.597 mm² vs. 0.675 mm², respectively, $p < 0.002$), for simulated 70 kg patient size. For simulated 120 kg patient size, low-iodine 55-keV VMI provided better segmentation both regarding accuracy (0.998 vs. 1.684 mm², respectively, $p < 0.001$) and precision (0.982 vs. 1.229 mm², respectively, $p < 0.001$). Regardless of the patient size and CM concentration, the highest segmentation precision and accuracy were achieved at lower VMI energy levels (i.e., 40 and 55 keV), as shown in Fig. 1. The favorable effect of VMI reconstructions in reduced-CM-dose dual-energy CCTA was

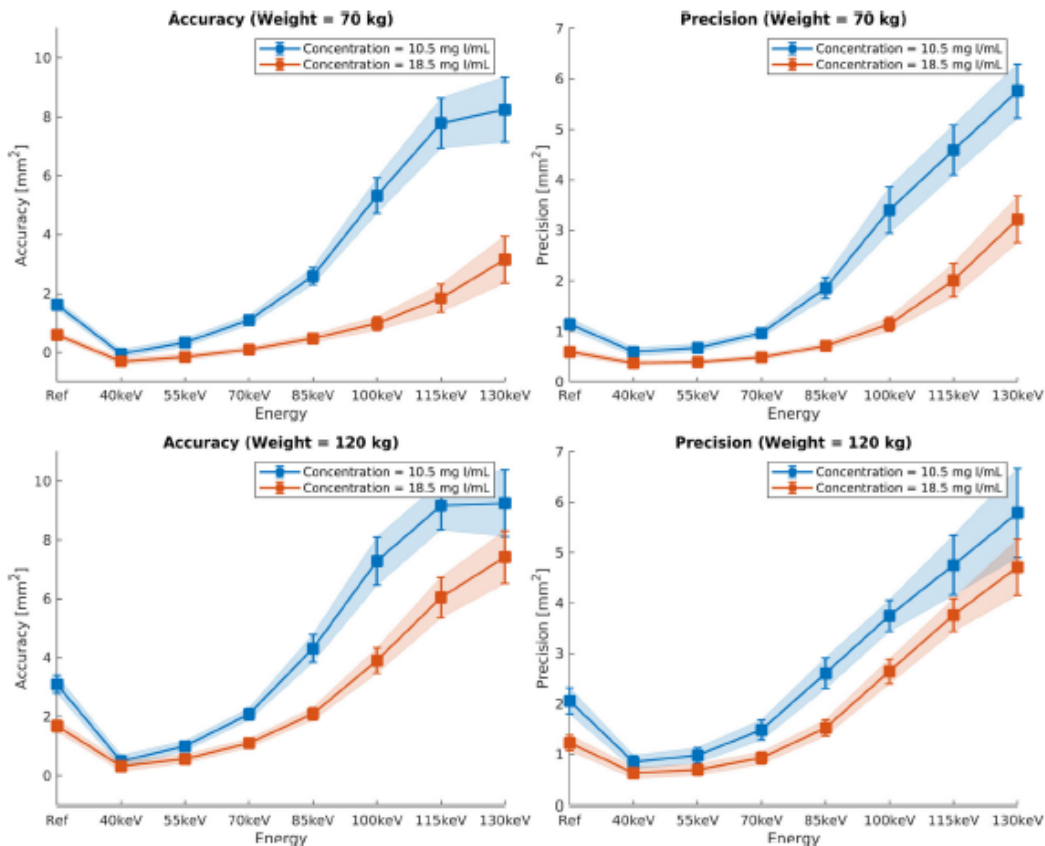


Fig. 1 In vitro accuracy and precision of vessel lumen segmentation as a function of iodine dose (10.5 or 18.5 mg/mL) and patient size (70 or 120 kg). The conventional reconstruction “Ref” at 18.5 mL approximates protocol A in the clinical study, whereas the virtual monochromatic

images (VMI) at 10.5 mg/mL approximate protocol B. Whatever the scanning condition, low VMI energies, up to a maximum of 55 keV, yielded peak segmentation accuracy and precision

even larger with simulated 120 kg patient size. Besides deteriorating the segmentation precision and accuracy themselves, higher VMI reconstruction energy levels also increased the measurement variability as indicated by the error bars in Fig. 1. On the one hand, CNR between vessels and surrounding background material indicated that low-iodine 55-keV VMI preserve or improve (depending on phantom size) the CNR compared with regular-iodine conventional images and, on the other hand, suggested substantial noise reduction on VMI (Supplementary Figure E).

Clinical study

Thirty-two (13.6%) patients were excluded due to a calcium score > 400. In the 203 patients included in the analysis, there were no significant differences in age, sex, or patient size between groups A and B (all $p \geq 0.36$; Table 1). Patients in group B more often had hypertension ($p = 0.03$); otherwise, there were no differences regarding risk factors between groups. Examination-related characteristics are detailed in

Table 2. In group B, the venous catheter was more often positioned in the left upper limb ($p = 0.03$) and more often in the forearm or wrist ($p < 0.001$). Injected CM volume was significantly higher in protocol A than in B (70.0 (IQR 8.8) mL and 40.0 (IQR 10.0) mL, respectively; $p < 0.001$). We observed no extravasation and mild allergic reaction occurred in 3/203 patients, with no significant difference between groups.

Quantitative image analysis

The 55-keV VMI provided the closest attenuation compared with conventional reconstructions and were used for the qualitative analysis. Mean coronary lumen attenuation was significantly higher in protocol A (conventional image reconstruction) versus in B (55-keV VMI) (397.4 (IQR 131.4) HU and 380.1 (IQR 136.4) HU, respectively; $p = 0.019$). Detailed per-segment and tissue attenuation values are presented in Table 3. The attenuation in all vessel segments and tissues (fat, muscle, and bone) was significantly influenced by the VMI reconstruction energy (all $p < 0.001$). CNR between

Table 2 CT examination characteristics and univariate comparisons

	Group A, 5 mL/s (n = 103)	Group B, 2.5 mL/s (n = 100)	p value
Venous catheter side, n (%)			
Right	86 (83.5%)	70 (70%)	0.031
Left	17 (16.5%)	30 (30%)	
Catheter location, n (%)			
Antecubital fossa	89 (86.4%)	64 (64%)	< 0.001
Forearm	12 (11.6%)	19 (19%)	
Hand or wrist	2 (1.9%)	17 (17%)	
Heart rate before injection [bpm]	67 [16.5]	69 [14.5]	0.617
Heart rate during injection [bpm]	63 [14]	66 [13]	0.043
Contrast medium volume [mL]	70 [8.8]	40 [10]	< 0.001
Contrast medium extravasation	None	None	
Allergy (%)			
Mild	1 (0.9%)	2 (1.8%)	0.973
Moderate	0	0	
Severe	0	0	
CTDI _{vol}	23 [13.5]	21.6 [13.6]	0.540
DLP	430.7 [266.1]	392.8 [251.7]	0.620

Data are medians [IQR], or numbers (percentage). *Bpm* beats per minute, *CTDI_{vol}* volume computed tomography dose index, *DLP* dose-length product

lumen and fat was significantly lower in protocol A versus in B (19.3 (IQR 11.6) and 24.9 (IQR 19.7), respectively; $p < 0.001$). CNR between lumen and muscle was significantly lower in protocol A versus in B (12.2 (IQR 8.5) and 14.3 (IQR 12.4), respectively; $p < 0.001$). Finally, CNR between lumen and bone was maintained with dual-energy CCTA (6.8 (IQR 7.3) (protocol A) and 6.7 (IQR 8.9) (protocol B), respectively; $p = 0.423$). A graphical representation (Fig. 2) across all energy levels in group B shows that reduced-CM-dose VMI reconstructions up to a maximum of 55 keV improve

CNR compared with conventional CCTA ($p = 0.012$, < 0.001 , and < 0.001 for lumen vs. fat, muscle, and bone, respectively).

Qualitative image analysis

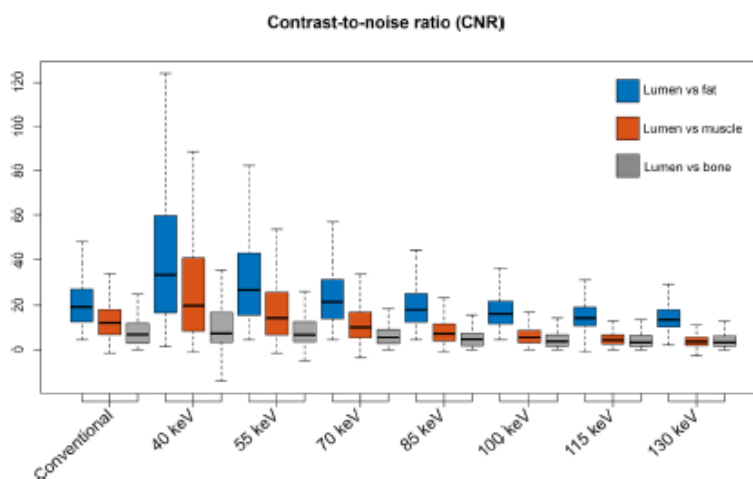
Examples of CCTA in two patients from groups A and B are illustrated in Fig. 3. While the image quality is excellent with protocol B, note that the distal LAD has slightly less lumen attenuation in protocol B than in A. Figure 4 and Table 4 summarize the results of the qualitative image analysis. The

Table 3 CT numbers in HU of the vascular lumen, epicardial fat, and muscle

	Reconstruction								p value
	Conventional	40 keV	55 keV	70 keV	85 keV	100 keV	115 keV	130 keV	
CM flow rate [mL/s]	5	2.5	2.5	2.5	2.5	2.5	2.5	2.5	
Proximal RCA	425 [116.9]	743.5 [262]	413.4 [130.6]	258.7 [80.4]	188.2 [57.6]	143.5 [45.2]	118.1 [38.2]	102 [36.8]	< 0.001
Distal RCA	414.9 [143.1]	606.3 [288.4]	346 [143.3]	222.7 [79.1]	163.9 [59.3]	130.4 [47.1]	109.4 [45.2]	95 [44]	< 0.001
LM	4451.1 [123]	828 [252]	463.5 [128.3]	284 [69.3]	205 [50.1]	160.1 [42.9]	131.1 [38.2]	114.8 [38.5]	< 0.001
Distal LAD	292.5 [135.8]	413 [244]	236.3 [134]	160 [70.9]	119.8 [55.5]	94.6 [52.6]	80 [48.6]	69.5 [45.3]	< 0.001
Distal LCx	337.9 [115.5]	496.1 [265.6]	279.6 [146.4]	185.2 [91.5]	139.8 [63.8]	116.7 [56.7]	99 [52.9]	90.7 [49]	< 0.001
Ascending aorta	466 [154.1]	871.9 [246.9]	486 [130.6]	301.4 [76.3]	211.4 [52.3]	161.4 [40.8]	130.6 [29.5]	114.2 [27.3]	< 0.001
Median	397.4 [131.4]	691.8 [259.9]	380.1 [136.4]	243.2 [77.9]	172.6 [56.4]	135.9 [47.5]	113 [42.1]	99 [40.1]	< 0.001
Epicardial fat	-87.1 [28.6]	-178 [47.6]	-124 [25.3]	-101 [19.9]	-90 [17.3]	-85 [16.4]	-81.2 [17.9]	-78.5 [15.5]	< 0.001
Muscle	103.4 [36.8]	163.1 [56.9]	108 [33.1]	81.8 [21.3]	70.5 [15.2]	63.1 [13.3]	58.4 [14.1]	56 [13]	< 0.001
Trabecular bone	201.8 [100.1]	481.6 [399.1]	297.4 [318.2]	208.5 [236.5]	169.6 [142.6]	149 [126]	138 [112.5]	130.6 [103]	< 0.001

Data are median [IQR]—univariate comparison with the Kruskal-Wallis test. IQR indicates data variability across all patients in the group. *CM* contrast medium, *keV* kilo-electronvolt, *RCA* right coronary artery, *LM* left main, *LAD* left anterior descending, *LCx* left circumflex

Fig. 2 Boxplots show contrast-to-noise ratios (CNR) for different scenarios: lumen vs. fat to approximate an epicardial vessel surrounded by fat, lumen vs. muscle to approximate a non-calcified plaque, and lumen vs. trabecular bone to approximate a calcified plaque. When comparing group A (5 mL/s) with group B (2.5 mL/s reconstructed at 55 keV), no significant difference in lumen to bone CNR was found, but group B had significantly better lumen to fat and lumen to muscle CNR



overall success rate was 88.4% ($n = 91/103$) in group A and 89% ($n = 89/100$) in group B ($p = 0.884$). Noninferiority of protocol B compared to A was inferred (95% CI of the difference = -0.0937 to 0.0807), with a prespecified noninferiority margin of 10%. Among the segments deemed non-diagnostic, 80% (44/55) in group A and 74.6% (47/63) in group B had motion artifacts ($p = 0.47$). The inter-rater agreement was substantial ($\kappa = 0.627$ and 0.755 in groups A and B, respectively). Per segment image quality analysis (Fig. 5) showed that segments in group A had a slightly higher mean score than in group B, except for the RCA and D2, where differences were not statistically significant. Nevertheless, the mean scores were between good (score 3) and excellent (score 4) in all segments and groups.

Discussion

Our study aimed to compare conventional CCTA with reduced-CM-dose dual-energy CCTA in both a resolution phantom and large patient cohort; the reduced-iodine-dose spectral CT protocol outperformed conventional CT in vitro and was noninferior in vivo. This is the largest study assessing the potential to reduce CM with dual-energy CCTA, and the only one using an appropriate noninferiority statistical analysis.

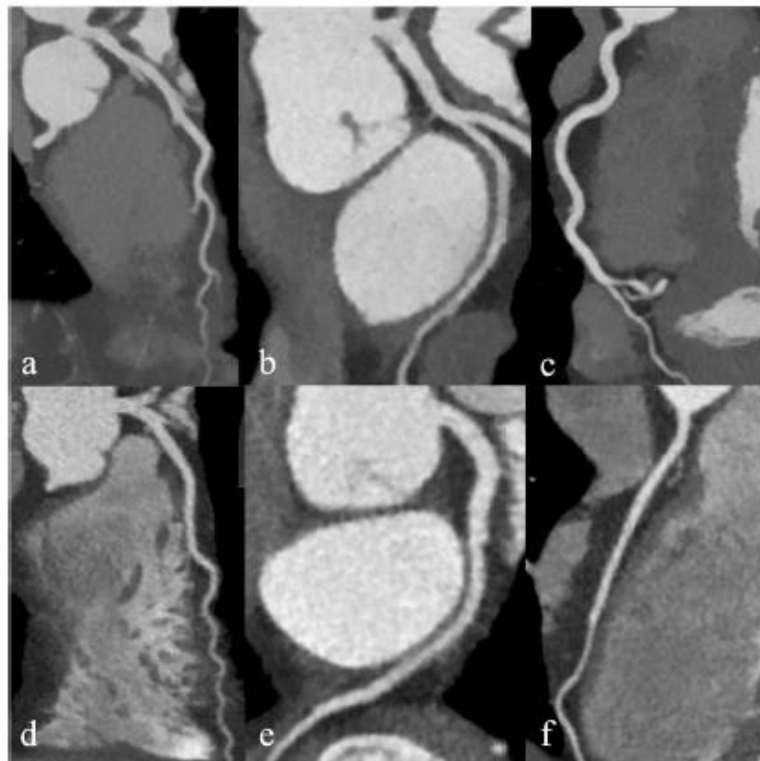
Today, CCTA is used in a broad range of clinical applications, even in high-risk coronary artery disease [22]. That is, upon plaque detection, quantification is required to guide patient management. Stenosis quantification must be precise, whether through semi-automatic stenosis assessment by a

Table 4 Qualitative analysis

	Group A, 5 mL/s	Group B, 2.5 mL/s	<i>p</i> value
<i>n</i> patients	103	100	
Patients with diagnostic CCTA, <i>n</i> (%)	91/103 (88.4%)	89/100 (89%)	0.884
Patients with non-diagnostic CCTA, <i>n</i> (%)	12/103 (11.6%)	11/100 (11%)	
	Non-diagnostic due to motion artifacts	10/11 (90.9%)	0.29
	Non-diagnostic due to inadequate enhancement	1/11 (9.1%)	
Total segments analyzed	1441	1310	
Image quality score			
Excellent, <i>n</i> (%)	1220/1441 (84.7%)	949/1310 (72.4%)	
Good, <i>n</i> (%)	74/1441 (5.1%)	267/1310 (20.4%)	
Adequate 3, <i>n</i> (%)	35/1441 (2.4%)	31/1310 (2.4%)	
Poor (non-evaluable), <i>n</i> (%)	55/1441 (3.8%)	63/1310 (4.8%)	
	Poor due to motion artifacts	47/63 (74.6%)	0.486
	Poor due to inadequate enhancement	16/63 (25.4%)	
Average image quality score per segment (\pm SD)	3.9 (\pm 0.4)	3.7 (\pm 0.5)	< 0.001

Data are numbers with percentages in parentheses or mean \pm standard deviation. CCTA coronary computed tomography angiography

Fig. 3 Coronary CT angiography obtained with 40 mL contrast medium injected at 2.5 mL/s and reconstructed as virtual monoenergetic images at 55 keV, depicting the LAD, LCx, and RCA (a–c), in a 68-year-old male. Coronary CT angiography obtained with 70 mL contrast agent injected at 5 mL/s and reconstructed as conventional polychromatic images, depicting the LAD, LCx, and RCA (d–f), in a 48-year-old female. LAD, left anterior descending; Cx, circumflex artery; RCA, right coronary artery; keV, kilo-electronvolt



radiologist or with automated fractional flow reserve CT (FFR-CT) [23]. Both methods rely on an accurate representation of the vessel's cross-sectional area, which led us to conduct a phantom study to evaluate cross-sectional segmentation accuracy. Not only did VMI help preserve the segmentation accuracy and precision with reduced CM, but VMI even improved segmentation in the phantom setup simulating larger

patients. CCTA in obese patients remains challenging and usually results in a higher radiation dose [24]. Contrary to low-tube-voltage scanning (70–80 kVp), dual-energy CCTA with VMI allowed CM reduction even in patients $> 25 \text{ kg/m}^2$ [25], since our study included patients with BMI up to 40 kg/m^2 . The optimal VMI energy level for image analysis is still debated and may depend upon the system used; in the early

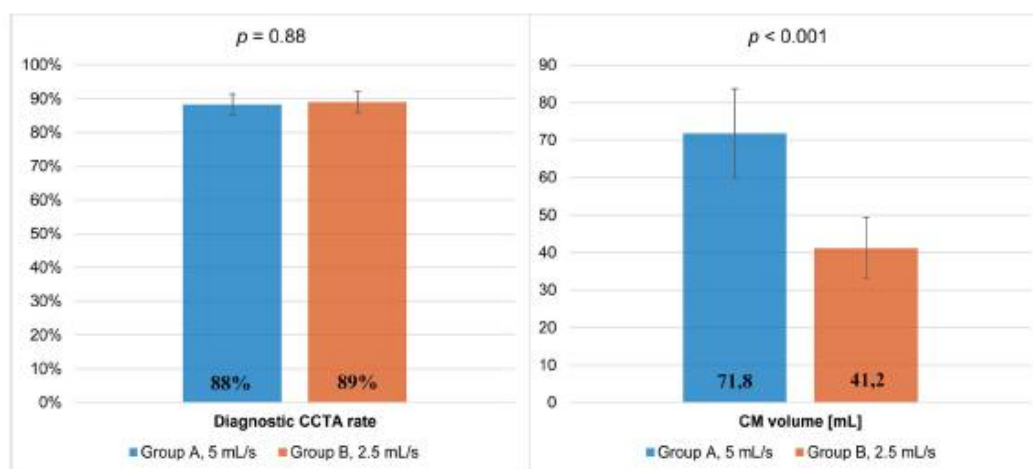


Fig. 4 Proportion of interpretable CCTA (\pm standard error) and contrast agent volume (\pm standard deviation) in groups A and B. CM, contrast medium; CCTA, coronary computed tomography angiography.

Conventional polychromatic images in group A and virtual monoenergetic images at 55 keV in group B

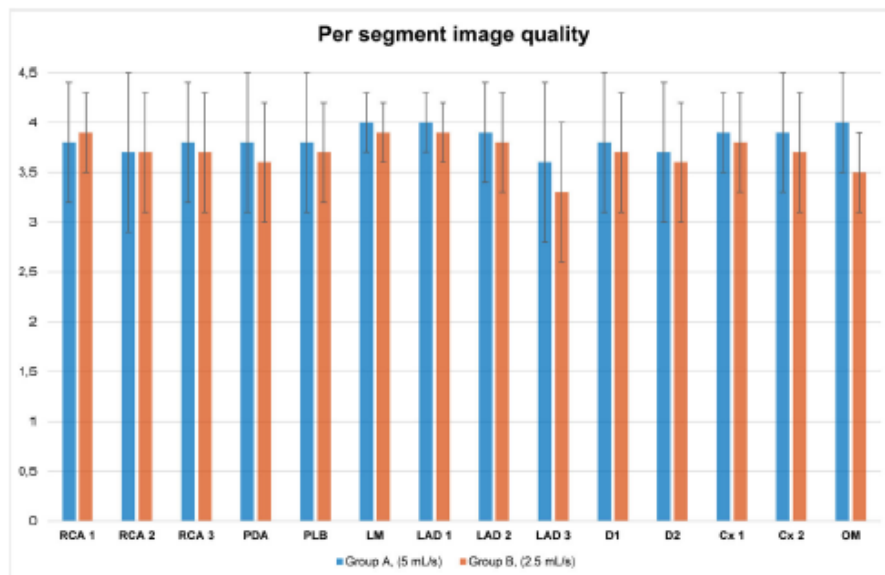


Fig. 5 Per segment qualitative image analysis in group A and B and univariate comparison. Error bars represent standard deviation. Proximal right coronary artery (RCA 1), $p = 0.96$; mid right coronary artery (RCA 2), $p = 0.552$; distal right coronary artery (RCA 3), $p = 0.216$; posterior descending artery (PDA), $p = 0.001$; posterolateral branch (PLB), $p = 0.010$; left main (LM), $p = 0.05$; proximal left anterior descending (LAD 1), $p = 0.004$; mid left anterior descending

(LAD 2), $p = 0.023$; distal left anterior descending (LAD 3), $p = 0.001$; first diagonal (D1), $p = 0.031$; second diagonal (D2), $p = 0.059$; proximal circumflex (Cx 1), $p = 0.009$; distal circumflex (Cx 2), $p < 0.001$; obtuse marginal (OM), $p = 0.003$. LAD, left anterior descending; LCx, left circumflex; LM, left main; OM, obtuse marginal; PDA, posterior descending artery; PLB, posterolateral branch; RCA, right coronary artery

days of DECT, low-keV VMI had higher noise, and initial reports advocated VMI in the range of 65–80 keV [12, 26]. Nevertheless, much has already been achieved for making low-energy VMI suitable for clinical use, and more recent studies emphasize the value of reconstructions at lower energies [14, 27].

In the patient study, we found a minimal compromise regarding qualitative image quality, which agrees with Raju et al [7]. Specifically, the distal coronary segments received slightly lower image quality scores in group B. Nevertheless, the mean image quality scores were between good and excellent in both study groups, and CM reduction did not impair the diagnosis. We calculated CNR between the lumen and various densities approximating calcified, non-calcified, and lipid-rich plaques to evaluate whether the detectability of different plaque types was maintained on low-iodine CCTA images. While such CNR measurements do not directly relate to calcified or non-calcified coronary atherosclerotic plaques, the analyses account for the specific spectral behavior of fat, soft-tissue, and calcium-containing materials to show trends that can be expected when using VMI. The CNR between the lumen and calcium was comparable in groups A and B, despite a lower lumen-to-bone contrast on VMI, which is attributed to the lower noise present on spectral-based images. VMI and other dual-layer CT-derived spectral reconstructions use noise anti-correlation to reduce the overall noise magnitude [28]. On the other hand, the CNR between the lumen and fat

was significantly higher in group B, mostly because fat exhibits lower attenuation at 55 keV (−122 HU in our study) than on conventional images (−88 HU), which confirms early findings by Oda et al [8]. This indicates that plaque composition analysis may be improved with reduced CM and lower energy VMI, but also highlights the potential usefulness of lower energy VMI reconstructions for plaque composition analysis, especially the detection of lipid-rich core, a clinically relevant determinant of plaque vulnerability [29].

To achieve proper arterial enhancement, current guidelines recommend the use of high contrast medium (CM) injection rates and doses, typically on the order of 5–7 mL/s, at a concentration of 270–400 mg I/mL, and a total volume of 50–120 mL [30]. Such injection parameters ideally involve 18-G venous catheters located in the right antecubital fossa. Nevertheless, we found that almost a quarter of patients had their catheter placed in the forearm or the wrist, which is reflective of the challenges faced in daily patient management. Patients with a catheter inserted in the forearm or the wrist were almost three times more likely to be subjected to the group with lower CM delivery rate, indicating that protocol B may have helped manage patients with poor vein integrity.

Despite careful design, our study has several limitations. First, we could not reliably assess the accuracy of stenosis quantification in vivo because of the low incidence of coronary artery disease in our study population; less than 10% of patients had a coronary artery stenosis $\geq 70\%$. Evaluation of

diagnostic accuracy should be considered in another patient population for whom an indication for invasive coronary angiography exists. However, the phantom study provides encouraging results in that field. Second, we used retrospective ECG-gating resulting in relatively high radiation dose delivery. This choice was linked to z-axis coverage of the dual-layer spectral detector, which is 4 cm; still, a new platform with 8 cm detector coverage is in the process of being released, and wide-area (16 cm) detectors are expected to become available for spectral ECG-gated cardiac CT. Third, we did not test pre- and post-injection serum creatinine levels, nor did we include at-risk patients (with an estimated glomerular filtration rate < 30 mL/min); therefore, we cannot comment on the impact of CM on kidney function. Fourth, the injection protocol was chosen individually by the radiologist in charge; however, since patients with poor vein integrity more often received reduced-CM-dose dual-energy CCTA, we do not expect a relevant bias towards too good image quality in this group. Finally, our results might not apply to other DECT systems since ECG-gated DECT scanning is not available on all DECT platforms and because certain vendors need to cut back temporal resolution when using spectral mode, some of which may result in increased radiation dose, motion, or misalignment artifacts. Despite this, when dual-source CT is used in spectral mode, its temporal resolution is still similar to that of dual-layer CT, and that fast kVp switching platforms will soon support faster gantry rotation speed, which may compensate for the loss of temporal resolution.

In conclusion, dual-energy CCTA allows for a 40% iodine dose and 50% injection rate reduction while preserving diagnostic image quality and may facilitate the management of patients with poor venous access. Furthermore, low-keV VMI improve the CNR between lumen versus fat and muscle, offering an opportunity to enhance the contrast between various plaque components, which is key for the quantification of the lipid-rich core. In vitro results indicate that low-keV VMI improve vessel area quantification, especially in simulated overweight subjects.

Supplementary Information The online version contains supplementary material available at <https://doi.org/10.1007/s00330-021-07809-w>.

Funding Open Access funding provided by Université de Lausanne. This study has received funding by Bracco Imaging, France.

Declarations

Guarantor The scientific guarantor of this publication is Prof. Philippe C. Douek, MD, PhD.

Conflict of Interest The authors of this manuscript declare no relationships with any companies whose products or services may be related to the subject matter of the article.

Statistics and biometry One of the authors has significant statistical expertise.

Informed consent Written informed consent was waived by the Institutional Review Board.

Ethical approval Institutional Review Board approval was obtained.

Methodology

- retrospective
- observational
- multicenter study

Open Access This article is licensed under a Creative Commons Attribution 4.0 International License, which permits use, sharing, adaptation, distribution and reproduction in any medium or format, as long as you give appropriate credit to the original author(s) and the source, provide a link to the Creative Commons licence, and indicate if changes were made. The images or other third party material in this article are included in the article's Creative Commons licence, unless indicated otherwise in a credit line to the material. If material is not included in the article's Creative Commons licence and your intended use is not permitted by statutory regulation or exceeds the permitted use, you will need to obtain permission directly from the copyright holder. To view a copy of this licence, visit <http://creativecommons.org/licenses/by/4.0/>.

References

1. Schoepf UJ, Zwemer PL, Savino G, Herzog C, Kerl JM, Costello P (2007) Coronary CT angiography. *Radiology* 244:48–63
2. Brown JR, Robb JF, Block CA et al (2010) Does safe dosing of iodinated contrast prevent contrast-induced acute kidney injury? *Circ Cardiovasc Interv* 3:346–350
3. Van Cauteren T, Honoria Da Silva E, Van Gompel G et al (2019) Iodine dose of administered contrast media affects the level of radiation-induced DNA damage during cardiac CT scans. *AJR Am J Roentgenol* 213:404–409
4. American College of Radiology (2020) ACR manual on contrast media v10.3. Available via https://www.acr.org/-/media/ACR/Files/Clinical-Resources/Contrast_Media.pdf. Accessed Apr 18 2020
5. van Hamersvelt RW, Eijssvoegel NG, Mihal C et al (2018) Contrast agent concentration optimization in CTA using low tube voltage and dual-energy CT in multiple vendors: a phantom study. *Int J Cardiovasc Imaging* 34:1265–1275
6. Carrascosa P, Leipsic JA, Capunay C et al (2015) Monochromatic image reconstruction by dual energy imaging allows half iodine load computed tomography coronary angiography. *Eur J Radiol* 84:1915–1920
7. Raju R, Thompson AG, Lee K et al (2014) Reduced iodine load with CT coronary angiography using dual-energy imaging: a prospective randomized trial compared with standard coronary CT angiography. *J Cardiovasc Comput Tomogr* 8:282–288
8. Oda S, Takaoka H, Katahira K et al (2019) Low contrast material dose coronary computed tomographic angiography using a dual-layer spectral detector system in patients at risk for contrast-induced nephropathy. *Br J Radiol* 92:20180215
9. Yi Y, Zhao XM, Wu RZ et al (2019) Low dose and low contrast medium coronary CT angiography using dual-layer spectral detector CT. *Int Heart J* 60:608–617

10. Park SH, Ahn S, Hong N, Park JH, Hwang SS, Lee KH (2014) Quality of reporting noninferiority/similarity in research studies of diagnostic imaging. *Radiology* 270:241–247
11. Molloy S, Johnson T, Lipinski J, Ding H, Hubbard L (2019) A phantom based evaluation of vessel lumen area quantification for coronary CT angiography. *Int J Cardiovasc Imaging* 35:551–557
12. Fuchs TA, Stehli J, Fiechter M et al (2013) First experience with monochromatic coronary computed tomography angiography from a 64-slice CT scanner with Gemstone Spectral Imaging (GSI). *J Cardiovasc Comput Tomogr* 7:25–31
13. De Santis D, Caruso D, Schoepf UJ et al (2018) Contrast media injection protocol optimization for dual-energy coronary CT angiography: results from a circulation phantom. *Eur Radiol* 28:3473–3481
14. Huang X, Gao S, Ma Y, Lu X, Jia Z, Hou Y (2020) The optimal monoenergetic spectral image level of coronary computed tomography (CT) angiography on a dual-layer spectral detector CT with half-dose contrast media. *Quant Imaging Med Surg* 10:592–603
15. Verdun FR, Racine D, Ott JG et al (2015) Image quality in CT: from physical measurements to model observers. *Phys Med* 31: 823–843
16. Rotzinger DC, Racine D, Beigelman-Aubry C et al (2018) Task-based model observer assessment of a partial model-based iterative reconstruction algorithm in thoracic oncologic multidetector CT. *Sci Rep* 8:17734
17. Yerly J, Becce F, van Heeswijk RB et al (2019) In vitro optimization and comparison of CT angiography versus radial cardiovascular magnetic resonance for the quantification of cross-sectional areas and coronary endothelial function. *J Cardiovasc Magn Reson* 21:11
18. Baroldi G (1983) Disease of the coronary arteries. In: *Cardiovascular pathology*, Churchill Livingstone, New York
19. Yerly J, Gubian D, Knebel JF et al (2018) A phantom study to determine the theoretical accuracy and precision of radial MRI to measure cross-sectional area differences for the application of coronary endothelial function assessment. *Magn Reson Med* 79:108–120
20. Hausleiter J, Martinoff S, Hadamitzky M et al (2010) Image quality and radiation exposure with a low tube voltage protocol for coronary CT angiography results of the PROTECTION II Trial. *JACC Cardiovasc Imaging* 3:1113–1123
21. Achenbach S, Paul JF, Laurent F et al (2017) Comparative assessment of image quality for coronary CT angiography with iobitridol and two contrast agents with higher iodine concentrations: iopromide and iomeprol. A multicentre randomized double-blind trial. *Eur Radiol* 27:821–830
22. Linde JJ, Kelbæk H, Hansen TF et al (2020) Coronary CT angiography in patients with non-ST-segment elevation acute coronary syndrome. *J Am Coll Cardiol* 75:453–463
23. Min JK, Leipsic J, Pencina MJ et al (2012) Diagnostic accuracy of fractional flow reserve from anatomic CT angiography. *JAMA* 308: 1237–1245
24. Segev OL, Gaspar T, Halon DA et al (2012) Image quality in obese patients undergoing 256-row computed tomography coronary angiography. *Int J Cardiovasc Imaging* 28:633–639
25. Feng R, Tong J, Liu X, Zhao Y, Zhang L (2017) High-pitch coronary CT angiography at 70 kVp adopting a protocol of low injection speed and low volume of contrast medium. *Korean J Radiol* 18:763–772
26. Scheske JA, O'Brien JM, Earls JP et al (2013) Coronary artery imaging with single-source rapid kilovolt peak-switching dual-energy CT. *Radiology* 268:702–709
27. Symons R, Choi Y, Cork TE et al (2018) Optimized energy of spectral coronary CT angiography for coronary plaque detection and quantification. *J Cardiovasc Comput Tomogr* 12:108–114
28. Ehn S, Sesslerer T, Muenzel D et al (2018) Assessment of quantification accuracy and image quality of a full-body dual-layer spectral CT system. *J Appl Clin Med Phys* 19:204–217
29. Dwivedi G, Liu Y, Tewari S, Inacio J, Pelletier-Galarneau M, Chow BJ (2016) Incremental prognostic value of quantified vulnerable plaque by cardiac computed tomography: a pilot study. *J Thorac Imaging* 31:373–379
30. Abbara S, Blanke P, Maroules CD et al (2016) SCCT guidelines for the performance and acquisition of coronary computed tomographic angiography: a report of the society of Cardiovascular Computed Tomography Guidelines Committee: Endorsed by the North American Society for Cardiovascular Imaging (NASCI). *J Cardiovasc Comput Tomogr* 10:435–449

Publisher's note Springer Nature remains neutral with regard to jurisdictional claims in published maps and institutional affiliations.

6.2 Tissue contrast and characterization

6.2.1 Effect of contrast material injection protocol on first-pass myocardial perfusion assessed by dual-energy CT

Paper submitted to journal “Quantitative Imaging in Medicine and Surgery” at time of writing.

Implications for patient care

Myocardial perfusion CT is a means of evaluating ischemic cardiac disease. This study draws attention to the critical importance of carefully selecting the injection protocol when conducting quantitative DECT perfusion analysis. Injection protocols are not interchangeable and can affect the diagnosis. Furthermore, this work demonstrates the potential of VMI to improve image quality.

Author contribution

Co-author: initiated the study, constituted the patient cohort, collected data, performed first analyses, and presented abstract at the European Society of Cardiovascular Radiology conference. Supported literature review and participated in draft editing.

Effect of contrast material injection protocol on first-pass myocardial perfusion assessed by dual-energy dual-layer CT

Contrast injection protocol effect on myocardial perfusion

Sara Boccalini, MD, PhD^{1,2*}; Salim Si-Mohamed, MD^{1,3*}; Maxime Matzuzzi, Msc⁴; Manon Tillier, Msc⁴; David Rotzinger, MD⁵; Didier Revel, MD^{1,3}, PhD; Loic Boussel, MD, PhD^{1,3}; Philippe Douek, MD, PhD^{1,3}



¹ Department of Cardiovascular and Thoracic Radiology, Hospices Civils de Lyon, Lyon, France

² University Claude Bernard Lyon 1, Lyon, France

³ University Claude Bernard Lyon 1, CREATIS, CNRS UMR 5220, INSERM U1206, INSA-Lyon, France

⁴ Faculty of Medicine Rockefeller, University Claude Bernard Lyon 1, Lyon, France

⁵ Department of Radiology, Centre Hospitalier Universitaire Vaudois, Lausanne, Switzerland

Sara Boccalini and Salim Si-Mohamed contributed equally and share first authorship

Corresponding author:

Sara Boccalini

Service d'Imagerie Cardio-vasculaire et Thoracique

Hôpital Louis Pradel - Hospices Civils de Lyon

28 Avenue de Doyen Lépine

69500 Bron

Telephone: +330472357396

Email: sara.boccalini@chu-lyon.fr ; sara.boccalini@yahoo.com

Abstract

Background: Dual-energy dual-layer CT scanners (DE-DLCT) can provide useful tools, such as iodine maps and virtual monochromatic images (VMI), for the evaluation of myocardial perfusion defects. Data about the influence of acquisition protocols and normal values are still lacking.

Methods: Clinically indicated coronary CT-angiographies performed between January-July 2018 with DE-DLCT and different injection protocols were retrospectively evaluated. The two protocols were: 35mL in patients <80kg and 0.5mL/kg in patients >80kg at 2.5mL/sec (A) or double contrast dose at 5mL/sec (B). Patients with coronary stenosis >50% were excluded. ROIs were manually drawn on 16 myocardial segments and iodine concentration was measured in mg/mL. Signal-to-noise, contrast-to-noise ratios (SNR, CNR) and image noise were measured on conventional images and VMI.

Results: 30 patients were included for each protocol. With iodine concentrations of 1.38 ± 0.41 mg/mL for protocol A and 2.07 ± 0.73 mg/mL for protocol B, the two groups were significantly different ($p<0.001$). No significant iodine concentration differences were found between the 16 segments, between basal, mid and apical segments for group A and B ($p=0.47$ and $p=0.09$; $p=0.28$ and $p=0.12$, respectively) and between wall regions for group A ($p=0.06$ on normalised data). In group B, iodine concentration was significantly different between three wall regions (highest values for the lateral wall, median= $2.03(1.06)$ mg/mL). Post-hoc analysis showed highest CNR and SNR in VMI at 40eV ($p<0.05$).

Conclusion: Iodine concentration in healthy myocardium varied depending on the injection protocol and appeared more heterogeneous at faster injection rate and greater iodine load. VMI demonstrated the potential of DE-DLCT to enhance image quality.

Abbreviations and acronyms:

-BMI: body mass index

-CNR: contrast-to-noise ratio

-CT: computed tomography

-CTDI: CT dose index

-DE-DLCT: dual-energy dual-layer computed tomography

-IQR: interquartile range

-ROI: region of interest

-SNR: signal-to-noise ratio

-VMI: virtual monochromatic image

1. Introduction

Coronary computed tomography (CT) angiography is the standard non-invasive diagnostic technique for the anatomic detection of coronary stenosis. However, in the case of intermediate stenosis, it is difficult to determine whether it results in a perfusion defect. In fact, the presence of a coronary stenosis is not necessarily related to an impairment of myocardial blood flow that, on the contrary, is the factor guiding clinical management of patients with coronary artery disease.^{1,2} In recent years, multiple CT protocols have been proposed to assess, in a single diagnostic test, not only coronary artery anatomy but also myocardial perfusion under stress and at rest.^{3,4}

Dual-energy computed tomography (DECT) has been proposed to assess myocardial ischemia. Currently, several DECT methods are available based on the source (dual source, fast kilovoltage switching, double rotation and split beam) or detector (dual-layer).^{5,6} With DECT, in addition to conventional images, virtual monochromatic images (VMI) and iodine maps can be derived. Due to its specific technology, dual-energy dual-layer CT (DE-DLCT) presents several features of interest for its feasibility and broad applicability in clinical practice. These include the possibility to perform an examination with standard parameters that does not need to be chosen beforehand, without any loss of temporal resolution and without temporal or spatial disalignment.⁷

Separating low and high energy X photons, DECT increases tissue contrast and enhances iodine attenuation.⁸ Low energy VMI have been shown to improve vascular contrast enhancement and therefore could facilitate the detection of perfusion defect. Moreover, monochromatic images could help reduce beam hardening artifacts.⁷

To date, the evaluation of static first-pass perfusion images with conventional CT and DECT is performed qualitatively by visual assessment of alterations in myocardial density or iodine maps.⁹⁻¹¹ However,

quantification of iodine density could provide a more objective assessment and has been regarded to as a surrogate biomarker for myocardial perfusion. Only a few studies investigated myocardial iodine concentration in the attempt to establish cut-off values to distinguish healthy, ischemic and necrotic segments.^{12,13} Moreover, for DE-DLCT, although a few phantom studies have demonstrated the accuracy of iodine concentration measurements¹⁴⁻¹⁶, there are no clinical data about such analysis in human myocardium. In addition, to the best of our knowledge, there are no data available regarding the effect of CT acquisition parameters on iodine concentration such as contrast material injection protocols.

Therefore, the purpose of this study was twofold: (a) to demonstrate the effect of contrast material injection rate on the iodine distribution in healthy myocardium during first-pass perfusion; (b) to evaluate the impact of virtual monochromatic images (VMI) on image noise, signal-to-noise ratio and contrast-to-noise ratio.

2. Methods

2.1 Study Design

This single-centre, retrospective analysis was approved by the local ethics committee (19-382). Informed consent was waived due to the retrospective nature of the study.

2.2 Population

Consecutive coronary-CTA scans performed from January to October 2018 in the clinical practice of a single university academic centre with a DE-DLCT were retrospectively included. All subjects underwent a preliminary non-contrast acquisition to calculate the calcium score and only those with an Agatston score < 400 were further evaluated.

Each patient underwent either a reduced flow protocol (2.5 mL/s rate, group A) or a standard injection protocol (5 mL/s rate, group B) depending on the quality of the venous access.

Subjects with coronary artery stenosis >50%, anomalous malignant origin of coronary arteries, myocardial hypertrophy (myocardial thickness >15 mm) and artefacts impeding the analysis of most segments were excluded from the analysis.

The flow chart of the study is depicted in **Figure 1**.

2.3 Contrast material injection

Iomeprol 400 mg I/mL (Iomeron[®]; Bracco) was the only contrast material employed; it was heated before use and injected using a double head power injector. Starting from a standard injection protocol (that was employed in group B) and keeping the injection time constant, the parameters for the group with low injection rate and iodine content (group A) were calculated. For group A patients, the contrast

material was administered into an 18G catheter, with a flow rate reduced to 2.5 mL/s (iodine rate = 1 g/s) and followed by a 20 mL saline rinse at the same rate. The injection time being kept constant and the flow reduced by half, the volume of the contrast material bolus was reduced by half in group A: 35 mL in patients <80 kg and 0.5 mL / kg in patients > 80 kg, maximum 45 mL. Group B patients underwent a standard coronary CTA injection protocol, consisting of a contrast material bolus injected at 5 mL/s (iodine rate = 2 g/s) into an 18G catheter, followed by a 20 mL saline rinse at the same rate. The volume of the bolus was determined according to the weight of the patient: 70 mL for patients <80 kg and 1 mL / kg for patients > 80 kg, to a maximum of 90 mL.

2.4 Image acquisition

All examinations were performed on a commercially available dual-layer spectral CT (IQon spectral CT; Philips Healthcare). This novel scanner acquires spectral data per default at each CT scan. Patients were placed in supine position, arms above the head. If necessary, patients received intravenous beta-blocker to reach a pre-scan heart rate of ≤ 65 bpm. Retrospective ECG-gating was used for the acquisition of the arterial phase. The detailed scanning parameters were: tube potential: 120 kVp; tube current: 220 mAs; gantry revolution time: 0.27s; automatic exposure control (angular and longitudinal), combined xyz axis; detector collimation: 64x0.625 mm, scanning field of view: 22 cm. Bolus tracking was used, with a region of interest (ROI) placed in the descending aorta and a cutoff value of 130 HU.

2.5 Image reconstruction

Data acquired with both protocols were reconstructed with the same parameters. The same iterative reconstruction strength was employed (iDose 3). Data were reconstructed at a specific targeted mid-

diastolic phase (78%) of the R-R interval with a slice thickness of 3 mm (increment 1.5 mm) for visualisation, using a soft kernel. To assess the myocardium, a field-of-view (FOV) of 500 mm was employed.

2.6 Image segmentation and analysis

Regions of interest were drawn manually in the 16 myocardial segments according to the American Heart Association recommendations (apex excluded) by a radiologist specialized in cardiac imaging (x, 6 years of experience) on multiplanar reconstructions of the heart in short axis planes (**Figure 2**). Abnormal segments, for instance due to motion artefacts, were excluded. The subendocardial and epicardial regions and coronary arteries were avoided. Circular ROIs were drawn in the lumen of the left ventricular cavity at basal, mid and apical level as well as in homogeneous areas of the paravertebral and intercostal muscles. Mean values and standard deviation were recorded for each of the reconstructed series (conventional images, iodine maps and virtual monochromatic images).

Virtual monochromatic images (VMI) between 40 and 70 keV in 10 keV increments were reconstructed and analysed (**Figure 2**).

A quantitative assessment of iodine concentration (in mg/mL) in each myocardial segment was performed using the dedicated software package (Spectral IntelliSpace Portal, ISP) on the iodine maps generated with a two material-based (iodine-water) decomposition (**Figure 2**).

2.7 Iodine concentration

Average iodine concentration of the 16 segments in the two groups was compared. For each group, iodine concentrations in each of the 16 segments, in basal, mid and apical segments (basal segments:

1, 2, 3, 4, 5, 6; mid segments: 7, 8, 9, 10, 11, 12; apical segments: 13, 14, 15, 16) as well as in three regions defined as anteroseptal-anterior (corresponding to segments: 1, 2, 7, 8, 13, 14), inferoseptal-inferior (corresponding to segments: 3, 4, 9, 10, 15) and lateral (corresponding to segments: 5, 6, 11, 12, 16) were compared.

The same comparisons were repeated for iodine values of myocardial segments normalized for the iodine concentration of the left ventricle at the corresponding level.

2.8 Objective quality analysis

Image noise, signal-to-noise ratio (SNR) and contrast-to-noise ratio (CNR) between the myocardial segments and paravertebral muscle were measured using the ROIs measurement on the conventional and VMI images as follows:

$$\text{Image noise} = \frac{SD \text{ myocardial} + SD \text{ paravertebral muscle}}{2}, \text{ SNR} = \frac{\text{Mean value}}{\text{Standard deviation}} \text{ for each ROI,}$$

$$\text{CNR} = \frac{(\text{Mean value myocardial} - \text{Mean value paravertebral muscle})}{\left(\frac{SD \text{ myocardial} + SD \text{ paravertebral muscle}}{2}\right)}.$$

Average image noise, SNR and CNR values of each myocardium were compared between conventional images and the four monochromatic reconstructions for the two groups.

2.9 Statistical Analysis

All statistical analyses were performed with R (R v. 3.4.3, R Foundation for Statistical Computing, Vienna, Austria). Continuous values were presented as mean \pm standard deviation (SD) or as median with interquartile ranges (IQR). Student's t-test and Wilcoxon were employed to compare patients'

characteristics. Wilcoxon Mann Whitney and Kruskal-Wallis were employed for comparison between different myocardial segments, territories and protocols. The pairwise Wilcoxon test with Bonferroni correction was used for comparison between groups and post hoc analysis. Values of $p < 0.05$ were considered statistically significant.

3. Results

3.1 Population

A total of 60 patients were analysed, of whom 30 underwent protocol A (group A) and 30 protocol B (group B). The characteristics of the 60 patients are shown in **Table 1**. The comparison of the two patient groups did not reveal any significant differences in age, gender, heart rate, weight and height, BMI and radiation dose.

Due to motion artefacts, 1 segment out of 480 (0.2%) and 7 segments out of 480 (1.5%) were excluded from analysis in group A and B respectively.

3.2 Iodine density maps

The mean iodine concentration values in healthy myocardial segments were 1.38 ± 0.41 (range: 0.6-2.24; median: 1.33; IQR: 0.66) mg/mL for protocol A and 2.07 ± 0.73 (range: 1.17-3.94; median: 1.87; IQR: 1.02) mg/mL for protocol B (**Figure 3**), corresponding to a significant difference ($p < 0.001$). For normalised values the difference was also significant ($p < 0.001$) but with higher values in group A (median: 1.54, IQR: 0.13 for group A; median 0.12, IQR: 0.06 for group B).

Iodine concentration values of the 16 segments, of basal, mid and apical segments and in the three wall regions are shown in **Table 2**.

A sub-analysis comparing iodine concentration in the 16 segments showed no significant difference for both protocols ($p = 0.47$ and $p = 0.09$ for iodine concentrations; $p = 0.81$ and $p = 0.26$ for normalized values in protocol A and B respectively). The segments showing the lowest values were segment 4 in group A (median=1.16; IQR=0.47) and segments 13 (median=1.57; IQR=0.91) and 4 in group B (median=1.62; IQR=1.07) (**Figure 4**).

In both groups no statistical significant difference was found between basal, mid-ventricular and apical segments ($p=0.28$ and $p=0.12$ for iodine concentrations; $p=0.67$ and $p=0.38$ for normalized values respectively for protocol A and B). Significant differences were found for both groups between different wall regions ($p=0.04$ and $p<0.001$ for group A and B) (**Figure 4**). However, in group A analysis of normalized data ($p=0.06$) did not show significant differences between wall regions. In group B the lateral territory showed the highest values (median=2.07 mg/mL; IQR=0.4) and was significantly different from the anteroseptal-anterior (median=1.72; IQR=1.04) and inferoseptal-inferior (median=1.74; IQR=0.8) territories ($p<0.01$ for both absolute and normalised values) (**Figures 4 and 5**).

3.4 Objective quality

The values of noise, SNR and CNR for conventional images and VMI are displayed in **Table 3** and **Figure 6**.

3.4.1 Image noise

Noise values showed significant differences in multiple group testing ($p<0.01$). In group A post-hoc analysis showed significant differences for 70keV vs 50keV and between 40keV and all other reconstructions ($p=0.05$). In group B differences were significant for conventional vs 70 keV, 50keV vs 70keV and 60keV as well as 40keV and all other reconstructions ($p=0.05$).

3.4.2 Signal to noise ratio

SNR presented significant differences in multiple groups testing for both injection protocols ($p < 0.01$). Post-hoc testing revealed significant results in the following groups: conventional vs 60 keV, conventional vs 50 keV, conventional vs 40 keV for protocol A and between conventional and all VMI for protocol B.

3.4.3 Contrast to noise ratio

The CNR values were significantly different in multiple groups testing in both groups ($p < 0.01$). In group A, post-hoc testing found significant differences for all associations except for conventional vs 70keV. In group B, differences were not significant for groups conventional vs 70keV, 70keV vs 60keV, 60keV vs 50keV, 50keV vs 40keV.

3.4.4 Differences of noise, CNR and SNR between the two groups

CNR and noise values presented significant differences between corresponding reconstructions of the two groups, except for CNR at 40keV and noise at 70keV, with higher values for group B. SNR did not show significant differences between corresponding reconstructions in the two groups (**Table 3** and **Figure 6**).

4. Discussion

The present study demonstrated a significant difference in iodine concentration of healthy myocardium between two groups undergoing different injection protocols with higher values in the higher flow rate and iodine load cohort. In both groups, iodine concentration was homogeneous between the 16 segments, as well as in basal, mid and apical territories. In both groups significant differences between wall regions were found although more pronounced in the higher flow rate group. This difference among territories was confirmed on normalized iodine values only for the group with higher flow rate and iodine load. CNR and SNR but also image noise showed gradually increasing values as keV values decreased.

We found an iodine concentration of 1.38 ± 0.41 mg/mL for group A and 2.07 ± 0.73 mg/mL for group B with lowest values of 0.6 mg/mL and 1.17 mg/mL respectively. Previous studies demonstrated that iodine concentration can reliably be quantified even for values as low as 0.5 mg/ml or 1 mg/ml in 20 cm or 30x40 cm phantoms, respectively, and with minimum detectable differences of 0.4 mg/ml.¹⁷⁻²⁰ Thus, both proposed protocols could be employed in clinical practice, although the one with higher rate might provide more accurate calculations as different studies have shown an increase in accuracy for higher iodine concentrations.^{14,16}

The results of our study showed that iodine concentration in healthy myocardium as assessed with DE-DLCT differs according to contrast injection protocol. Iodine concentration has been regarded as a surrogate of myocardial perfusion and its objective quantification as a potentially helpful tool not only for the detection of focal perfusion defects but also for the determination of global perfusion reduction in three vessel disease.^{9,10,12,13} Different studies aimed at establishing a precise threshold value of iodine concentration to distinguish normal, ischemic and necrotic myocardium based on DECT acquisitions.

^{12,13} Delgado et al. found that a cut-off value of 2.1 mg/mL had a sensitivity of 75 % and a specificity of 73.6 % to differentiate normal from hypoperfused territories on stress exams.¹² Distinction between ischemic and necrotic segments was not possible due to overlap between iodine values. Van Assen et al. found optimal values of 2.5 mg/mL at rest and 2.1 mg/mL during stress for distinction of healthy and diseased segments.¹³ Only at rest a threshold value could be defined to distinguish ischemic from necrotic territories corresponding to 1.00 mg/mL, with a sensitivity of 80% and a specificity of 100%. However, in these studies all scans were performed under the same injection conditions. On the contrary, our study demonstrates that fist-pass healthy myocardial perfusion is a function of injection protocols. Therefore, an absolute threshold might be more challenging to define and should definitely take into account scan parameters as well as left ventricle iodine content.

Furthermore, we showed that injection parameters influence iodine concentration homogeneity in the myocardium. Indeed, we found significant differences in iodine concentrations between wall regions. Although clearly demonstrated in the high flow and high iodine load group, this difference was doubtful in the low flow and low dose group. To the best of our knowledge this is the first study assessing healthy myocardium homogeneity with DE-DLCT. However, other studies demonstrated myocardial heterogeneity in healthy volunteers with different imaging techniques.²¹⁻²³ Kim et al. found perfusion differences between segments as high as 32% at rest and 28% during stress with the septum showing lower values (although not significantly so).²² Similarly to our results, Ho et al demonstrated higher perfusion values in the lateral wall of low risk patients both at rest and under stress.²¹ Whether the differences we observed could have an impact on detectability of hypoperfusion areas in patients with coronaropathy still has to be investigated. Nevertheless, it should be kept in mind that higher injection rates and contrast dose influence iodine distribution homogeneity in healthy subjects.

Although not statistically significant in either of the two groups, some of the 16 segments showed lower iodine concentrations. The lowest values were found in segments 4 and 13 for protocol B. Segmental HU values lower than remote myocardium have been previously described and have been referred mainly to beam hardening artefacts.^{7,24,25} Our findings suggest that also iodine maps are affected by these artefacts.

Virtual monoenergetic reconstructions have been considered of particular interest in cardiovascular imaging. As the peak of mass attenuation coefficient for iodine can be found at low energy levels, the density of iodinated contrast material is higher on monoenergetic images at lower keV.^{5,8} Accordingly we found that both SNR and CNR increased as the energetic value of the reconstruction decreased with the highest values at 40keV. Nevertheless, image noise showed the opposite pattern increasing as the energetic value of the reconstruction decreased. Therefore, the optimal images for clinical evaluation are most likely not found at lowest values but around 50keV. Furthermore, both CNR and image noise were significantly higher in group B without corresponding increase of SNR. Further studies are needed to confirm if the combination of first-pass DE-DLCT myocardial perfusion with low flow rate and iodine load and assessment on iodine maps and low energy monoenergetic reconstructions will improve the detection of hemodynamic significant stenosis.

The first limitation of our study is the lack of a standard of reference for both iodine quantification and its homogeneity. Therefore, not only the accuracy of absolute values but also the presence relative regional differences could not be confirmed. As a consequence, the influence and impact of artefacts (beam hardening but not only) could not be distinguished from intrinsic perfusion variability. Secondly, we investigated only two injection protocols that differed in both injection rate and contrast media volume. Although the differences we found are more probably related to the different injection rate,

we cannot exclude an influence of other parameters. The two injection rates were quite apart from each other and it is likely the best protocol being in-between.

To conclude, we demonstrated that injection protocols influence first pass myocardial iodine concentration. At higher flow rates healthy myocardium presents higher iodine concentration and presents different iodine concentrations in the anterior, inferior and lateral myocardial regions. Both factors should be considered when assessing the presence of perfusion defects both subjectively and quantitatively.

Disclosures: All authors have reported they have no relationships relevant to the contents of this paper to disclose.

Funding: This research did not receive any specific grant from funding agencies in the public, commercial, or not-for-profit sectors.

References

1. Tonino, P. a L. *et al.* Angiographic Versus Functional Severity of Coronary Artery Stenoses in the FAME Study. Fractional Flow Reserve Versus Angiography in Multivessel Evaluation. *J. Am. Coll. Cardiol.* **55**, 2816–2821 (2010).
2. Tonino, P. A. L. *et al.* Fractional Flow Reserve versus Angiography for Guiding Percutaneous Coronary Intervention. *N. Engl. J. Med.* **360**, 213–224 (2009).
3. Takx, R. a. P. *et al.* Diagnostic accuracy of stress myocardial perfusion imaging compared to invasive coronary angiography with fractional flow reserve meta-analysis. *Circ. Cardiovasc. Imaging* **8**, 1–7 (2014).
4. Rossi, A. *et al.* Stress Myocardial Perfusion: Imaging with Multidetector CT. *Radiology* **270**, 25–46 (2014).
5. Johnson, T. R. C. Dual-energy CT: general principles. *AJR. Am. J. Roentgenol.* **199**, 3–8 (2012).
6. McCollough, C. H., Leng, S., Yu, L. & Fletcher, J. G. Dual- and Multi-Energy CT: Principles, Technical Approaches, and Clinical Applications. *Radiology* **276**, 637–653 (2015).
7. So, A. *et al.* Dual-energy CT and its potential use for quantitative myocardial CT perfusion. *J. Cardiovasc. Comput. Tomogr.* **6**, 308–317 (2012).
8. Vlahos, I., Chung, R., Nair, A. & Morgan, R. Dual-energy CT: vascular applications. *AJR. Am. J. Roentgenol.* **199**, 87–97 (2012).
9. Ko, S. M. *et al.* Myocardial perfusion imaging using adenosine-induced stress dual-energy computed tomography of the heart: comparison with cardiac magnetic resonance imaging and conventional coronary angiography. *Eur. Radiol.* **21**, 26–35 (2011).
10. Wang, R. *et al.* Incremental value of dual-energy CT to coronary CT angiography for the detection of significant coronary stenosis: Comparison with quantitative coronary angiography and single photon emission computed tomography. *Int. J. Cardiovasc. Imaging* **27**, 647–656 (2011).
11. Ruzsics, B. *et al.* Comparison of Dual-Energy Computed Tomography of the Heart With Single Photon Emission Computed Tomography for Assessment of Coronary Artery Stenosis and of the Myocardial Blood Supply. *Am. J. Cardiol.* **104**, 318–326 (2009).
12. Delgado Sánchez-Gracián, C. *et al.* Quantitative myocardial perfusion with stress dual-energy CT: iodine concentration differences between normal and ischemic or necrotic myocardium. Initial experience. *Eur. Radiol.* **26**, 3199–3207 (2016).
13. van Assen, M. *et al.* Iodine quantification based on rest / stress perfusion dual energy CT to differentiate ischemic, infarcted and normal myocardium. *Eur. J. Radiol.* **112**, 136–143 (2019).
14. Sauter, A. P. *et al.* Accuracy of iodine quantification in dual-layer spectral CT: Influence of iterative reconstruction, patient habitus and tube parameters. *Eur. J. Radiol.* **102**, 83–88 (2018).
15. van Hamersvelt, R. W. *et al.* Feasibility and accuracy of dual-layer spectral detector computed tomography for quantification of gadolinium: a phantom study. *Eur. Radiol.* **27**, 3677–3686

(2017).

16. Pelgrim, G. J. *et al.* Accuracy of iodine quantification using dual energy CT in latest generation dual source and dual layer CT. *Eur. Radiol.* **27**, 3904–3912 (2017).
17. Li, Y., Shi, G., Wang, S., Wang, S. & Wu, R. Iodine quantification with dual-energy CT: Phantom study and preliminary experience with VX2 residual tumour in rabbits after radiofrequency ablation. *Br. J. Radiol.* **86**, (2013).
18. Sellerer, T. *et al.* Dual-energy CT: a phantom comparison of different platforms for abdominal imaging. *Eur. Radiol.* **28**, 2745–2755 (2018).
19. Euler, A., Solomon, J., Mazurowski, M. a., Samei, E. & Nelson, R. C. How accurate and precise are CT based measurements of iodine concentration? A comparison of the minimum detectable concentration difference among single source and dual source dual energy CT in a phantom study. *Eur. Radiol.* (2018) doi:10.1007/s00330-018-5736-0.
20. Jacobsen, M. C. *et al.* Dual-Energy CT: Lower Limits of Iodine Detection and Quantification. *Radiology* 182870 (2019) doi:10.1148/radiol.2019182870.
21. Ho, K. T., Ong, H. Y., Tan, G. & Yong, Q. W. Dynamic CT myocardial perfusion measurements of resting and hyperaemic blood flow in low-risk subjects with 128-slice dual-source CT. *Eur. Heart J. Cardiovasc. Imaging* **16**, 300–306 (2015).
22. Kim, E. Y. *et al.* Normal range and regional heterogeneity of myocardial perfusion in healthy human myocardium: Assessment on dynamic perfusion CT using 128-slice dual-source CT. *Int. J. Cardiovasc. Imaging* **30**, 33–40 (2014).
23. Chareonthaitawee, P., Kaufmann, P. a., Rimoldi, O. & Camici, P. G. Heterogeneity of resting and hyperemic myocardial blood flow in healthy humans. *Cardiovasc. Res.* **50**, 151–161 (2001).
24. Rodríguez-Granillo, G. a., Rosales, M. a., Degrossi, E. & Rodriguez, A. E. Signal density of left ventricular myocardial segments and impact of beam hardening artifact: Implications for myocardial perfusion assessment by multidetector CT coronary angiography. *Int. J. Cardiovasc. Imaging* **26**, 345–354 (2010).
25. Ko, S. M. *et al.* Diagnostic Performance of Combined Noninvasive Anatomic and Functional Assessment With Dual-Source CT and Adenosine-Induced Stress Dual-Energy CT for Detection of Significant Coronary Stenosis. *Am. J. Roentgenol.* **198**, 512–520 (2012).

Table titles

Table 1. Characteristics of the 60 patients

Table 2. Iodine concentration values

Table 3. Noise, SNR and CNR values

Figure Legends

Figure 1. Flow-chart of the study.

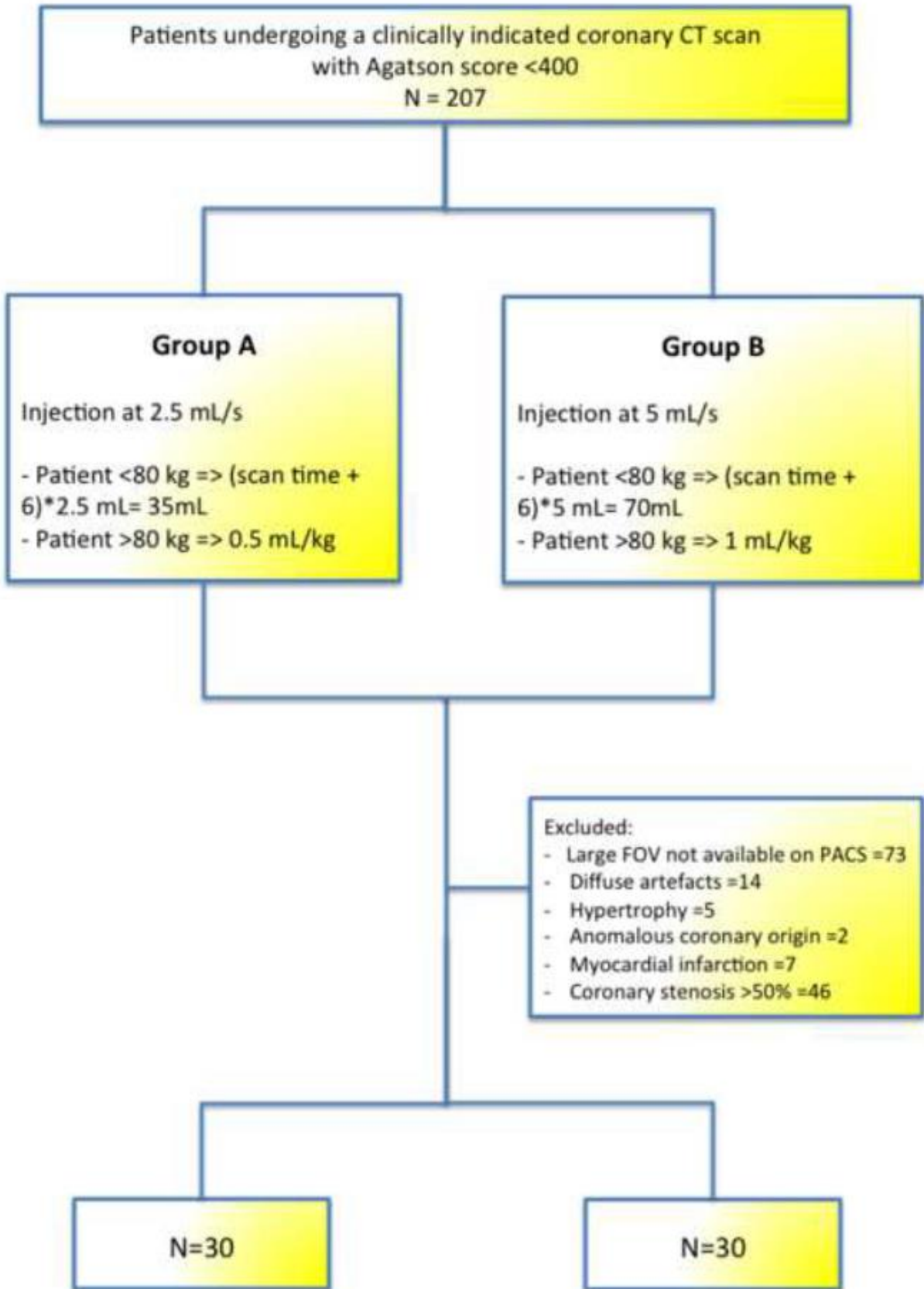
Figure 2. A - Myocardial segmentation into 16 segments according to the American Heart Association recommendation. **B** - Display of all assessed spectral images (iodine maps, conventional, VMI 70-60-50-40 keV) in a case example of first pass myocardial perfusion for protocol A (rate at 2.5 mL/s).

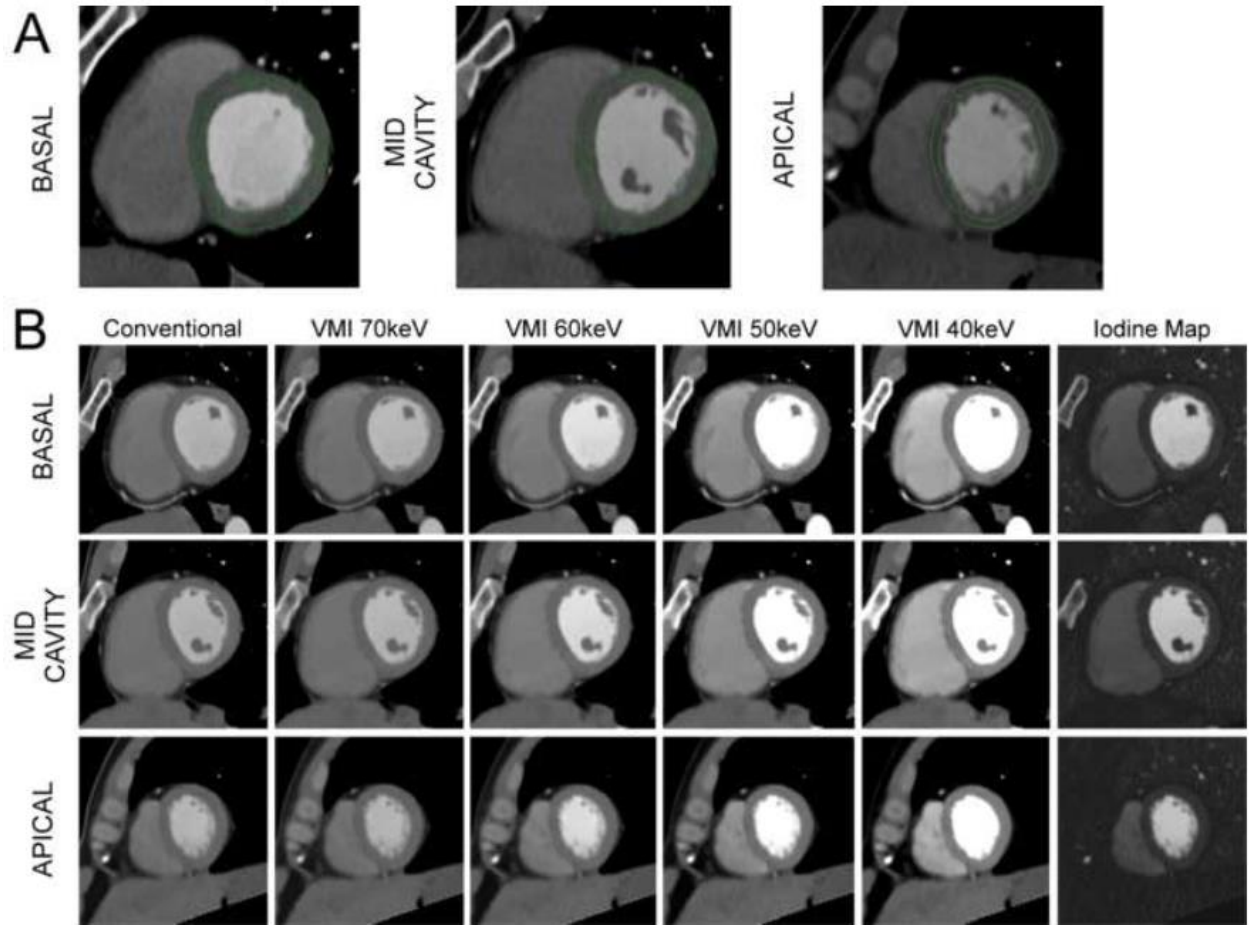
Figure 3. Box plots of overall myocardial iodine concentrations measured in the two protocols (A: 2.5 mL/s, B: 5 mL/s).

Figure 4. A - Display of color-coded iodine density in the 16 segments, basal, mid and apical segments and anterior, inferior and lateral wall regions in the two groups. **B** - Box plots of the iodine concentrations measured in the 3 different wall regions for the two protocols. To be noticed that the range of values of the y-axis is different for the two groups.

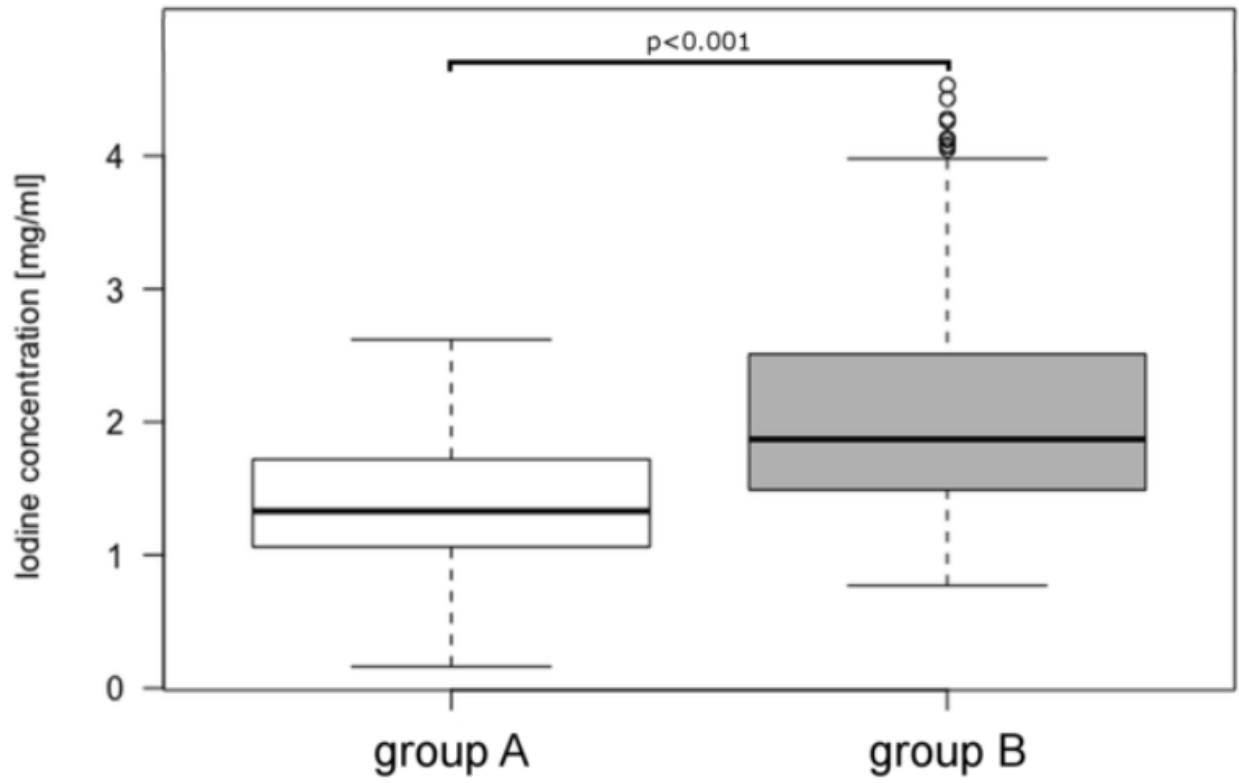
Figure 5. On the left, iodine maps of two cases from the group with low dose and slow injection rate show a homogeneous myocardium. On the contrary, a case example from the group with high dose at high injection rate demonstrates a heterogeneous myocardium with a higher iodine density in the lateral wall.

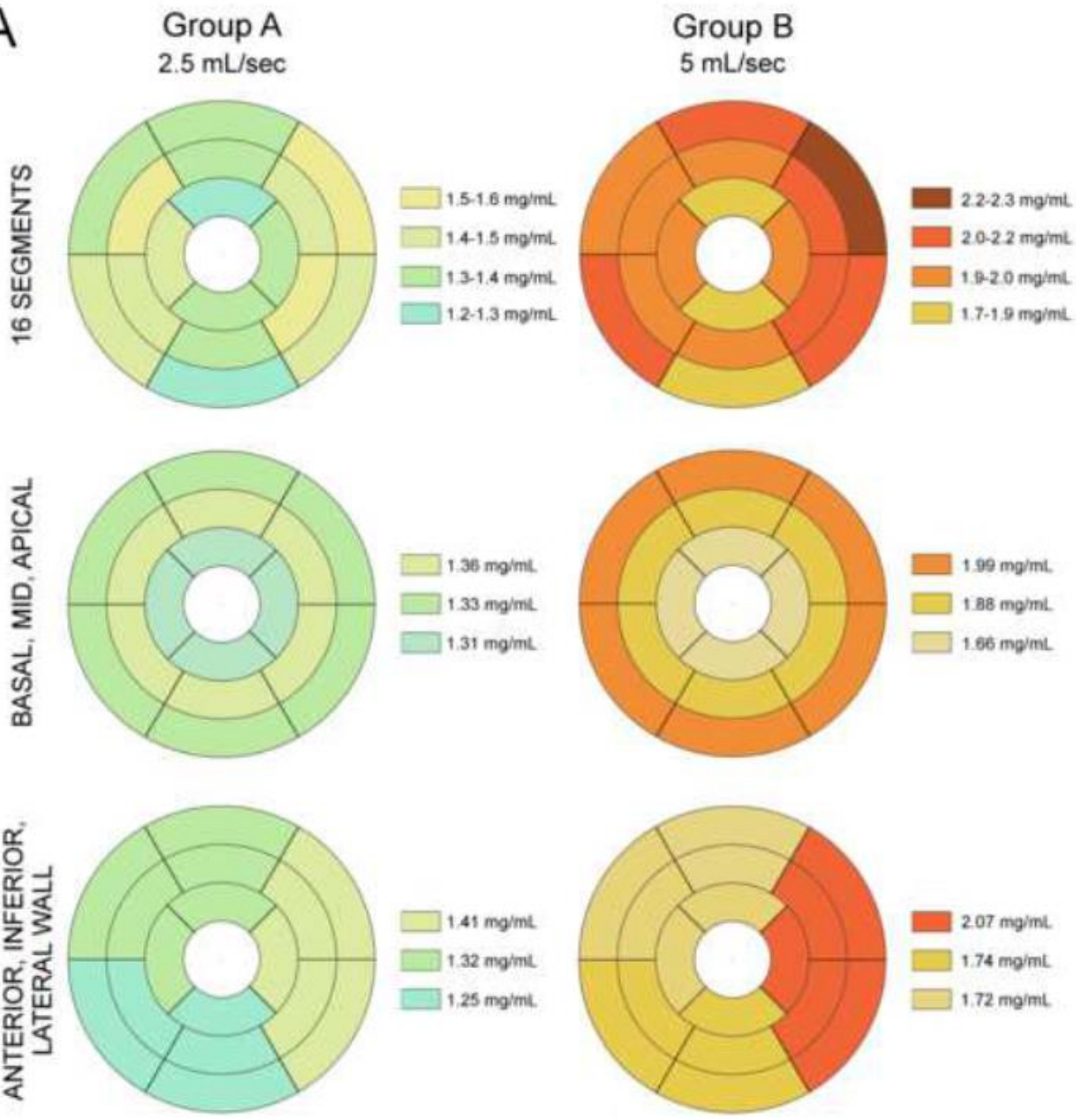
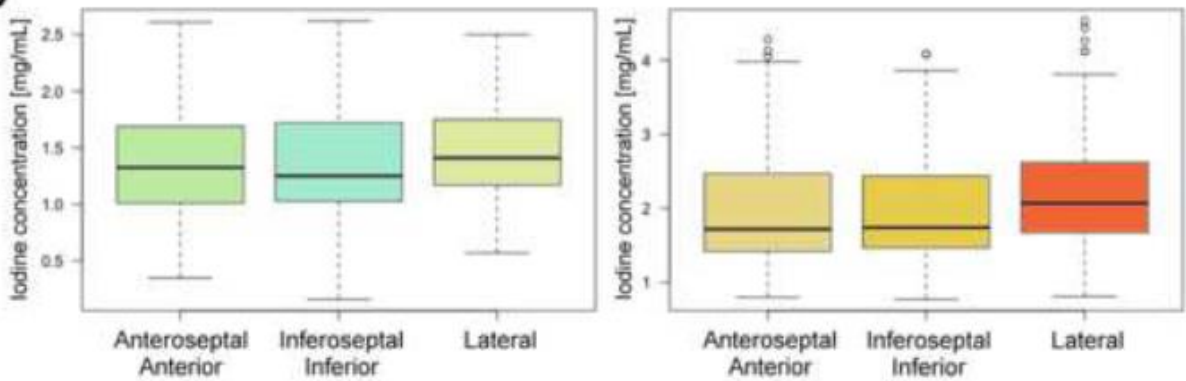
Figure 6. Box plots of image noise, SNR and CNR ratios measured with the conventional and mono-energetic images (70, 60, 50, 40 keV) for the two protocols (A=2.5 mL/s, B=5mL/s).





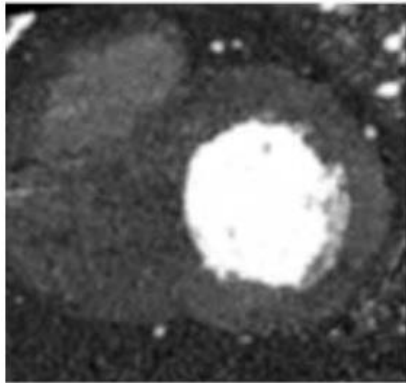
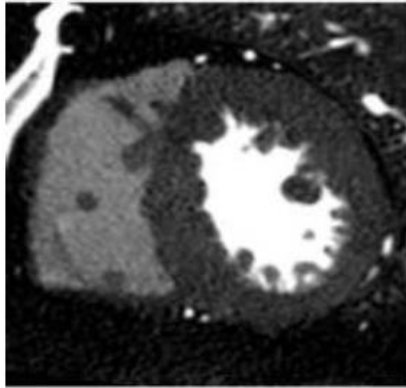
Iodine concentration in group A and B



A**B**

Cases 1 and 2

Group A - 2.5 mL/sec



Case 3

Group B - 5 mL/sec

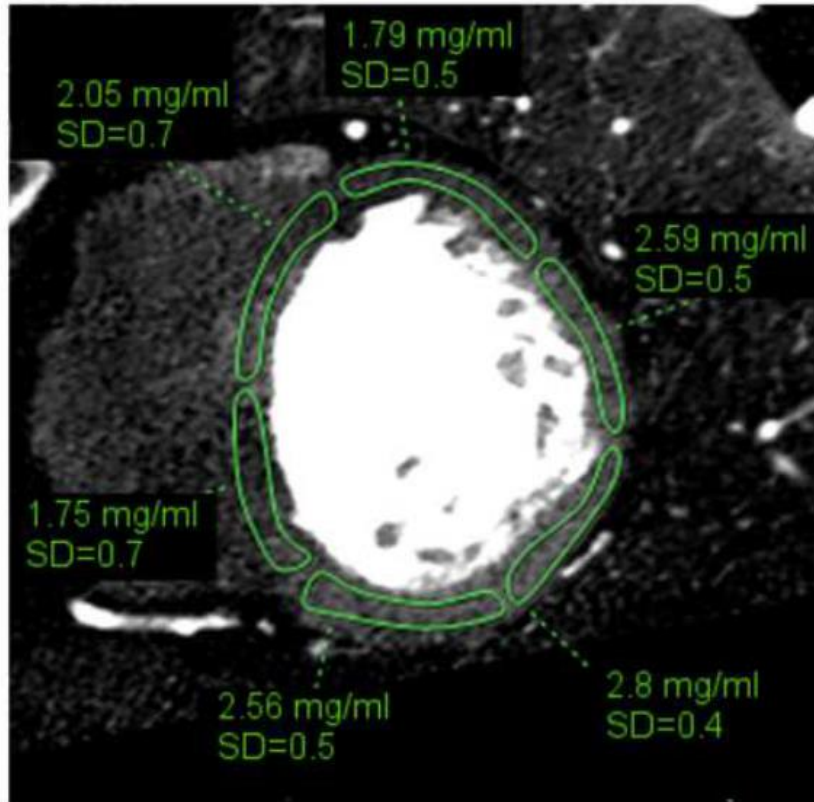
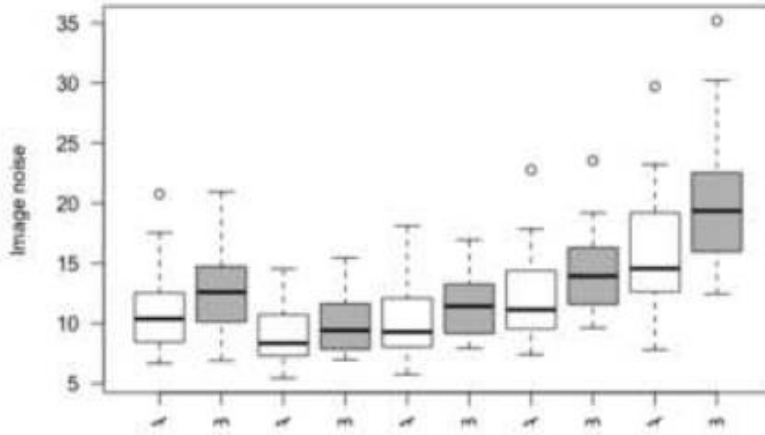
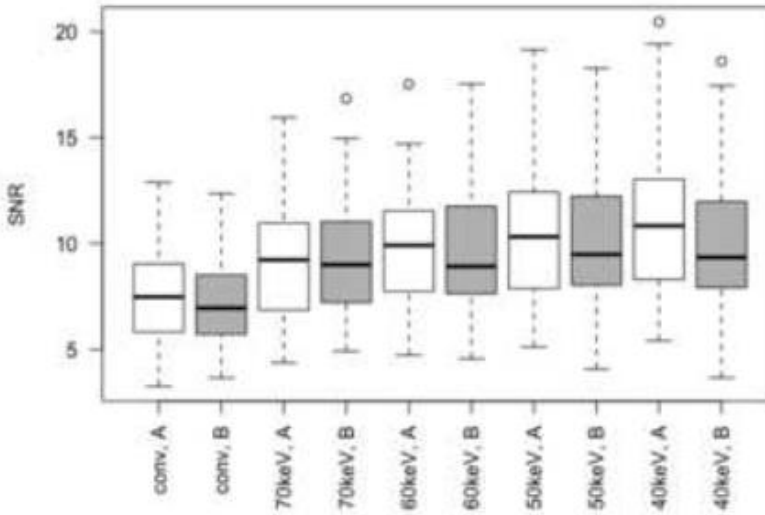


Image noise in the two groups



SNR in the two groups



CNR in the two groups

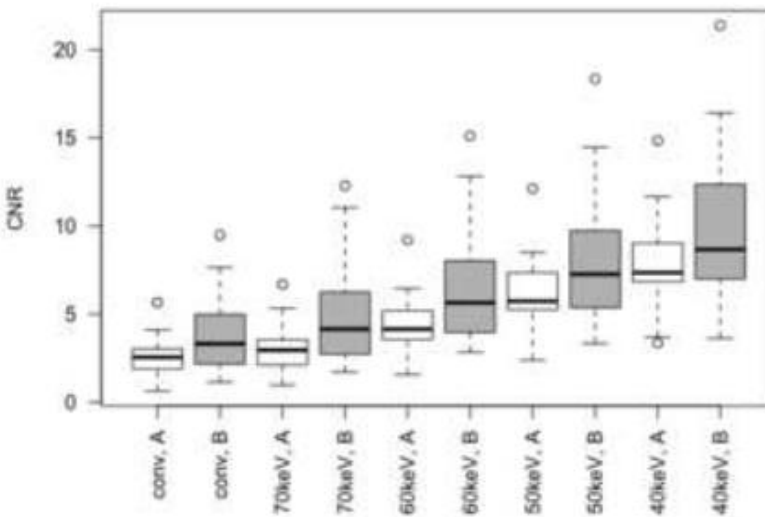


Table 1. Characteristics of the 60 patients.

Criteria	Group A (n=30)	Group B (n=30)	p value
Age (years)	50.1 ± 17.3 (18-77)	50.8 ± 18 (22-80)	0.87
Gender (N, % men)	19 (63%)	20 (67%)	0.8
Weight (kg)	68 (22.3)	73.5 (24)	0.08
Height (cm)	170 ± 10.1 (153-198)	170 ± 9.7 (152-186)	0.96
BMI (kg/m²)	23.9 (5.2)	25.8 (6.8)	0.05
HR (bpm)	69 ± 10 (52-85)	67.8 ± 11.2 (53-88)	0.69
Dose (CTDI mGy)	17.5 (10.9)	22.7 (15.8)	0.06

Data are presented as mean ± standard deviation (range) or median (IQ range). BMI, body mass index;

HR, heart rate.

Table 2. Iodine concentration values

	Group A		Group B		
Total	1.33	(0.62)	1.87	(1.02)	<0.001
Segments					
Segment 1	1.32	(0.53)	1.92	(0.76)	<0.001
Segment 2	1.34	(0.79)	1.86	(0.95)	0.003
Segment 3	1.34	(0.68)	2.02	(0.73)	<0.001
Segment 4	1.16	(0.47)	1.62	(1.07)	<0.001
Segment 5	1.41	(0.58)	2.15	(1)	<0.001
Segment 6	1.46	(0.55)	2.2	(1.05)	<0.001
Segment 7	1.26	(0.62)	1.71	(0.98)	<0.001
Segment 8	1.39	(0.73)	1.69	(1.15)	0.002
Segment 9	1.25	(0.74)	1.77	(1)	<0.001
Segment 10	1.28	(0.72)	1.79	(1.26)	<0.001
Segment 11	1.44	(0.5)	1.95	(0.8)	<0.001
Segment 12	1.41	(0.52)	2.06	(0.9)	<0.001
Segment 13	1.25	(0.59)	1.57	(0.91)	0.001
Segment 14	1.37	(0.86)	1.68	(1.08)	0.003
Segment 15	1.27	(0.58)	1.66	(1.03)	<0.001
Segment 16	1.34	(0.57)	1.78	(0.91)	<0.001
Basal, mid, apical					
Basal	1.33	(0.65)	1.99	(0.99)	<0.001
Mid	1.36	(0.63)	1.88	(1.06)	<0.001
Apical	1.31	(0.61)	1.66	(1.04)	<0.001
Wall regions					
Anteroseptal-anterior	1.32	(0.68)	1.72	(1.05)	<0.001
Inferoseptal-inferior	1.25	(0.22)	1.74	(0.28)	<0.001
Lateral	1.41	(0.24)	2.07	(0.4)	<0.001

Data regarding iodine concentration [mg/mL] are presented as: median (IQR)

Table 3. Noise, SNR and CNR values

		Conventional		VMI												
				70keV		60keV		50keV		40keV						
		A	B	A	B	A	B	A	B	A	B	A	B			
Noise	median	0.83	2.11	p<0.01	0.43	1.32	P=0.04	0.85	2.46	p<0.01	1.28	3.72	p<0.01	2.28	6.15	p<0.01
	IQR	1.66	2.16		1.19	2.17		1.34	2.53		2.58	2.98		3.65	4.28	
SNR	median	7.48	6.95	p=0.64	9.22	9.00	p=0.83	9.91	8.92	p=0.8	10.31	9.48	p=0.55	10.84	9.34	p=0.26
	IQR	3.10	2.78		3.96	3.73		3.65	3.89		4.31	3.90		4.71	3.89	
CNR	median	2.55	3.32	p=0.047	2.96	4.15	p<0.01	4.14	5.64	p<0.01	5.73	7.27	p=0.02	7.35	8.67	p=0.08
	IQR	-0.89	-1.16		-1.77	-1.98		-2.80	-3.12		-3.15	-4.29		-3.70	-4.39	

VMI – Virtual monochromatic image

6.2.2 “Dark-blood” dual-energy computed tomography angiography for thoracic aortic wall imaging [111]

Implications for patient care

This study is based on the previous work “True versus virtual non-contrast dual-energy CT imaging for the diagnosis of aortic intramural hematoma” where VNC images proved equivalent to TNC. Because a sharp and accurate delineation of the aortic wall to determine the presence of IMH is challenging on both TNC and VNC, we developed a novel material decomposition to enhance the visibility of the vascular wall referred to as “Dark blood” because the vascular lumen appears hypodense. In other terms, we used the spectral information provided by DECT to optimize the visual contrast between the aortic wall and the lumen. The study demonstrates that dark blood images improve the qualitative and quantitative image quality in aortic CTA, helping characterize aortic wall’s pathology.

Author contribution

Lead author; image post-processing, image assessment, statistical analysis, literature review, manuscript drafting and editing.



“Dark-blood” dual-energy computed tomography angiography for thoracic aortic wall imaging

David C. Rotzinger^{1,2} · Salim A. Si-Mohamed^{3,4} · Nadav Shapira⁵ · Philippe C. Douek^{3,4} · Reto A. Meuli^{1,2} · Loïc Boussel^{3,4}

Received: 22 March 2019 / Revised: 23 May 2019 / Accepted: 21 June 2019 / Published online: 22 July 2019
© European Society of Radiology 2019

Abstract

Objectives To assess the capability of a newly developed material decomposition method from contrast-enhanced dual-energy CT images, aiming to better visualize the aortic wall and aortic intramural hematoma (IMH), compared with true non-contrast (TNC) CT.

Materials and methods Twenty-two patients (11 women; mean age, 61 ± 20 years) with acute chest pain underwent 25 dual-layer non-contrast and contrast-enhanced CT. CT-angiography images were retrospectively processed using two-material decomposition analysis, where we defined the first material as the content of a region of interest placed in the ascending aorta for each patient, and the second material as water. Two independent radiologists assessed the images from the second material termed “dark-blood” images and the TNC images regarding contrast-to-noise ratio (CNR) between the wall and the lumen, diagnostic quality regarding the presence of aortic wall thickening, and the inner/outer vessel wall conspicuity.

Results Diagnostic quality scores in normal aortic segments were 0.9 ± 0.3 and 2.7 ± 0.6 ($p < 0.001$) and wall conspicuity scores were 0.7 ± 0.5 and 1.8 ± 0.3 ($p < 0.001$) on TNC and dark-blood images, respectively. In aortic segments with IMH, diagnostic quality scores were 1.7 ± 0.5 and 2.4 ± 0.6 ($p < 0.001$) and wall conspicuity scores were 0.7 ± 0.7 and 1.8 ± 0.3 ($p < 0.001$) on TNC and dark-blood images, respectively. In normal aortic segments, CNRs were 0.3 ± 0.2 and 2.8 ± 0.9 on TNC and dark-blood images, respectively ($p < 0.001$). In aortic segments with IMH, CNRs were 0.3 ± 0.2 and 4.0 ± 1.0 on TNC and dark-blood images, respectively ($p < 0.001$).

Conclusions Compared with true non-contrast CT, dark-blood material decomposition maps enhance quantitative and qualitative image quality for the assessment of normal aortic wall and IMH.

Key Points

- Current dual-energy CT-angiography provides virtual non-contrast and bright-blood images.
- Dark-blood images represent a new way to assess the vascular wall structure with dual-energy CT and can improve the lumen-to-wall contrast compared with true non-contrast CT.
- This dual-energy CT material decomposition method is likely to improve contrast resolution in other applications as well, taking advantage of the high spatial resolution of CT.

Keywords Computed tomography angiography · Aorta · Hematoma · Thorax · Technology assessment

✉ David C. Rotzinger
david.rotzinger@chuv.ch

¹ Department of Diagnostic and Interventional Radiology, Lausanne University Hospital (CHUV), Rue du Bugnon 46, 1011 Lausanne, Switzerland

² Faculty of Biology and Medicine (FBM), University of Lausanne (UNIL), Lausanne, Switzerland

³ Radiology Department, Hospices Civils de Lyon (HCL), Lyon, France

⁴ University Claude Bernard Lyon 1, CREATIS, CNRS UMR 5220, INSERM U1206, INSA-Lyon, Lyon, France

⁵ CT/AMI Research and Development, Philips Medical Systems, Haifa, Israel

Abbreviations

AAS	Acute aortic syndrome
CNR	Contrast-to-noise ratio
CTA	Computed tomography angiography
DECT	Dual-energy computed tomography
HU	Hounsfield unit
IMH	Intramural hematoma
NIST	National Institute of Standards and Technology
ROI	Region of interest
TNC	True non-contrast
VNC	Virtual non-contrast

Introduction

In acute aortic syndrome (AAS), the detection of intramural hematoma (IMH) is challenging and requires a non-contrast CT acquisition in addition to CT-angiography (CTA) [1, 2]. Thanks to its ability to create virtual non-contrast (VNC) images, dual-energy CT (DECT) technology has been recently proposed to improve the detection of IMH. Nevertheless, the contrast between the aortic lumen and the vessel wall remains relatively low on VNC images and makes the detection of subtle thickening of the wall difficult [3]. Conversely, aortic magnetic resonance angiography offers the possibility to obtain “dark-blood” images by suppressing the signal of the aortic lumen and thus facilitating the depiction of the aortic wall [4] but is not generally available in emergency settings. On this same principle, we sought to develop a DECT CTA-based algorithm allowing to suppress the signal of the aortic lumen based on a modified pair material decomposition in the image domain. In this decomposition, the first material was defined as the content of a region of interest (ROI) placed in the ascending aorta, and the second material was water.

This study aimed to assess the capability of this newly developed arterial wall enhancement algorithm, termed as dark-blood imaging, to visualize the aortic wall and aortic IMH better, compared with true non-contrast (TNC) CT.

Materials and methods

Study design and patients

The institutional ethics committee approved this single-center retrospective study and waived informed consent.

We selected 25 CT examinations from 22 patients (11 men; age range, 25–89 years and 11 women; 33–86 years), referred to aortic CTA for clinically suspected AAS. From July 2017 to January 2018, all patients with IMH proven upon aortic CTA or surgery were included ($n = 11$). For those who underwent medical therapy, the diagnosis of normal aortic CTA or acute IMH was based on a consensus. Subsequently, 11 randomly

selected control subjects with acute chest pain, but with normal aortic CTA, were included as well, within the same time frame. Demographics are detailed in Table 1.

Dual-layer DECT protocols and image reconstruction

All patients underwent aortic dual-layer detector DECT consisting of a TNC acquisition followed by a contrast-enhanced arterial-phase acquisition on a 64-row spectral detector CT system (IQon, Philips Healthcare). Acquisition parameters for both acquisitions were as follows: tube potential, 120 kVp; beam collimation geometry, 64×0.625 mm; gantry rotation time, 0.27 s; beam pitch, 1.234; and tube load, 55 mAs. An iodinated contrast agent (Iomeron® 400 mg I/mL, Bracco) was injected into an antecubital vein and followed by a saline flush. The acquisition was triggered by the bolus tracking technique. Reconstruction parameters were as follows: section thickness, 1.5 mm; reconstruction filter, B; iterative reconstruction algorithm, iDose 3; and display field-of-view, 300 mm.

Conventional HU images were reconstructed for the TNC acquisition. Regarding the contrast-enhanced DECT CTA acquisition, we reconstructed virtual monochromatic image series at 54 and 100 keV using the post-processing software provided with the DECT system (ISP v9.0, Philips Healthcare). The 54-keV value was chosen as the first energy level as it is sufficiently far away from the K-edge of iodine (33 keV) while being low enough to exhibit a photoelectric effect. The 100-keV value was chosen as the second energy level as it is high enough to exhibit more Compton scattering effect. We fed these two virtual monochromatic image series into a dedicated in-house software (developed using Microsoft Visual C++ 2017) to perform a two-material decomposition termed as ROI/Water (see below) and generate maps thereof. In this step, we drew an ROI in the ascending aorta on the 54-keV images and then copied and pasted it onto the 100-keV images for each patient. The mean value of these ROIs in HU was recorded and termed ROI₅₄ and ROI₁₀₀, respectively. Then, a two-material decomposition algorithm was applied with the following method. In the (x,y) coordinate system where “ x ” and “ y ” represent the values of attenuation at 100 and 54 keV, respectively, two unit vectors were set: the first

Table 1 Patients' demographics

	IMH patients	Controls
<i>n</i>	11	11
Scans	14	11
Female sex (%)	45.5	54.5
Age mean \pm SD (range)	74.5 \pm 15.3 (43–89)	45.8 \pm 14.8 (25–67)
Stanford A-type IMH (%)	45.5	None

IMH, intramural hematoma; SD, standard deviation

one pointing from the air point $(x,y) = (0,0)$ to the NIST-based water attenuation coefficients (ν/ρ) at 54 keV and 100 keV; the second one pointing from the air point to the (x,y) attenuation values corresponding to the ascending aorta ROI (ROI₅₄ and ROI₁₀₀). These unit vectors were used to determine a new coordinate system termed ROI/Water axes. The value of each pixel of the monochromatic images was then represented in this new coordinate system. The magnitude of the projection on the Water axis was used to generate the dark-blood image. The projection on the ROI axis was not analyzed in this study.

Image analysis

For the qualitative analysis, we divided the aortic lumen cross-sectional area into 4 equiangular quadrants, taken on 4 pre-specified slices per patient: ascending post sinotubular segment, ascending aorta at the level of the left pulmonary artery, descending aorta at the level of the left main bronchus, and descending aorta at the level of the left atrium. Based on the presence or absence of IMH on conventional CTA, we categorized each slice as normal versus abnormal, which allowed us to evaluate the false-positive and negative rate of dark-blood images compared with TNC. Subsequently, two independent radiologists, DCR and SAS, with 6 years of experience in cardiovascular radiology reviewed dark-blood and TNC images for signs of aortic IMH on a 4-point diagnostic quality scale (3 = exemplary, 2 = diagnostic, 1 = limited, 0 = non-diagnostic), per quadrant. They also evaluated the inner and outer vessel wall conspicuity on a 3-point scale (2 = circumscribed margin, 1 = indistinct margin, 0 = obscured margin) as per the Radiologic Society of North America radiology

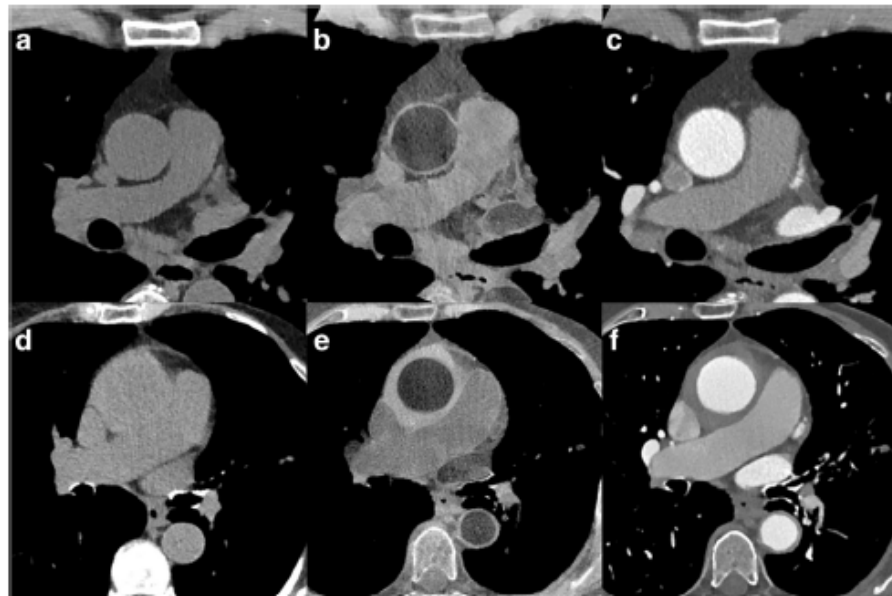
lexicon [5], per quadrant. Overall conspicuity was derived from the separate scores of the inner and outer wall conspicuity. The same slices served for the quantitative analysis, performed by one radiologist with 6 years of experience in cardiovascular imaging (DCR), who placed an ROI in the periaortic fat. Using the abovementioned in-house software, the same radiologist placed two concentric ROIs encompassing the aortic wall and the lumen to extract pixel values of the aortic wall. The observer noted the mean and standard deviation of the voxels' value in each ROI (in HU) and calculated the contrast-to-noise ratio (CNR) between the wall and the lumen and between the wall and the periaortic fat, on both dark-blood and TNC images using the following formula:

$$CNR = \frac{|\text{mean ROI value}_{\text{wall}} - \text{mean ROI value}_{\text{tissue}}|}{\sqrt{\frac{1}{2} (SD_{\text{wall}}^2 + SD_{\text{tissue}}^2)}}$$

where the subscript “tissue” refers to mean ROI values in the aortic lumen and periaortic fat, respectively, and “wall” refers to the ROI values of the aortic wall. We also extracted the mean vessel wall thickness for each patient using our in-house software, on dark-blood images.

Quantitative variables are presented as mean and standard deviation unless stated otherwise. Statistical analysis was conducted using R (R v. 3.4.3, R Foundation for Statistical Computing), using the Wilcoxon-Mann-Whitney test to compare ordinal and continuous variables, as the data was not normally distributed according to the Shapiro-Wilk test. Interrater agreement was evaluated using the weighted kappa test. One observer repeated the evaluation 1 week later to assess intra-observer agreement, using the weighted kappa

Fig. 1 Healthy patient (a–c) and patient with a Stanford A-type intramural hematoma (d–f). Note the enhanced visibility of the aortic vessel wall on dark-blood material decomposition (b and e), as compared to the true non-contrast (a and d) and arterial-phase contrast-enhanced images (c and f)



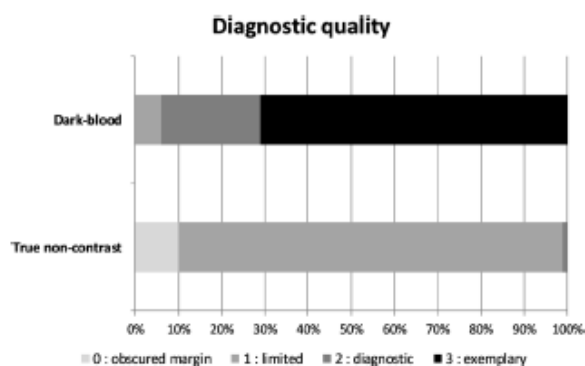


Fig. 2 Bar graph shows qualitative diagnostic quality mean scores of observers. Dark-blood images were mostly rated diagnostic or exemplary, while true non-contrast images were mostly rated limited

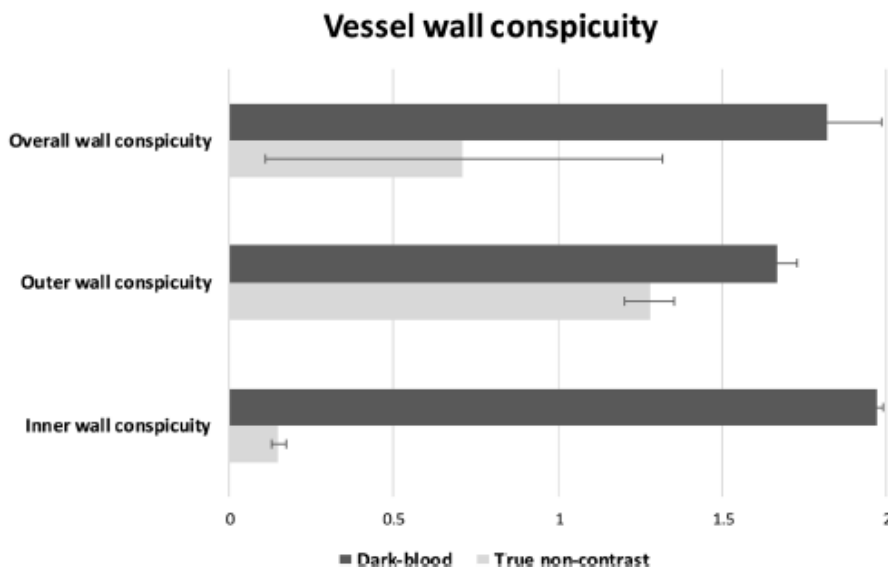
test. *P* values of less than 0.05 were considered statistically significant.

Results

Two typical examples of TNC, dark-blood, and conventional CTA images are provided in Fig. 1, in a control subject and a patient suffering from Stanford A-type IMH. In both cases, dark-blood images provide improved visualization of the aortic vessel wall structure.

Qualitative diagnostic quality scores in normal aortic segments were 0.9 ± 0.3 and 2.7 ± 0.6 on TNC and dark-blood images, respectively ($p < 0.001$). Aortic vessel wall conspicuity scores were 0.7 ± 0.5 and 1.8 ± 0.3 on TNC and dark-blood images, respectively ($p < 0.001$). Similarly, in aortic segments with IMH, the diagnostic quality scores were 1.7 ± 0.5 and 2.4 ± 0.6 on TNC and dark-blood images, respectively

Fig. 3 Qualitative analysis of vessel conspicuity on a 3-point Likert scale (2 = circumscribed margin, 1 = indistinct margin, 0 = obscured margin). Bar graph represents mean scores of observers one and two. Overall conspicuity is the average of outer and inner wall conspicuity. Error bars represent standard deviation



($p < 0.001$). Aortic vessel wall conspicuity scores were 0.7 ± 0.7 and 1.8 ± 0.3 on TNC and dark-blood images, respectively ($p < 0.001$). The intra-rater agreement was substantial (weighted kappa = 0.77 and 0.71 for diagnostic quality and aortic wall conspicuity, respectively). The interrater agreement was substantial (weighted kappa = 0.74 and 0.66 for diagnostic quality and aortic wall conspicuity, respectively). Average qualitative diagnostic quality scores, including both IMH patients and control subjects, are shown in Fig. 2, and average vessel wall conspicuity scores, including both IMH patients and control subjects, are shown in Fig. 3. Finally, dark-blood images did not lead to false-positives or negatives for IMH identification.

In the quantitative analysis (Fig. 4), normal aortic segment CNRs between the vessel wall and lumen were 0.3 ± 0.2 and 2.8 ± 0.9 on TNC and dark-blood images, respectively ($p < 0.001$); CNRs between the vessel wall and the periaortic fat were 9.5 ± 2.6 and 2.6 ± 1.2 on TNC and dark-blood images, respectively ($p < 0.001$). Similarly, in aortic segments with IMH, CNRs between the vessel wall and lumen were 0.3 ± 0.2 and 4.0 ± 1.0 on TNC and dark-blood images, respectively ($p < 0.001$); CNRs between the vessel wall and the periaortic fat were 11.2 ± 4.5 and 4.7 ± 1.5 on TNC and dark-blood images, respectively ($p < 0.001$). Finally, mean aortic vessel wall thickness was 1.6 ± 0.3 mm in normal segments and 4.7 ± 2.3 mm in segments with IMH ($p < 0.001$).

Discussion

Our results indicate that contrast-enhanced DECT-derived dark-blood CT imaging is feasible and may facilitate the analysis of arterial vessel walls.

Contrast-to-noise ratio

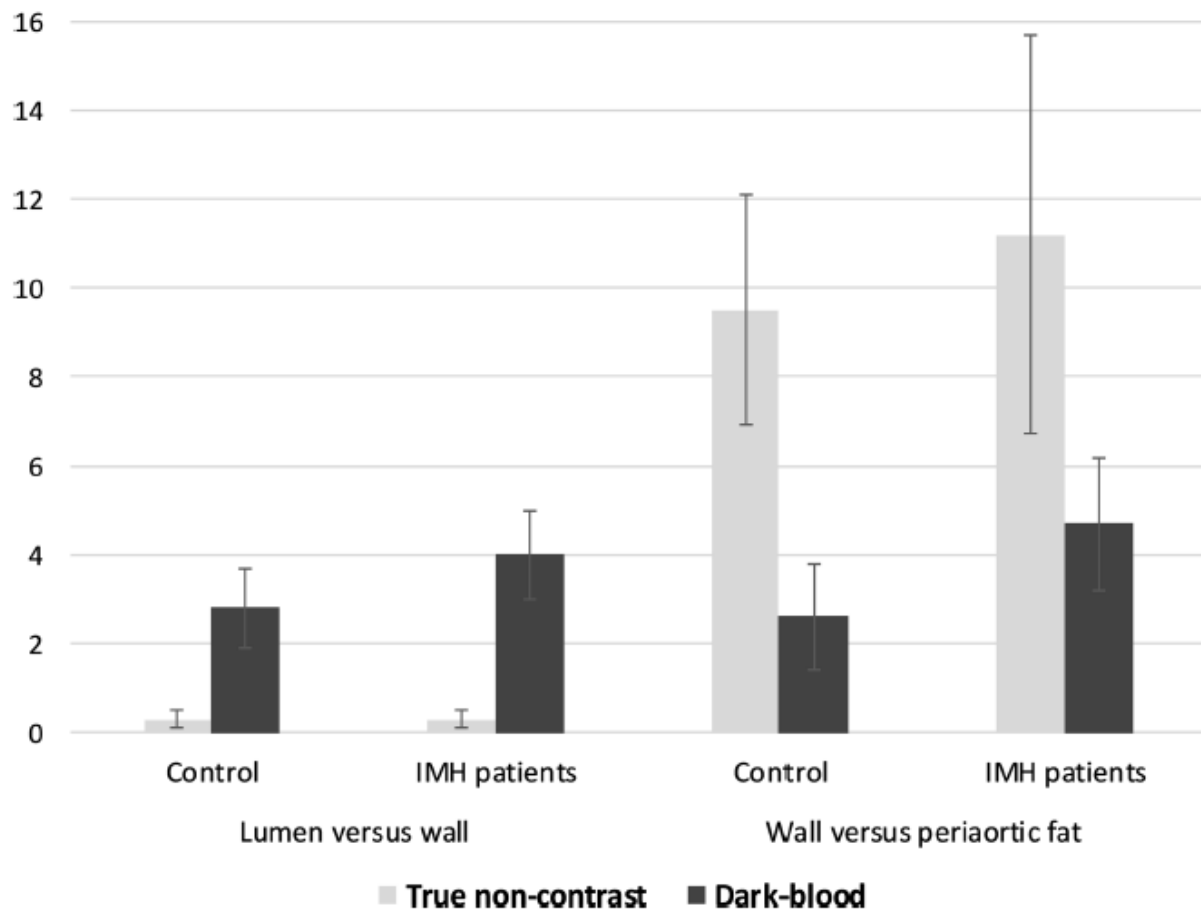


Fig. 4 Bar graph shows contrast-to-noise ratios (CNR) obtained on true non-contrast and dark-blood images. CNR was calculated between the aortic vessel wall and lumen, as well as between vessel wall and periaortic fat, in control subjects and patients with intramural hematoma (IMH).

Error bars represent standard deviation. Dark-blood images improve CNR between the lumen and the aortic wall but offer no advantage in wall versus periaortic fat CNR.

In our study, dark-blood CT images significantly improved arterial wall conspicuity, resulting in better qualitative diagnostic quality. Results from the quantitative image analysis mostly support the qualitative analysis, demonstrating improved CNR between the vessel wall—with or without IMH—and the vessel lumen. Nevertheless, CNR between the vessel wall and periaortic fat was substantially lower in dark-blood images, as compared to TNC, but these results hold only as long as the aorta is indeed surrounded by fat. The aorta may be in close proximity to many organs. The reason why the observers gave better scores to the outer vessel wall delineation on dark-blood images probably comes from the impact of the material decomposition on adjacent vascular structures, such as the superior vena cava, the pulmonary artery, or any additional contrast medium-containing blood vessels, helping to demarcate the outer aortic contour. Finally, the

mean aortic wall thickness in healthy patients was approximately 1.6 mm, which is in agreement with MRI studies [6].

Regarding the method to calculate the dark-blood images, our main idea was to use a traditional two-material water/iodine decomposition, but to replace the iodine component by a value directly measured in the aortic lumen. Indeed, the exact concentration and composition of the elements present in the lumen is unknown and represents a patient and contrast material injection-dependent mixture of iodine, hemoglobin, water, platelets, and other components. By directly using the attenuation measured in the aortic lumen, we calibrated the slope of the non-water axis used for the two-material decomposition and thus accurately canceled the attenuation of the lumen on the water axis used to generate the dark-blood images. It is important to notice that, with our method, we directly used the HU values measured in the aortic lumen on the

two monochromatic images (i.e., 54 and 100 keV) and did not unscale them to their physical attenuation values. This results in an additional scaling factor, which in fact is also dependent on the measured HU values of the aortic lumen. The geometric interpretation of this scaling factor can be seen as a decrease in the slope of the calibrated aortic lumen material, resulting in negative calculated projections along the water material for the aortic lumen values. As a consequence, the two-material decomposition we applied does not result in concentration maps but rather in a map of geometric projections that allow for optimized contrast between the lumen and the surrounding tissues, while keeping a contrast between the surrounding tissues themselves. Unfortunately, despite their added value for visualization, these projection maps do not have any meaningful physical interpretation and are not intended to be a quantitative method. An analogy can be performed with MRI. The absolute T1 of the tissue can be measured with MRI to create T1 maps, commonly used in cardiac MRI, for example [7]. However, most of the time, T1-weighted images are used, where the contrast relies on the differences in T1 between tissues consisting of unknown elements, such as performed with our method in DECT.

Our study highlights the potential benefit of dark-blood aortic CT imaging compared with the current state-of-the-art aortic CT imaging, usually consisting of TNC CT followed by CTA [8]. As of today, TNC CT combined with CTA is still recommended for suspected AAS patients. CTA alone may provide inferior diagnostic accuracy [1] due to the high luminal attenuation that can mask the IMH, as CTA requires wide window settings to display images [9–11]. This two-acquisition approach increases the total examination radiation dose. Furthermore, TNC CT results in a low visual contrast between the vessel wall and the lumen it provides, causing interpretive difficulties in assessing structural changes in the vessel wall. In this context, dark-blood CT images could potentially overcome these current protocol limitations by providing high wall-to-lumen contrast from a single contrast-enhanced acquisition. This last statement would need a more extensive study, involving more patients, which was beyond the scope of the present feasibility study.

Our study has several limitations. First, a true blinded design was not achievable given the unique nature of dark-blood images compared to TNC. Then, the comparison between dark-blood images and other results available from spectral CTA, such as HU or different levels of monochromatic images, in IMH but also in other conditions leading to acute aortic syndrome, has not been performed in this study. This would certainly be of interest but was beyond the scope of the present study.

In conclusion, we describe a dark-blood image decomposition method that provides a new way to show contrast between tissues. We took the example of producing dark-blood CT images of the aorta to visualize the vessel wall, to help

diagnose conditions associated with changes in the vessel wall structure, compared with TNC. The same method may improve contrast resolution in other applications.

Funding The authors state that this work has not received any funding.

Compliance with ethical standards

Guarantor The scientific guarantor of this publication is Prof. Philippe C. Douek, MD, PhD.

Conflict of interest The authors of this manuscript declare relationships with the following companies: Dr. Nadav Shapira, PhD, is employed by Philips Healthcare, the manufacturer of the DECT system used in this study.

Statistics and biometry No complex statistical methods were necessary for this paper.

Informed consent Written informed consent was waived by the Institutional Review Board.

Ethical approval Institutional Review Board approval was obtained.

Methodology

- retrospective
- cross-sectional study
- performed at one institution

References

1. Lemos AA, Pezzullo JC, Fasani P et al (2014) Can the unenhanced phase be eliminated from dual-phase CT angiography for chest pain? Implications for diagnostic accuracy in acute aortic intramural hematoma. *AJR Am J Roentgenol* 203:1171–1180
2. Erbel R, Aboyans V, Boileau C et al (2014) 2014 ESC Guidelines on the diagnosis and treatment of aortic diseases: Document covering acute and chronic aortic diseases of the thoracic and abdominal aorta of the adult. The Task Force for the Diagnosis and Treatment of Aortic Diseases of the European Society of Cardiology (ESC). *Eur Heart J* 35:2873–2926
3. Lehti L, Söderberg M, Höglund P, Nyman U, Gottsäter A, Wassélius J (2018) Reliability of virtual non-contrast computed tomography angiography: comparing it with the real deal. *Acta Radiol Open* 7:205846011879011
4. Simonetti OP, Finn JP, White RD, Laub G, Henry DA (1996) “Black blood” T2-weighted inversion-recovery MR imaging of the heart. *Radiology* 199:49–57
5. RSNA RadLex radiology lexicon. <http://radlex.org/>. Accessed 14 Jun 2018
6. Mensel B, Kühn JP, Schneider T et al (2013) Mean thoracic aortic wall thickness determination by cine MRI with steady-state free precession: validation with dark blood imaging. *Acad Radiol* 20:1004–1008
7. Burt JR, Zimmerman SL, Kamel IR, Halushka M, Bluemke DA (2014) Myocardial T1 mapping: techniques and potential applications. *Radiographics* 34(2):377–395
8. Gutschow SE, Walker CM, Martínez-Jiménez S, Rosado-de-Christenson ML, Stowell J, Kunin JR (2016) Emerging concepts in intramural hematoma imaging. *Radiographics* 36:660–674

9. Manghat NE, Morgan-Hughes GJ, Roobottom CA (2005) Multi-detector row computed tomography: imaging in acute aortic syndrome. *Clin Radiol* 60:1256–1267
10. Holloway BJ, Rosewarne D, Jones RG (2011) Imaging of thoracic aortic disease. *Br J Radiol* 84(Spec No 3):S338–S354
11. Zatz LM (1981) Basic principles of computed tomography scanning. In: Newton TH, Potts DG (eds) *Technical aspects of computed tomography*. Mosby, St. Louis, pp 3853–3876

Publisher's note Springer Nature remains neutral with regard to jurisdictional claims in published maps and institutional affiliations.

6.1.3 Identification and quantification of monosodium urate crystals in coronary atheroma “COROGOUT”

Gout is the most common inflammatory arthropathy in developed countries [114, 115], characterized by the precipitation and deposition of monosodium urate crystals (MSU) in various tissues. Several studies have shown that hyperuricemia is a risk factor for developing atherosclerotic coronary artery disease and major cardiovascular events [98-103]. In addition, it has been demonstrated that MSU crystals can be demonstrated *ex vivo* in coronary atherosclerotic plaques in hyperuricemic patients [104]. Spectral computed tomography (CT), makes it possible to distinguish and quantify materials, including MSU crystals [116]. Spectral CT currently comes in two primary designs: the most widely available are DECT systems, available in the form of 4 clinical platforms: dual-layer detector CT [DLCT], fast kVp-switching CT [FSCT], twin-beam CT [TBCT], and dual-source CT [DSCT] (see Table 1 in section 4.3 for more details). The more recent and most advanced technological development is PCCT, extensively discussed before and only available as a pre-clinical experimental prototypes from two leading manufacturers, in selected university hospitals. Despite the diversity of spectral CT systems gradually appearing in radiology facilities, detecting and quantifying MSU crystals in vessels and plaques as small as coronary arteries are far from straightforward.

Detection of MSU deposits in coronary arteries using spectral CT imaging would be a major scientific breakthrough as there is no other "non-invasive" technique to identify and quantify such crystal deposits, which are found in atherosclerotic plaque composition (*ex vivo*, optical microscopy in polarized light). Once established, this technique could be secondarily transposed to other clinical vascular applications (aortic arch and supra-aortic

vessels) or other systems (including urogenital and musculoskeletal). Phantom studies simulating musculoskeletal diagnostic tasks succeeded in differentiating MSU from other crystals such as calcium pyrophosphate (CPP) and calcium hydroxyapatite (HA) [78].

To date, one study by Klauser et al. attempted at detecting coronary deposits of MSU in vivo [117]; however, due to several serious challenges associated with coronary DECT, spatial and spectral resolution undermining the validity of the presented results, the veracity of that particular study is still a matter of debate [118], all the more so an international cohort study with larger sample size and less challenging objective of assessing peripheral arteries (which are larger and not affected by cardiac motion and attenuation due to the chest wall) found DECT to be insufficiently accurate for clinical use [97]. Given the existing controversy and specific challenges of spectral coronary artery CT, a phantom proof of concept evaluation is a relevant approach.

Consequently, we designed a custom phantom containing various crystal suspensions (MSU, HA, CPP) in two different backgrounds (resin and agar-based) at multiple concentrations. Much effort was put into the preparations to achieve state-of-the-art purity and concentration accuracy. See Fig. 18 for further details about the phantom.

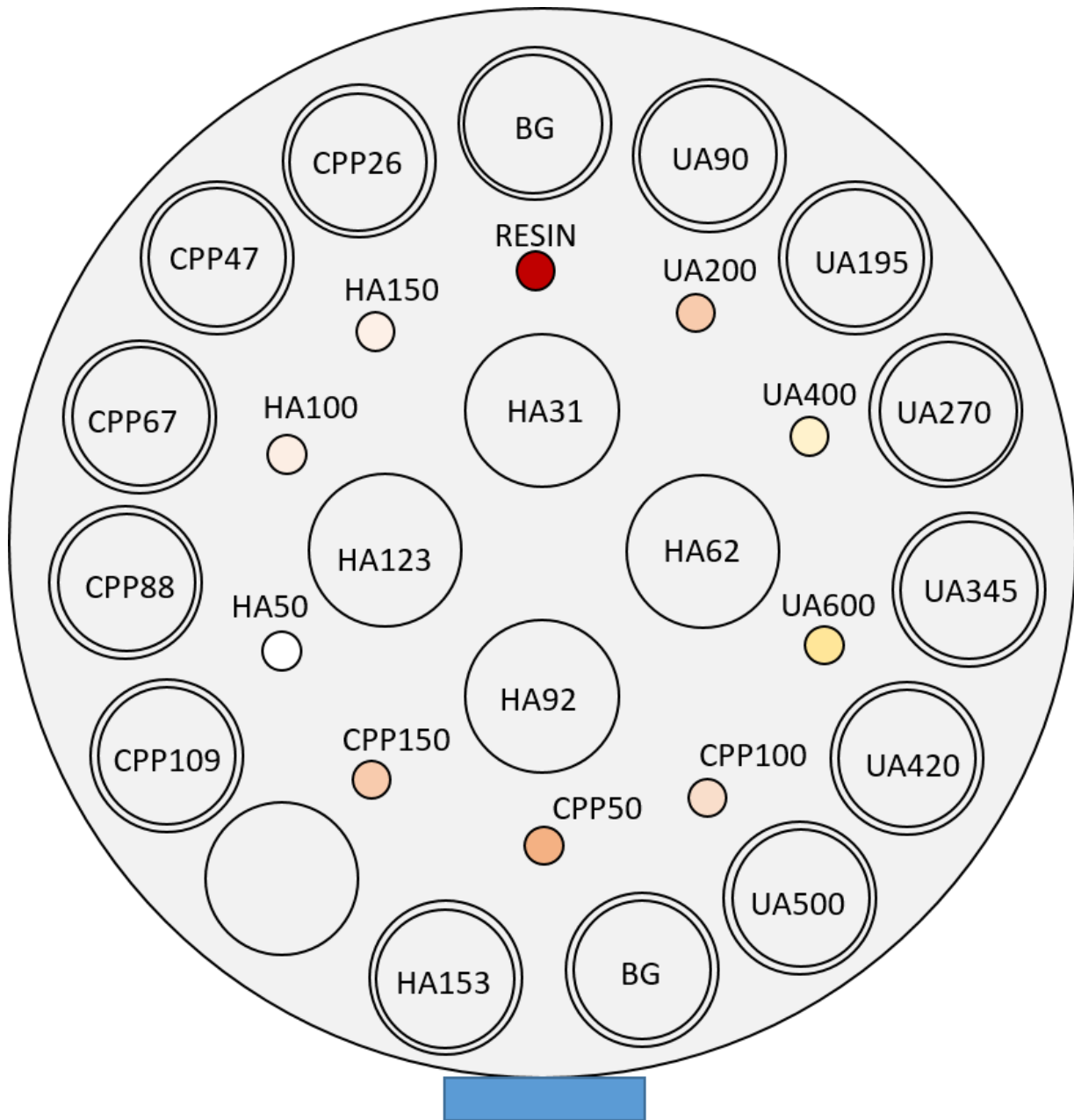


Fig. 18 Phantom schematic indicating crystal preparation location in the polyethylene phantom module and concentration (in [mg/mL]). Larger preparations at the module's periphery and central area (coded in grey) are agar-based, whereas the smaller rods located in-between (coded in various colors other than grey) are resin-based. UA = uric acid, HA = hydroxyapatite, CPP = calcium pyrophosphate. Courtesy Dr. Fabio Becce, MD, Lausanne University Hospital (CHUV),

Switzerland, and Dr. Lucia Gallego Manzano, PhD, scientific collaborator, Lausanne University Hospital (CHUV), Switzerland.

The phantom was scanned (on DECT and SPCCT systems) as is with a musculoskeletal protocol for comparison with existing studies, and inside a chest phantom to replicate the additional attenuation and noise resulting from the surrounding spine and chest wall. From this data, we can analyze the detection performance of the SPCCT vs. DECT, the influence of the preparation background (agar versus resin), and estimate the accuracy decline in an extremity versus cardiac scan.

As part of an ancillary study conducted in collaboration with Zurich University, the COROGOUT phantom was also scanned on a pre-clinical prototype PCCT system from another vendor. The latter is located at Zurich University Hospital (Prof. J Hodler, Prof A Alkadhi, PD Dr. R Guggenberger). An abstract co-authored with a multidisciplinary team was accepted at the RNSA 2021 annual meeting congress (please see below).

Crystal characterization and differentiation by spectral photon-counting CT: Initial results with the first clinical scanner of its generation.

Proposed author list:

Florian A. Huber, Fabio Becce, Matthias Zadory, David Rotzinger, Johannes M Froehlich, Bernhard Schmidt, Markus Jürgens, André Euler, Hatem Alkadhi, Roman Guggenberger

Abstract:

***Purpose:** To investigate the first clinically approved spectral photon-counting CT (SPCCT) in the differentiation of crystals related with gout (monosodium urate, MSU) vs. pseudogout (calcium pyrophosphate, CPP), and to compare its performance with energy-integrating dual-energy CT (DECT) scanners of the previous generation.

***Methods and Materials:** Agar-based (AG) gels mimicking attenuation of the articular cartilage and synthetic crystal suspensions of MSU and CPP at different concentrations (90-500 and 26-109 mg/mL, respectively) were inserted in a phantom. All samples were scanned with SPCCT (NAEOTOM Alpha, Siemens), dual-source (DS), single-source split-filter (SF) and sequential scan (SS) DECT at comparable dose levels (CTDI_{vol}: 4.4-12.5 for each) and tube potentials (80/140, 120 and 140 kV). Images were post-processed using DE overlay (DEO) values optimized for gout/MSU detection with dual-energy ratios as recommended by the literature (DECT) and vendor (SPCCT). Generated low/high kV HU-values and DEO values were measured for all samples by drawing same-sized ROIs (0.3cm²) on every second axial image for ten consecutive steps. Sample consistency and differences between radiation doses and scanners were investigated for all parameters, separately for concentrations and materials, respectively, using post-hoc corrected ANOVA, t-testing and analysis of mean differences. A p-value <0.05 was considered statistically significant.

***Results:** Regardless of scanner type, all crystal suspensions showed excellent homogeneity (p=0.23-1). HU-values in SPCCT did not depend on radiation dose overall. Apart from that, all quantitative parameters differed between CT scanner types and dose levels (p<0.01). However, mean differences were comparable between scanners [14.3-28.2]. Both CPP and MSU showed significant concentration-dependent differences in HU and DEO (all p<0.01). Correspondingly, concentrations of at least 195 mg/mL MSU and 47 mg/mL CPP crystals could be reliably differentiated with all techniques (mean DEO in SPCCT: -10.9+/-7.4 vs. -36.7+/-15.4, respectively).

***Conclusions:** Differentiation of gout/MSU from pseudogout/ CPP crystals at typical clinical concentrations is feasible with a clinical SPCCT system. Related quantitative measurements are comparable with values from DECT-scanners of the latest generation. First results may indicate better dose-related robustness in SPCCT for material decomposition tasks in the future.

***Clinical Relevance/Application:** This is the first in vitro proof-of-concept for material decomposition in a clinical SPCCT workflow. Further investigations in vivo with ex vivo confirmation are needed to transition current knowledge and DECT-based reference values of material decomposition in musculoskeletal and other settings to a new era of quantitative color CT imaging.

Abstract Word Count: 374

Abstract Character Count: 2335

Total Character Count: 2335

Character Maximum Limit 2400
Character Minimum Limit 300

Category (Complete): Physics -> CT - Dual Energy/Spectral CT

Format Preference (Complete): Oral Paper

Questions (Complete):

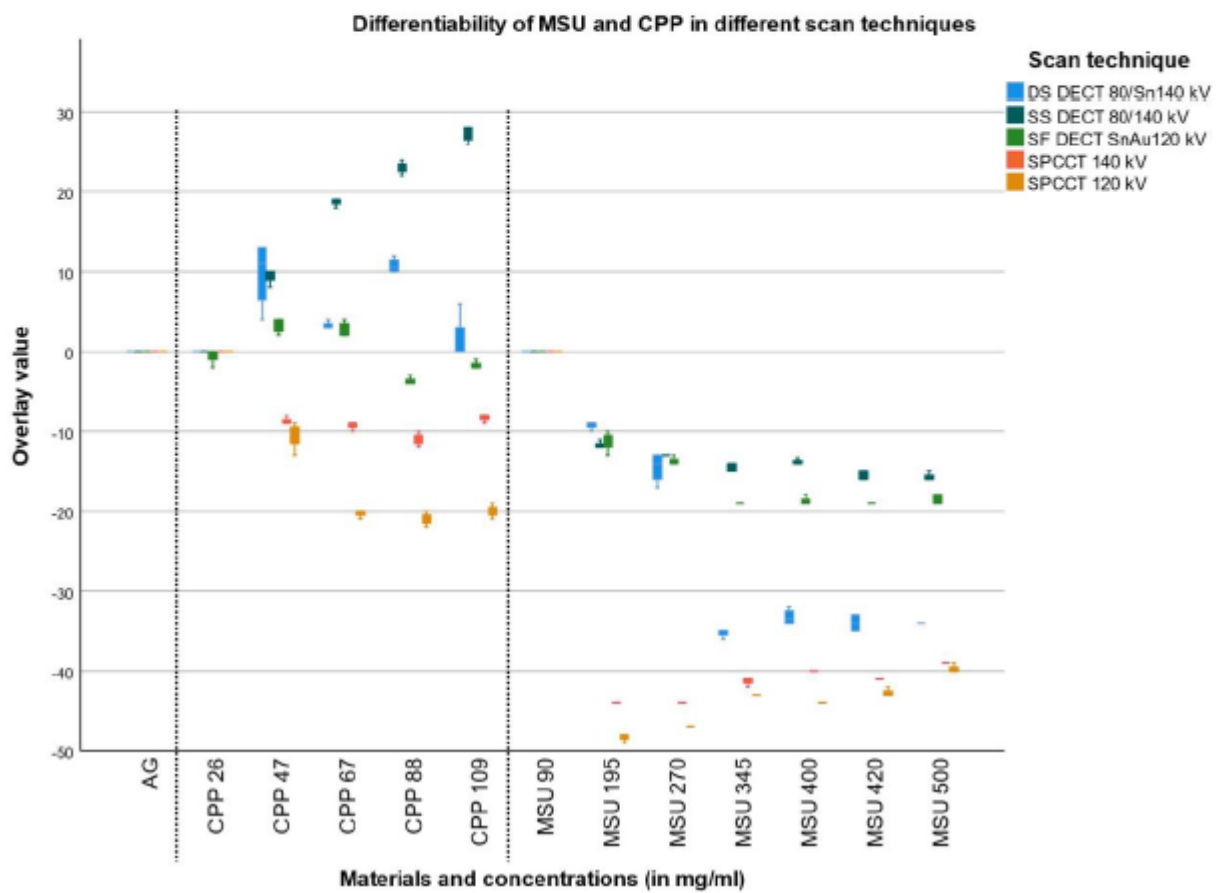
Trainee Research Prize: Resident/Physics Trainee

Disclosure of "Off-Label" usage: No, I do not intend to discuss off-label uses

IRB / IACUC Response: Not applicable/None of the above (explain)

If needed, please explain: : phantom study, no biological data involved

Has this work been previously presented or published?: No



COROGOUT preliminary results are available from acquisitions performed with a simpler phantom, built around a phantom containing only resin-based rods with suspensions of HA, CPP, and MSU. Only HA and MSU were analyzed; CPP preparations are meant to be interpreted as part of a study with a musculoskeletal focus. To approximate a physiological background for coronary arteries, we built a custom polyethylene module exhibiting CT numbers close to -100 HU (at 120 kVp) to simulate fat as if the rods were coronary arteries surrounded by epicardial fat. 5-mm-diameter holes were drilled into the module to hold the rods. Fig. 19 shows how the rods are inserted into the module.

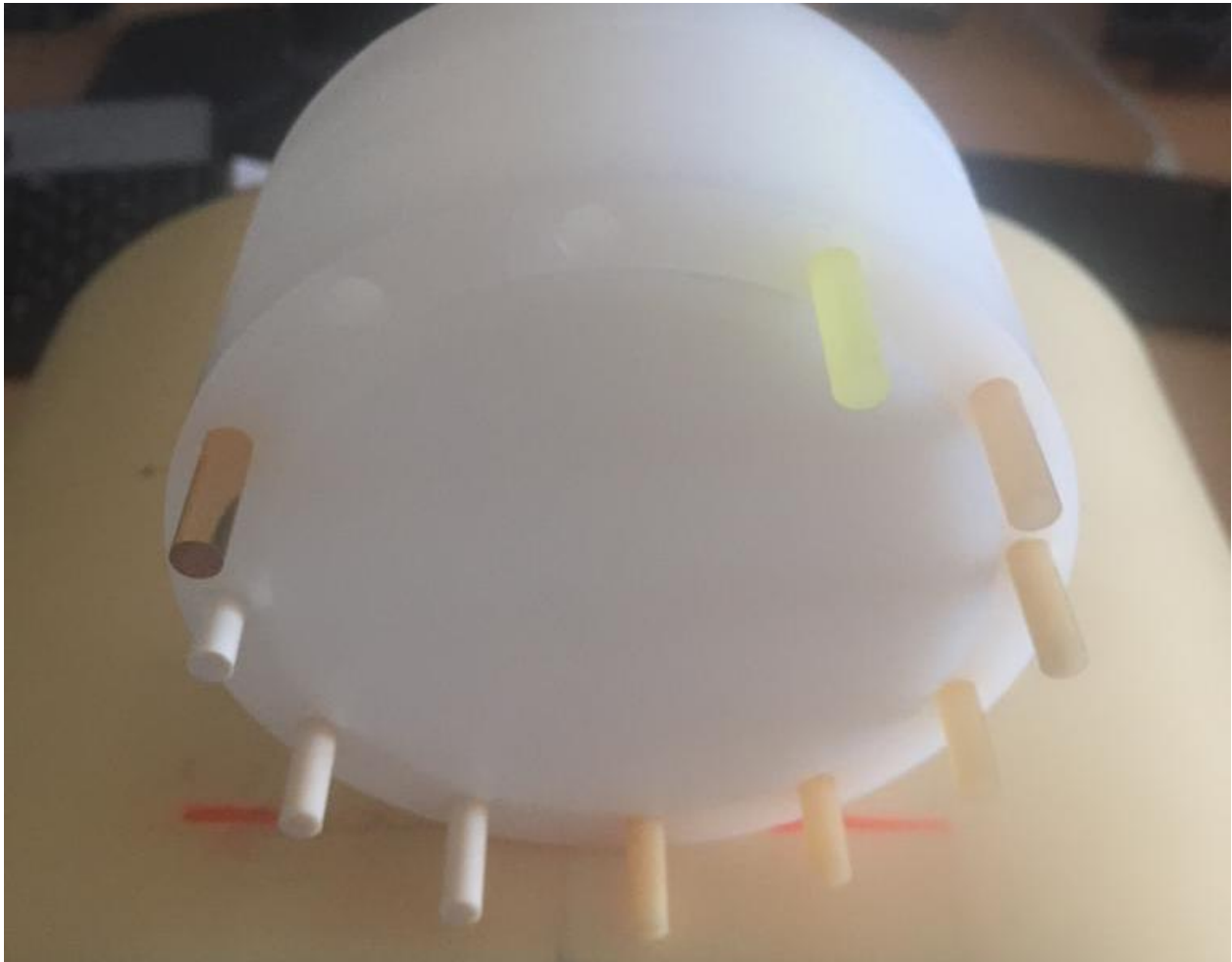


Fig. 19 Polyethylene module with halfway inserted resin-based rods and two spare holes not containing any sample.

This 10-cm-diameter polyethylene module is designed to fit in an anthropomorphic chest phantom (QRM Chest, QRM, Germany). The chest phantom was placed on a trolley allowing to move the setup. Moreover, a stepper motor driving a wooden rod connected to the trolley could be operated to simulate heart movements at a rate of 60 beats per minute. Fig. 20 shows the polyethylene module, the anthropomorphic chest phantom, the trolley, and the wooden rod.

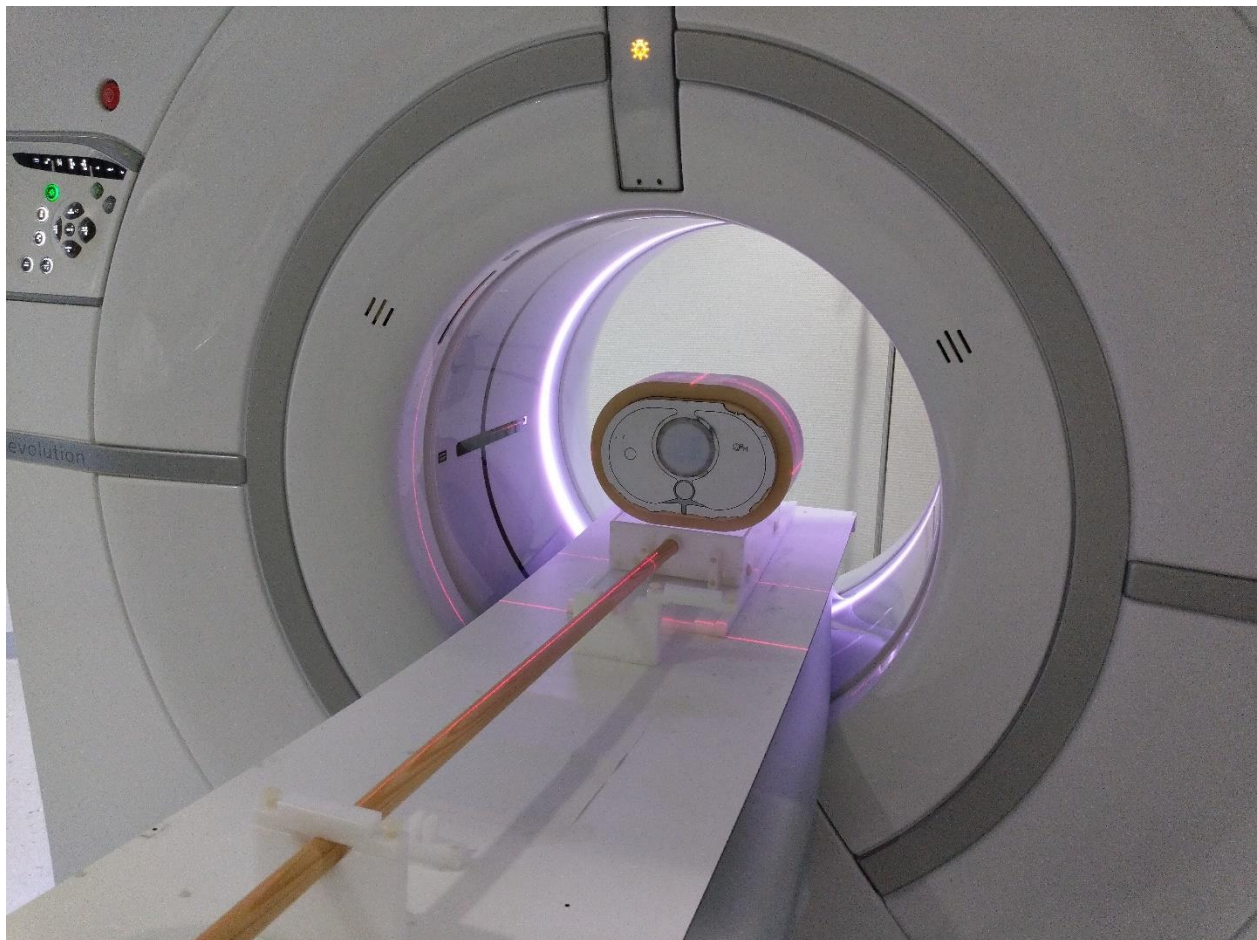


Fig. 20 Polyethylene module inside the QRM anthropomorphic phantom centered in a DECT system's bore, placed on a trolley allowing to move the setup to simulate heartbeats. The wooden stick is connected to the trolley and a computer programmable stepper motor (not shown).

The whole setup was scanned at standard coronary CTA dose levels (CTDI = 10 mGy) in static and dynamic (moving) conditions, in DECT mode. Images were reconstructed at a lower (50 keV) and a higher (100 keV) VMI energy level, with a standard kernel, section thickness of 0.625 mm, no overlap, and no iterative reconstruction. In moving conditions, the acquisition was performed in "CINE" mode (without ECG simulation) over 20 seconds, and 12 series were reconstructed. The image stack visually exhibiting the lowest motion artifacts was selected manually for analysis (series volume #1). Ten regions-of-interest (ROI) were placed in each UA and MSU rod to measure the CT numbers and standard deviation. Each ROI had a surface of 5 mm² and was placed in the rods' center. Dual-energy ratios (DER) were calculated using the following formula:

$$\text{DER} = \frac{\text{CT number (50keV)}}{\text{CT number (100 keV)}}$$

Different materials' DERs were compared using the Kruskal-Wallis test with Dunn's post hoc test, and p-values were corrected with the Holm method. A basic approach to approximate CT number reproducibility on static and moving acquisitions was to compare all ROI's standard deviation with the Wilcoxon test.

Fig. 21 shows a CT image (in HU) reconstructed at 70 keV, which is considered equivalent to a polychromatic image acquired at 120 kVp tube potential. MSU (on the phantom's right

side) and HA (on the left side) have overlapping CT numbers and cannot be readily distinguished.

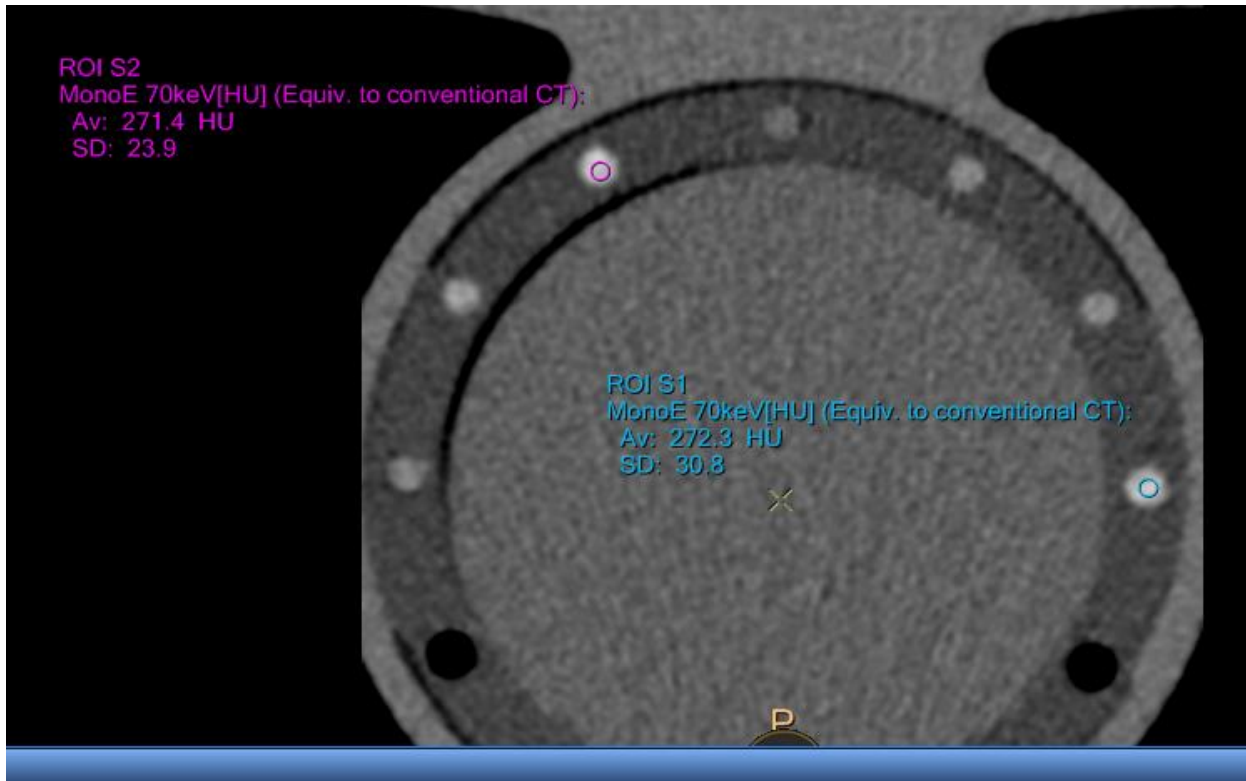


Fig. 21 CT image of the phantom's module, reconstructed at 70 keV (assumed to be equivalent to a polychromatic spectrum at 120 kVp), for illustration purposes. CT numbers are similar for MSU 600 mg/mL (ROI S1, 272 HU), and HA 200 mg/mL (ROI S2, 271 HU) and are thus indistinguishable without more advanced spectral analysis. The 12 o'clock position harbors a pure resin rod for reference; 1 o'clock, MSU 200 mg/mL; 2 o'clock, MSU 400 mg/mL; 3 o'clock, MSU 600 mg/mL; 9 o'clock, HA 50 mg/mL; 10 o'clock, HA 100 mg/mL; 11 o'clock, HA 200 mg/mL.

We then performed the quantitative image analysis and computed DERs in static and dynamic conditions. Fig. 22 shows DER boxplots in static scan mode. Visually, a difference between HA and MSU can be seen. The statistical analysis showed that the DER distribution was significantly different across the rods ($p < 0.001$). Post hoc testing revealed that the differences were significant only for DER.HA100 vs. DER.MSU200 ($p = 0.001$), DER.HA200 vs. DER.MSU200 ($p < 0.001$), DER.HA50 vs. DER.MSU200 ($p < 0.001$), DER.HA200 vs. DER.MSU400 ($p < 0.001$), DER.HA50 vs. DER.MSU400 ($p = 0.001$), and DER.HA200 vs. DER.MSU600 ($p = 0.002$).

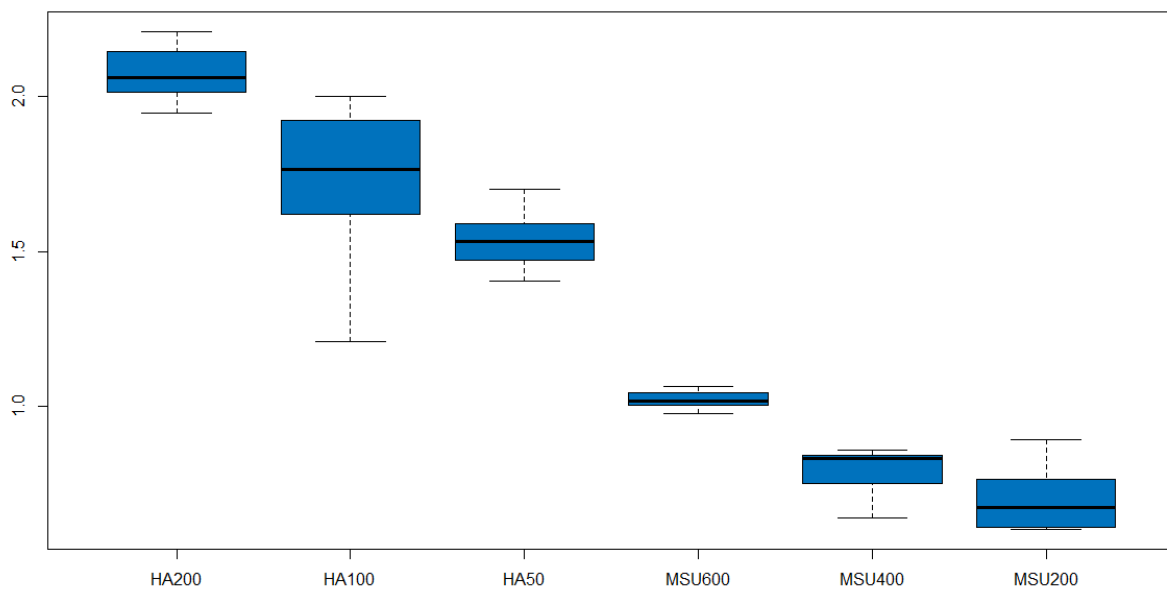


Fig. 22 Boxplots of dual-energy ratios (DER) for HA and MSU at various concentrations in static acquisition conditions.

We performed the same analysis in dynamic conditions in a second step. Fig. 23 shows DER boxplots in static scan mode. Visually, the difference between HA and MSU was not clearly visible. Moreover, a high DER variability was observed in the HA 200 mg/mL insert due to motion artifacts. The statistical analysis showed that the DER distribution was significantly different across the rods ($p < 0.001$). Post hoc testing revealed that the differences were significant only for DER.HA100 vs. DER.HA200 ($p < 0.001$), DER.HA200 vs. DER.MSU200 ($p = 0.002$), DER.HA200 vs. DER.MSU400 ($p < 0.001$), DER.HA50 vs. DER.MSU400 ($p = 0.001$), DER.HA200 - DER.MSU600 ($p < 0.001$).

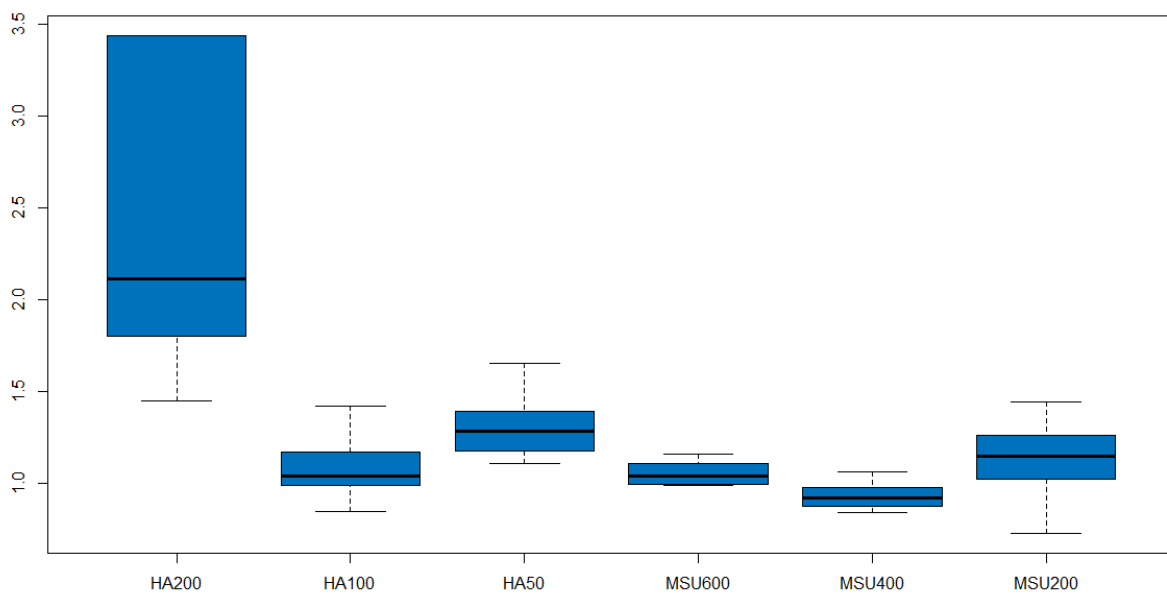


Fig. 23 Boxplots of dual-energy ratios (DER) for HA and MSU at various concentrations in dynamic acquisition conditions. CT numbers were overlapping much more than in static conditions, and motion artifacts led to exceptionally high CT number variation in the HA 200 mg/mL insert.

Finally, we combined all ROIs' standard deviations in the static and the dynamic scans to assess the effect of movement on CT number reproducibility. Fig. 24 shows box plots of standard deviation; the median value is significantly higher in dynamic conditions ($p < 0.001$), as well as the data variability indicated by the larger box size in dynamic conditions.

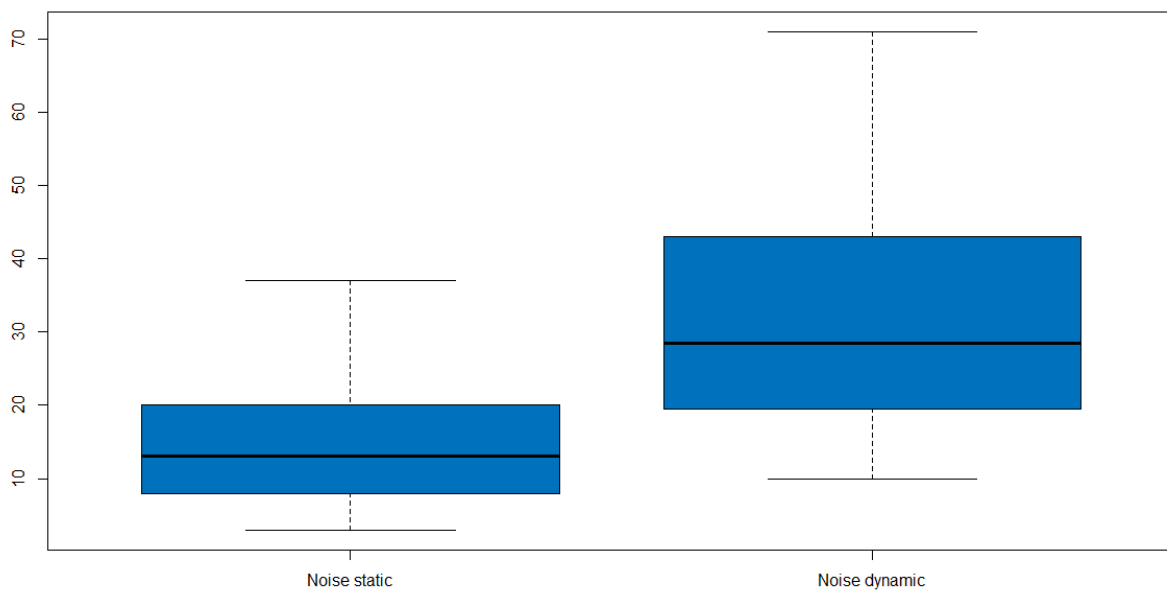


Fig. 24 CT number variability, assessed by the standard deviation

The bottom line is that DECT has some potential to distinguish MSU from HA, in ideal experimental conditions (pure samples with a 5 mm diameter). The challenge in vivo is that MSU deposits in blood vessels are expectedly much smaller. Moreover, when simulating heartbeats causing coronary artery motion, the DERs' accuracy seems to decrease steeply. This undermines the finding of significantly more prevalent MSU

deposits demonstrated in vivo by DECT in gout patients than controls reported by a research group [117], given the probability of misregistration due to motion artifacts and DER variability. The COROGROUT project is ongoing, and the primary analyses to be conducted will be to assess the added value of PCCT over DECT to detect and characterize MSU, especially in smaller ROIs.

6.3 Spatial resolution, noise and detection performance

6.3.1 Feasibility of spectral photon-counting coronary CT angiography and comparison with energy-integrating-detector CT: objective assessment with model observer

Submitted to the journal “European Radiology”, under review at time of writing.

Implications for patient care

Coronary CT angiography is one of the most demanding CT applications in contemporary radiology practice. This is due to two main factors: (a) because the heart is moving, the gantry has to be operated at maximum speed to reach the best possible spatial resolution; the consequence is increased image noise, especially when using the smallest tube focal spot – which is advisable for the sake of spatial resolution; (b) because coronary arteries are relatively small (less than 2mm in diameter distally), running along the epicardium with complex geometry, high spatial resolution is required to resolve lumen and wall-related anatomical details. Furthermore, plaque characterization tasks deal with low-contrast, e.g., for lipid core detection. The sum of all these constraints results in the CT system being used at the edge of its performance, and any improvement in noise, spatial resolution, contrast resolution, or even better spectral resolution will benefit the patient. PCCT is expected to provide incremental value in all the latter topics, a future application of PCCT we validated in the phantom study. The awaited implications for patient care involve radiation dose reduction or improved diagnostic performance in overweight subjects. Additionally, in line with the need to identify vulnerable plaques, we assessed

lipid core detection performance and demonstrated PCCT's superiority over dual-layer detector CT for this specific task.

Author contribution

Lead author; performed acquisitions, coordinated image reconstruction with the help of academic and industry partners across Europe and Middle East, interpreted data, completed the literature review, manuscript drafting, and editing.

Feasibility of spectral photon-counting coronary CT angiography and comparison with energy-integrating-detector CT: objective assessment with model observer
 --Manuscript Draft--

Manuscript Number:	EURA-D-21-02592	
Full Title:	Feasibility of spectral photon-counting coronary CT angiography and comparison with energy-integrating-detector CT: objective assessment with model observer	
Article Type:	Original Article	
Funding Information:	horizon 2020 framework programme (643694)	Not applicable
Abstract:	<p>Objectives</p> <p>To evaluate the feasibility of spectral photon-counting CT (SPCCT) coronary angiography in vitro by investigating its objective image quality characteristics compared with a standard-of-care energy-integrating-detector (EID) CT system.</p> <p>Methods</p> <p>We scanned an anthropomorphic thorax phantom with a coronary artery module at 10 mGy on a preclinical SPCCT and a clinical dual-layer EID-CT under various conditions of simulated patient size (small, medium, large). Images were reconstructed using filtered back-projection with a soft-tissue kernel. We assessed noise and contrast-dependent spatial resolution with noise power spectra (NPS) and target transfer functions (TTF), respectively. Detectability indexes (d') of simulated non-calcified and lipid-rich atherosclerotic plaques were computed using the non-prewhitening with eye filter model observer.</p> <p>Results</p> <p>For all patient sizes, SPCCT provided markedly lower noise magnitude (9-38% lower NPS amplitude) and overall higher noise frequency peaks (sharper noise texture). Furthermore, SPCCT provided consistently higher spatial resolution than EID-CT (30-33% better TTF10). In the resulting detectability analysis, SPCCT outperformed EID-CT in all investigated conditions, providing superior d'. Of note, SPCCT reached almost perfect detectability (estimated AUC\approx95%) for simulated non-calcified plaques measuring as low as 0.5-mm-thickness (for large-sized patients), whereas EID-CT had lower d' (AUC\approx75%). For lipid-rich atherosclerotic plaques, SPCCT achieved 85% AUC, whereas EID-CT reached only 77.5% AUC.</p> <p>Conclusions</p> <p>Photon-counting coronary CTA is feasible not only for small or medium-sized patients but also for large subjects. Furthermore, SPCCT outperformed EID-CT in the quantitative analysis and might enhance the overall diagnostic accuracy by providing lower noise magnitude, markedly improved spatial resolution, and superior lipid core detectability.</p>	
Corresponding Author:	David Christian Rotzinger, M.D. Centre Hospitalier Universitaire Vaudois Lausanne, SWITZERLAND	
Corresponding Author Secondary Information:		
Corresponding Author's Institution:	Centre Hospitalier Universitaire Vaudois	
Corresponding Author's Secondary Institution:		
First Author:	David Christian Rotzinger, M.D.	

First Author Secondary Information:	
Order of Authors:	David Christian Rotzinger, M.D.
	Damien Racine, PhD
	Fabio Becce, MD
	Elias Lahoud, PhD
	Klaus Erhard, PhD
	Salim A. Si-Mohamed, MD, PhD
	Joël Greffier, PhD
	Anaïs Viry, PhD
	Loïc Bousset, MD, PhD
	Reto A. Meuli, MD, PhD
	Yoad Yagil, PhD
	Pascal Monnin, MSc
	Philippe C. Douek, MD, PhD
Order of Authors Secondary Information:	
Author Comments:	
Opposed Reviewers:	

Feasibility of spectral photon-counting coronary CT angiography and comparison with energy-integrating-detector CT: objective assessment with model observer

Authors and affiliations

David C. Rotzinger, MD^{1,2*}, Damien Racine, PhD^{2,3*}, Fabio Becce, MD^{1,2}, Elias Lahoud, PhD⁴, Klaus Erhard, PhD⁵, Salim A. Si-Mohamed, MD, PhD^{6,7}, Joël Greffier, PhD⁸, Anaïs Viry, PhD^{2,3}, Loïc Boussel, MD, PhD^{6,7}, Reto A. Meuli, MD, PhD^{1,2}, Yoad Yagil⁴, Pascal Monnin, MSc^{2,3}, Philippe C. Douek, MD, PhD^{6,7}

1. Department of Diagnostic and Interventional Radiology, Lausanne University Hospital (CHUV), Rue du Bugnon 46, Lausanne, Switzerland
2. Faculty of Biology and Medicine (FBM), University of Lausanne (UNIL), Switzerland
3. Institute of Radiation Physics, Lausanne University Hospital (CHUV), Lausanne, Switzerland.
4. CT/AMI Research and Development, Philips Medical Systems, Haifa, Israel
5. Philips Research Laboratories, Hamburg, Germany
6. University Claude Bernard Lyon 1, CREATIS, CNRS UMR 5220, INSERM U1206, INSA-Lyon, Lyon, France
7. Radiology Department, Hospices Civils de Lyon, 69500, Lyon, France.
8. Department of Medical Imaging, CHU Nimes, Univ Montpellier, Medical Imaging Group, 2415, Nimes, EA, France.

Corresponding author:

David C. Rotzinger, MD

Abstract

Objectives

To evaluate the feasibility of spectral photon-counting CT (SPCCT) coronary angiography in vitro by investigating its objective image quality characteristics compared with a standard-of-care energy-integrating-detector (EID) CT system.

Methods

We scanned an anthropomorphic thorax phantom with a coronary artery module at 10 mGy on a preclinical SPCCT and a clinical dual-layer EID-CT under various conditions of simulated patient size (small, medium, large). Images were reconstructed using filtered back-projection with a soft-tissue kernel. We assessed noise and contrast-dependent spatial resolution with noise power spectra (NPS) and target transfer functions (TTF), respectively. Detectability indexes (d') of simulated non-calcified and lipid-rich atherosclerotic plaques were computed using the non-prewhitening with eye filter model observer.

Results

For all patient sizes, SPCCT provided markedly lower noise magnitude (9-38% lower NPS amplitude) and overall higher noise frequency peaks (sharper noise texture). Furthermore, SPCCT provided consistently higher spatial resolution than EID-CT (30-33% better TTF_{10}). In the resulting detectability analysis, SPCCT outperformed EID-CT in all investigated conditions, providing superior d' . Of note, SPCCT reached almost perfect detectability (estimated $AUC \approx 95\%$) for simulated non-calcified plaques measuring as low as 0.5-mm-thickness (for large-sized patients), whereas EID-CT had lower d' ($AUC \approx 75\%$). For lipid-rich atherosclerotic plaques, SPCCT achieved 85% AUC, whereas EID-CT reached only 77.5% AUC.

Conclusions

Photon-counting coronary CTA is feasible not only for small or medium-sized patients but also for large subjects. Furthermore, SPCCT outperformed EID-CT in the quantitative analysis and might enhance the overall diagnostic accuracy by providing lower noise magnitude, markedly improved spatial resolution, and superior lipid core detectability.

Keywords

Computed tomography angiography; Coronary vessels; Cardiac Imaging Techniques; Phantoms imaging; Image quality enhancement

Keypoints

- Spectral photon-counting CT outperformed dual-layer CT in terms of spatial resolution and noise magnitude in atherosclerotic plaque detection
- Photon-counting coronary CTA is feasible not only for small or medium-sized patients but also for large subjects
- Large simulated patient size had detrimental effects on both CT systems' performance; however, non-calcified plaque detectability remained excellent down to a 0.5-mm-diameter on the photon-counting system (vs. 1.0 mm on the dual-layer CT)

Abbreviations and acronyms

- AUC = area under the curve
- CCTA = coronary computed tomography angiography
- CM = contrast material
- CT = computed tomography
- CTDI_{vol} = volumetric computed tomography dose index

- DECT = dual-energy computed tomography
- EID = energy-integrating detector
- NPS = noise power spectrum
- PCD = photon-counting detector
- PE = polyethylene
- ROI = region of interest
- SPCCT = spectral photon-counting computed tomography
- TTF = target transfer function

Introduction

Since its inception in 1973, computed tomography (CT) has undergone steady improvements on both the data acquisition and image reconstruction aspects, quickly becoming a key player in cardiovascular imaging and establishing itself as the primary non-invasive coronary artery disease assessment tool [1]. Although the initial CT report by Hounsfield already mentioned the potential advantages of acquiring data at various energy levels [2], CT systems capable of collecting two distinct energy bands routinely were made available commercially only three decades later, with the introduction of dual-energy CT (DECT) platforms. DECT is becoming widely available clinically and can now be used in everyday practice to improve patient safety and diagnostic performance. In cardiovascular medicine, in particular, DECT helps reduce iodine dose [3; 4], improve vessel opacification [5], save radiation dose with virtual non-contrast reconstruction [6], among others. On the other hand, DECT suffers from some fundamental limitations, including the absence of notable improvement in spatial resolution or electronic noise compared with single-energy systems, which could be addressed by photon-counting-detector (PCD) technology [7].

PCDs' principle is to operate without generating visible light inside detector elements, thereby eliminating the challenges related to scintillators and associated electronic noise while providing a refined spectral analysis. Contrary to conventional energy-integrating detectors (EID) – which are used in single-energy and DECT systems – that measure the total energy deposited in the detector, PCDs quantify the energy of each incident photon according to two or more thresholds called "energy bins", and can be produced with a much smaller detector element size to increase spatial resolution. For these reasons, PCD-CT is expected to address some major limitations of EID-based DECT [8-10].

Coronary CTA (CCTA) is one of the most demanding CT imaging examinations due to heart motion and high spatial resolution requirements; it is especially challenging to perform

because the gantry needs to be operated at maximum speed for the sake of temporal resolution. Because CCTA requires both low noise and great anatomical detail, it remains a challenging examination, especially in overweight subjects. Technological advances constantly push the limits of the possible and promote CCTA as a reproducible, accurate, and reliable diagnostic test. The advent of PCD-CT is one of these technological advances that can shift the patient management paradigm in the next ten years. EIDs have been in use for almost five decades and have been CT's backbone until now, more recently bringing CCTA to clinical routine.

Our purpose was to thoroughly characterize the image quality properties of a preclinical spectral photon-counting CT (SPCCT) prototype compared with a clinical standard-of-care EID-CT system in the setting of CCTA. To this end, we measured image noise and contrast-dependent spatial resolution properties under various simulated patient size conditions. Joint effects of noise properties and spatial resolution were modeled using state-of-the-art mathematical model observers, evaluating the systems' performance to detect simulated non-calcified atherosclerotic plaques and lipid core in CCTA.

Materials and methods

Experimental design

We used a custom-made 10-cm-diameter cylindrical module made of low-density polyethylene (PE, average CT number at 100 kVp \approx -100 HU). This module had a 5-cm-diameter central hole that was filled with an iodinated contrast material (CM) solution (Iomeron 400® mixed with normal saline) at a concentration of 18 mg I/mL, yielding CT numbers in the range of clinical CCTA at 100 kVp (approximately 350 HU) [4]. This CM solution and the surrounding PE created a pair of materials approaching the object-to-background contrast difference (Δ HU) encountered in CCTA, assuming that coronary arteries are opacified by iodinated CM and are surrounded by epicardial fat whose CT number is around -100 HU. The

transition between PE and the CM solution served to measure the contrast-dependent spatial resolution using the target transfer function (TTF), an advanced physical metric particularly suited for CT taking into account the contrast-dependency of spatial resolution [11; 12]. We inserted the CCTA module into an anthropomorphic thorax phantom (QRM, Moehrendorf, Germany) that was scanned as is ("small" patient size) and with additional fat-mimicking extension rings to simulate heavier bodyweights ("medium" and "large" patient size). The corresponding approximate patient weights are 50 kg (small), 80 kg (medium), and 100 kg (large size). Pictures of the phantom setup are provided in **Figure 1**. The phantom's background was used to compute the noise power spectrum (NPS), a further advanced image quality metric providing a comprehensive assessment of noise by plotting noise magnitude as a function of spatial frequency [11; 12]. Approval of the institutional ethics committee was not required since no living beings were involved.

Acquisition protocol and image reconstruction

We scanned the phantom on a clinically available 64-detector row dual-layer detector EID-CT system (IQon Spectral CT, Philips Healthcare) following the standard clinical acquisition protocol for CCTA in our University hospital, at a dose of 10 mGy. Volume CT dose indexes ($CTDI_{vol}$) were computed for a 32-cm-diameter (polymethyl methacrylate) reference phantom, and retrieved from radiation-dose structured reports. Dose modulation was disabled to achieve comparable dose on both CT systems. Next, we scanned the same phantom setup using a similar acquisition protocol on a preclinical SPCCT system (SPCCT, Philips Healthcare), aiming to generate comparable datasets by matching tube potential and loading and image reconstruction parameters with the EID-CT platform. The SPCCT is a large field-of-view (500 mm) system equipped with 2-mm thick Cadmium-Zinc-Telluride detectors yielding a pixel pitch of $270 \times 270 \mu\text{m}$ at isocenter and a z-coverage of 17.5 mm arranged in

64 detector rows. Each detector channel has its own application-specific integrated circuit providing discrimination of 5 separate energy bands. Further technical details can be found here [13; 14]. To ensure optimal precision of image quality metrics, the phantom was scanned eight times consecutively on each CT system, without any repositioning or parameter variation, to obtain datasets with a sufficiently large number of images. These eight acquisitions served to improve the statistics and are not intended to evaluate measurement uncertainties. **Table 1** presents the detailed settings for data acquisition and image reconstruction.

Images were reconstructed using the "high-resolution B" kernel (a similar one for both CT systems), which is suited for coronary artery imaging. Also, to keep the comparison as accurate and fair as possible, we refrained from using advanced image reconstruction algorithms such as iterative reconstruction. This resulted in a total of 6 different CT datasets available for analysis: 2 CT systems (EID vs. SPCCT) \times three phantom sizes (small, medium, and large).

Image analysis

Noise power spectrum (NPS)

We assessed image noise in the homogeneous background area of the phantom made of PE. To quantify and characterize noise, we calculated noise power spectra (NPS) following the International Commission on Radiation Units and Measurements' reports 54 and 87 [12]. NPS has established itself as state of the art for CT noise characterization, based on its unique ability to provide noise magnitude evaluation and noise texture analysis [15; 16]. Four square regions of interest (ROI) of 100×100 pixels positioned at different locations in the background of the phantom in 214 axial CT slices were used to compute 2D NPS (total of 856 ROIs), which were then radially averaged to yield 1D NPS. NPS was analyzed in terms of NPS peak frequency shift and noise magnitude reduction. NPS peak frequency was defined as the NPS's

maximum amplitude. The noise magnitude was defined as the integral of the area under the NPS curve.

The NPS peak frequency shift was calculated according to the following formula:

$$\text{NPS peak frequency shift}_i = \frac{f_{\max(\text{patient size}_i, \text{PCD})} - f_{\max(\text{patient size}_i, \text{EID})}}{f_{\text{peak}(\text{patient size}_i, \text{EID})}} \times 100$$

The noise magnitude reduction was calculated according to the following formula:

$$\begin{aligned} \text{Noise magnitude reduction}_i \\ = \frac{\int \text{NPS}(\text{patient size}_i, \text{PCD}) - \int \text{NPS}(\text{patient size}_i, \text{EID})}{\int \text{NPS}(\text{patient size}_i, \text{EID})} \times 100 \end{aligned}$$

where i corresponds to small, medium, or large patient size

Target transfer function (TTF)

We investigated contrast-dependent spatial resolution in the phantom region containing the iodine solution. The transition between PE and the CM solution served to measure the TTF at a contrast close to 450 HU. A total of 214 axial CT sections were used to calculate the TTF. Square ROIs of 68×68 mm were extracted from the CT image to obtain 2D TTFs from edge spread functions, using an angular aperture and a pitch of 15° and 10° , respectively. 1D TTFs were subsequently generated by radially averaging 2D TTFs. Spatial resolution performances of the SPCCT and EID-CT systems were compared in terms of TTF frequency shift at 50% (TTF_{50}) and 10% (TTF_{10}) of its value at zero frequency for the three patient sizes. TTF frequency shifts were calculated using the following formula:

$$\text{TTF frequency shift}_j = \frac{f_{j(\text{patient size}_i, \text{PCD})} - f_{j(\text{patient size}_i, \text{EID})}}{f_{j(\text{patient size}_i, \text{EID})}} \times 100$$

where j is equal to 10 or 50%, and i corresponds to small, medium, or large patient size.

Non pre-whitening with eye filter (NPWE) model

To account for noise magnitude, noise texture, and contrast-dependent spatial resolution at the same time, we computed detectability indices (d') using the following model:

$$d' = \frac{\sqrt{2\pi}|\Delta\text{HU}| \int_0^{f_{\text{Ny}}} S^2(f) \text{TTF}^2(f) \text{VTF}^2(f) f df}{\sqrt{\int_0^{f_{\text{Ny}}} S^2(f) \text{TTF}^2(f) \text{NPS}(f) \text{VTF}^4(f) f df}}$$

where $|\Delta\text{HU}|$ is the contrast in absolute CT numbers between an object (i.e. non-calcified atherosclerotic plaque and lipid-rich plaque, respectively) and the surrounding homogenous background (i.e. coronary lumen and lipid-poor plaque, respectively), f the radial spatial frequency, f_{Ny} the radial Nyquist frequency, S the magnitude of the Fourier transform of the input signal (here, $S = \frac{r}{f} J_1(2\pi r f)$, with r the disk radius and J_1 the Bessel function of the first kind), and VTF the visual transfer function of the human eye.

The model was adjusted to simulate two distinct but clinically relevant tasks. First, we assessed a high (400 HU) object-to-background contrast to simulate a non-calcified atherosclerotic plaque in the coronary artery wall [17]. The plaque was simulated as a half-disc of varying size whose upper (semicircular) portion causes lumen narrowing, and its flat portion abuts the vessel wall. The second task was designed to assess low-attenuation (also called "lipid-rich") plaques' detectability. Low attenuation composition is a known determinant of atherosclerotic plaque vulnerability histologically defined as a necrotic or lipidic core measuring $>200 \mu\text{m}$ [18]. According to existing data, fibrous plaques have average CT numbers around 60 HU. In contrast, the lipid core's CT number is close to 30 HU, meaning that the contrast between the fibrous and lipid plaque components is about 30 HU [19; 20]. Consequently, we modeled the lipid core as a circular area whose object-to-background contrast $|\Delta\text{HU}|$ is 30 HU, with a diameter ranging from 0.5 to 3 mm in 0.5-mm steps. The NPWE model provides d' varying from 0 to infinity, and is directly related to the accuracy. The link between d' and the area under the receiver operating characteristic curve (AUC) can be

used to assess the accuracy obtained for a specific task; a $d' > 2$ corresponds to an AUC of 90% [12].

Results

Noise power spectrum

The preclinical SPCCT impacted both the overall noise magnitude and noise texture (NPS peak frequency) compared with the clinical EID-CT, as demonstrated in **Figure 2**. Not only did the PCD system exhibit consistently lower noise magnitude, but it also had higher frequency noise since NPS peak frequency shifted towards high frequencies (from 0.38 to 0.47 mm^{-1}) compared with the EID system (from 0.27 to 0.3 mm^{-1}). Increasing the phantom size resulted in a stronger noise magnitude on both CT systems, with no substantial noise texture change (no NPS peak frequency shift). At small phantom size, the SPCCT system's NPS peaked at a 51% higher frequency while providing a 9% lower noise magnitude than the EID-CT (**Table 2**). At medium and large phantom sizes, the NPS peak frequency was 37% and 26% higher on the SPCCT, respectively, while the noise magnitude was 33% and 38% lower, respectively.

Target transfer function

The SPCCT's spatial resolution performance was measured using the TTF and is plotted in **Figure 3**. The SPCCT provided a noticeably higher spatial resolution than the EID-CT, with a 35%, 37%, and 38% better TTF_{50} and 30%, 31%, and 33% better TTF_{10} , for the small, medium, and large size phantoms, respectively (**Table 3**). Furthermore, we found that increasing the phantom size had a limited detrimental effect on the spatial resolution of both CT systems. Still, the EID-CT was slightly more prone to resolution loss at large phantom size.

Nonprewhitening with eye filter model observer

For both non-calcified atherosclerotic plaque and lipid core detection tasks, the SPCCT outperformed the EID-CT regardless of the plaque size. Specifically, the SPCCT provided 22% to 43% better d' for non-calcified plaque detection and 21 to 48% better d' for lipid core characterization, depending on plaque and phantom size (Figures 4 and 5). For detecting the smallest simulated non-calcified plaque (0.5 mm), both systems reached the threshold of 90% AUC ($d' > 2$) with the small and medium-sized phantom. For the large phantom, only the SPCCT achieved 90% AUC (EID-CT AUC = 75%). For characterizing the lipid core, the limit of 90% AUC in the small phantom was 1.5 and 1 mm with the EID-CT and SPCCT, respectively. In the medium phantom, the EID-CT system did not reach the limit of 90% AUC – even for the largest simulated lipid core (3.0 mm) – while the SPCCT achieved 90% AUC down to a lipid core size of around 2.0 mm. Neither system achieved 90% AUC in the large phantom and 3.0 mm lipid core, but the SPCCT system achieved 85% AUC, whereas EID-CT reached only 77.5% AUC.

Figure 6 illustrates the visual appearance of the CCTA phantom scanned on the EID-CT and SPCCT systems at varying phantom sizes. Image noise increased at medium and large sizes. Still, regardless of the simulated patient size, the iodinated solution vs. PE interface appeared sharper on the SPCCT system, confirming the trends demonstrated in the quantitative analysis.

Discussion

Our phantom study assessed the feasibility of CCTA using a preclinical prototype SPCCT system and compared the system's performance with the current clinical standard of care that is a dual-layer EID-CT system. We characterized the image quality using NPS (image noise) and TTF (spatial resolution) metrics and performed a specific task-based investigation

of CCTA. We showed that at equivalent regular radiation dose (10 mGy), the SPCCT operating with PCDs provides solid performance for detecting non-calcified atherosclerotic plaque and lipid-rich components down to a size of 0.5 mm and 1.5 mm, actually outperforming the EID-CT system. Cardiac PCD-CT has recently been used in an animal study advocating the transition from EID to PCD [21], and our work is a step further in that direction.

NPS analysis confirmed the significantly lower noise magnitude of SPCCT, which is an anticipated improvement [22] owing to the ability of PCDs to void electronic noise almost completely and showed differences in noise texture, with NPS peaks occurring at a significantly higher spatial frequency with the SPCCT. Higher frequency peak visually translates to "finer" noise texture, facilitating lesion detection [16], especially when small and with low object-to-background contrast, such as for lipid-rich plaques. A further noteworthy fact was that the noise increase associated with larger phantom sizes was steeper on the EID-CT, which bodes well for dose savings while maintaining appropriate image quality in overweight patients with PCD-CT in the future.

The systems' spatial resolution performance assessment also showed considerable differences. Of note, the SPCCT provided markedly improved spatial resolution over the conventional CT system, on par with recent previous investigations [22-24]. Because they do not require septa physically separating detector elements, PCDs can be manufactured in much smaller dimensions, in the order of 100-500 μm , overcoming one of EIDs' major limitation: dose-inefficiency at small detector element size. In PCDs, pixels are recovered by anode parceling and can be subdivided if needed. Interestingly, our study showed that the SPCCT is also less prone to spatial resolution deterioration when scanning the large phantom. Spatial resolution is critically important in CCTA for three main reasons: first to resolve small atherosclerotic plaques in any plane, since coronary arteries measure ≤ 2 mm distally, meaning that as little as 4-6 voxels may be available to quantify stenoses depending on the intrinsic

spatial resolution [25]. PCD can utilize sharper filters to enable more voxels, with higher noise that can be managed with noise reduction algorithms. Second, the detection of lipid-rich plaque components has a predictive value [18] but is challenging due to the lipid-rich core's small size [20; 26], hence the need for higher spatial resolution. Our model observer assessment demonstrated SPCCT's potential to address both of these issues, providing consistently higher d' than conventional EID-CT. Model observers are particularly relevant image quality indicators because they exhibit a stronger correlation with human observer performance than the classic contrast-to-noise ratio [27]. On the other hand, model observers do not allow for an anatomic representation of the image's features because lesions are simulated in the frequency domain. The third reason CCTA requires high spatial resolution is that, in calcified plaques, blooming artifacts can lead to stenosis overestimation [28]. This is caused by the convolution of the system's point-spread function [29], and PCD-CT has shown promising results in mitigating this effect [23; 30]. Also, SPCCT can improve vascular imaging in the presence of metal stents that cause blooming artifacts for the same reasons as calcium [31; 32].

Our study has several limitations. First, we demonstrated that SPCCT yields higher spatial resolution, even though we reconstructed only 512^2 matrices. The underlying reasons were first to keep the investigation clinical since 512^2 matrices are standard-of-care, and second, we wanted to keep noise low enough, especially with the large phantom. SPCCT offers larger matrices, including 1024^2 or 2048^2 , with sharper reconstruction filters that could potentially be clinically relevant for stenosis quantification, particularly in calcified plaques with associated blooming artifacts. Larger matrices come at the cost of increased noise but could be combined with advanced reconstruction algorithms in the future, such as iterative or deep-learning-based reconstructions [33; 34]. Furthermore, calcified plaque, which challenges CCTA interpretation when present in high quantities, was not assessed in this study. As mentioned earlier, PCD-CT has already shown promise to improve calcified coronary artery

analysis ex vivo [23]. Additionally, by design, we investigated only one radiation dose level because we aimed to understand the effect of patient size. While we could have used higher doses for the large phantom, the future trend will be to reduce radiation dose for normal-sized patients rather to increase dose for large patients. Finally, the cardiac phantom was static, which may lead to an overestimation of the detectability performance. However, at equal gantry revolution time, the overestimation magnitude is the same for both systems; noise and spatial resolution properties are given by the systems' design.

Conclusions

SPCCT outperformed conventional EID-CT in the task of detecting non-calcified and lipid-rich plaque in coronary arteries, more so with the large phantom. The SPCCT's lower noise and higher spatial resolution could be translated into improved accuracy for stenosis quantification and plaque characterization or reduced radiation dose, particularly in large patients often subjected to increased radiation dose and decreased diagnostic performance tests.

References

- 1 Schoepf UJ, Zwerner PL, Savino G, Herzog C, Kerl JM, Costello P (2007) Coronary CT angiography. *Radiology* 244:48-63
- 2 Hounsfield GN (1973) Computerized transverse axial scanning (tomography). 1. Description of system. *Br J Radiol* 46:1016-1022
- 3 Cavallo AU, Patterson AJ, Thomas R et al (2020) Low dose contrast CT for transcatheter aortic valve replacement assessment: Results from the prospective SPECTACULAR study (spectral CT assessment prior to TAVR). *Journal of cardiovascular computed tomography* 14:68-74
- 4 Rotzinger DC, Si-Mohamed SA, Yerly J et al (2021) Reduced-iodine-dose dual-energy coronary CT angiography: qualitative and quantitative comparison between virtual monochromatic and polychromatic CT images. *Eur Radiol*. 10.1007/s00330-021-07809-w
- 5 Bae K, Jeon KN, Cho SB et al (2018) Improved Opacification of a Suboptimally Enhanced Pulmonary Artery in Chest CT: Experience Using a Dual-Layer Detector Spectral CT. *AJR Am J Roentgenol* 210:734-741
- 6 Si-Mohamed S, Dupuis N, Tatard-Leitman V et al (2019) Virtual versus true non-contrast dual-energy CT imaging for the diagnosis of aortic intramural hematoma. *Eur Radiol* 29:6762-6771
- 7 Sandfort V, Persson M, Pourmorteza A, Noël PB, Fleischmann D, Willemink MJ (2020) Spectral photon-counting CT in cardiovascular imaging. *Journal of cardiovascular computed tomography*. 10.1016/j.jcct.2020.12.005
- 8 Taguchi K BI, Iniewski K (2020) Spectral, Photon Counting Computed Tomography: Technology and Applications. CRC Press

- 9 Taguchi K, Iwanczyk JS (2013) Vision 20/20: Single photon counting x-ray detectors in medical imaging. *Medical Physics* 40:100901
- 10 Si-Mohamed S, Bar-Ness D, Sigovan M et al (2017) Review of an initial experience with an experimental spectral photon-counting computed tomography system. *Nuclear Instruments and Methods in Physics Research Section A: Accelerators, Spectrometers, Detectors and Associated Equipment* 873:27-35
- 11 Samei E, Bakalyar D, Boedeker KL et al (2019) Performance evaluation of computed tomography systems: Summary of AAPM Task Group 233. *Med Phys* 46:e735-e756
- 12 Verdun FR, Racine D, Ott JG et al (2015) Image quality in CT: From physical measurements to model observers. *Phys Med* 31:823-843
- 13 *blinded*
- 14 *blinded*
- 15 Sharp P, Barber DC, Brown DG et al (2016) Report 54. *Journal of the International Commission on Radiation Units and Measurements* 52:NP-NP
- 16 Rotzinger DC, Racine D, Beigelman-Aubry C et al (2018) Task-Based Model Observer Assessment of A Partial Model-Based Iterative Reconstruction Algorithm in Thoracic Oncologic Multidetector CT. *Sci Rep* 8:17734
- 17 Johnson TR, Nikolaou K, Wintersperger BJ et al (2007) Optimization of contrast material administration for electrocardiogram-gated computed tomographic angiography of the chest. *J Comput Assist Tomogr* 31:265-271
- 18 Dwivedi G, Liu Y, Tewari S, Inacio J, Pelletier-Galarneau M, Chow BJ (2016) Incremental Prognostic Value of Quantified Vulnerable Plaque by Cardiac Computed Tomography: A Pilot Study. *J Thorac Imaging* 31:373-379
- 19 Saremi F, Achenbach S (2015) Coronary plaque characterization using CT. *AJR Am J Roentgenol* 204:W249-260

- 20 Schlett CL, Maurovich-Horvat P, Ferencik M et al (2013) Histogram analysis of lipid-core plaques in coronary computed tomographic angiography: ex vivo validation against histology. *Investigative radiology* 48:646-653
- 21 Clark DP, Holbrook M, Lee CL, Badea CT (2019) Photon-counting cine-cardiac CT in the mouse. *PLoS One* 14:e0218417
- 22 Si-Mohamed SA, Greffier J, Miaillhes J et al (2021) Comparison of image quality between spectral photon-counting CT and dual-layer CT for the evaluation of lung nodules: a phantom study. *Eur Radiol*. 10.1007/s00330-021-08103-5
- 23 Sandstedt M, Marsh J, Jr., Rajendran K et al (2021) Improved coronary calcification quantification using photon-counting-detector CT: an ex vivo study in cadaveric specimens. *Eur Radiol*. 10.1007/s00330-021-07780-6
- 24 Leng S, Gutjahr R, Ferrero A et al (2017) Ultra-High Spatial Resolution, Multi-Energy CT using Photon Counting Detector Technology. *Proc SPIE Int Soc Opt Eng* 10132
- 25 Lin E, Alessio A (2009) What are the basic concepts of temporal, contrast, and spatial resolution in cardiac CT? *Journal of cardiovascular computed tomography* 3:403-408
- 26 Puchner SB, Ferencik M, Maurovich-Horvat P et al (2015) Iterative image reconstruction algorithms in coronary CT angiography improve the detection of lipid-core plaque--a comparison with histology. *Eur Radiol* 25:15-23
- 27 Solomon J, Mileto A, Ramirez-Giraldo JC, Samei E (2015) Diagnostic Performance of an Advanced Modeled Iterative Reconstruction Algorithm for Low-Contrast Detectability with a Third-Generation Dual-Source Multidetector CT Scanner: Potential for Radiation Dose Reduction in a Multireader Study. *Radiology* 275:735-745
- 28 Budoff MJ, Dowe D, Jollis JG et al (2008) Diagnostic performance of 64-multidetector row coronary computed tomographic angiography for evaluation of coronary artery stenosis in individuals without known coronary artery disease: results from the

- prospective multicenter ACCURACY (Assessment by Coronary Computed Tomographic Angiography of Individuals Undergoing Invasive Coronary Angiography) trial. *J Am Coll Cardiol* 52:1724-1732
- 29 Do S, Karl WC, Liang Z, Kalra M, Brady TJ, Pien HH (2011) A decomposition-based CT reconstruction formulation for reducing blooming artifacts. *Physics in Medicine and Biology* 56:7109-7125
- 30 Gutjahr R, Halaweish AF, Yu Z et al (2016) Human Imaging With Photon Counting-Based Computed Tomography at Clinical Dose Levels: Contrast-to-Noise Ratio and Cadaver Studies. *Investigative radiology* 51:421-429
- 31 Bratke G, Hicketier T, Bar-Ness D et al (2020) Spectral Photon-Counting Computed Tomography for Coronary Stent Imaging: Evaluation of the Potential Clinical Impact for the Delineation of In-Stent Restenosis. *Investigative radiology* 55:61-67
- 32 Sigovan M, Si-Mohamed S, Bar-Ness D et al (2019) Feasibility of improving vascular imaging in the presence of metallic stents using spectral photon counting CT and K-edge imaging. *Sci Rep* 9:19850
- 33 Racine D, Becce F, Viry A et al (2020) Task-based characterization of a deep learning image reconstruction and comparison with filtered back-projection and a partial model-based iterative reconstruction in abdominal CT: A phantom study. *Phys Med* 76:28-37
- 34 Niu S, Zhang Y, Zhong Y et al (2018) Iterative reconstruction for photon-counting CT using prior image constrained total generalized variation. *Comput Biol Med* 103:167-182

Table and figure legends

Table 1

Detailed settings for data acquisition and image reconstruction for the investigated coronary CT angiography protocols on both CT systems.

Table 2

Noise magnitude reduction and NPS peak frequency shift in percentage differences for PCD-CT in comparison with EID-CT at the three investigated patient sizes.

Table 3

TTF frequency shifts (percentage differences) for PCD-CT compared with EID-CT at the three investigated patient sizes.

Figure 1. SPCCT system with phantom at isocenter. CCTA module made of PE is shown with empty cavity (blue star), to be filled with iodinated contrast material solution for the experiments. The anthropomorphic thorax phantom is shown with a fat-mimicking extension ring ("medium" patient size configuration). CCTA, coronary computed tomography angiography; PE, polyethylene; SPCCT, spectral photon-counting computed tomography.

Figure 2. NPS curves obtained on a clinical EID-CT (solid lines) and a preclinical PCD-CT (dashed lines) system at various phantom sizes. The area under the curve is representative of the noise magnitude, whereas the NPS center frequency indicates differences in noise texture. NPS, noise power spectrum; PCD-CT, photon-counting computed detector computed tomography; EID-CT, energy-integrating computed tomography.

Figure 3. TTF curves obtained on a clinical EID-CT (solid lines) and a preclinical PCD-CT (dashed lines) system at various phantom sizes. The area under the curve indicates spatial resolution performance. TTF, target transfer function; PCD-CT, photon-counting detector computed tomography; EID-CT, energy-integrating computed tomography.

Figure 4. Bar chart show detectability indexes (d') of non-calcified atherosclerotic plaque with an object-to-background contrast $|\Delta HU|$ of 450 HU and CTDI = 10 mGy. A d' of 2 corresponds to 90% accuracy (AUC). The SPCCT consistently provided higher detectability indexes than the conventional system. Note that at large phantom size, only the PCD-CT system could accurately detect (i.e., with a $d' \geq 2$ indicating an AUC of 90%) the smallest simulated plaque (0.5mm). CTDI, computed tomography dose index; PCD-CT, photon-counting detector computed tomography. CTDI, computed tomography dose index; PCD-CT, photon-counting detector computed tomography; EID-CT, energy-integrating computed tomography; AUC, area under the curve.

Figure 5. Bar chart shows detectability indexes (d') of lipid-rich atherosclerotic plaque with an object-to-background contrast $|\Delta HU|$ of 30 HU. A d' of 2 corresponds to 90% accuracy (AUC), plotted on the graphs as a black dashed line. The PCD-CT consistently provided higher detectability indexes than the conventional system. At the tested CTDI of 10 mGy, neither the EID nor the SPCCT reached 90% AUC to detect a 0.5mm lipid core. With the small phantom, the EID and SPCCT systems reached 90% AUC down to a lipid core size of 1.5 and 1 mm, respectively. AUC, area under the curve; CTDI, computed tomography dose index; EID, energy-integrating detector; PCD-CT, photon-counting detector computed tomography.

Figure 6. Visual appearance of the TTF phantom inserted in a small (a and b), medium (c and d), and large (e and f) anthropomorphic chest phantom. Conventional reconstructions obtained from acquisitions on the EID-CT (a, c, and e) and the PCD-CT (b, d, and f) systems. Zoomed views of the polyethylene/iodinated solution transition better depict the finer noise texture and sharper transition yielded by the PCD-CT. TTF, target transfer function; PCD-CT, photon-counting computed detector computed tomography; EID-CT, energy-integrating computed tomography.

Table 1

Detailed settings for data acquisition and image reconstruction for the investigated coronary CT angiography protocols on both CT systems.

CT system	EID-CT	PCD-CT
Radiation dose level		
CTDI _{vol} (mGy)	10	10
Data acquisition		
Tube potential (kVp)	120	120
Tube current (mA)	330	330
Gantry revolution time (s)	0.5	0.5
Beam collimation (mm)	32 × 0.672	64 × 0.2724
Scan mode	Axial	Axial
Image reconstruction		
Display field of view (mm)	200 × 200	200 × 200
Matrix size	512 × 512	512 × 512
Section thickness (mm)	0.6	0.6
Section increment (mm)	0.6	0.6
Kernel	High-res B	PCD-High-res B
Algorithm	Filtered back-projection	Filtered back-projection

CTDI_{vol} = volume CT dose index, EID = energy-integrating detector, PCD = photon-counting detector

Table 2

Noise magnitude reduction and NPS peak frequency shift in percentage differences for PCD-CT in comparison with EID-CT at the three investigated patient sizes.

Phantom size	Noise magnitude reduction (%)	Peak frequency shift (%)
Small	-9	47
Medium	-33	37
Large	-38	27

NPS, noise power spectrum; PCD-CT, photon-counting computed detector computed tomography; EID-CT, energy-integrating computed tomography.

Table 3

TTF frequency shifts (percentage differences) for PCD-CT compared with EID-CT at the three investigated patient sizes.

	TTF frequency shifts (%)	
Phantom size	TTF₅₀	TTF₁₀
Small	35	30
Medium	37	31
Large	38	33

TTF, target transfer function; PCD-CT, photon-counting computed detector computed tomography; EID-CT, energy-integrating computed tomography.



Figure 1

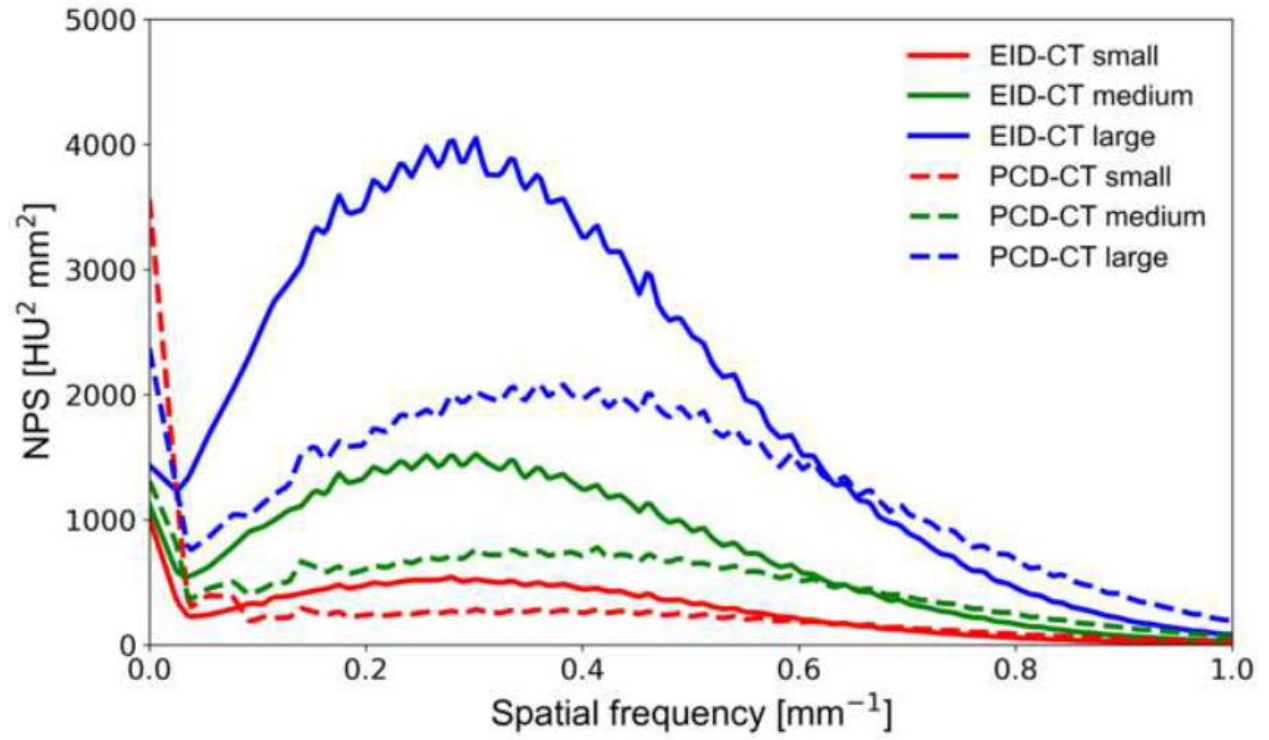


Figure 2

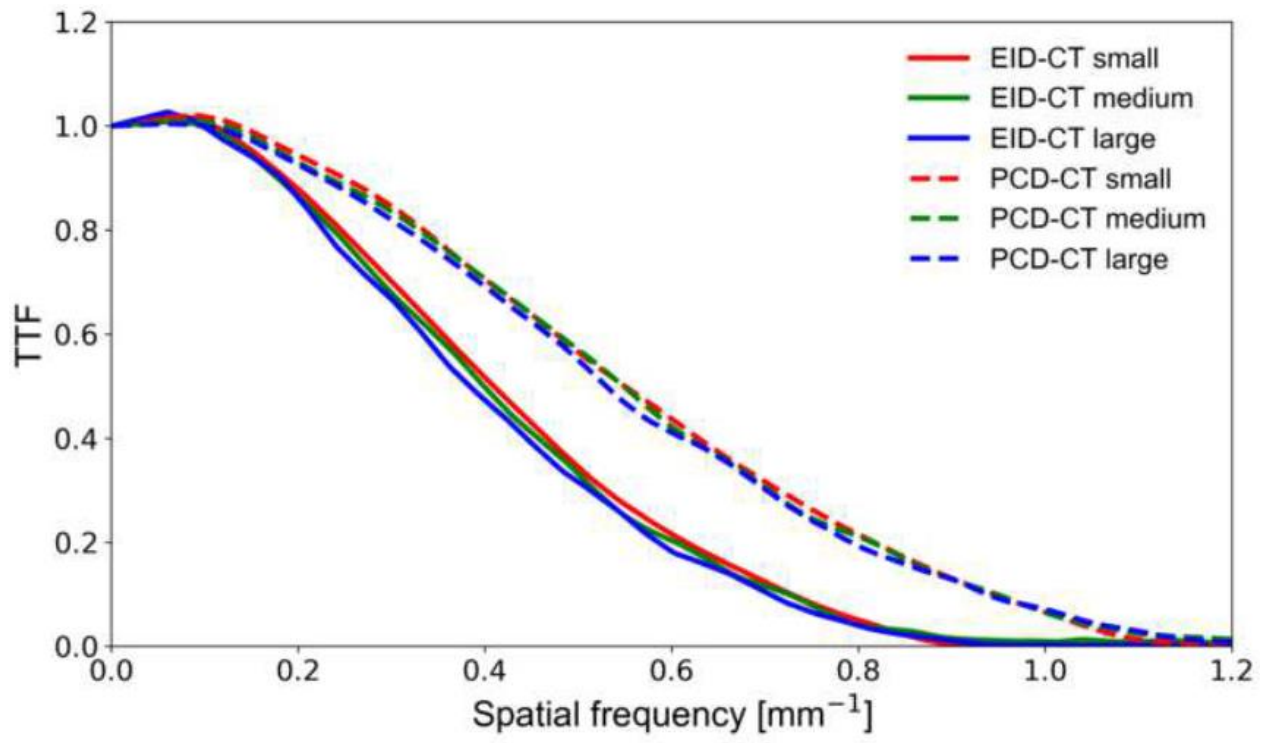


Figure 3

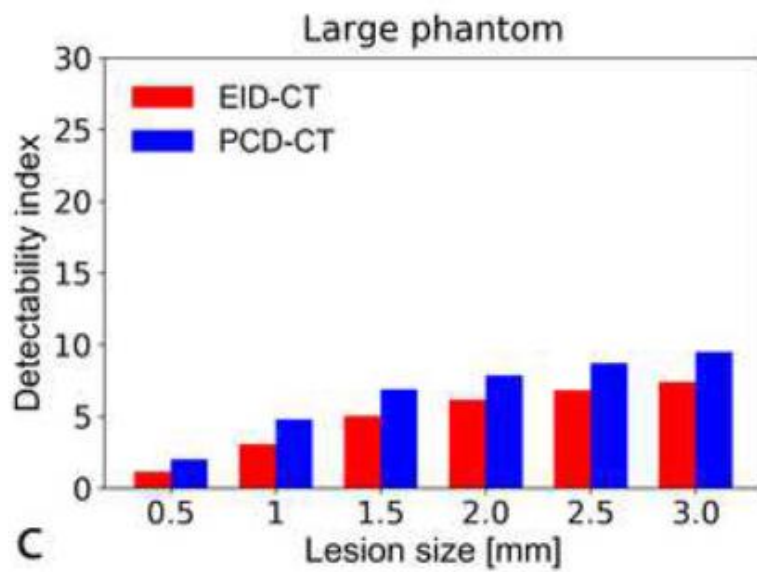
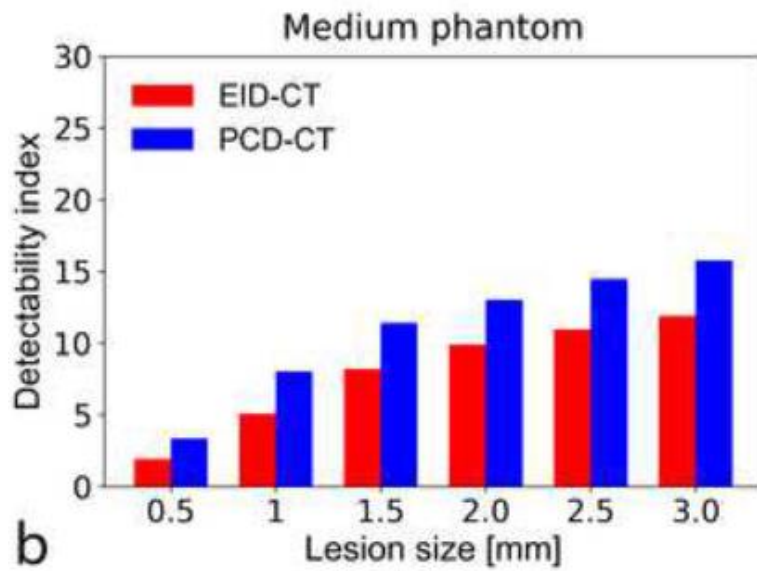
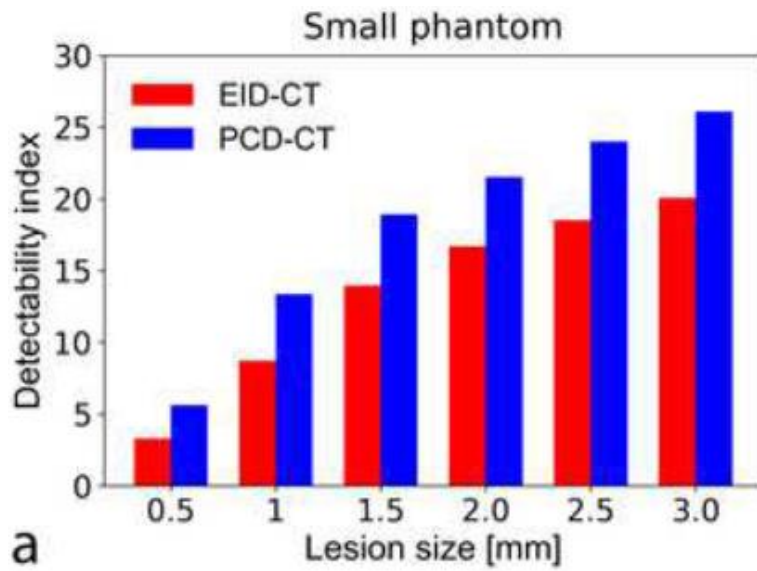


Figure 4

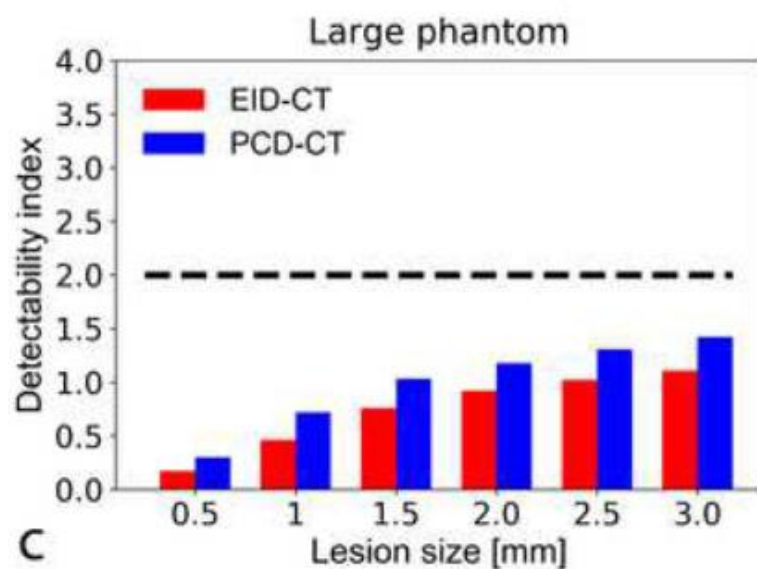
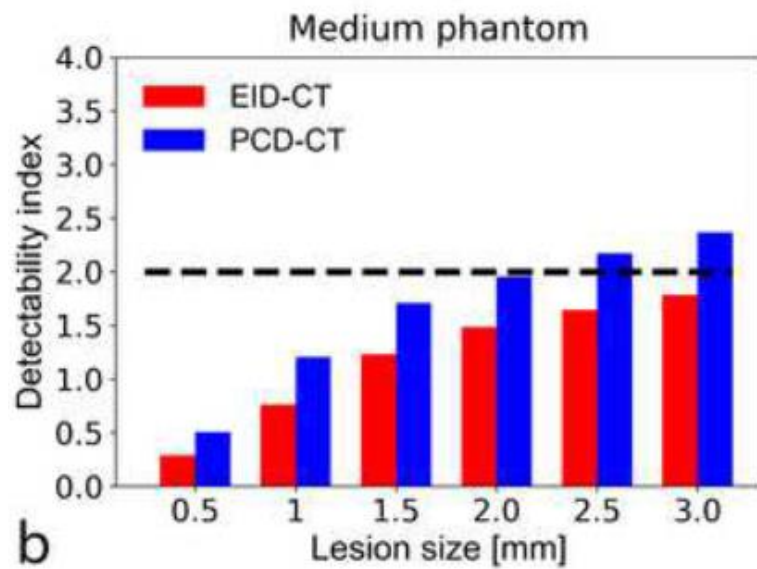
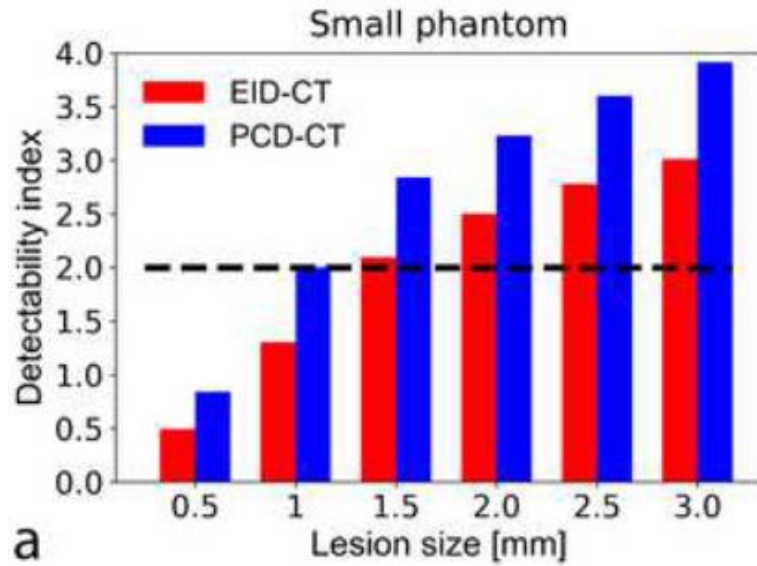


Figure 5

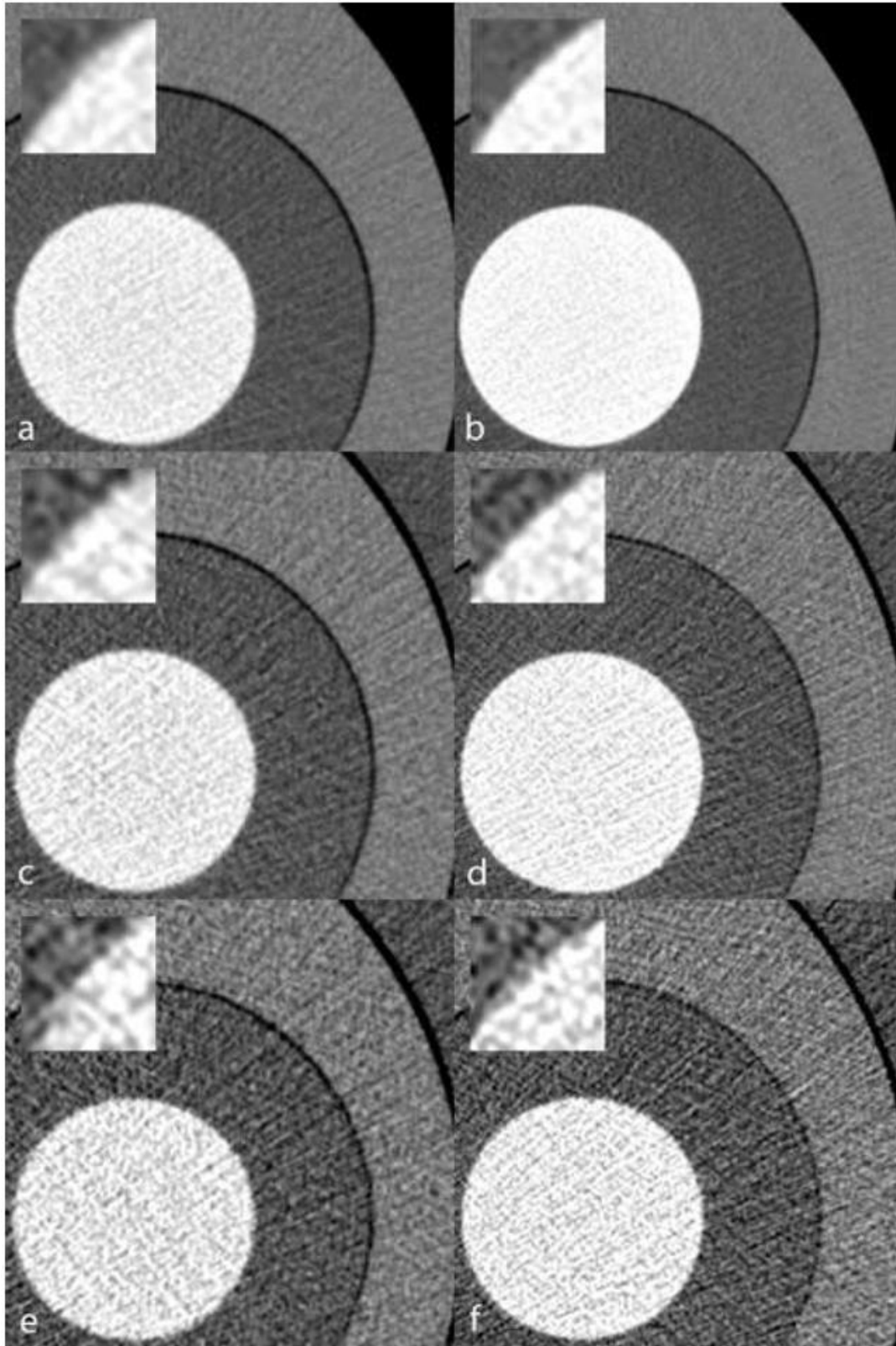


Figure 6

Compliance with ethical standards:**Guarantor:**

The scientific guarantor of this publication is Prof. Philippe C. Douek, MD, PhD.

Conflict of interest:

Yoad Yagil, Klaus Erhard, and Elias Lahoud declare relationships with the following companies:

Philips Healthcare.

Funding:

This work was supported by the European Union Horizon 2020 (grant no. 643694) and France Life Imaging (FLI).

Acknowledgements:

David C. Rotzinger is supported by a grant from the Leenaards Foundation.

Statistics and biometry:

No complex statistical methods were necessary for this paper.

Informed consent:

Not applicable.

Ethical approval:

Approval from the institutional animal care committee was not required because no living beings were involved in the experiments.

Methodology:

Comparative phantom study.

7. Excerpts from related publications leveraging spectral CT

7.1 Quantitative imaging with spectral CT helps understand COVID-19 [119]

We routinely use DECT to manage patients with COVID-19 pneumonia and are often puzzled by the severity of hypoxemia observed clinically and the limited extent of parenchymal lesions radiologically. In the article entitled “Intrapulmonary Arteriovenous Anastomoses in COVID-19-Related Pulmonary Vascular Changes: A New Player in the Arena?” [119], we show how contrast-enhanced DECT can be integrated into quantitative analysis and provide additional information regarding microvascular changes in COVID-19 pneumonia. In this case, inflammation-related microvascular hyper-perfusion was demonstrated with iodine-water material decomposition (iodine density map) and helped formulate hypotheses to explain the deep hypoxemic state sometimes observed in severe COVID-19. Specifically, DECT supported the theory of arteriovenous anastomosis activation as a contributory factor to hypoxemia; however, observations from a single case as published here have to be validated in an unselected patient cohort. This is what comes next with the Swiss COVID-CAVA registry described in section 7.2.



Case Report: Intrapulmonary Arteriovenous Anastomoses in COVID-19-Related Pulmonary Vascular Changes: A New Player in the Arena?

Salah D. Qanadli*, Ana Carolina Rocha and David C. Rotzinger*

Cardiothoracic and Vascular Division, Department of Diagnostic and Interventional Radiology, Lausanne University Hospital and University of Lausanne, Lausanne, Switzerland

OPEN ACCESS

Edited by:

Fabrizio Ricci,
University of Studies G. D'Annunzio
Chieti and Pescara, Italy

Reviewed by:

Jonathan E. Elliott,
Oregon Health and Science University,
United States
Cesare Mantini,
University of Studies G. d'Annunzio
Chieti and Pescara, Italy

*Correspondence:

David C. Rotzinger
david.rotzinger@chuv.ch
Salah D. Qanadli
salah.qanadli@chuv.ch

Specialty section:

This article was submitted to
Infectious Diseases - Surveillance,
Prevention and Treatment,
a section of the journal
Frontiers in Medicine

Received: 08 December 2020

Accepted: 06 January 2021

Published: 09 February 2021

Citation:

Qanadli SD, Rocha AC and
Rotzinger DC (2021) Case Report:
Intrapulmonary Arteriovenous
Anastomoses in COVID-19-Related
Pulmonary Vascular Changes: A New
Player in the Arena?
Front. Med. 8:639152.
doi: 10.3389/fmed.2021.639152

Up to now, COVID-19-related vascular changes were mainly described as thromboembolic events. A handful of researchers reported another type of vascular abnormality referred to as “vascular thickening” or “vascular enlargement,” without specifying whether the dilated vessels are arteries or veins nor providing a physiopathological hypothesis. Our observations indicate that the vascular dilatation occurs in the venous compartment, and underlying mechanisms might include increased blood flow due to inflammation and the activation of arteriovenous anastomoses.

Keywords: COVID-19, computed tomography, perfusion, pulmonary embolism, arteriovenous anastomoses, respiratory failure

INTRODUCTION

Early in the coronavirus disease 2019 (COVID-19) pandemic, a high prevalence of vascular disorders has been reported (1). Such abnormalities were mainly described in the lung and covered a broad spectrum of patterns revealed at histology—including microangiopathy, intussusceptive angiogenesis, and microthrombosis—and at imaging with vessel dilatation, tortuosity, thrombosis, and perfusion abnormalities. Up to now, no convincing theory has helped understand the relationship between virus-induced inflammatory disorders and biological and morphological changes, especially those observed on computed tomography (CT). Furthermore, the refractory hypoxemia observed in COVID-19 patients appears to be driven by more complex processes than alveolar damage with low gas exchange alone because COVID-19 leads to severe respiratory failure despite relatively well-preserved lung gas volume (2). This suggests the contribution of vascular phenomena beyond a simple ventilation–perfusion mismatch.

VASCULAR CHANGES IN COVID-19 PNEUMONIA

Imaging-based morphological vascular abnormalities in the lung described at CT may be categorized into three groups: thromboembolic events (3), vascular dilatation, also known as vascular “thickening” or “engorgement” (4, 5), and perfusional changes (6). Mechanisms leading to vascular remodeling remain unclear, and their prevalence and distribution are a matter of debate. We analyzed CT data from a patient who presented all the three groups of abnormalities

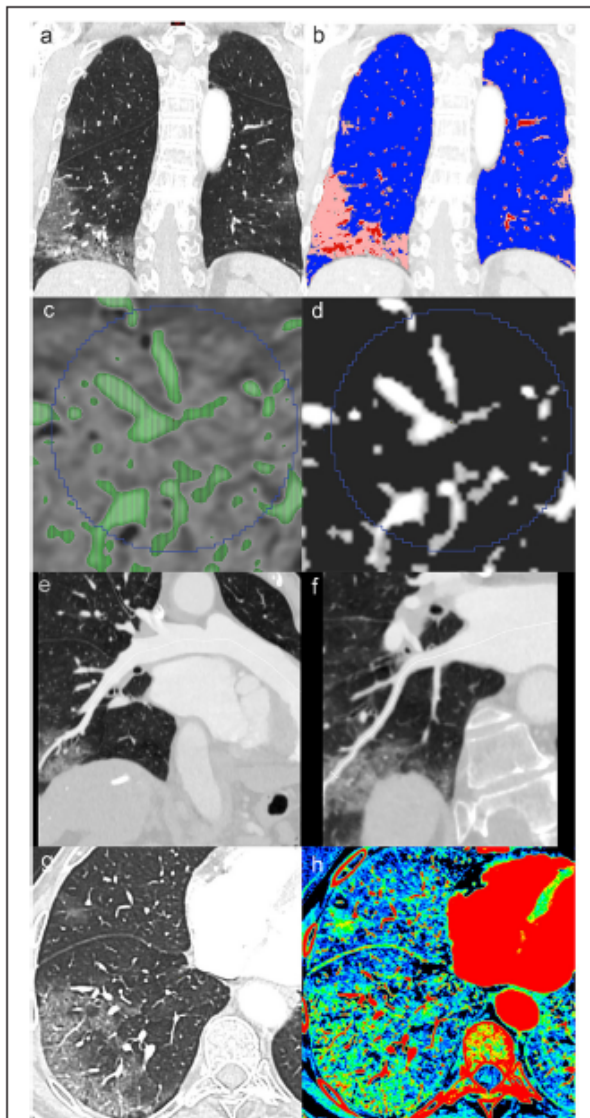


FIGURE 1 | Contrast-enhanced chest CT in a patient admitted for COVID-19. Coronal reformatted image (a) shows peripheral ground-glass opacity (GGO) predominantly involving the right lower lobe. Tissue classification (b) distinguishing alveolar opacity (peach color code) from normal parenchyma (blue) and vascular components (red) visually indicates vascular enlargement in COVID-19 pneumonia. Specific thresholds to isolate voxels, mostly containing vascular elements (c,d), enable vascular volume extraction in regions-of-interest. Center-line reconstructions of the right posterior basal artery and vein (e,f) allow diameter measurement in GGO. Axial conventional image in lung window (g) with peripheral COVID-19-related GGO and corresponding dual-energy CT iodine density map (h) show increased iodine distribution in GGO consistent with hyperperfusion.

simultaneously and thoroughly assessed vascular findings, trying to understand the different groups' relationships and elucidate the underlying mechanisms.

A man in his 70's with fever, tachypnea, bilateral basal crackling sounds, and reverse transcription-PCR (RT-PCR)-proven severe acute respiratory syndrome coronavirus 2 (SARS-CoV-2) infection underwent dual-energy CT pulmonary angiography to rule out pulmonary embolism. Arterial PaO₂ was 64 mmHg, and SpO₂ was 92% on room air. The examination was carried out on a fast kV-switching dual-energy CT platform (Revolution CT, GE Healthcare), with the following parameters: rotation speed, 0.5 s; tube load, 180 mAs; reconstructed slice thickness, 1.25 mm; and section interval, 1 mm. Using a power injector, 50 ml of iodinated contrast material (Accupaque 300®) was injected through an 18G venous catheter in the right antecubital fossa at a rate of 4 ml/s and followed by a saline chaser. Findings included zones of COVID-19 ground-glass opacity (GGO) surrounded by healthy parenchyma, enlarged blood vessels within GGO, and acute pulmonary embolism in a lung segment without GGO. We applied automatic tissue classification to distinguish alveolar opacity, normal parenchyma, and vascular components (Figures 1a,b). In a second step, we used a threshold-based automatic segmentation to extract the (macroscopic) intravascular blood volume in a region-of-interest (ROI) in both normal parenchyma and GGO (Figures 1c,d). Calculated intravascular blood volumes showed that in the areas presenting with typical parenchymal changes, the vascular volume was increased by 40% (5.27/300 and 9.0/300 cm³ vessel-to-tissue ratio in healthy and GGO zones, respectively). Of note, no venous thrombosis was seen. Furthermore, we demonstrate that the increased volume primarily depended on venous dilatation in the involved lung areas (Figures 1e,f). Arterial and venous diameters at a sub-segmental level in GGO were 3.6 and 4.9 mm, respectively, whereas in the healthy contralateral posterior basal segment, diameters were 3.0 and 3.1 mm, respectively. The corresponding artery-to-vein ratios are 0.97 (3.0/3.1) in healthy parenchyma and 0.73 (3.6/4.9) in GGO, and the vein-to-vein ratio (GGO vs. healthy segment) was 1.58 (4.9/3.1), indicating marked venous enlargement in COVID-19-related GGO. Note that the artery-to-artery ratio (GGO vs. healthy segment) was 1.2 (3.6/3), indicating a moderate arterial dilatation in GGO consistent with hyperemia.

DISCUSSION

Inflammation-mediated hyperemia is unlikely to be the only factor causing such a marked venous dilatation. We hypothesized that the upregulation of nitric oxide synthase, causing the activation of physiological arteriovenous anastomoses (7, 8) in the involved parenchyma, might explain venous engorgement; these anastomoses create a right-to-left shunt. The existence of pulmonary arteriovenous anastomoses has been suggested and studied by Tobin et al. since the 1950's, and their anatomical location was described as "at the apex of and within the lobular divisions of the lung" (9, 10). Available data suggest that such anastomoses can be activated passively by exercise or supine position, but also actively in the setting of vascular redistribution under both hyperoxia and hypoxia (11). In COVID-19 pneumonia, the consequence of combined

mechanisms is exacerbated hypoxia, giving a better explanation for the discrepancies between the relatively preserved ventilation mechanics, the severity of respiratory failure, and the limited response to invasive ventilation (2). Other injuries, such as endotheliitis (12) and/or distal microthrombosis (13), might potentialize the dysregulation of intrapulmonary arteriovenous anastomoses and the resulting shunting effect. In the case we discuss here, transthoracic saline echocardiography would have been a simple and effective means of evaluating the presence of intrapulmonary anastomoses and should have been performed if possible (14). Furthermore, recent evidence suggests that the recruitment of intrapulmonary arteriovenous anastomoses may be driven by the combination of increased cardiac output and increased pulmonary vascular pressure (8). Unfortunately, we could not provide a meaningful estimation of cardiac output based on the available data.

The observed phenomenon is consistent with previously described increased parenchymal perfusion in COVID-19 GGO with dual-energy CT (6). Likewise, our patient exhibited hyperperfusion in GGO zones on iodine density maps (Figures 1g,h). This distal hyperperfusion is attributed to hyperemia induced by the inflammation cascade in COVID-19 pneumonia.

It is also interesting to note that macro-thromboembolic changes (pulmonary embolism) were observed in a different territory than those with parenchymal involvement. This might be another consequence of the vascular shunting effect. This finding is also in agreement with a previous report (15).

In conclusion, our observations indicate that COVID-19-related macroscopic vascular changes depicted *in vivo* are not

exclusively due to thromboembolic events. The observed vascular remodeling is mainly related to venous dilatation and might result from combined inflammation-induced hyperemia and dysregulation of arteriovenous anastomoses. Although difficult to establish *in vivo*, vascular shunts could explain the worse than expected clinical course given a relatively modest parenchymal involvement and no visible local thromboembolism. Further studies aiming to characterize those abnormalities in a large series, particularly their distribution and correlation to clinical findings, are needed. The core message of this letter is to frame the hypothesis of intrapulmonary arteriovenous anastomoses as an influencing factor in patients with COVID-19 pneumonia, and the images presented in this case study serve for illustration purposes. An ongoing investigation, the Swiss National Registry COVID-CAVA, is expected to provide relevant insights to address those crucial questions better.

DATA AVAILABILITY STATEMENT

The original contributions presented in the study are included in the article/supplementary material, further inquiries can be directed to the corresponding author/s.

AUTHOR CONTRIBUTIONS

SQ performed the literature research and built the concept. DR prepared the figure. All authors were involved in drafting the manuscript and revising it critically.

REFERENCES





- Qanadli SD, Beigelman-Aubry C, Rotzinger DC. Vascular changes detected with thoracic CT in coronavirus disease (COVID-19) might be significant determinants for accurate diagnosis and optimal patient management. *AJR Am J Roentgenol.* (2020) 215:W15. doi: 10.2214/AJR.20.23185
- Gattinoni L, Coppola S, Cressoni M, Busana M, Rossi S, Chiumello D. COVID-19 does not lead to a "typical" acute respiratory distress syndrome. *Am J Respir Crit Care Med.* (2020) 201:1299–300. doi: 10.1164/rccm.202003-0817LE
- Klok FA, Kruip MJHA, van der Meer NJM, Arbous MS, Gommers D, Kant KM, et al. Confirmation of the high cumulative incidence of thrombotic complications in critically ill ICU patients with COVID-19: an updated analysis. *Thromb Res.* (2020) 191:148–50. doi: 10.1016/j.thromres.2020.04.041
- Bai HX, Hsieh B, Xiong Z, Halsey K, Whae Choi J, My Linh Tran T, et al. Performance of radiologists in differentiating COVID-19 from non-COVID-19 viral pneumonia at chest CT. *Radiology.* (2020) 296:E46–54. doi: 10.1148/radiol.20200823
- Qanadli SD, Rotzinger DC. Vascular abnormalities as part of chest CT findings in COVID-19. *Radiol Cardiothoracic Imaging.* (2020) 2:e200161. doi: 10.1148/ryct.20200161
- Si-Mohamed S, Chebib N, Sigovan M, Zumbihl L, Turquier S, Boccalini S, et al. *In vivo* demonstration of pulmonary microvascular involvement in COVID-19 using dual-energy computed tomography. *Eur Respir J.* (2020) 56:2020. doi: 10.1183/13993003.02608-2020
- Lovering AT, Riemer RK, Thébaud B. Intrapulmonary arteriovenous anastomoses. Physiological, pathophysiological, or both? *Ann Am Thorac Soc.* (2013) 10:504–8. doi: 10.1513/AnnalsATS.201308-265ED
- Elliott JE, Duke JW, Hawn JA, Halliwill JR, Lovering AT. Increased cardiac output, not pulmonary artery systolic pressure, increases intrapulmonary shunt in healthy humans breathing room air and 40% O₂. *J Physiol.* (2014) 592:4537–53. doi: 10.1113/jphysiol.2014.2754829
- Tobin CE. Arteriovenous shunts in the peripheral pulmonary circulation in the human lung. *Thorax.* (1966) 21:197–204. doi: 10.1136/thx.21.3.197
- Tobin CE, Zariquiey MO. Arteriovenous shunts in the human lung. *Proc Soc Exp Biol Med.* (1950) 75:827–9. doi: 10.3181/00379727-75-18360
- Lovering AT, Duke JW, Elliott JE. Intrapulmonary arteriovenous anastomoses in humans—response to exercise and the environment. *J Physiol.* (2015) 593:507–20. doi: 10.1113/jphysiol.2014.275495
- Ackermann M, Verleden SE, Kuehnel M, Haverich A, Welte T, Laenger F, et al. Pulmonary vascular endothelialitis, thrombosis, and angiogenesis in covid-19. *N Engl J Med.* (2020) 383:120–8. doi: 10.1056/NEJMoa2015432
- Fox SE, Akmatbekov A, Harbert JL, Li G, Quincy Brown J, Vander Heide RS, et al. Pulmonary and cardiac pathology in African American patients with COVID-19: an autopsy series from New Orleans. *Lancet Respir Med.* (2020) 8:681–6. doi: 10.1016/S2213-2600(20)30243-5
- Lovering A, Goodman R. *Detection of Intracardiac and Intrapulmonary Shunts at Rest and During Exercise Using Saline Contrast Echocardiography.* London, UK: IntertechOpen (2012). Available online at: <https://www.intechopen.com/books/applied-aspects-of-ultrasonography-in-humans/detection-of-intracardiac-and-intrapulmonary-shunts-at-rest-and-during-exercise-and-stress-using-ech>
- Patel BV, Arachchilage DJ, Ridge CA, Bianchi P, Doyle JE, Garfield B, et al. Pulmonary angiopathy in severe COVID-19:

7.2 Application of spectral CT in COVID-19-related vascular involvement [120]

Several small case studies indicated that DECT could provide value for understanding the pathophysiological mechanisms underlying COVID-19 pneumonia that cause morphological changes and hypoxemic states which do not match parenchymal changes properly. Soon after the COVID-19 outbreak, it became clear that vascular involvement plays a central role in severe disease and outcome [121, 122]. A thorough analysis of potential links between severe COVID-19 disease, vascular remodeling, and perfusion changes as assessed with contrast-enhanced DECT is needed to deliver the right treatments. This led us to design the Swiss national COVID-CAVA registry involving all 5 University Hospitals, which expects to extract several morphological variables to understand cardiovascular involvement. Most importantly, patients who underwent contrast-enhanced DECT can be subjected to a thorough analysis of the lung parenchyma, including semi-quantitative perfusion. DECT provides iodine distribution data that can be gathered from iodine basis images (iodine versus water material decomposition) or Z_{eff} maps. Both hyper and hypoperfusion states have been described in COVID-19 pneumonia [123, 124] but no study provides an integrative approach taking into account vascular remodeling, perfusion abnormalities, and clinical severity. This is a gap to be filled with the help of spectral CT.

Study Protocol

Vascular Abnormalities Detected with Chest CT in COVID-19: Spectrum, Association with Parenchymal Lesions, Cardiac Changes, and Correlation with Clinical Severity (COVID-CAVA Study)

Salah D. Qanadli ¹, Alexander W. Sauter ², Hatem Alkadhi ³, Andreas Christe ⁴, Pierre-Alexandre Poletti ⁵, Lukas Ebner ⁶ and David C. Rotzinger ^{1,*}



Citation: Qanadli, S.D.; Sauter, A.W.; Alkadhi, H.; Christe, A.; Poletti, P.-A.; Ebner, L.; Rotzinger, D.C. Vascular Abnormalities Detected with Chest CT in COVID-19: Spectrum, Association with Parenchymal Lesions, Cardiac Changes, and Correlation with Clinical Severity (COVID-CAVA Study). *Diagnostics* **2021**, *11*, 606. <https://doi.org/10.3390/diagnostics11040606>

Academic Editor: Giorgio Treglia

Received: 19 March 2021

Accepted: 26 March 2021

Published: 29 March 2021

Publisher's Note: MDPI stays neutral with regard to jurisdictional claims in published maps and institutional affiliations.



Copyright © 2021 by the authors. Licensee MDPI, Basel, Switzerland. This article is an open access article distributed under the terms and conditions of the Creative Commons Attribution (CC BY) license (<https://creativecommons.org/licenses/by/4.0/>).

- ¹ Department of Diagnostic and Interventional Radiology, Lausanne University Hospital and University of Lausanne, Rue du Bugnon 46, 1011 Lausanne, Switzerland; salah.qanadli@chuv.ch
 - ² Department of Radiology, University Hospital Basel, University of Basel, 4031 Basel, Switzerland; alexander.sauter@usb.ch
 - ³ Institute of Diagnostic and Interventional Radiology, University Hospital Zurich, University of Zurich, 8006 Zurich, Switzerland; Hatem.Alkadhi@usz.ch
 - ⁴ Department of Radiology, Division City and County Hospitals, Inselgroup, Bern University Hospital, University of Bern, 3004 Bern, Switzerland; Andreas.Christe@insel.ch
 - ⁵ Emergency Radiology Unit, Service of Radiology Division of Clinical Epidemiology Service of Radiology, Geneva University Hospital, 1205 Geneva, Switzerland; Pierre-Alexandre.Poletti@hcuge.ch
 - ⁶ Department of Diagnostic, Interventional and Pediatric Radiology, Inselspital, Bern University Hospital, University of Bern, 3010 Bern, Switzerland; Lukas.Ebner@insel.ch
- * Correspondence: david.rotzinger@chuv.ch

Abstract Although vascular abnormalities are thought to affect coronavirus disease 2019 (COVID-19) patients' outcomes, they have not been thoroughly characterized in large series of unselected patients. The Swiss national registry coronavirus-associated vascular abnormalities (CAVA) is a multicentric cohort of patients with severe acute respiratory syndrome coronavirus 2 (SARS-CoV-2) infection who underwent a clinically indicated chest computed tomography (CT) aiming to assess the prevalence, severity, distribution, and prognostic value of vascular and non-vascular-related CT findings. Clinical outcomes, stratified as outpatient treatment, inpatient without mechanical ventilation, inpatient with mechanical ventilation, or death, will be correlated with CT and biological markers. The main objective is to assess the prevalence of cardiovascular abnormalities—including pulmonary embolism (PE), cardiac morphology, and vascular congestion. Secondary objectives include the predictive value of cardiovascular abnormalities in terms of disease severity and fatal outcome and the association of lung inflammation with vascular abnormalities at the segmental level. New quantitative approaches derived from CT imaging are developed and evaluated in this study. Patients with and without vascular abnormalities will be compared, which is supposed to provide insights into the prognostic role and potential impact of such signs on treatment strategy. Results are expected to enable the development of an integrative score combining both clinical data and imaging findings to predict outcomes.

Keywords: COVID-19; computed tomography; perfusion; pulmonary embolism; vascular congestion; respiratory failure

1. Introduction

A subset of patients infected with severe acute respiratory syndrome coronavirus 2 (SARS-CoV-2) will develop pneumonia and severe disease [1,2], challenging healthcare providers because the physiopathological mechanisms are unsatisfactorily understood. Hypoxemia leading to mechanical ventilation may be the consequence of several factors, of

which thromboembolism is emerging as a key component since blood hypercoagulability is common among hospitalized patients with coronavirus disease 2019 (COVID-19) [3–7].

Since the SARS-CoV-2 outbreak, computed tomography (CT) imaging has almost immediately established itself as the primary non-invasive test for diagnosis, monitoring of COVID-19 pneumonia, and complications thereof, including deep-learning-based analysis [8–14].

While most of the currently available literature relies on non-contrast CT [10,15], the need to assess vascular abnormalities is being recognized as an increasingly important factor [16–19], both to help distinguish COVID-19 pneumonia from other viral infections and to exclude pulmonary embolism (PE). Acute PE is believed to be a significant contributory factor in patients with adverse outcomes [3,6,7,20], and anticoagulation therapy was found to reduce mortality in severe COVID-19 disease [21].

Although vascular involvement is thought to aggravate COVID-19 morbidity and mortality, there are still unresolved issues regarding the nature and impact of cardiovascular abnormalities. Furthermore, no convincing theory helps understand the interaction between virus-induced inflammatory disorders and morphologic changes, especially those observed on CT. In addition, the severity of hypoxemia in COVID-19 patients seems to be related to more complex mechanisms than morphologic damages observed in CT [22].

The prevalence of PE in unselected patients is still debated regarding thromboembolic complications. Clot burden/distribution (anatomic distribution, relationship to ground-glass opacity, and clinical severity) is yet to define. Moreover, the association between PE and important clinical variables lack, including time from onset, severity, age of patients, risk factors for venous thromboembolic disease (VTE), and anticoagulation prophylaxis regimen.

Recently vascular changes other than PE have drawn attention [23]. Additional knowledge is, however, required and not yet available to confirm and better understand early observations. In particular, a radiological sign referred to as “vascular thickening”, “vascular enlargement”, or “vascular congestion” (VC) that is thought to be a specific marker of COVID-19 pneumonia calls for a thorough assessment. Quantitative analysis of this sign and correlation to clinical presentation is highly desirable and may help understand its pathophysiology [24].

Most valuable information to address these open issues will likely come from severely ill patients and those who die since a recent autopsy study reports thromboembolism in 50% of people who died from COVID-19, emphasizing the critical role of PE in adverse outcomes [25].

Consequently, we probably underestimate the role of vascular changes and complications induced directly or indirectly by the coronavirus. Seeking a better understanding of the disease is undoubtedly a step toward better managing COVID-19 and its cardiovascular complications.

2. Methods and Analysis

2.1. Study Design

This study aims to explore COVID-19 features on CT with specific regard to vascular changes.

The data and the conclusions of this study could enhance the clinical care, risk stratification, and, ultimately, clinical outcomes of patients affected with severe COVID-19.

Specifically, this multicenter observational study is designed to comprehensively picture the spectrum of vascular findings related to COVID-19 pneumonia and find correlations with outcomes.

To this end, we will analyze lung parenchymal findings in patients with COVID-19 infection, including their relationship to vascular changes. Vascular abnormalities will be subdivided into PE and non-PE-related lesions. Qualitative interpretation by expert cardiothoracic radiologists and state-of-the-art quantitative analyses will be conducted, including computer-based assessment.

2.1.1. Primary Objective

The study aims to describe the prevalence of vascular abnormalities in COVID-19 pneumonia, especially PE.

2.1.2. Secondary Objectives

Secondary objectives include the frequency of various other factors (as described hereafter) and their potential impact on outcome or treatment.

We will measure the frequency of specific vascular abnormalities related or not to PE and compare their prevalence.

2.2. Patient Selection

Patients will be recruited in six Swiss university-affiliated institutions from five cantons (Basel, Bern, Geneva, Vaud, Zurich). For this purpose, each center needs to screen hundreds of COVID-19 patients to select those who meet the inclusion criteria and do not have any exclusion criteria.

2.2.1. Inclusion Criteria

Patients admitted for COVID-19 (with positive reverse transcription polymerase chain reaction for SARS-CoV-2) who had a chest CT within the specified timeframe.

2.2.2. Exclusion Criteria

Age less than 18 years, patients with another pre-existing infectious process, non-optimal CT scan or incomplete CT data, documented refusal of the reuse of medical data.

2.2.3. Sample Size Calculation

The sample size estimate is based on the primary objective of the study. We assume that PE-positive patients have clots in two lung segments on average; the sample size is designed for 80% power and a type-one error rate of 5% [26]. Under the hypothesis that macroscopic PE is related to a systemic hypercoagulability status and does not result from in situ thrombosis due to alveolar inflammation, the probability of an embolus to be located in a segment with vs. without alveolar opacity should be roughly 50-50. To reject this hypothesis and determine a statistically significantly higher incidence of PE in lung segments with alveolar inflammation (20% increase, from 50% to 70%), we need to analyze 182 lung segments with PE. In other words, we need to enroll 91 patients with PE; since the literature reports a PE incidence of 20% in COVID-19 pneumonia [27], we need to enroll at least 500 patients with COVID-19 taking into account a safety margin for excluded patients and those who have declined to participate. By recruiting patients in the most prominent centers in Switzerland, we may reach 1000 patients with COVID-19 pneumonia, of which around 20% will also have PE.

3. Methodology and Data Analysis

We will retrieve clinical, laboratory, and imaging data of eligible patients. Demographic data, including age and sex composition, will be analyzed. Intra-hospital medical records, laboratory test results, and data from chest CT performed in the participating centers will be collected in a Research Electronic Data Capture (REDCap)-based multicenter registry. The study flowchart is reported in Figure 1.

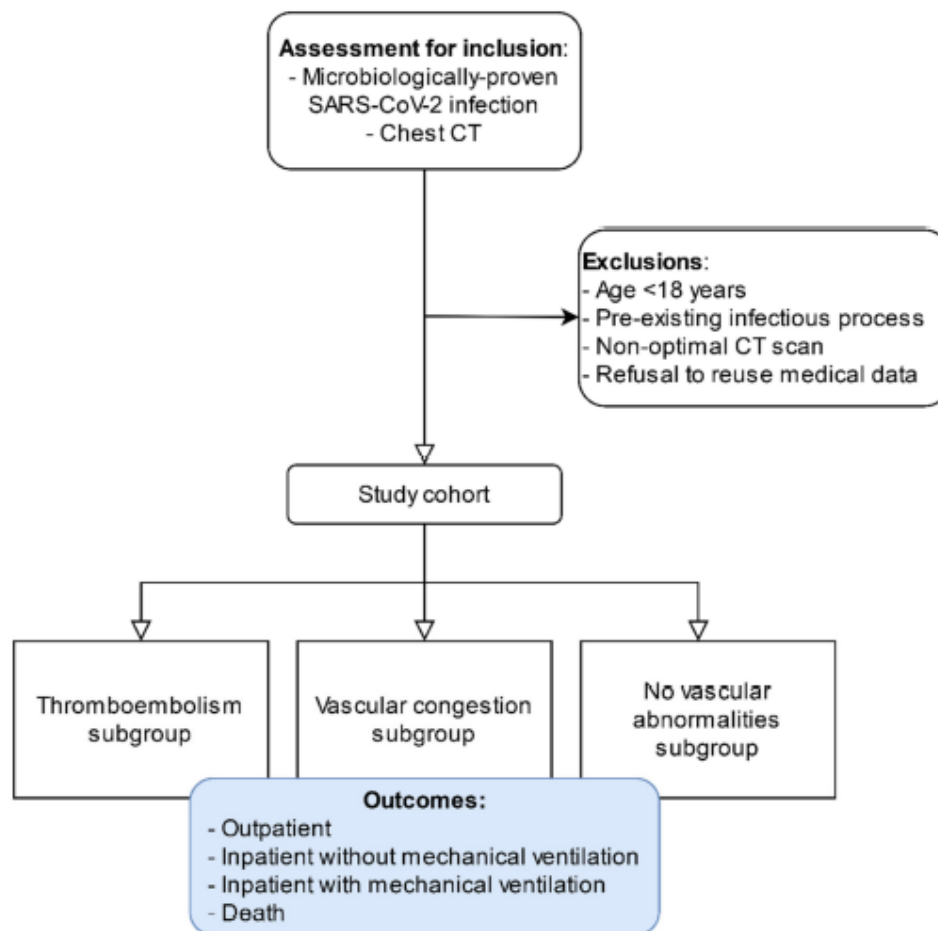


Figure 1. Study flowchart.

3.1. CT Analysis

CT Scans Are Analyzed to Identify:

- PE related abnormalities: the presence of embolic material, anatomic distribution based on segmental arteries, parenchymal changes and their distribution (PE present in the region of interest subject of parenchymal changes induced by the coronavirus), presence of perfusion defect—using iodine vs. water material decomposition if dual-energy CT was performed—assessment of right ventricle, left atrium, and pulmonary artery dimensions (diameters), and quantification of vascular obstruction using the Qanadli obstruction index (QOI) [28,29] and a modified Qanadli obstruction index (mQOI) based on the segmental analysis as follows:

$$mQOI = (\sum SQOI + \sum LQOI + \sum TQOI) / 120$$

where

S: segmental QOI calculated for each segmental artery

L: lobar QOI calculated for each lobar artery

T: troncular QOI calculated for each pulmonary artery

- Non-PE-related vascular abnormalities consist of visual assessment of VC (arterial and venous), manually drawn regions-of-interest in normal and abnormal parenchyma,

quantification of vascular volumes and tissue volumes, quantification of venous dilatation, and arterial enlargement.

- Non-vascular abnormalities include ground-glass opacities, consolidation, cysts, nodules, and pleural changes. Semi-quantitative assessment of SARS-CoV-2-related opacities is provided per segment: alveolar opacities (none, <50%, >50%) and per patient. A new relative volume-based index is calculated as follows:

$$\frac{\sum VROI}{\sum VL}$$

where

V: volume

ROI: region of interest with parenchymal changes

L: pulmonary lobe

Finally, predictive modeling will be performed to derive an integrative score accounting for both clinical variables and imaging findings to classify the disease severity better and predict patient outcomes.

3.2. Data Management

All data will be coded and gathered using REDCap, a Human Research Act (HRA)-compliant electronic data collection platform [30]. REDCap is a secure, web-based platform providing data collection and management in research.

3.3. Statistical Analysis

For statistical analysis, we will conduct correlation analysis with Spearman’s rank test, group comparison of qualitative data with Wilcoxon signed-rank test, group comparison of quantitative data with Pearson’s Chi-square test. The inter-observer agreement will be measured by Cohen’s Kappa test for ordinal data and with the intra-class correlation coefficient for continuous data. Outcome modeling will be performed using logistic regression analysis.

Collected data and variables under evaluation are summarized in Tables 1 and 2. Depending on the evolution of this worldwide pandemic and increasing knowledge concerning new drugs to manage COVID-19 pneumonia, e.g., tamoxifen [31], an amendment might be submitted to the Ethics Committee to analyze additional variables.

Table 1. Clinical and laboratory data to be collected.

Variable	Data	Variable Type
Disease severity	Outpatient, inpatient, death	Qualitative
Composite outcome	ICU admission or death	Dichotomic
Cardiovascular comorbidities	Hypertension Atrial fibrillation Coronary artery disease Heart failure Peripheral vascular disease Stroke Chronic kidney disease Hemodialysis Diabetes COPD Asthma Cystic fibrosis	

Table 1. Cont.

Onset to CT delay	Number of days	Ordinal
Onset to recovery delay	Number of days	Ordinal
Thromboprophylaxis or anticoagulants	Qualitative	Dichotomic
D-dimers	Plasma concentration	Continuous
PaO2	Arterial blood partial pressure	Continuous
SaO2	Venous blood O2 saturation	Continuous
C-reactive protein	Plasma concentration	Continuous
Thrombocytes	Count per microliter	Integer

Table 2. Imaging variables under test.

Variable	Data	Variable Type	Segment	Lung	Patient
Left atrium size	2 axes, continuous	Continuous			x
Right ventricle (RV)	Small axis	Continuous			x
Left ventricle (LV)	Small axis	Continuous			x
Pulmonary artery (PA)	Diameter	Continuous			x
Vascular congestion (VC)	Qualitative	Dichotomic	x	x	x
Vascular volume (VV)	Volumetric	Continuous		x	x
Perfusion (PF)	Qualitative, iodine density map	Ordinal (decreased, normal, increased)		x	x
Venous-to-artery ratio (VRR)	Diameter ratio	Continuous	x	x	x
Pulmonary embolism (PE)	Qualitative	Dichotomic	x	x	x
Qanadli obstruction index (QOI)	Percentage	Ordinal (0–100% in 2.5% steps)	x	x	x
Modified QOI (mQOI)	Percentage	Ordinal (0–100% in 2.5% steps)	x	x	x
Ground glasses opacities (GGO)	Qualitative	Dichotomic	x	x	x
Alveolar consolidation	Qualitative	Dichotomic	x	x	x
Cyst	Qualitative	Dichotomic	x	x	x
Nodule	Qualitative	Dichotomic	x	x	x
Lung tissue volume (TV)	Volumetric	Continuous		x	x

4. Discussion and Clinical Relevance

While most of the currently available literature relies on non-contrast CT, the need to assess vascular abnormalities is being recognized as an increasingly important factor, both to help distinguish COVID-19 pneumonia from other viral infections and to exclude pulmonary embolism (PE). Acute PE is believed to be a significant contributory factor in patients with adverse outcomes.

The nature of blood clots (arterial thrombosis versus arterial embolism) in the context of COVID-19 is currently debated [32]. Because of this, one of the most critical analyses we will conduct is to assess whether pulmonary blood clots are systematically associated with signs of pneumonia (in the same lung segment) and shed light on the mechanisms underlying vascular changes. Moreover, the association between unfavorable outcomes and alveolar opacities and/or PE will be an essential result for a better insight into the disease course.

Arterial thrombosis in COVID-19 may be due to inflammatory cytokines (suggestive of PE), endothelial dysfunction, or hypoxia (suggestive of local thrombosis). Likewise, VC can be linked to hyperemia in the context of lung inflammation or other factors such as in situ venous thrombosis or vasodilatation triggered by cytokines. A better understanding of these processes would support decision-making, specifically regarding the use and dosing of anticoagulation therapy in severe COVID-19.

Several factors might potentially limit this study. First, some relevant biological markers of cytokine storm, such as interleukin 6 (IL-6), are not routinely collected in all centers and are not expected to be available for analysis. Second, a common pitfall is linked to the enrollment process; since this study only considers patients with microbiologically

proven SARS-CoV-2 infection for inclusion, a potentially significant proportion of patients will remain undetected and excluded from the analysis. However, since the endpoints are mainly related to patients with serious or severe disease, the impact should be limited. Finally, should the data fail to offer a predictive value concerning patient outcomes, we may need to review the data and elucidate if potential confounders influence the main effect.

5. Ethics and Dissemination

The study protocol was submitted through the Swiss Business Administration System for Ethics Committee (BASEC) and approved by the independent Cantonal ethics committees in charge. All procedures will be conducted by the leading institution (Lausanne University Hospital) and participating institutions (Bern, Zurich, Basel, and Geneva University Hospitals) under the Federal Act on Research involving Human Beings (Human Research Act, HRA). The study will be conducted in compliance with the protocol, the current version of the Declaration of Helsinki, the International Conference on Harmonization Good Clinical Practices (ICH-GCP), and other locally relevant legal and regulatory requirements. Baseline patients characteristics, primary and secondary outcomes will be published in scientific peer-reviewed journals.

Author Contributions: Conceptualization, S.D.Q. and D.C.R.; methodology, S.D.Q. and D.C.R.; writing—original draft preparation, S.D.Q. and D.C.R.; writing—review and editing, all authors; critical review of manuscript, all authors; supervision, S.D.Q.; project administration, S.D.Q.; patient recruitment, all authors. All authors have read and agreed to the published version of the manuscript.

Funding: This research received no external funding.

Institutional Review Board Statement: The study was conducted according to the guidelines of the Declaration of Helsinki, and approved by the Swiss Association of Research Ethics Committees (protocol code 2020-01469, date of approval 24 November 2020).

Informed Consent Statement: Patient consent was waived due to the observational nature of the study.

Data Availability Statement: The datasets generated and/or analysed during this study are will be available from the corresponding authors on reasonable request.

Acknowledgments: David C. Rotzinger is supported by a grant from the Leenaards Foundation.

Conflicts of Interest: The authors declare that they have no known competing financial interests or personal relationships that may influence the procedures or conclusions of this work.

References

1. Chen, N.; Zhou, M.; Dong, X.; Qu, J.; Gong, F.; Han, Y.; Qiu, Y.; Wang, J.; Liu, Y.; Wei, Y.; et al. Epidemiological and clinical characteristics of 99 cases of 2019 novel coronavirus pneumonia in Wuhan, China: A descriptive study. *Lancet* **2020**, *395*, 507–513. [[CrossRef](#)]
2. Grasselli, G.; Zangrillo, A.; Zanella, A.; Antonelli, M.; Cabrini, L.; Castelli, A.; Cereda, D.; Coluccello, A.; Foti, G.; Fumagalli, R.; et al. Baseline Characteristics and Outcomes of 1591 Patients Infected with SARS-CoV-2 Admitted to ICUs of the Lombardy Region, Italy. *JAMA* **2020**, *323*, 1574–1581. [[CrossRef](#)] [[PubMed](#)]
3. Cui, S.; Chen, S.; Li, X.; Liu, S.; Wang, F. Prevalence of venous thromboembolism in patients with severe novel coronavirus pneumonia. *J. Thromb. Haemost.* **2020**, *18*, 1421–1424. [[CrossRef](#)] [[PubMed](#)]
4. Escher, R.; Breakey, N.; Lämmle, B. Severe COVID-19 infection associated with endothelial activation. *Thromb. Res.* **2020**, *190*, 62. [[CrossRef](#)] [[PubMed](#)]
5. Klok, F.A.; Kruip, M.; van der Meer, N.J.M.; Arbous, M.S.; Gommers, D.; Kant, K.M.; Kaptein, E.H.J.; van Paassen, J.; Stals, M.A.M.; Huisman, M.V.; et al. Incidence of thrombotic complications in critically ill ICU patients with COVID-19. *Thromb. Res.* **2020**, *191*, 145–147. [[CrossRef](#)] [[PubMed](#)]
6. Poor, H.D.; Ventetuolo, C.E.; Tolbert, T.; Chun, G.; Serrao, G.; Zeidman, A.; Dangayach, N.S.; Olin, J.; Kohli-Seth, R.; Powell, C.A. COVID-19 critical illness pathophysiology driven by diffuse pulmonary thrombi and pulmonary endothelial dysfunction responsive to thrombolysis. *Clin. Transl. Med.* **2020**, *10*, e44. [[CrossRef](#)]
7. Zhang, L.; Yan, X.; Fan, Q.; Liu, H.; Liu, X.; Liu, Z.; Zhang, Z. D-dimer levels on admission to predict in-hospital mortality in patients with Covid-19. *J. Thromb. Haemost.* **2020**, *18*, 1324–1329. [[CrossRef](#)]

8. Cheng, Z.; Lu, Y.; Cao, Q.; Qin, L.; Pan, Z.; Yan, F.; Yang, W. Clinical Features and Chest CT Manifestations of Coronavirus Disease 2019 (COVID-19) in a Single-Center Study in Shanghai, China. *AJR Am. J. Roentgenol.* **2020**, *215*, 121–126. [CrossRef]
9. Müller, N.L.; Ooi, G.C.; Khong, P.L.; Nicolaou, S. Severe acute respiratory syndrome: Radiographic and CT findings. *AJR Am. J. Roentgenol.* **2003**, *181*, 3–8. [CrossRef]
10. Rubin, G.D.; Ryerson, C.J.; Haramati, L.B.; Sverzellati, N.; Kanne, J.P.; Raouf, S.; Schluger, N.W.; Volpi, A.; Yim, J.J.; Martin, I.B.K.; et al. The Role of Chest Imaging in Patient Management during the COVID-19 Pandemic: A Multinational Consensus Statement from the Fleischner Society. *Chest* **2020**, *158*, 106–116. [CrossRef]
11. Wang, Y.; Dong, C.; Hu, Y.; Li, C.; Ren, Q.; Zhang, X.; Shi, H.; Zhou, M. Temporal Changes of CT Findings in 90 Patients with COVID-19 Pneumonia: A Longitudinal Study. *Radiology* **2020**, *296*, E55–E64. [CrossRef]
12. Zhou, S.; Wang, Y.; Zhu, T.; Xia, L. CT Features of Coronavirus Disease 2019 (COVID-19) Pneumonia in 62 Patients in Wuhan, China. *AJR Am. J. Roentgenol.* **2020**, *214*, 1287–1294. [CrossRef]
13. Zhu, Y.; Liu, Y.-L.; Li, Z.-P.; Kuang, J.-Y.; Li, X.-M.; Yang, Y.-Y.; Feng, S.-T. Clinical and CT imaging features of 2019 novel coronavirus disease (COVID-19). *J. Infect.* **2020**. [CrossRef] [PubMed]
14. Mergen, V.; Kobe, A.; Blüthgen, C.; Euler, A.; Flohr, T.; Frauenfelder, T.; Alkadhi, H.; Eberhard, M. Deep learning for automatic quantification of lung abnormalities in COVID-19 patients: First experience and correlation with clinical parameters. *Eur. J. Radiol. Open* **2020**, *7*, 100272. [CrossRef] [PubMed]
15. ACoR. ACR Recommendations for the use of Chest Radiography and Computed Tomography (CT) for Suspected COVID-19 Infection. 2020. Available online: <https://www.acr.org/Advocacy-and-Economics/ACR-Position-Statements/Recommendations-for-Chest-Radiography-and-CT-for-Suspected-COVID19-Infection> (accessed on 29 April 2020).
16. Grillet, F.; Behr, J.; Calame, P.; Aubry, S.; Delabrousse, E. Acute Pulmonary Embolism Associated with COVID-19 Pneumonia Detected with Pulmonary CT Angiography. *Radiology* **2020**, *296*, E186–E188. [CrossRef] [PubMed]
17. Léonard-Lorant, I.; Delabranche, X.; Séverac, F.; Helms, J.; Pauzet, C.; Collange, O.; Schneider, F.; Labani, A.; Bilbault, P.; Molière, S.; et al. Acute Pulmonary Embolism in Patients with COVID-19 at CT Angiography and Relationship to d-Dimer Levels. *Radiology* **2020**, *296*, E189–E191. [CrossRef]
18. Qanadli, S.D.; Beigelman-Aubry, C.; Rotzinger, D.C. Vascular Changes Detected with Thoracic CT in Coronavirus Disease (COVID-19) Might Be Significant Determinants for Accurate Diagnosis and Optimal Patient Management. *AJR Am. J. Roentgenol.* **2020**, *215*, W15. [CrossRef] [PubMed]
19. Rotzinger, D.C.; Beigelman-Aubry, C.; von Garnier, C.; Qanadli, S.D. Pulmonary embolism in patients with COVID-19: Time to change the paradigm of computed tomography. *Thromb. Res.* **2020**, *190*, 58–59. [CrossRef] [PubMed]
20. Marongiu, F.; Grandone, E.; Barcellona, D. Pulmonary thrombosis in 2019-nCoV pneumonia? *J. Thromb. Haemost.* **2020**, *18*, 1511–1513. [CrossRef]
21. Tang, N.; Bai, H.; Chen, X.; Gong, J.; Li, D.; Sun, Z. Anticoagulant treatment is associated with decreased mortality in severe coronavirus disease 2019 patients with coagulopathy. *J. Thromb. Haemost.* **2020**, *18*, 1094–1099. [CrossRef]
22. Gattinoni, L.; Coppola, S.; Cressoni, M.; Busana, M.; Rossi, S.; Chiumello, D. COVID-19 Does Not Lead to a “Typical” Acute Respiratory Distress Syndrome. *Am. J. Respir. Crit. Care Med.* **2020**, *201*, 1299–1300. [CrossRef]
23. Henkel, M.; Weikert, T.; Marston, K.; Schwab, N.; Sommer, G.; Haslbauer, J.; Franzeck, E.; Anastasopoulos, C.; Stieltjes, B.; Michel, A.; et al. Lethal COVID-19: Radiologic-Pathologic Correlation of the Lungs. *Radiol. Cardiothorac. Imaging* **2020**, *2*, e200406. [CrossRef]
24. Qanadli, S.D.; Rocha, A.C.; Rotzinger, D.C. Case Report: Intrapulmonary Arteriovenous Anastomoses in COVID-19-Related Pulmonary Vascular Changes: A New Player in the Arena? *Front. Med.* **2021**, *8*. [CrossRef]
25. Deshpande, C. Thromboembolic Findings in COVID-19 Autopsies: Pulmonary Thrombosis or Embolism? *Ann. Intern. Med.* **2020**, *173*, 394–395. [CrossRef]
26. Chow, S.C.; Shao, J.; Wang, H. *Sample Size Calculations in Clinical Research*, 2nd ed.; CRC Biostatistics Series; Chapman & Hall: London, UK, 2008; p. 89.
27. Lodigiani, C.; Iapichino, G.; Carenzo, L.; Cecconi, M.; Ferrazzi, P.; Sebastian, T.; Kucher, N.; Studt, J.D.; Sacco, C.; Bertuzzi, A.; et al. Venous and arterial thromboembolic complications in COVID-19 patients admitted to an academic hospital in Milan, Italy. *Thromb. Res.* **2020**, *191*, 9–14. [CrossRef]
28. Qanadli, S.D.; El Hajjam, M.; Vieillard-Baron, A.; Joseph, T.; Mesurole, B.; Oliva, V.L.; Barré, O.; Bruckert, F.; Dubourg, O.; Lacombe, P. New CT index to quantify arterial obstruction in pulmonary embolism: Comparison with angiographic index and echocardiography. *AJR Am. J. Roentgenol.* **2001**, *176*, 1415–1420. [CrossRef]
29. Rotzinger, D.C.; Knebel, J.-F.; Jouannic, A.-M.; Adler, G.; Qanadli, S.D. CT Pulmonary Angiography for Risk Stratification of Patients with Nonmassive Acute Pulmonary Embolism. *Radiol. Cardiothorac. Imaging* **2020**, *2*, e190188. [CrossRef]
30. Harris, P.A.; Taylor, R.; Thielke, R.; Payne, J.; Gonzalez, N.; Conde, J.G. Research electronic data capture (REDCap)—A metadata-driven methodology and workflow process for providing translational research informatics support. *J. Biomed. Inform.* **2009**, *42*, 377–381. [CrossRef] [PubMed]
31. Smetana, K., Jr.; Rosel, D.; BrÁbek, J. Raloxifene and Bazedoxifene Could Be Promising Candidates for Preventing the COVID-19 Related Cytokine Storm, ARDS and Mortality. *In Vivo* **2020**, *34*, 3027–3028. [CrossRef] [PubMed]
32. Cavagna, E.; Muratore, F.; Ferrari, F. Pulmonary Thromboembolism in COVID-19: Venous Thromboembolism or Arterial Thrombosis? *Radiol. Cardiothorac. Imaging* **2020**, *2*, e200289. [CrossRef]

7.4 Emerging role of spectral CT chronic thromboembolic pulmonary hypertension diagnosis [125]

Chronic thromboembolic pulmonary hypertension (CTEPH) is a frequent and debilitating complication of acute PE with an estimated incidence of 3 to 5 per 100'000 inhabitants. It is to be distinguished from other pulmonary hypertension subtypes because it is the only form to be amenable to curative treatment. For this reason, accurately diagnosing CTEPH is critical to offer patients the right treatment. In this review, we cover both the diagnosis and modern treatment approach to CTEPH, emphasizing the role of DECT along the diagnostic pathway. DECT's ability to provide semi-quantitative pulmonary perfusion by means of iodine density maps helps identify arterial abnormalities leading to perfusional changes. Correct evaluation of perfusion deficits is equally essential to diagnose CTEPH and to guide therapy. Section 3 in the article emphasizes the emerging role of DECT in that setting; note that only section 3 of the article, as well the corresponding references, are reproduced here.



ELSEVIER

Contents lists available at ScienceDirect

European Journal of Radiology

journal homepage: www.elsevier.com/locate/ejrad



Review

Pulmonary angioplasty: A step further in the continuously changing landscape of chronic thromboembolic pulmonary hypertension management



David C. Rotzinger^{a,1,*}, Kiara Rezaei-Kalantari^{b,1}, John-David Aubert^{c,d}, Salah D. Qanadli^a

^a Cardiothoracic and Vascular Division, Department of Diagnostic and Interventional Radiology, Lausanne University Hospital and University of Lausanne, Rue du Bugnon 46, 1011, Lausanne, Switzerland

^b Rajaie Cardiovascular Medical and Research Center, Iran University of Medical Sciences, Tehran, Iran

^c Transplantation Center, Department of Medicine, Lausanne University Hospital and University of Lausanne, Lausanne, Switzerland

^d Service of Pulmonology, Department of Medicine, Lausanne University Hospital and University of Lausanne, Lausanne, Switzerland

ARTICLE INFO

Keywords:

Chronic thromboembolic pulmonary hypertension
Pulmonary embolism
Pulmonary angioplasty
Endovascular procedure

ABSTRACT

Chronic thromboembolic pulmonary hypertension (CTEPH) is a potentially fatal and frequently undiagnosed form of pulmonary hypertension (PH), classified within group 4 by the World Health Organization (WHO). It is a type of precapillary PH, which uncommonly develops as a peculiar sequel of acute pulmonary embolism due to the partial resolution of the mechanically obstructing thrombus with a coexisting inflammatory response from pulmonary vessels. CTEPH is one of the potentially treatable forms of PH whose current standard of care is surgical pulmonary endarterectomy. Medical therapy with few drugs in non-operable disease is approved and has shown improvement in patients' hemodynamic condition and functional ability. Recently, balloon pulmonary angioplasty (BPA) has shown promising results as a treatment option for technically inoperable patients, those with unacceptable risk-to-benefit ratio and in a case of residual PH after endarterectomy. Lack of meticulous CTEPH screening programs in post-pulmonary embolism patients leading to underdiagnosis of this condition, complex operability assessment, and diversity in BPA techniques among different institutions are still the issues that need to be addressed. In this paper, we review the recent achievements in the management of non-operable CTEPH, their outcome and safety, based on available data.

3. CTEPH imaging and classification

Several imaging modalities find their place in the workup of suspected CTEPH (Fig. 1). Transthoracic echocardiography is a simple and effective means of assessing the right heart chambers and the probability of PH. RV hypertrophy (wall thickness >5 mm) and RV dilation are indicative of chronic RV loading and adaptive remodeling, and echocardiography can suggest elevated PVR before RHC [33]. According to the latest diagnostic algorithm from the European Society of Cardiology (ESC) [24], patients with intermediate or high probability of PH at echocardiography benefit from radionuclide ventilation-perfusion (V/Q) lung scintigraphy, which accurately detects suggestive abnormalities, typically large mismatched perfusion defects. Sensitivity and specificity are excellent (>90 %) with both planar V/Q, and V/Q single-photon computed tomography (SPECT) [34]. Additionally, due to its nearly perfect negative predictive value, V/Q can safely exclude CTEPH and avoid unnecessary additional diagnostic tests. On the other hand, in the presence of mismatched perfusion abnormalities, further diagnostic tests are required because of the limited specificity of V/Q scintigraphy.

CT pulmonary angiography has established itself as the principal non-invasive instrument to assess the pulmonary vasculature, with the ability to evaluate the pulmonary anatomy and cardiac morphology at the same time [35,36]. While the sensitivity of V/Q was long considered higher than that of CTPA for the detection of CTEPH, recent data show equivalent sensitivities for these two imaging tests, which has been attributed to technological improvements [3,37]. The sensitivity and specificity of CTPA to detect CTEPH findings are excellent at the main and lobar arterial segments (97.0 % and 97.1 %, respectively) and slightly lower at the segmental and subsegmental levels (85.8 % and 94.6 %) [38]. Besides the detection of typical CTEPH signs including increased right-to-left ventricular ratio, dilated main pulmonary artery, organized chronic emboli, peripheral tapering of pulmonary arteries, systemic collaterals, and mosaic attenuation pattern, CTPA has the potential to unveil alternative diagnoses (mimickers of CTEPH) such as systemic vasculitis, arterial sarcoma, fibrosing mediastinitis, or pulmonary veno-occlusive disease [39,40]. More recently, dual-energy CT systems have become available for clinical use, opening the door to a new era of combined morphological and functional vascular assessment. Dual-energy CT (Figs. 2,3 and 5) platforms acquire spectral X-ray attenuation data without additional radiation or iodine dose [41] and allow semi-quantitative evaluation of pulmonary perfusion [42,43], as well as blood volume (Fig. 3, panel b). Whereas iodine density maps show promising initial results as a surrogate marker of pulmonary perfusion [44], further evaluation with prospective studies is warranted to establish this technology as a clinical standard [45].

Recently, pulmonary magnetic resonance imaging has gained interest as a radiation-free alternative to other imaging techniques in CTEPH. It has limited spatial resolution compared to CTPA but offers the advantage of measuring cardiac and pulmonary hemodynamics. Drawbacks include the required level of training and expertise to perform it properly and its time-consuming nature [46,47].

Right heart catheterization is the final diagnostic procedure that will confirm PH with invasive hemodynamic assessment and remains the gold standard to diagnose PH. Care must be taken in patients with normal resting mPAP (< 20 mmHg) but high clinical or radiological suspicion of CTEPH because abnormal mPAP may become apparent only during exercise. This condition is named Chronic Thrombo-Embolic Disease (CTED), and its management remains poorly defined. RHC is usually combined with catheter-based pulmonary angiography, which helps determine the distribution and extent of thromboembolic burden, especially at the subsegmental level. Diagnostic angiography remains a mainstay in evaluating surgical accessibility, and the development of BPA restores the importance of accurate mapping of occlusive target lesions with transcatheter angiography. Findings include vessel narrowing (Fig. 4), webs and bands (Fig. 2), pouch defects, or occlusions

(Fig. 5). The latest proposed angiographic classification of pulmonary vascular lesions specifically tailored for BPA identifies five lesion types. Type A: ring-like stenosis lesion; type B: web lesion; type C: subtotal lesion; type D: total occlusion lesion; and type E: tortuous lesion [48]. The highest success rate and lowest complication rate of BPA were attributed to type A lesions followed by type B, while type D and E lesions had the least success rate, and the highest complication rate was noticed in type E lesions [49].

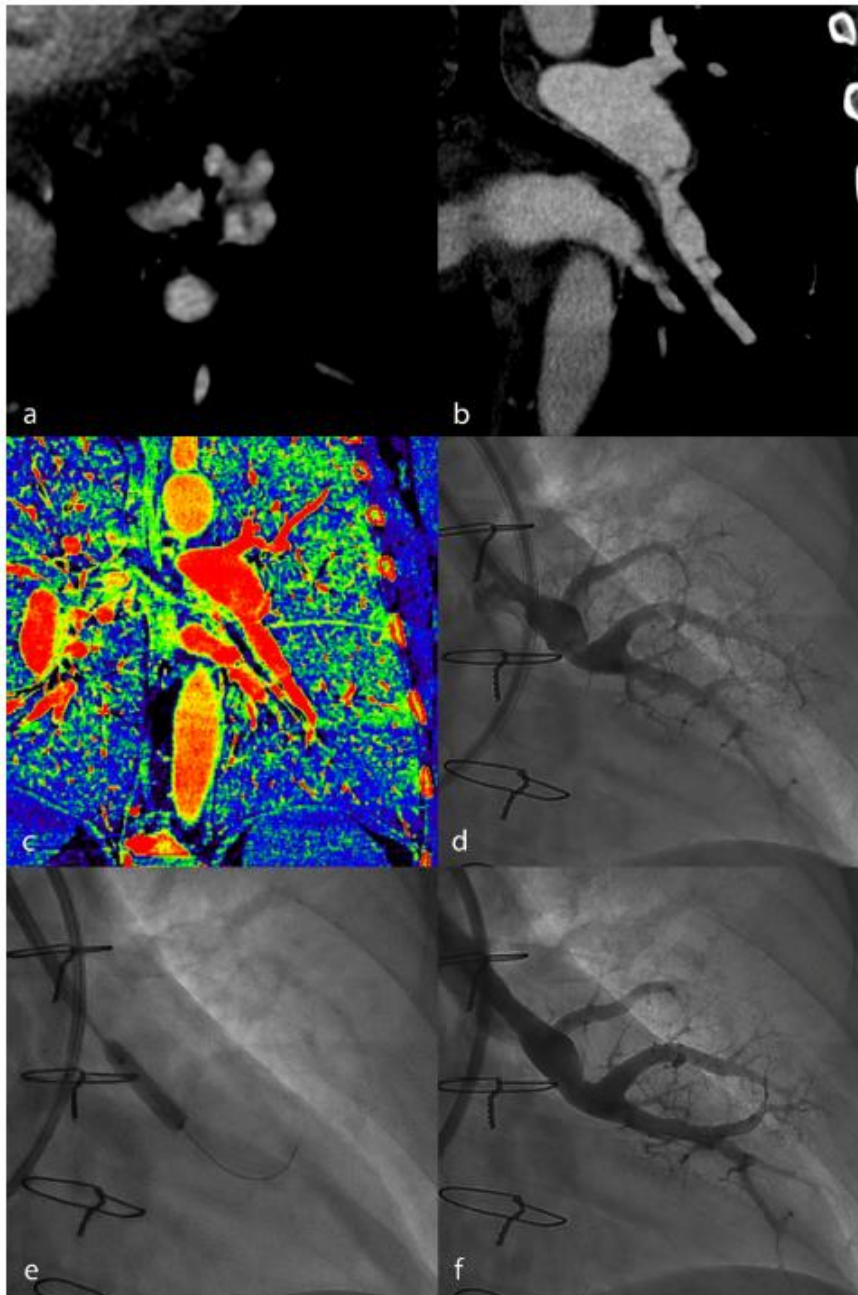


Fig. 2. Dual-energy CT pulmonary angiography shows several webs in the left lower lobe's anterior and lateral segmental arteries on axial (a) and coronal reformatted (b) images. Coronal reformatted iodine density map reveals impaired perfusion in the left lower lobe (c). Selective transcatheter pulmonary angiography shows incomplete opacification of the anterior segmental artery due to webs (d). Following treatment with balloon pulmonary angioplasty (e), a final angiogram shows the absence of stenosis (f).

limitations, BPA should not be considered in total unilateral occlusion or large central clots [48].

6. Target groups, indications, contraindications

Eligibility assessment is a challenging and multifactorial task requiring a multidisciplinary team of CTEPH experts whose members may vary depending on local practice. Core members may include PH pulmonologists, diagnostic cardiologists and radiologists, interventional radiologists/cardiologists. Including cardiothoracic surgeons is an attractive means of providing a balanced and thorough multidisciplinary discussion of tailored treatment. Depending on patients' ability

to receive general anesthesia, input from anesthesiologists can influence treatment decisions. Whenever a BPA program is started, a concomitant PEA track should be available and discussed in the multidisciplinary team since PEA remains the method of choice for eligible patients with CTEPH. Furthermore, due to the absence of systematic post-PE screening programs, PH management teams should closely collaborate with pulmonary embolism response teams since most CTEPH patients are identified through acute PE referrals. Although consensus regarding PEA and BPA's merits gradually develops, there may still be considerable variability in practice across institutions and nations. Patients who have the highest benefit from BPA are those with an unfavorable risk/benefit ratio for PEA, more distal location of obstructive thrombotic lesions, and

- [5] H. Gall, M.M. Hoepfer, M.J. Richter, W. Cacheris, B. Hinzmann, E. Mayer, An epidemiological analysis of the burden of chronic thromboembolic pulmonary hypertension in the USA, Europe and Japan, *Eur Respir Rev.* 26 (143) (2017).
- [6] Y.M. Ende-Verhaar, S.C. Cannegieter, A. Vonk Noordegraaf, M. Delcroix, P. Pruszczyk, A.T. Mairuhu, et al., Incidence of chronic thromboembolic pulmonary hypertension after acute pulmonary embolism: a contemporary view of the published literature, *Eur. Respir. J.* 49 (2) (2017).
- [7] N. Coquoz, D. Weilenmann, D. Stolz, V. Popov, A. Azzola, J.M. Fellrath, et al., Multicentre observational screening survey for the detection of CTEPH following pulmonary embolism, *Eur. Respir. J.* 51 (4) (2018).
- [8] M. Riedel, V. Stanek, J. Widimsky, I. Prerovsky, Longterm follow-up of patients with pulmonary thromboembolism: late prognosis and evolution of hemodynamic and respiratory data, *Chest.* 81 (2) (1992) 151-158.
- [9] P. Fedullo, K.M. Kerr, N.H. Kim, W.R. Auger, Chronic thromboembolic pulmonary hypertension, *Am. J. Respir. Crit. Care Med.* 183 (12) (2011) 1605-1613.
- [10] M.M. Madani, W.R. Auger, V. Pretorius, N. Sakakibara, K.M. Kerr, N.H. Kim, et al., Pulmonary endarterectomy: recent changes in a single institution's experience of more than 2,700 patients, *Annl. thoracic surgery* 94 (1) (2012) 97-103.
- [11] M. Gerges, M. Yacoub, Chronic thromboembolic pulmonary hypertension - still evolving, *Glob. Cardiol. Sci. Pract.* 2020 (1) (2020), e202011.
- [12] J. Pepke-Zaba, M. Delcroix, I. Lang, E. Mayer, P. Jansa, D. Ambroz, et al., Chronic thromboembolic pulmonary hypertension (CTEPH): results from an international prospective registry, *Circulation* 124 (18) (2011) 1973-1981.
- [13] H.A. Ghofrani, A.M. D'Armini, F. Grimminger, M.M. Hoepfer, P. Jansa, N.H. Kim, et al., Riociguat for the treatment of chronic thromboembolic pulmonary hypertension, *N. Engl. J. Med.* 369 (4) (2013) 319-329.
- [14] H.A. Ghofrani, G. Simonneau, A.M. D'Armini, P. Fedullo, L.S. Howard, X. Jais, et al., Macitentan for the treatment of inoperable chronic thromboembolic pulmonary hypertension (MERIT-1): results from the multicentre, phase 2, randomised, double-blind, placebo-controlled study, *Lancet Respir. Med.* 5 (10) (2017) 785-794.
- [15] R. Sadushi-Kolicic, P. Jansa, G. Kopec, A. Torbicki, N. Skoro-Sajer, I.A. Campean, et al., Subcutaneous treprostinil for the treatment of severe non-operable chronic thromboembolic pulmonary hypertension (CTREPH): a double-blind, phase 3, randomised controlled trial, *Lancet Respir. Med.* 7 (3) (2019) 239-248.
- [16] M.M. Hoepfer, Pharmacological therapy for patients with chronic thromboembolic pulmonary hypertension, *Eur. Respir. Rev.* 24 (136) (2015) 272-282.
- [17] Y. Zhang, X. Yu, Q. Jin, Q. Luo, Z. Zhao, Q. Zhao, et al., Advances in targeted therapy for chronic thromboembolic pulmonary hypertension, *Heart Fail. Rev.* 24 (6) (2019) 949-965.
- [18] S. Malekzadeh, T. Rolf, F. Doenz, A. Chouiter, A.M. Jouannic, S.D. Qanadli, Safety of elective percutaneous peripheral revascularization in outpatients: a 10-year single-center experience, *Diagn. Interv. Imaging* 100 (6) (2019) 347-352.
- [19] J.A. Voorburg, V.M. Cats, B. Buis, A.V. Brusilko, Balloon angioplasty in the treatment of pulmonary hypertension caused by pulmonary embolism, *Chest* 94 (6) (1988) 1249-1253.
- [20] J.A. Feinstein, S.Z. Goldhaber, J.E. Lock, S.M. Ferdandes, M.J. Landzberg, Balloon pulmonary angioplasty for treatment of chronic thromboembolic pulmonary hypertension, *Circulation* 103 (1) (2001) 10-13.
- [21] M. Kataoka, T. Inami, K. Hayashida, N. Shimura, H. Ishiguro, T. Abe, et al., Percutaneous transluminal pulmonary angioplasty for the treatment of chronic thromboembolic pulmonary hypertension, *Circ. Cardiovasc. Interv.* 5 (6) (2012) 756-762.
- [22] H. Mizoguchi, A. Ogawa, M. Munemasa, H. Mikouchi, H. Ito, H. Matsubara, Refined balloon pulmonary angioplasty for inoperable patients with chronic thromboembolic pulmonary hypertension, *Circ. Cardiovasc. Interv.* 5 (6) (2012) 748-755.
- [23] K. Sugimura, Y. Fukumoto, K. Satoh, K. Nochioka, Y. Miura, T. Aoki, et al., Percutaneous transluminal pulmonary angioplasty markedly improves pulmonary hemodynamics and long-term prognosis in patients with chronic thromboembolic pulmonary hypertension, *Circ. J.* 76 (2) (2012) 485-488.
- [24] N. Galie, M. Humbert, J.L. Vachiery, S. Gibbs, I. Lang, A. Torbicki, et al., ESC/ERS guidelines for the diagnosis and treatment of pulmonary hypertension: the joint task force for the diagnosis and treatment of pulmonary hypertension of the European society of cardiology (ESC) and the European respiratory society (ERS): endorsed by: association for European paediatric and congenital cardiology (AEPC), international society for heart and lung transplantation (ISHLT), *Eur. Heart J.* 37 (1) (2015) 67-119, 2016.
- [25] Q. Jin, Z.H. Zhao, Q. Luo, Q. Zhao, L. Yan, Y. Zhang, et al., Balloon pulmonary angioplasty for chronic thromboembolic pulmonary hypertension: state of the art, *World J. Clin. Cases* 8 (13) (2020) 2679-2702.
- [26] P.F. Fedullo, L.J. Rubin, K.M. Kerr, W.R. Auger, R.N. Channick, The natural history of acute and chronic thromboembolic disease: the search for the missing link, *Eur. Respir. J.* 15 (3) (2000) 435-437.
- [27] D. Bonderman, J. Jakowitsch, B. Redwan, H. Bergmeister, M.K. Renner, H. Panzenböck, et al., Role for staphylococci in misguided thrombus resolution of chronic thromboembolic pulmonary hypertension, *Arterioscler. Thromb. Vasc. Biol.* 28 (4) (2008) 678-684.
- [28] N. Galie, N.H. Kim, Pulmonary microvascular disease in chronic thromboembolic pulmonary hypertension, *Proc. Am. Thorac. Soc.* 3 (7) (2006) 571-576.
- [29] P. Dorfmueller, S. Gunther, M.R. Ghigna, V. Thomas de Montpreville, D. Boulate, J. F. Paul, et al., Microvascular disease in chronic thromboembolic pulmonary hypertension: a role for pulmonary veins and systemic vasculature, *Eur. Respir. J.* 44 (5) (2014) 1275-1288.

Declaration of Competing Interest

The authors report no declarations of interest.

Acknowledgements

David C. Rotzinger is supported by a grant from the Leenaards Foundation.

References

- [1] Centre HaSci, National Audit of Pulmonary Hypertension 2015 [Available from: 2016 <http://www.hascic.gov.uk/pubs/npha2015>].
- [2] P. Escribano-Subias, I. Blanco, M. Lopez-Meseguer, C.J. Lopez-Guarch, A. Roman, P. Morales, et al., Survival in pulmonary hypertension in Spain: insights from the Spanish registry, *Eur. Respir. J.* 40 (3) (2012) 596-603.
- [3] J. Hurdman, R. Condliffe, C.A. Elliot, C. Davies, C. Hill, J.M. Wild, et al., ASPIRE registry: assessing the spectrum of pulmonary hypertension identified at a REferral centre, *Eur. Respir. J.* 39 (4) (2012) 945-955.
- [4] S. Mueller-Mottet, H. Stricker, G. Domenighetti, A. Azzola, T. Geiser, M. Schwerzmann, et al., Long-term data from the Swiss pulmonary hypertension registry, *Respiration* 89 (2) (2015) 127-140.

- [30] R. Condliffe, D.G. Kiely, J.S. Gibbs, P.A. Corris, A.J. Peacock, D.P. Jenkins, et al., Prognostic and aetiological factors in chronic thromboembolic pulmonary hypertension, *Eur. Respir. J.* 33 (2) (2009) 332–338.
- [31] Y.M. Ende-Verhaar, M.V. Huisman, F.A. Klok, To screen or not to screen for chronic thromboembolic pulmonary hypertension after acute pulmonary embolism, *Thromb. Res.* 151 (2017) 1–7.
- [32] L. Donahoe, R. Vanderlaan, J. Thenganatt, K. McRae, A. Bykova, J. Moric, et al., Symptoms are more useful than echocardiography in patient selection for pulmonary endarterectomy, *Ann. Thorac. Surg.* 104 (4) (2017) 1179–1185.
- [33] J.S. Park, J. Ahn, J.H. Choi, H.W. Lee, J.H. Oh, H.C. Lee, et al., The predictive value of echocardiography for chronic thromboembolic pulmonary hypertension after acute pulmonary embolism in Korea, *Korean J. Intern. Med.* 32 (1) (2017) 85–94.
- [34] L. Wang, M. Wang, T. Yang, D. Wu, C. Xiong, W.A. Fang, Prospective, comparative study of planar and single-photon emission computed tomography ventilation/perfusion imaging for chronic thromboembolic pulmonary hypertension, *J. Nucl. Med.* (2020).
- [35] M.A. King, M. Ysrael, C.J. Bergin, Chronic thromboembolic pulmonary hypertension: CT findings, *AJR Am. J. Roentgenol.* 170 (4) (1998) 955–960.
- [36] E. Biri, A. Hsiao, K. Kerr, N. Kim, M. Madani, S. Kligerman, et al., Quantification of CTEPH disease burden on CT angiogram correlates with patient presurgical hemodynamic severity and hemodynamic improvement after PTE surgery, *J. Heart Lung Transplant.* 39 (4, Supplement) (2020). S170–S1.
- [37] S. Ley, J. Ley-Zaporozhan, M.B. Pitton, J. Schneider, G.M. Wirth, E. Mayer, et al., Diagnostic performance of state-of-the-art imaging techniques for morphological assessment of vascular abnormalities in patients with chronic thromboembolic pulmonary hypertension (CTEPH), *Eur. Radiol.* 22 (3) (2012) 607–616.
- [38] T. Sugiura, N. Tanabe, Y. Matsumura, A. Shigeta, N. Kawata, T. Jujo, et al., Role of 320-slice CT imaging in the diagnostic workup of patients with chronic thromboembolic pulmonary hypertension, *Chest* 143 (4) (2013) 1070–1077.
- [39] S. Narechania, R. Renapurkar, G.A. Hereci, Mimickers of chronic thromboembolic pulmonary hypertension on imaging tests: a review, *Pulm. Circ.* 10 (1) (2020), 2045894019882620.
- [40] K.R. Kalantari, H. Malek, A. Amin, J. Moosavi, O. Shafe, P. Sadehipour, Chronic thromboembolic pulmonary hypertension versus fibrosing mediastinitis, *Anatol. J. Cardiol.* 21 (2) (2019) E4–e5.
- [41] S. Aldosari, Z. Sun, A systematic review of double low-dose CT pulmonary angiography in pulmonary embolism, *Curr. Med. Imaging Rev.* 15 (5) (2019) 453–460.
- [42] A. Sakamoto, I. Sakamoto, H. Nagayama, H. Koike, E. Sueyoshi, M. Uetani, Quantification of lung perfusion blood volume with dual-energy CT: assessment of the severity of acute pulmonary thromboembolism, *AJR Am. J. Roentgenol.* 203 (2) (2014) 287–291.
- [43] E.G. Kikano, M. Rajdev, K.Z. Salem, K. Laukamp, C.D. Felice, R.C. Gilkeson, et al., Utility of iodine density perfusion maps from dual-energy spectral detector CT in evaluating cardiothoracic conditions: a primer for the radiologist, *AJR Am. J. Roentgenol.* 214 (4) (2020) 775–785.
- [44] S. Si-Mohamed, C. Moreau-Tribby, P. Tytski, V. Tatar-Leitman, Q. Wdowik, S. Boccalini, et al., Head-to-head Comparison of Lung Perfusion With Dual-energy CT and SPECT-CT, *Diagn. Interv. Imaging.* 2020.
- [45] S. Lysdahlgaard, S. Hess, O. Gerke, M. Weber Kusk, A systematic literature review and meta-analysis of spectral CT compared to scintigraphy in the diagnosis of acute and chronic pulmonary embolisms, *Eur. Radiol.* (2020).
- [46] W.M. Bradlow, J.S. Gibbs, R.H. Mohiaddin, Cardiovascular magnetic resonance in pulmonary hypertension, *J. Cardiovasc. Magn. Reson.* 14 (1) (2012) 6.
- [47] S. Rajaram, A.J. Swift, D. Capener, A. Telfer, C. Davies, C. Hill, et al., Diagnostic accuracy of contrast-enhanced MR angiography and unenhanced proton MR imaging compared with CT pulmonary angiography in chronic thromboembolic pulmonary hypertension, *Eur. Radiol.* 22 (2) (2012) 310–317.
- [48] I. Lang, B.C. Meyer, T. Ogo, H. Matsubara, M. Kurzyrna, H.A. Ghofrani, et al., Balloon pulmonary angioplasty in chronic thromboembolic pulmonary hypertension, *Eur. Respir. Rev.* 26 (143) (2017).
- [49] T. Kawakami, A. Ogawa, K. Miyaji, H. Mizoguchi, H. Shimokawahara, T. Naito, et al., Novel angiographic classification of each vascular lesion in chronic thromboembolic pulmonary hypertension based on selective angiogram and results of balloon pulmonary angioplasty, *Circ. Cardiovasc. Interv.* 9 (10) (2016).
- [50] M.M. Hoepfer, E. Mayer, G. Simonneau, L.J. Rubin, Chronic thromboembolic pulmonary hypertension, *Circulation* 113 (16) (2006) 2011–2020.
- [51] P. Herve, E.M. Lau, O. Sibon, L. Savale, D. Montani, L. Godinas, et al., Criteria for diagnosis of exercise pulmonary hypertension, *Eur. Respir. J.* 46 (3) (2015) 728–737.
- [52] J. Lewczuk, P. Piszko, J. Jagas, A. Porada, S. Wojciak, B. Sobkowicz, et al., Prognostic factors in medically treated patients with chronic pulmonary embolism, *Chest* 119 (3) (2001) 818–823.
- [53] G. Piazza, S.Z. Goldhaber, Chronic thromboembolic pulmonary hypertension, *N. Engl. J. Med.* 364 (4) (2011) 351–360.
- [54] S. Fukui, T. Ogo, Y. Morita, A. Tsuji, E. Tateishi, K. Ozaki, et al., Right ventricular reverse remodelling after balloon pulmonary angioplasty, *Eur. Respir. J.* 43 (5) (2014) 1394–1402.
- [55] S. Collaud, P. Brenot, O. Mercier, E. Fadel, Rescue balloon pulmonary angioplasty for early failure of pulmonary endarterectomy: the earlier the better? *Int. J. Cardiol.* 222 (2016) 39–40.
- [56] M. Roik, D. Wretowski, A. Łabys, K. Irzyk, B. Lichodziejewska, O. Dzikowska-Diuch, et al., Refined balloon pulmonary angioplasty-A therapeutic option in very elderly patients with chronic thromboembolic pulmonary hypertension, *J. Interv. Cardiol.* 30 (3) (2017) 249–255.
- [57] A. Ogawa, T. Satoh, T. Fukuda, K. Sugimura, Y. Fukumoto, N. Emoto, et al., Balloon pulmonary angioplasty for chronic thromboembolic pulmonary hypertension: results of a multicenter registry, *Circ. Cardiovasc. Qual. Outcomes* 10 (11) (2017).
- [58] T. Aoki, K. Sugimura, S. Tabebe, M. Miura, S. Yamamoto, N. Yaoita, et al., Comprehensive evaluation of the effectiveness and safety of balloon pulmonary angioplasty for inoperable chronic thrombo-embolic pulmonary hypertension: long-term effects and procedure-related complications, *Eur. Heart J.* 38 (42) (2017) 3152–3159.
- [59] Y. Taniguchi, K. Miyagawa, K. Nakayama, H. Kinutani, T. Shinke, K. Okada, et al., Balloon pulmonary angioplasty: an additional treatment option to improve the prognosis of patients with chronic thromboembolic pulmonary hypertension, *EuroIntervention* 10 (4) (2014) 510–525.
- [60] T. Inami, M. Kataoka, M. Ando, K. Fukuda, H. Yoshino, T. Satoh, A new era of therapeutic strategies for chronic thromboembolic pulmonary hypertension by two different interventional therapies; pulmonary endarterectomy and percutaneous transluminal pulmonary angioplasty, *PLoS One* 9 (4) (2014), e94587.
- [61] K. Sumimoto, H. Tanaka, J. Mukai, K. Yamashita, Y. Tanaka, A. Shono, et al., Effects of balloon pulmonary angioplasty for chronic thromboembolic pulmonary hypertension on remodeling in right-sided heart, *Int. J. Cardiovasc. Imaging* (2020).
- [62] T. Nishiyama, S. Takatsuki, T. Kawakami, Y. Katsumata, T. Kimura, M. Kataoka, et al., Improvement in the electrocardiograms associated with right ventricular hypertrophy after balloon pulmonary angioplasty in chronic thromboembolic pulmonary hypertension, *Int. J. Cardiol. Heart Vasc.* 19 (2018) 75–82.
- [63] X. Jais, P. Brenot, H. Bouvaist, M. Canuet, C. Chabanne, A. Chaouat, et al., Late breaking Abstract - Balloon pulmonary angioplasty versus riociguat for the treatment of inoperable chronic thromboembolic pulmonary hypertension: results from the randomised controlled RACE study, *Eur. Respir. J.* 54 (suppl 63) (2019), RCT1886.
- [64] T. Tsugu, M. Murata, T. Kawakami, M. Kataoka, Y. Nagatomo, H. Tsuruta, et al., Amelioration of right ventricular function after hybrid therapy with riociguat and balloon pulmonary angioplasty in patients with chronic thromboembolic pulmonary hypertension, *Int. J. Cardiol.* 221 (2016) 227–229.
- [65] S. Minatsuki, M. Hatano, A. Kiyosue, A. Saito, H. Maki, E. Takimoto, et al., Clinically worsening chronic thromboembolic pulmonary hypertension by riociguat after balloon pulmonary angioplasty, *Int. Heart J.* 59 (5) (2018) 1186–1188.
- [66] T. Kawakami, H. Matsubara, K. Abe, M. Kataoka, S. Kohsaka, Y. Sato, et al., Multicentre randomised controlled trial of balloon pulmonary angioplasty and riociguat in patients with chronic thromboembolic pulmonary hypertension: protocol for the MR BPA study, *BMJ Open* 10 (2) (2020), e028831.
- [67] C.B. Wiedenroth, C. Liebetrau, A. Breithecker, S. Guth, H.J. Lautze, E. Ortmann, et al., Combined pulmonary endarterectomy and balloon pulmonary angioplasty in patients with chronic thromboembolic pulmonary hypertension, *J. Heart Lung Transplant.* 35 (5) (2016) 591–596.
- [68] M. Nakamura, O. Sunagawa, H. Tsuchiya, T. Miyara, Y. Taba, T. Touma, et al., Rescue balloon pulmonary angioplasty under veno-arterial extracorporeal membrane oxygenation in a patient with acute exacerbation of chronic thromboembolic pulmonary hypertension, *Int. Heart J.* 56 (1) (2015) 116–120.
- [69] A. Tsuji, T. Ogo, J. Demachi, Y. Ono, Y. Sando, Y. Morita, et al., Rescue balloon pulmonary angioplasty in a rapidly deteriorating chronic thromboembolic pulmonary hypertension patient with liver failure and refractory infection, *Pulm. Circ.* 4 (1) (2014) 142–147.
- [70] K.M. Olsson, C.B. Wiedenroth, J.C. Kamp, A. Breithecker, J. Fuge, G.A. Krombach, et al., Balloon pulmonary angioplasty for inoperable patients with chronic thromboembolic pulmonary hypertension: the initial German experience, *Eur. Respir. J.* 49 (6) (2017).
- [71] T. Inami, M. Kataoka, N. Shimura, H. Ishiguro, R. Yanagisawa, T. Kawakami, et al., Incidence, avoidance, and management of pulmonary artery injuries in percutaneous transluminal pulmonary angioplasty, *Int. J. Cardiol.* 201 (2015) 35–37.
- [72] T. Inami, M. Kataoka, N. Shimura, H. Ishiguro, R. Yanagisawa, H. Taguchi, et al., Pulmonary edema predictive scoring index (PEPSI), a new index to predict risk of reperfusion pulmonary edema and improvement of hemodynamics in percutaneous transluminal pulmonary angioplasty, *JACC Cardiovasc. Interv.* 6 (7) (2013) 725–736.
- [73] T. Inami, M. Kataoka, N. Shimura, H. Ishiguro, R. Yanagisawa, K. Fukuda, et al., Pressure-wire-guided percutaneous transluminal pulmonary angioplasty: a breakthrough in catheter-interventional therapy for chronic thromboembolic pulmonary hypertension, *JACC Cardiovasc. Interv.* 7 (11) (2014) 1297–1306.
- [74] M. Kurzyrna, S. Darocha, R. Pietura, A. Pietrasik, J. Norwa, R. Mańczak, et al., Changing the strategy of balloon pulmonary angioplasty resulted in a reduced complication rate in patients with chronic thromboembolic pulmonary hypertension. A single-centre European experience, *Kardiol. Pol.* 75 (7) (2017) 645–654.
- [75] K. Hosokawa, K. Abe, K. Oi, Y. Mukai, Y. Hirooka, K. Sunagawa, Balloon pulmonary angioplasty-related complications and therapeutic strategy in patients with chronic thromboembolic pulmonary hypertension, *Int. J. Cardiol.* 197 (2015) 224–226.
- [76] S. Nagayoshi, A. Ogawa, H. Matsubara, Spontaneous enlargement of pulmonary artery after successful balloon pulmonary angioplasty in a patient with chronic thromboembolic pulmonary hypertension, *EuroIntervention* 12 (11) (2016), e1435.
- [77] N. Skoro-Sajer, G. Marta, C. Gerges, G. Hlavin, P. Nierlich, S. Taghavi, et al., Surgical specimens, haemodynamics and long-term outcomes after pulmonary endarterectomy, *Thorax.* 69 (2) (2014) 116–122.

8. Discussion and future directions

Despite its ubiquitous availability and established clinical value, conventional CT suffers from several drawbacks: (a) spatial resolution, although better than in magnetic resonance imaging or nuclear medicine, is limited to about 500 μm and has hardly evolved in the last years. (b) contrast resolution, which is especially challenging for assessing soft tissue composed of elements having similar mass density, makes low-contrast tasks such as perfusion imaging or lipid core detection demanding and particularly noise-sensitive. (c) The absence of material specificity and quantification; even though CT is a quantitative imaging modality measuring linear attenuation coefficients, the exact chemical composition of a sample cannot be determined. (d) Radiation dose and (e) intravenous iodine are drawbacks, have to be considered when ordering a CT (especially in children and patients with underlying kidney or cardiac disease) and may cause adverse effects. Actually, both foster DNA damage, and iodine as a CM has no biological specificity for targeting pathological processes.

DECT, released about 15 years ago, has gone a long way in finding its place in medical care. DECT was the first technological leap that could address some of the limitations mentioned above. While early systems were often accused of delivering higher ionizing doses, recent data shows the opposite, as do our experiments. We showed that non-contrast acquisitions could be skipped for assessing acute aortic syndrome, and spectral CT's improved CNR, demonstrated in three of our studies (see section 6), can be translated into dose reduction. For low-contrast tasks such as myocardial perfusion imaging or atherosclerotic plaque characterization, spectral CT can be operated at dose levels equal to conventional CT and yield improved CNR (as we showed for myocardial

perfusion and CCTA) or detection (as we showed in vitro for lipid core). Improved CNR achieved with lower energy VMI can also be translated into markedly reduced iodine dose, as we showed in a CCTA study. The same reduced-iodine-dose CCTA study ended up with some unexpected positive news as the reduced-iodine lower energy VMI's assessment demonstrated improved spatial resolution compared with full-iodine dose single energy imaging.

Furthermore, DECT can quantify certain chemical elements, provided they exhibit a solid photoelectric effect – calcium and iodine are typical examples encountered in clinical practice. Quantification is especially attractive when performing myocardial perfusion imaging; however, normalization methods should be developed to compensate for injection protocol and cardiac output variability. Quantification was also possible for uric acid in phantom experiments, which is clinically relevant because gout patients have an increased risk of major cardiovascular events due to a higher atherosclerotic burden. Detecting vascular uric acid deposits non-invasively may impact therapy and ultimately outcomes in patients with known or unknown hyperuricemia. When diligently applied for specific tasks, DECT can create new tissue-to-background contrast. In this context, we demonstrated the usefulness of patient-specific material decomposition (aortic lumen versus water) to highlight the aortic wall; the concept, however, could be applied to any tissue exhibiting strong enough spectral response at clinical energy levels (i.e., mainly chemical elements with strong photoelectric absorption). To sum up, DECT helps address four of the five limitations stated above; its scintillator-based detectors still need physical separation of detector elements by an opaque grid structure, physically limiting the opportunity to increase spatial resolution.

As far as PCCT is concerned, the main hurdle that has delayed its availability body imaging use was the challenge of pulse-pile up at high the count rates used in CT. The latter has now been mostly overcome, and pre-clinical systems are running at different places across the globe. Currently, PCCT is the answer to the need for improved spatial resolution since its small detector elements provide reported spatial resolutions down to 150 μm [126], even on full field-of-view PCD systems [127]. We also observed improved spatial resolution of PCCT over DECT in our TTF experiments, which, combined with the low noise performance and refined spectral resolution of PCDs, will bring patient benefits. More specifically, we showed that the combination of high spatial resolution and low noise of PCDs allows for markedly improved detection of non-calcified atherosclerotic plaques down to a size of 0.5 mm and lipid core down to a size of 1 mm in a normal-sized simulated patient. The challenge of cardiac imaging in obese patients remains, but PCCT improves the prospects of achieving diagnostic image quality at manageable dose levels.

Project continuity

Various further analyses can be conducted using existing data or data to be produced shortly. As mentioned earlier, the COROGOUT project, requiring a highly precise concentration of materials in suspension, will evaluate the performance of spectral CT to detect and quantify uric acid crystals. Because of uric acid's moderate spectral response at clinical X-ray energy ranges, the challenge of detection and quantification remains substantial with DECT, and benefits are particularly expected from PCCT. If possible, an

ex-vivo analysis based on excised human tissue samples will supplement the phantom study.

In addition, the project "Model observer assessment of photon-counting-detector coronary CT angiography and comparison with energy-integrating-detector CT" can be expanded since more data is available for analysis, included reduced X-ray dose acquisitions and reduced-iodine dose acquisitions. PCCT's potential to perform CTA with reduced radiation and iodine doses could be approximated from such analyses, and due to PCCT's low noise and refined spectral resolution, its impact will surpass DECT.

Future approaches

Clinical implementation of spectral CT in cardiovascular imaging is now becoming more of a reality as some systems allow for ECG-gating while sampling in DECT mode [105, 109, 128]. Despite the fact that early PCCT prototypes did not support ECG-gating [69], new generations do. This also means that experimental studies conducted as part of this thesis should be expanded with heart motion simulation platforms to perform more experiments with moving phantoms. ECG-gated spectral CT will be offered for more CT systems and will become standard in the short term, promising new clinical applications.

One aspect that was not addressed as part of the scientific part of the thesis is spectral CT's capability to reduce artifacts. Several advantages of DECT in that field are known already, including artifact reduction from dense CM in the subclavian and brachiocephalic veins [129], port systems [130], sternal wires, coronary artery bypass clips and stents [131], PCCT has further beam hardening and metal artifact reduction potential [132, 133],

but currently lacks in vivo validation, particularly in cardiac imaging where metal devices such as stents, coils, pacemaker wires and more massive equipment including left ventricular assist devices challenge image interpretation.

With regard to technology, the emergence of PCCT does not necessarily mean immediate obsolescence of DECT systems. While going for spectral CT systems means looking into the future, healthcare facilities will continue to rely on cost-effectiveness analyses to decide whether they should invest in DECT or PCCT equipment. DECT will likely continue to improve, and new models, e.g., with narrower energy spectra, would undoubtedly prove valuable in clinical practice. Also, PCDs are expected to improve and might someday provide the option of performing grating-based phase-contrast imaging (GBPCI) [134]. GBPCI enables the measurement of extremely small X-ray refraction angles occurring due to electron density variations of a given chemical component, thereby providing markedly improved soft-tissue contrast compared to the established attenuation-based CT imaging. Tissue contrast reminiscent of that yielded by magnetic resonance imaging can be achieved with GBPC-CT, but with CT's higher spatial resolution [135, 136].

Likewise, full potential has not been reached yet on the reconstruction side since deep learning image reconstruction (DLIR) has recently been introduced in single-energy CT [91, 137] and could theoretically be implemented in PCCT prototypes. DLIR algorithms provide markedly improved noise performance while maintaining spatial resolution. On a PCCT system, DLIR could push the boundaries of low contrast detectability and radiation dose reduction even further.

Additionally, spectral CT in general and PCCT, in particular, allow the use of new CMs and combinations of CMs providing different information in a single acquisition (single-acquisition multi-phase imaging) [138].

Finally, a promising scientific approach to plaque rupture prediction using CT is to assess plaques that have actually ruptured and caused lethal myocardial infarction. This can be achieved with post mortem CCTA, which is routinely performed as part of autopsy evaluation at the Centre Universitaire Romand de Médecine Légale (CURML) in Lausanne and Geneva. Using single-energy CT, a group composed of forensic pathologists, forensic radiologists, and cardiovascular radiologists investigated the potential role of plaque inflammation as a marker of plaque severity. In a congress abstract co-authored with Magnin V, Van Der Wal AC, Grabherr S, Qanadli SD, and Michaud K, [139], we demonstrate that enhancement detected in lethal coronary artery plaques by post mortem CCTA correlates with the histopathological presence of perivascular plaque inflammation and increase of vasa vasorum. Arterial wall enhancement has been investigated in animal (pig) carotid arteries using PCCT before and appeared feasible [140]. The next step in post mortem plaque analysis will obviously be to take advantage of the high spatial resolution and spectral performance of PCCT, understand what characterizes a vulnerable plaque, and hopefully predict plaque rupture in vivo.

9. Conclusion

Spectral CT is still a young imaging modality but is gaining worldwide acceptance. Its role in cardiovascular imaging is becoming increasingly important, and evidence is needed both to clarify its usefulness and acknowledge limitations. The various studies conducted as part of this thesis are a building block to improve patient safety and leverage diagnostic value in cardiovascular medicine, especially with the increasingly available DECT platforms. We also highlight the advantage of considering PCCT for cardiovascular imaging in clinical routine. In the continuum of X-ray imaging's 125-year success story, our results confirm that spectral CT does not take us anything away. Quite the contrary: less radiation and iodine doses become commonplace, CT's quantitative nature is being reinforced, and diagnostic accuracy raises. CT is just becoming better.

8. References

1. Ambrose, J., *Computerized transverse axial scanning (tomography). 2. Clinical application.* Br J Radiol, 1973. **46**(552): p. 1023-47.
2. Hounsfield, G.N., *Computerized transverse axial scanning (tomography). 1. Description of system.* Br J Radiol, 1973. **46**(552): p. 1016-22.
3. Merritt, R.B. and S.G. Chenery, *Quantitative CT measurements: the effect of scatter acceptance and filter characteristics on the EMI 7070.* Phys Med Biol, 1986. **31**(1): p. 55-63.
4. Curry, T.S., J.E. Dowdey, and R.C. Murry, *Christensen's physics of diagnostic radiology.* 1990: Lippincott Williams & Wilkins.
5. Bottinor, W., P. Polkampally, and I. Jovin, *Adverse reactions to iodinated contrast media.* Int J Angiol, 2013. **22**(3): p. 149-54.
6. Gado, M.H., M.E. Phelps, and R.E. Coleman, *An extravascular component of contrast enhancement in cranial computed tomography. Part I. The tissue-blood ratio of contrast enhancement.* Radiology, 1975. **117**(3 Pt 1): p. 589-93.
7. Brown, J.R., et al., *Does safe dosing of iodinated contrast prevent contrast-induced acute kidney injury?* Circ Cardiovasc Interv, 2010. **3**(4): p. 346-50.
8. Van Cauteren, T., et al., *Iodine Dose of Administered Contrast Media Affects the Level of Radiation-Induced DNA Damage During Cardiac CT Scans.* AJR Am J Roentgenol, 2019. **213**(2): p. 404-409.
9. Huda, W. and R.M. Slone, *Review of radiologic physics.* 2003: Lippincott Williams & Wilkins.

10. Iwanczyk, J.S., et al., *Photon Counting Energy Dispersive Detector Arrays for X-ray Imaging*. IEEE Trans Nucl Sci, 2009. **56**(3): p. 535-542.
11. McCollough, C.H., et al., *Dual- and Multi-Energy CT: Principles, Technical Approaches, and Clinical Applications*. Radiology, 2015. **276**(3): p. 637-53.
12. Rutherford, R.A., B.R. Pullan, and I. Isherwood, *Measurement of effective atomic number and electron density using an EMI scanner*. Neuroradiology, 1976. **11**(1): p. 15-21.
13. Genant, H.K. and D. Boyd, *Quantitative bone mineral analysis using dual energy computed tomography*. Invest Radiol, 1977. **12**(6): p. 545-51.
14. Chiro, G.D., et al., *Tissue signatures with dual-energy computed tomography*. Radiology, 1979. **131**(2): p. 521-3.
15. Millner, M.R., et al., *Extraction of information from CT scans at different energies*. Med Phys, 1979. **6**(1): p. 70-1.
16. Kelcz, F., P.M. Joseph, and S.K. Hilal, *Noise considerations in dual energy CT scanning*. Med Phys, 1979. **6**(5): p. 418-25.
17. Schwarz, F., et al., *Dual-energy CT of the heart--principles and protocols*. Eur J Radiol, 2008. **68**(3): p. 423-33.
18. Johnson, T.R., et al., *Material differentiation by dual energy CT: initial experience*. Eur Radiol, 2007. **17**(6): p. 1510-7.
19. Flohr, T., et al., *Photon-counting CT review*. Phys Med, 2020. **79**: p. 126-136.
20. Kulkarni, N.M., et al., *Determination of renal stone composition in phantom and patients using single-source dual-energy computed tomography*. J Comput Assist Tomogr, 2013. **37**(1): p. 37-45.

21. Vlahos, I., et al., *Dual-energy CT: vascular applications*. AJR Am J Roentgenol, 2012. **199**(5 Suppl): p. S87-97.
22. Goo, H.W. and J.M. Goo, *Dual-Energy CT: New Horizon in Medical Imaging*. Korean J Radiol, 2017. **18**(4): p. 555-569.
23. Yu, L., S. Leng, and C.H. McCollough, *Dual-energy CT-based monochromatic imaging*. AJR Am J Roentgenol, 2012. **199**(5 Suppl): p. S9-s15.
24. Kuchenbecker, S., et al., *Dual energy CT: how well can pseudo-monochromatic imaging reduce metal artifacts?* Med Phys, 2015. **42**(2): p. 1023-36.
25. Patino, M., et al., *Material Separation Using Dual-Energy CT: Current and Emerging Applications*. Radiographics, 2016. **36**(4): p. 1087-105.
26. Megibow, A.J., A. Kambadakone, and L. Ananthakrishnan, *Dual-Energy Computed Tomography: Image Acquisition, Processing, and Workflow*. Radiol Clin North Am, 2018. **56**(4): p. 507-520.
27. Kikano, E.G., et al., *Utility of Iodine Density Perfusion Maps From Dual-Energy Spectral Detector CT in Evaluating Cardiothoracic Conditions: A Primer for the Radiologist*. AJR Am J Roentgenol, 2020. **214**(4): p. 775-785.
28. Bredella, M.A., et al., *Marrow Adipose Tissue Quantification of the Lumbar Spine by Using Dual-Energy CT and Single-Voxel (1)H MR Spectroscopy: A Feasibility Study*. Radiology, 2015. **277**(1): p. 230-5.
29. Gibney, B., et al., *A Review of the Applications of Dual-Energy CT in Acute Neuroimaging*. Can Assoc Radiol J, 2020. **71**(3): p. 253-265.
30. Schoepf, U.J. and P.M. Colletti, *New dimensions in imaging: the awakening of dual-energy CT*. AJR Am J Roentgenol, 2012. **199**(5 Suppl): p. S1-2.

31. Cavallo, A.U., et al., *Low dose contrast CT for transcatheter aortic valve replacement assessment: Results from the prospective SPECTACULAR study (spectral CT assessment prior to TAVR)*. J Cardiovasc Comput Tomogr, 2020. **14**(1): p. 68-74.
32. Bae, K., et al., *Improved Opacification of a Suboptimally Enhanced Pulmonary Artery in Chest CT: Experience Using a Dual-Layer Detector Spectral CT*. AJR Am J Roentgenol, 2018. **210**(4): p. 734-741.
33. Patel, A.A., et al., *Arterial Phase CTA Replacement by a Virtual Arterial Phase Reconstruction from a Venous Phase CTA: Preliminary Results Using Detector-Based Spectral CT*. Cardiovasc Intervent Radiol, 2019. **42**(2): p. 250-259.
34. Jawad, S., et al., *Acute Pulmonary Embolism Severity Assessment Evaluated with Dual Energy CT Perfusion Compared to Conventional CT Angiographic Measurements*. Diagnostics (Basel), 2021. **11**(3).
35. Rotzinger, D.C., et al., *CT Pulmonary Angiography for Risk Stratification of Patients with Nonmassive Acute Pulmonary Embolism*. Radiol Cardiothorac Imaging, 2020. **2**(4): p. e190188.
36. Jin, K.N., et al., *Myocardial perfusion imaging with dual energy CT*. Eur J Radiol, 2016. **85**(10): p. 1914-1921.
37. Hur, J., et al., *Cardioembolic stroke: dual-energy cardiac CT for differentiation of left atrial appendage thrombus and circulatory stasis*. Radiology, 2012. **263**(3): p. 688-95.
38. Ohta, Y., et al., *Myocardial Delayed Enhancement CT for the Evaluation of Heart Failure: Comparison to MRI*. 2018. **288**(3): p. 682-691.

39. Graça Santos, L., et al., *Dual-energy cardiac computed tomography: the 'one-stop-shop' for acute myocarditis*. Eur Heart J Cardiovasc Imaging, 2021. **22**(1): p. 129.
40. Darras, K.E., et al., *Virtual monoenergetic reconstruction of contrast-enhanced dual energy CT at 70keV maximizes mural enhancement in acute small bowel obstruction*. Eur J Radiol, 2016. **85**(5): p. 950-6.
41. Lourenco, P.D.M., et al., *Dual-Energy CT Iodine Mapping and 40-keV Monoenergetic Applications in the Diagnosis of Acute Bowel Ischemia*. AJR Am J Roentgenol, 2018. **211**(3): p. 564-570.
42. Neuhaus, V., et al., *Metal artifact reduction by dual-layer computed tomography using virtual monoenergetic images*. Eur J Radiol, 2017. **93**: p. 143-148.
43. Persson, A., et al., *Advances of dual source, dual-energy imaging in postmortem CT*. Eur J Radiol, 2008. **68**(3): p. 446-55.
44. Lee, Y.H., et al., *Metal artefact reduction in gemstone spectral imaging dual-energy CT with and without metal artefact reduction software*. Eur Radiol, 2012. **22**(6): p. 1331-40.
45. Symons, R., et al., *Feasibility of Dose-reduced Chest CT with Photon-counting Detectors: Initial Results in Humans*. Radiology, 2017. **285**(3): p. 980-989.
46. Thivolet, A., et al., *Spectral photon-counting CT imaging of colorectal peritoneal metastases: initial experience in rats*. Sci Rep, 2020. **10**(1): p. 13394.
47. Danielsson, M., M. Persson, and M. Sjölin, *Photon-counting x-ray detectors for CT*. Phys Med Biol, 2020.
48. Sandfort, V., et al., *Spectral photon-counting CT in cardiovascular imaging*. J Cardiovasc Comput Tomogr, 2020.

49. Benjaminov, O., Perlow, E, Romman, Z, Levinson, R, Bashara, B, Cohen, M, Zelikovsky, A, et al, *Novel, Energy-Discriminating Photon Counting CT System (EDCT): First Clinical Evaluation—CT Angiography: Carotid Artery Stenosis*, in *Radiological Society of North America 2008 Scientific Assembly and Annual Meeting*, RSNA, Editor. 2008: Chicago, IL.
50. Yu, Z., et al., *Noise performance of low-dose CT: comparison between an energy integrating detector and a photon counting detector using a whole-body research photon counting CT scanner*. J Med Imaging (Bellingham), 2016. **3**(4): p. 043503.
51. Si-Mohamed, S., et al., *Review of an initial experience with an experimental spectral photon-counting computed tomography system*. Nuclear Instruments and Methods in Physics Research Section A, Accelerators, Spectrometers, Detectors and Associated Equipment, 2017: p. 27-35.
52. Samsung. *Samsung Introduces Its Latest Radiology Innovations at RSNA 2020*. 2020 [cited 2021 May 5]; Available from: <https://news.samsung.com/global/samsung-introduces-its-latest-radiology-innovations-at-rsna-2020>.
53. Sundberg, C., et al., *Silicon photon-counting detector for full-field CT using an ASIC with adjustable shaping time*. J Med Imaging (Bellingham), 2020. **7**(5): p. 053503.
54. Grönberg, F., et al., *Feasibility of unconstrained three-material decomposition: imaging an excised human heart using a prototype silicon photon-counting CT detector*. Eur Radiol, 2020. **30**(11): p. 5904-5912.
55. Bolotnikov, A.E., et al., *Factors limiting the performance of CdZnTe detectors*. IEEE Transactions on Nuclear Science, 2005. **52**(3): p. 589-598.

56. Rafati Rahimzadeh, M., et al., *Cadmium toxicity and treatment: An update*. Caspian journal of internal medicine, 2017. **8**(3): p. 135-145.
57. Wang, J., et al., *Quantification of iron in the presence of calcium with dual-energy computed tomography (DECT) in an ex vivo porcine plaque model*. Phys Med Biol, 2011. **56**(22): p. 7305-16.
58. Si-Mohamed, S., et al., *Spectral Photon-Counting Computed Tomography (SPCCT): in-vivo single-acquisition multi-phase liver imaging with a dual contrast agent protocol*. Sci Rep, 2019. **9**(1): p. 8458.
59. Moghiseh, M., et al., *Spectral Photon-Counting Molecular Imaging for Quantification of Monoclonal Antibody-Conjugated Gold Nanoparticles Targeted to Lymphoma and Breast Cancer: An *In Vitro* Study*. Contrast Media & Molecular Imaging, 2018. **2018**: p. 2136840.
60. Taguchi, K. and J.S. Iwanczyk, *Vision 20/20: Single photon counting x-ray detectors in medical imaging*. Med Phys, 2013. **40**(10): p. 100901.
61. Hsieh, S.S. and N.J. Pelc, *Improving pulse detection in multibin photon-counting detectors*. Journal of medical imaging (Bellingham, Wash.), 2016. **3**(2): p. 023505-023505.
62. Gutjahr, R., et al., *Human Imaging With Photon Counting-Based Computed Tomography at Clinical Dose Levels: Contrast-to-Noise Ratio and Cadaver Studies*. Invest Radiol, 2016. **51**(7): p. 421-9.
63. Ferda, J., et al., *Computed tomography with a full FOV photon-counting detector in a clinical setting, the first experience*. Eur J Radiol, 2021. **137**: p. 109614.

64. Goodman, T.R., A. Mustafa, and E. Rowe, *Pediatric CT radiation exposure: where we were, and where we are now*. *Pediatr Radiol*, 2019. **49**(4): p. 469-478.
65. Symons, R., et al., *Photon-Counting Computed Tomography for Vascular Imaging of the Head and Neck: First In Vivo Human Results*. *Invest Radiol*, 2018. **53**(3): p. 135-142.
66. Shikhaliev, P.M., *Soft tissue imaging with photon counting spectroscopic CT*. *Phys Med Biol*, 2015. **60**(6): p. 2453-74.
67. Si-Mohamed, S., et al., *Feasibility of lung imaging with a large field-of-view spectral photon-counting CT system*. *Diagn Interv Imaging*, 2021.
68. Bratke, G., et al., *Spectral Photon-Counting Computed Tomography for Coronary Stent Imaging: Evaluation of the Potential Clinical Impact for the Delineation of In-Stent Restenosis*. *Invest Radiol*, 2020. **55**(2): p. 61-67.
69. Sigovan, M., et al., *Feasibility of improving vascular imaging in the presence of metallic stents using spectral photon counting CT and K-edge imaging*. *Sci Rep*, 2019. **9**(1): p. 19850.
70. Lee, C.L., et al., *Metal artifact reduction and tumor detection using photon-counting multi-energy computed tomography*. *PLoS One*, 2021. **16**(3): p. e0247355.
71. Si-Mohamed, S., et al., *Evaluation of spectral photon counting computed tomography K-edge imaging for determination of gold nanoparticle biodistribution in vivo*. *Nanoscale*, 2017. **9**(46): p. 18246-18257.
72. Otrakji, A., et al., *Dual-Energy CT: Spectrum of Thoracic Abnormalities*. *Radiographics*, 2016. **36**(1): p. 38-52.

73. Goo, H.W., *Dual-energy lung perfusion and ventilation CT in children*. *Pediatr Radiol*, 2013. **43**(3): p. 298-307.
74. Li, X., et al., *Gemstone spectral imaging dual-energy computed tomography: a novel technique to determine urinary stone composition*. *Urology*, 2013. **81**(4): p. 727-30.
75. Alzen, G. and G. Benz-Bohm, *Radiation protection in pediatric radiology*. *Dtsch Arztebl Int*, 2011. **108**(24): p. 407-14.
76. Maddox, T.G., *Adverse reactions to contrast material: recognition, prevention, and treatment*. *Am Fam Physician*, 2002. **66**(7): p. 1229-34.
77. Lohöfer, F.K., et al., *Improved detection rates and treatment planning of head and neck cancer using dual-layer spectral CT*. *Eur Radiol*, 2018. **28**(12): p. 4925-4931.
78. Døssing, A., et al., *Dual-Energy Computed Tomography for Detection and Characterization of Monosodium Urate, Calcium Pyrophosphate, and Hydroxyapatite: A Phantom Study on Diagnostic Performance*. *Invest Radiol*, 2021. **56**(7): p. 417-424.
79. Alessio, A.M. and L.R. MacDonald, *Quantitative material characterization from multi-energy photon counting CT*. *Med Phys*, 2013. **40**(3): p. 031108.
80. Spectral Photon Counting Computed Tomography (SPCCT) project. *For an improved detection and monitoring of cardiovascular and neurovascular diseases*. 2017 [cited 2021 May 5]; Available from: <http://www.spcct.eu/ambition.html>.
81. Hunink, M.G., *Outcomes research and cost-effectiveness analysis in radiology*. *Eur Radiol*, 1996. **6**(5): p. 615-20.

82. Wolf, G.L., *Poor quality of clinical research in radiology: another indictment.* Radiology, 1989. **170**(2): p. 311-2.
83. Blackmore, C.C., *The challenge of clinical radiology research.* AJR Am J Roentgenol, 2001. **176**(2): p. 327-31.
84. Blackmore, C.C., et al., *A critical synopsis of the diagnostic and screening radiology outcomes literature.* Acad Radiol, 1999. **6 Suppl 1**: p. S8-18.
85. Zygmunt, M.E., et al., *Radiology Research in Quality and Safety: Current Trends and Future Needs.* Acad Radiol, 2017. **24**(3): p. 263-272.
86. Verdun, F.R., et al., *Image quality in CT: From physical measurements to model observers.* Phys Med, 2015. **31**(8): p. 823-843.
87. Ghani, M.U., et al., *Investigation of spatial resolution characteristics of an in vivo micro computed tomography system.* Nuclear instruments & methods in physics research. Section A, Accelerators, spectrometers, detectors and associated equipment, 2016. **807**: p. 129-136.
88. Racine, D., et al., *Objective comparison of high-contrast spatial resolution and low-contrast detectability for various clinical protocols on multiple CT scanners.* Med Phys, 2017. **44**(9): p. e153-e163.
89. Rotzinger, D.C., et al., *Task-Based Model Observer Assessment of A Partial Model-Based Iterative Reconstruction Algorithm in Thoracic Oncologic Multidetector CT.* Sci Rep, 2018. **8**(1): p. 17734.
90. Morsbach, F., et al., *Noise Texture Deviation: A Measure for Quantifying Artifacts in Computed Tomography Images With Iterative Reconstructions.* Invest Radiol, 2017. **52**(2): p. 87-94.

91. Racine, D., et al., *Task-based characterization of a deep learning image reconstruction and comparison with filtered back-projection and a partial model-based iterative reconstruction in abdominal CT: A phantom study*. Phys Med, 2020. **76**: p. 28-37.
92. Bhalla, S. and O.C. West, *CT of nontraumatic thoracic aortic emergencies*. Semin Ultrasound CT MR, 2005. **26**(5): p. 281-304.
93. Romano, L., A. Pinto, and N. Gagliardi, *Multidetector-row CT evaluation of nontraumatic acute thoracic aortic syndromes*. Radiol Med, 2007. **112**(1): p. 1-20.
94. Si-Mohamed, S., et al., *Virtual versus true non-contrast dual-energy CT imaging for the diagnosis of aortic intramural hematoma*. Eur Radiol, 2019. **29**(12): p. 6762-6771.
95. Huber, F.A., et al., *Detection and Characterization of Monosodium Urate and Calcium Hydroxyapatite Crystals Using Spectral Photon-Counting Radiography: A Proof-of-Concept Study*. Eur J Radiol, 2020. **129**: p. 109080.
96. Singh, J.A., et al., *Dual-energy computed tomography versus ultrasound, alone or combined, for the diagnosis of gout: a prospective study of accuracy*. Rheumatology (Oxford), 2021.
97. Pascart, T., et al., *Identification and characterization of peripheral vascular color-coded DECT lesions in gout and non-gout patients: The VASCURATE study*. Semin Arthritis Rheum, 2021. **51**(4): p. 895-902.
98. Kuo, C.F., et al., *Gout: an independent risk factor for all-cause and cardiovascular mortality*. Rheumatology (Oxford), 2010. **49**(1): p. 141-6.

99. Cohen, S.D., et al., *Association of incident gout and mortality in dialysis patients*. J Am Soc Nephrol, 2008. **19**(11): p. 2204-10.
100. Choi, H.K. and G. Curhan, *Independent impact of gout on mortality and risk for coronary heart disease*. Circulation, 2007. **116**(8): p. 894-900.
101. De Vera, M.A., et al., *Independent impact of gout on the risk of acute myocardial infarction among elderly women: a population-based study*. Ann Rheum Dis, 2010. **69**(6): p. 1162-4.
102. Abbott, R.D., et al., *Gout and coronary heart disease: the Framingham Study*. J Clin Epidemiol, 1988. **41**(3): p. 237-42.
103. Krishnan, E., et al., *Gout and the risk of acute myocardial infarction*. Arthritis Rheum, 2006. **54**(8): p. 2688-96.
104. Park, J.J., et al., *Prevalence of birefringent crystals in cardiac and prostatic tissues, an observational study*. BMJ Open, 2014. **4**(7): p. e005308.
105. Carrascosa, P., et al., *Monochromatic image reconstruction by dual energy imaging allows half iodine load computed tomography coronary angiography*. Eur J Radiol, 2015. **84**(10): p. 1915-20.
106. Yi, Y., et al., *Low Dose and Low Contrast Medium Coronary CT Angiography Using Dual-Layer Spectral Detector CT*. Int Heart J, 2019. **60**(3): p. 608-617.
107. Oda, S., et al., *Low contrast material dose coronary computed tomographic angiography using a dual-layer spectral detector system in patients at risk for contrast-induced nephropathy*. Br J Radiol, 2019. **92**(1094): p. 20180215.

108. Raju, R., et al., *Reduced iodine load with CT coronary angiography using dual-energy imaging: a prospective randomized trial compared with standard coronary CT angiography*. J Cardiovasc Comput Tomogr, 2014. **8**(4): p. 282-8.
109. Rotzinger, D.C., et al., *Reduced-iodine-dose dual-energy coronary CT angiography: qualitative and quantitative comparison between virtual monochromatic and polychromatic CT images*. Eur Radiol, 2021.
110. Lin, E. and A. Alessio, *What are the basic concepts of temporal, contrast, and spatial resolution in cardiac CT?* J Cardiovasc Comput Tomogr, 2009. **3**(6): p. 403-8.
111. Rotzinger, D.C., et al., *"Dark-blood" dual-energy computed tomography angiography for thoracic aortic wall imaging*. Eur Radiol, 2020. **30**(1): p. 425-431.
112. Delgado Sánchez-Gracián, C., et al., *Quantitative myocardial perfusion with stress dual-energy CT: iodine concentration differences between normal and ischemic or necrotic myocardium. Initial experience*. Eur Radiol, 2016. **26**(9): p. 3199-207.
113. van Assen, M., et al., *Iodine quantification based on rest / stress perfusion dual energy CT to differentiate ischemic, infarcted and normal myocardium*. Eur J Radiol, 2019. **112**: p. 136-143.
114. Richette, P. and T. Bardin, *Gout*. Lancet, 2010. **375**(9711): p. 318-28.
115. Kuo, C.F., et al., *Global epidemiology of gout: prevalence, incidence and risk factors*. Nat Rev Rheumatol, 2015. **11**(11): p. 649-62.
116. Hajri, R., et al., *Dual-Energy Computed Tomography for the Noninvasive Diagnosis of Coexisting Gout and Calcium Pyrophosphate Deposition Disease*. Arthritis Rheumatol, 2019. **71**(8): p. 1392.

117. Klauser, A.S., et al., *Dual-Energy Computed Tomography Detection of Cardiovascular Monosodium Urate Deposits in Patients With Gout*. JAMA Cardiol, 2019. **4**(10): p. 1019-1028.
118. Becce, F., B. Ghoshhajra, and H.K. Choi, *Identification of Cardiovascular Monosodium Urate Crystal Deposition in Patients With Gout Using Dual-Energy Computed Tomography*. JAMA Cardiol, 2020. **5**(4): p. 486.
119. Qanadli, S.D., A.C. Rocha, and D.C. Rotzinger, *Case Report: Intrapulmonary Arteriovenous Anastomoses in COVID-19-Related Pulmonary Vascular Changes: A New Player in the Arena?* Front Med (Lausanne), 2021. **8**: p. 639152.
120. Qanadli, S.D., et al., *Vascular Abnormalities Detected with Chest CT in COVID-19: Spectrum, Association with Parenchymal Lesions, Cardiac Changes, and Correlation with Clinical Severity (COVID-CAVA Study)*. Diagnostics (Basel), 2021. **11**(4).
121. Rotzinger, D.C., et al., *Pulmonary embolism in patients with COVID-19: Time to change the paradigm of computed tomography*. Thromb Res, 2020. **190**: p. 58-59.
122. Qanadli, S.D., C. Beigelman-Aubry, and D.C. Rotzinger, *Vascular Changes Detected With Thoracic CT in Coronavirus Disease (COVID-19) Might Be Significant Determinants for Accurate Diagnosis and Optimal Patient Management*. AJR Am J Roentgenol, 2020. **215**(1): p. W15.
123. Santamarina, M.G., et al., *COVID-19: What Iodine Maps From Perfusion CT can reveal-A Prospective Cohort Study*. Crit Care, 2020. **24**(1): p. 619.

124. Arru, C.D., et al., *Qualitative and quantitative DECT pulmonary angiography in COVID-19 pneumonia and pulmonary embolism*. Clin Radiol, 2021. **76**(5): p. 392.e1-392.e9.
125. Rotzinger, D.C., et al., *Pulmonary angioplasty: A step further in the continuously changing landscape of chronic thromboembolic pulmonary hypertension management*. Eur J Radiol, 2021. **136**: p. 109562.
126. Leng, S., et al., *150- μ m Spatial Resolution Using Photon-Counting Detector Computed Tomography Technology: Technical Performance and First Patient Images*. Invest Radiol, 2018. **53**(11): p. 655-662.
127. Rajendran, K., et al., *High resolution, full field-of-view, whole body photon-counting detector CT: system assessment and initial experience*. SPIE Medical Imaging. Vol. 11595. 2021: SPIE.
128. Symons, R., et al., *Optimized energy of spectral coronary CT angiography for coronary plaque detection and quantification*. J Cardiovasc Comput Tomogr, 2018. **12**(2): p. 108-114.
129. Laukamp, K.R., et al., *Role of spectral-detector CT in reduction of artifacts from contrast media in axillary and subclavian veins: single institution study in 50 patients*. Acta Radiologica, 2020. **61**(4): p. 450-460.
130. Laukamp, K.R., et al., *CT artifacts from port systems: Virtual monoenergetic reconstructions from spectral-detector CT reduce artifacts and improve depiction of surrounding tissue*. European Journal of Radiology, 2019. **121**: p. 108733.
131. Secchi, F., et al., *Monoenergetic extrapolation of cardiac dual energy CT for artifact reduction*. Acta Radiol, 2015. **56**(4): p. 413-8.

132. Rajendran, K., et al., *Reducing beam hardening effects and metal artefacts in spectral CT using Medipix3RX*. Journal of Instrumentation, 2014. **9**(03): p. P03015-P03015.
133. Vanden Broeke, L., et al., *Feasibility of photon-counting spectral CT in dental applications—a comparative qualitative analysis*. BDJ Open, 2021. **7**(1): p. 4.
134. Scholz, J., et al., *Biomedical x-ray imaging with a GaAs photon-counting detector: A comparative study*. APL Photonics, 2020. **5**(10): p. 106108.
135. Rougé-Labriet, H., et al., *X-ray Phase Contrast osteo-articular imaging: a pilot study on cadaveric human hands*. Scientific Reports, 2020. **10**(1): p. 1911.
136. Hetterich, H., et al., *Phase-Contrast CT: Qualitative and Quantitative Evaluation of Atherosclerotic Carotid Artery Plaque*. Radiology, 2014. **271**(3): p. 870-878.
137. Bernard, A., et al., *Deep learning reconstruction versus iterative reconstruction for cardiac CT angiography in a stroke imaging protocol: reduced radiation dose and improved image quality*. Quant Imaging Med Surg, 2021. **11**(1): p. 392-401.
138. Si-Mohamed, S., et al., *Spectral Photon-Counting Computed Tomography (SPCCT): in-vivo single-acquisition multi-phase liver imaging with a dual contrast agent protocol*. Scientific Reports, 2019. **9**(1): p. 8458.
139. Rotzinger, D.C., et al. *Coronary CT angiography for the assessment of atherosclerotic plaque inflammation: post-mortem proof of concept with histological validation*. in *Association for european cardiovascular pathology biennial meeting*. 2021. Cambridge, UK.
140. Jorgensen, S.M., et al., *Arterial Wall Perfusion Measured with Photon Counting Spectral X-ray CT*. Proc SPIE Int Soc Opt Eng, 2016. **9967**.

Conference proceedings

First author

1. Rotzinger DC, Si-Mohamed SA, Matzuzzi M, Bousset L, Hanquier L, Douek P. First-pass myocardial perfusion using dual-layer detector CT in healthy subjects: impact of spectral reconstructions. In: joint meeting of ESTI and ESCR (European Society of Thoracic Imaging and European Society of Cardiovascular Radiology), Geneva, Switzerland, May 24-26, 2018
2. Rotzinger DC, Si-Mohamed S, Douek PC, Bousset L. "Dark Blood" Dual-Energy CT Imaging Using a Dedicated Material Decomposition Method. In: The Radiological Society of North America's (RSNA) 104th Scientific Assembly and Annual Meeting, Chicago, USA, November 25-30, 2018
3. Rotzinger DC, Si-Mohamed S, Douek PC, Bousset L. New dual-energy CT angiography method to generate "dark blood" images. In: European Congress of Radiology, Vienna, Austria, February 27 - March 3, 2019
4. Rotzinger DC, Si-Mohamed S, Bousset L, Bouin M, Meuli RA, Douek PC. Prospective noninferiority study of low iodine dose dual-layer spectral detector coronary CT angiography. In: ESCR (European Society of Cardiovascular Radiology) annual meeting, Antwerp, Belgium, October 24-26, 2019
5. Rotzinger DC, Si-Mohamed SA, Bousset L, Meuli RA, Douek PC. A prospective randomized non-inferiority study of low iodine dual-energy coronary CT-angiography. In: European Congress of Radiology, virtual meeting, July 15 – 19, 2020

6. Rotzinger DC, Si-Mohamed S, Yerly J, Becce F, Bousset L, Meuli RA, Douek PC. Reduced-Iodine-Dose Dual-Energy Coronary CT Angiography Compared with Conventional CT: Non-Inferiority Study. In: ARRS (American Roentgen Ray Society) annual meeting, online event, April 18 – 22, 2021
7. Rotzinger DC, Racine D, Becce F, Lahoud E, Erhard K, Si-Mohamed S, Greffier J, Meuli RA, Douek PC. Model observer assessment of photon-counting-detector coronary CT angiography and comparison with energy-integrating-detector CT. In: European Congress of Radiology, Vienna, Austria, March 3-7, 2021
8. Rotzinger DC, Si-Mohamed SA, Yerly J, Becce F, Qanadli SD, Meuli RA, Douek PC. Reduced-iodine-dose dual-energy coronary CT angiography compared with conventional CT: a non-inferiority study. In: Swiss Congress of Radiology, Online event, 2021
9. Rotzinger DC, Racine D, Becce F, Erhard K, Lahoud E, Si-Mohamed SA, Greffier J, Meuli RA, Douek PC. Task-based evaluation of photon-counting-detector coronary CT angiography and comparison with energy-integrating-detector CT. In: Swiss Congress of Radiology, Online event, 2021

Co-author

1. Si-Mohamed S, Dion M, Dupuis N, Rotzinger D, Douek P, Bousset L. Apport diagnostique des images virtuellement sans contraste pour l'hématome

- aortique intra-mural. In: Journées Francophones de Radiologie Diagnostique et Interventionnelle (JFR), Paris, France, October 12-15, 2018
2. Si-Mohamed SA, Dupuis N, Rotzinger DC, Boccalini S, Yagil Y, Coulon P, Shapira N, Douek P, Boussel L. Virtual non contrast imaging of aortic intramural hematoma for replacing the non contrast CT imaging. In: European Congress of Radiology, Vienna, Austria, February 27 - March 3, 2019
 3. Boccalini S, Si-Mohammed SA, Matzuzzi M, Plaine B, Rotzinger DC, Hanquier L, Boussel L, Revel D, Douek P. Characteristics of first-pass myocardial iodine distribution as assessed by dual layer CT with different injection protocols. In: European Congress of Radiology, Vienna, Austria, February 27 - March 3, 2019
 4. Boccalini S, Si-Mohamed SA, Matzuzzi M, Tillier M, Rotzinger DC, Hanquier L, Boussel L, Revel D, Douek PC. Effect of non-significant plaques on first pass myocardial iodine concentration at different injection protocols. In: ESCR (European Society of Cardiovascular Radiology) annual meeting, Antwerp, Belgium, October 24-26, 2019
 5. Huber FA, Becce F, Zadory M, Rotzinger D, Froehlich JM, Schmidt B, Jürgens M, Eurler A, Alkadhi H, Guggenberger R. Crystal characterization and differentiation by spectral photon-counting CT: Initial results with the first clinical scanner of its generation. In: The Radiological Society of North America's (RSNA) Scientific Assembly and Annual Meeting, Chicago, USA, November 28 – December 2, 2021

Curriculum vitae

Dr. med. David C. Rotzinger

PERSONAL DETAILS

Name, First name : Rotzinger, David Christian
Gender : Male
Date of birth : 11.07.1984
Nationality : Swiss
Languages : French, English and German
Prof. address : Department of Diagnostic and Interventional Radiology
Lausanne University Hospital (CHUV)
Rue du Bugnon 46, 1011 Lausanne, Switzerland

E-mail david.rotzinger@chuv.ch,

Web <https://www.chuv.ch/fr/rad/rad-home/le-service-en-bref/nos-collaborateurs/medecins-cadres/dr-d-rotzinger>

1. CURRENT POSITIONS AND FUNCTIONS

- Attending Physician, Cardiothoracic and Vascular Division, Department of Diagnostic and Interventional Radiology, CHUV, Lausanne
- Invited research fellow, Lyon University Hospital HCL
- Board member of Swiss board certification examination in Radiology (FMH I)

2. EDUCATION

2004 – 2010 : Medical degree, Faculty of Biology and Medicine, University of Lausanne
2013 : Swiss Medical Board of Radiology (FMH), Part 1
2016 : Swiss Medical Board of Radiology (FMH), Part 2
2016 : Swiss Diploma of Radiology (FMH)

- 2017 : Doctorate in Medicine (MD), “Site and rate of occlusive disease in cervicocerebral arteries: a CT angiography study of 2209 patients with Ischemic stroke”, University of Lausanne
- 2018-2021 (expected) : Doctorate of Philosophy (PhD), “Assessment of the arterial wall with spectral computed tomography”, University of Lausanne
- 2021 : Executive management course, Lausanne University Hospital

3. PROFESSIONAL AND ACADEMIC EXPERIENCE

- 2011 – 2015 : Resident, Department of Diagnostic and Interventional Radiology, CHUV, Lausanne, Prof. Reto A. Meuli
- 2015 – 2016 : Resident, Emergency department, CHUV, Lausanne, Prof. Bertrand Yersin
- 2015 : Radiologic-Pathologic Correlation Course, American Institute for Radiologic Pathology, Washington, D.C., Prof. Mark Murphey
- 2016 : Chief resident in emergency radiology, CHUV, Lausanne, Prof. Reto Meuli
- 2017-2018 : Clinical and research fellow in cardiovascular radiology, Hospices Civils de Lyon (HCL), Hôpital Louis Pradel, Prof. Philippe Douek
- 2018-2019 : Chief resident in cardiothoracic and vascular radiology, Department of Diagnostic and Interventional Radiology, CHUV, Lausanne, Prof. Reto Meuli
- 2019-2020 : Attending physician (médecin hospitalier) in cardiothoracic and vascular radiology, Department of Diagnostic and Interventional Radiology, CHUV, Lausanne, Prof. Reto Meuli
- 2020-2021 : Attending physician (médecin hospitalier) in cardiothoracic and vascular radiology, Department of Diagnostic and Interventional Radiology, CHUV, Lausanne, Prof. Alban Denys
- Since 2021 : Senior attending physician (médecin associé) in cardiothoracic and vascular radiology, Department of Diagnostic and Interventional Radiology, CHUV, Lausanne, Prof. Alban Denys

4. GRANTS/MAIN RESEARCH PROJECTS AS LEADING INVESTIGATOR

- “Identification and quantification of monosodium urate crystals in coronary atheroma” – PI: David C. Rotzinger (RAD-CHUV); Co-applicants: Fabio Becce (RAD-CHUV), Reto Meuli (RAD-CHUV), Francis R. Verdun (IRA-CHUV), Anais Viry (IRA-CHUV). University of Lyon partners: Philippe Douek, Loïc Bousset, Salim Si-Mohamed. Amount granted by Alliance Campus Rhodanien-UNIL: 16’000.- CHF
- “Comparative assessment of spectral coronary computed tomography angiography using reduced iodine dose”. PIs: David Rotzinger (RAD-CHUV). Amount granted by the Leenaards Foundation: 120’000 CHF.

5. SUPERVISED MMed, MD or PhD THESES

- Guillaume Jordan “Chest radiography findings in coronavirus 19 disease (COVID-19) pneumonia”, University of Lausanne, 2020 – 2021, MMed thesis co-director
- Jose Moreira Lopes “Characteristics of coronary plaques by postmortem small spectral CT”, University of Lausanne, 2020 – 2021, MMed thesis co-director

6. PRIZES AND DISTINGUISHED MEMBERSHIPS

a. Prizes

- AECVP, Cambridge, 2021 : Association for European Cardiovascular Pathology biennial meeting. Best free oral presentation award: Coronary CT angiography for the assessment of atherosclerotic plaque inflammation: post-mortem proof of concept with histological validation
- ESCR, Antwerp, 2019 : European Society for Cardiovascular Radiology annual meeting’s 10 best abstracts award: “Prospective noninferiority study of low iodine dose dual-layer spectral detector coronary CT angiography.”
- SCR, Lausanne, 2019 : Swiss Congress of Radiology. Best educational poster award: “Extracorporeal Membrane Oxygenation (ECMO) and contrast-enhanced CT: What needs the radiologist to know?”
- JFR, Paris, 2019 : Journées Francophones de Radiologie. Best electronic poster award: “Spectral CT: a technological advance at the service of the cardiovascular radiologist.”
- UNIL, Lausanne, 2018 : Lausanne University’s Faculty of Biology and Medicine award of excellence: “Site and rate of occlusive disease in cervicocerebral

- arteries: a CT angiography study of 2209 patients with Ischemic stroke.”
- ESCR, Geneva, 2018 : European Society for Cardiovascular Radiology annual meeting. “Young Abstract Presenter Programme (YAPP) 2018” award: “First-pass myocardial perfusion using dual-layer detector CT in healthy subjects: impact of spectral reconstructions.”
- ECR, Vienna, 2017 : European Congress of Radiology. “Invest In the Youth”, ESR (European Society of Radiology) award: “Site and rate of arterial occlusive disease in acute ischemic stroke: a CT angiography study of 50’807 cervico-cerebral arterial segments.”
- AIRP, Washington, 2015 : American Institute for Radiologic Pathology best case award: “Retroperitoneal leiomyosarcoma arising from the left ovarian vein.”

b. Distinguished Memberships

- Committee member (Anatomy) of Swiss Medical Board of Radiology (FMH), Part 1

7. MEMBERSHIPS IN PROFESSIONAL SOCIETIES

Swiss Society of Radiology, European Society of Radiology, American Roentgen Ray Society, Swiss Medical Association, Société Vaudoise de Médecine, section Vaud, European Society of Cardiovascular Radiology, Radiological Society of North America

8. TEACHING

Medical students (Faculty of Biology and Medicine, Lausanne University), hours/year

- Cardiovascular, respiratory, and musculoskeletal case reviews (5 hours)
- Imaging modalities and workflows in the Radiology Department (4 hours)
- Anatomy of the heart and great vessels (2 hours)
- Anatomy of the chest wall and pleural cavity (2 hours)
- Interactive radiology case review, 3 hours per year

Radiology residents (Lausanne University Hospital, CHUV), hours/year

- CT radiation protection for technologists (3 hours)
- Cardiac CT in the emergency department; how to acquire images, post-process, interpret and report? (2 hours)
- Coronary CT acquisition technique (1 hour)

- Cardiac CT post-processing using the Advantage Workstation (AW): basics and advanced applications (4 hours)
- Cardiac and aortic CT angiography prior to TAVI. Image acquisition and interpretation (1 hour)

9. EDITORIAL/REVIEWER EXPERIENCE

a. Journal Reviewer

European Respiratory Journal, Chest, Neuroradiology, European Radiology, Thrombosis Research, American Journal of Roentgenology, American Journal of Cardiology, The International Journal of Cardiovascular Imaging, Journal of Thrombosis and Thrombolysis, PlosOne, Quantitative Imaging in Medicine and Surgery, European Journal of Radiology, Frontiers in Cardiovascular Medicine, Frontiers in Medicine, Scientific Reports

b. Journal Editor

- Frontiers in Medicine, Frontiers in Cardiovascular Medicine
- European Radiology COVID-19 triage team member (Assistant to Editor-in-Chief for expedited COVID-19 manuscript processing)

10. PUBLICATION LIST

Most of the publications referenced below are available through these links:

<https://orcid.org/0000-0002-6321-3180>

<https://pubmed.ncbi.nlm.nih.gov/?term=rotzinger+d>

https://www.researchgate.net/profile/David_Rotzinger

a. Publications in international peer-reviewed scientific journals

1. Romascano D., Meskaldji D.E., Bonnier G., Simioni S., **Rotzinger D.**, Lin Y.C., Menegaz G., Roche A., Schlupe M., Pasquier R.D. et al., Multicontrast connectometry: A new tool to assess cerebellum alterations in early relapsing-remitting multiple sclerosis. *Human Brain Mapping*. 2015
2. Simioni S., Amarù F., Bonnier G., Kober T., **Rotzinger D.**, Du Pasquier R., Schlupe M., Meuli R., Sbarbati A., Thiran J.P. et al., MP2RAGE provides new clinically-compatible correlates of mild cognitive deficits in relapsing-remitting multiple sclerosis. *Journal of Neurology*. 2014
3. Bonnier G., Roche A., Romascano D., Simioni S., Meskaldji D.E., **Rotzinger D.**, Lin Y.C., Menegaz G., Schlupe M., Du Pasquier R. et al., Multicontrast MRI Quantification of Focal Inflammation and Degeneration in Multiple Sclerosis. *Biomed Research International*. 2015
4. Bonnier G., Roche A., Romascano D., Simioni S., Meskaldji D., **Rotzinger D.**, Lin Y.C., Menegaz G., Schlupe M., Du Pasquier R. et al., Advanced MRI unravels the nature of tissue alterations in early multiple sclerosis. *Annals of Clinical and Translational Neurology*. 2014
5. Fartaria MJ, Bonnier G, Roche A, Kober T, Meuli R, **Rotzinger D**, Frackowiak R, Schlupe M, Du Pasquier R, Thiran JP, Krueger G, Bach Cuadra M, Granziera C. Automated detection of white matter and cortical lesions in early stages of multiple sclerosis. *J Magn Reson Imaging*. 2016
6. Tagliabue L, **Rotzinger D**, Hugli O. Hemoperitoneum after blunt abdominal trauma 27 years after splenectomy: better think twice. *Am J Emerg Med*. 2016
7. **Rotzinger DC**, Mosimann PJ, Meuli RA, Maeder P, Michel P Site and rate of occlusive disease in cervicocerebral arteries: a CT angiography study of 2209 patients with acute ischemic stroke. *AJNR*. 2017
8. Guenego A, Zerlauth JB, Puccinelli F, Hajdu S, **Rotzinger DC**, Zibold F, Piechowiak EI, Mordasini P, Gralla J, Dobrocky T, Daniel RT, Chapot R, Mosimann PJ. Balloon-assisted coil embolization and large stent delivery for cerebral aneurysms with a new generation of dual lumen balloons (Copernic 2L). *J Neurointerv Surg*. 2017
9. Meyer IA, Cereda CW, Correia PN, Zerlauth JB, Puccinelli F, **Rotzinger DC**, Amiguet M, Maeder P, Meuli RA, Michel P. Factors Associated With Focal Computed Tomographic Perfusion

Abnormalities in Supratentorial Transient Ischemic Attacks. *Stroke*. 2017

10. Milani B, Ledoux JB, **Rotzinger DC**, Kanemitsu M, Vallée JP, Burnier M, Pruijm M. Image acquisition for intravoxel incoherent motion imaging of kidneys should be triggered at the instant of maximum blood velocity: evidence obtained with simulations and in vivo experiments. *Magn Reson Med*. 2018
11. **Rotzinger DC**, Racine D, Beigelman-Aubry C, Alfudhili KM, Keller N, Monnin P, Verdun FR, Becce F. Task-based model observer assessment of a partial model-based iterative reconstruction algorithm in thoracic oncologic multidetector CT. *Sci Rep*. 2018.
12. **Rotzinger DC**, Breault S, Knebel JF, Beigelman-Aubry C, Jouannic AM, Qanadli SD. Can a Trained Radiology Technician Do Arterial Obstruction Quantification in Patients With Acute Pulmonary Embolism? *Front Cardiovasc Med*. 2019
13. **Rotzinger DC**, Si-Mohamed SA, Shapira N, Douek PC, Meuli RA, Bousset L. “Dark-Blood” dual-energy computed tomography angiography for thoracic aortic wall imaging. *Eur Radiol*. 2019
14. Si-Mohamed S, Dupuis N, Tatard-Leitman V, **Rotzinger D**, Boccalini S, Dion M, Vlassenbroek A, Coulon P, Yagil Y, Shapira N, Douek P, Bousset L. Virtual versus true non-contrast dual-energy CT imaging for the diagnosis of aortic intramural hematoma. *Eur Radiol*. 2019
15. Tzimas G, **Rotzinger DC**, Muller O, Monney P. Myocardial oedema detected by T2-mapping: a key marker of recent ischaemia after resuscitated sudden cardiac death. *Eur Heart J Cardiovasc Imaging*. 2019
16. Demars Y, Barchi M, Marino L, ProdHom S, **Rotzinger D**, Vollenweider P. Une hyponatrémie inhabituelle. *Swiss Medical Forum*. 2019
17. **Rotzinger DC**, Dunet V, Ilic V, Hugli OW, Meuli RA, Schmidt S. Pulmonary embolism during pregnancy: a 17-year single-center retrospective MDCT pulmonary angiography study. *Eur Radiol*. 2020
18. Meier D, Skolidis I, De Bruyne B, Qanadli SD, **Rotzinger D**, Eeckhout E, Collet C, Muller O, Fournier S. Ability of FFR-CT to detect the absence of hemodynamically significant lesions in patients with high-risk NSTEMI-ACS admitted in the emergency department with chest pain, study design and rationale. *Int J Cardiol Heart Vasc*. 2020
19. Rubimbura V, **Rotzinger D**, Eeckhout E, Rutz T. Multimodality imaging for percutaneous closure of a post-surgical aorta to left ventricular tract outflow fistula. *Eur Heart J*. 2020
20. Qanadli SD, Beigelman-Aubry C, **Rotzinger DC**. Vascular changes detected with thoracic CT in coronavirus disease (COVID-19) might be significant determinants for accurate diagnosis and optimal patient management. *Am J Roentgenol*. 2020
21. **Rotzinger DC**, Lu TL, Kawkabani A, Marques-Vidal P, Fetz G, Qanadli SD. Computed

- tomography angiography in peripheral arterial disease: Comparison of three image acquisition techniques to optimize vascular enhancement – Randomized Controlled Trial. *Front Cardiovasc Med*. 2020
22. **Rotzinger DC**, Beigelman-Aubry C, von Garnier C, Qanadli SD. Pulmonary embolism in patients with COVID-19: Time to change the paradigm of computed tomography. *Thromb Res*. 2020
 23. Pozzessere C, **Rotzinger DC**, Ghaye B, Lamoth F, Beigelman-Aubry C. Incidentally discovered COVID-19 pneumonia: the role of diagnostic imaging. *Eur Radiol*. 2020
 24. Qanadli SD, **Rotzinger DC**. Vascular abnormalities as part of chest CT findings in COVID-19. *Radiology: Cardiothoracic Imaging*. 2020
 25. Pavon AG, Meier D, Samim D, **Rotzinger DC**, Fournier S, Marquis P, Monney P, Muller O, Schwitter J. First documentation of persistent SARS-CoV-2 infection presenting with late acute severe myocarditis. *Can J Cardiol*. 2020
 26. Qanadli SD, Gudmundsson L, **Rotzinger DC**. Catheter-directed thrombolysis in COVID-19 pneumonia with acute PE: Thinking beyond the guidelines. *Thromb Res*. 2020
 27. Qanadli SD, Malekzadeh S, Villard N, Jouannic AM, Bodenmann D, Tozzi P, **Rotzinger DC**. A new clinically driven classification for acute aortic dissection. *Front Surg*. 2020
 28. Racine D, Becce F, Viry A, Monnin P, Thomsen B, Verdun FR, **Rotzinger DC**. Task-based characterization of a deep learning image reconstruction and comparison with filtered back-projection and a partial model-based iterative reconstruction in abdominal CT: A phantom study. *Phys med*. 2020
 29. Darçot E, Delacoste J, Dunet V, Dournes G, **Rotzinger D**, Bernasconi M, Vremaroiu P, Simons J, Long O, Rohner C, Ledoux JB, Stuber M, Lovis A, Beigelman-Aubry C. Lung MRI assessment with high-frequency noninvasive ventilation at 3 T. *Magn Reson Imaging*. 2020
 30. **Rotzinger DC**, Knebel JF, Jouannic AM, Adler G, Qanadli SD. CT Pulmonary Angiography for Risk Stratification of Patients with Nonmassive Acute Pulmonary Embolism. *Radiology: Cardiothoracic Imaging*. 2020
 31. Qanadli SD, **Rotzinger DC**. Management of non-COVID-19 patients should not be the dark side of the pandemic. *Swiss Med Wkly*. 2020
 32. Douek P, **Rotzinger DC**, Meuli RA, Dunet V, Schmidt S. Impact of CT venography added to CT pulmonary angiography for the detection of deep venous thrombosis and relevant incidental CT findings. *Eur J Radiol*. 2020
 33. **Rotzinger DC**, Qanadli SD. Should vascular abnormalities be integrated into the chest CT imaging signature of COVID-19? *Chest*. 2021

34. Qanadli SD, Rocha AC, **Rotzinger DC**. Intrapulmonary Arteriovenous Anastomoses in COVID-19-Related Pulmonary Vascular Changes: A New Player in the Arena? *Front Med*. 2021
35. Qanadli SD, Rezaei-Kalantari K, Crivelli L, Doenz F, Jouannic AM, **Rotzinger DC**. Structured team-oriented program to follow patients after vena cava filter placement: a step forward in improving quality for filter retrieval. *Sci Rep*. 2021
36. **Rotzinger DC**, Rezaei-Kalantari K, Aubert JD, Qanadli SD. Pulmonary angioplasty: A step further in the continuously changing landscape of chronic thromboembolic pulmonary hypertension management. *Eur J Radiol*. 2021
37. **Rotzinger DC**, Si-Mohamed SA, Yerly J, Boccalini S, Becce F, Bousset L, Meuli RA, Qanadli SD, Douek PC. Reduced-iodine-dose dual-energy coronary CT angiography: qualitative and quantitative comparison between virtual monochromatic and polychromatic CT images. *Eur Radiol*. 2021
38. **Rotzinger D**, Roumy A, Tozzi P, Qanadli SD. Acute post-traumatic rupture of the right pulmonary artery: a modern approach for a rare condition. *Eur J Cardiothorac Surg*. 2021
39. Meier D, Depierre A, Topolsky A, Roguelov C, Dupré M, Rubimbura V, Eeckhout E, Qanadli SD, Muller O, Mahendiran T, **Rotzinger D**, Fournier S. Computed Tomography Angiography for the Diagnosis of Coronary Artery Disease Among Patients Undergoing Transcatheter Aortic Valve Implantation. *J Cardiovasc Transl Res*. 2021
40. Qanadli SD, Sauter AW, Alkadhi H, Christe A, Poletti PA, Ebner L, **Rotzinger DC**. Vascular Abnormalities Detected with Chest CT in COVID-19: Spectrum, Association with Parenchymal Lesions, Cardiac Changes, and Correlation with Clinical Severity (COVID-CAVA Study). *Diagnostics*. 2021
41. Qanadli SD, **Rotzinger DC**. Is management of major bleeding in patients on anticoagulation restricted to reversal strategies? *Eur J Vasc Endovasc Surg*. 2021
42. Qanadli SD, **Rotzinger DC**. Lower extremity vascular disease: call for a standardized and comprehensive name of the disease to improve public awareness. *Vasa*. 2021
43. Si-Mohamed S, Greffier J, Miahilhes J, Boccalini S, Rodesch PA, Vuillod A, Van Der Werf N, Dabli D, Racine D, **Rotzinger D**, Becce F, Yagil Y, Coulon P, Vlassenbroek A, Bousset L, Beregi JP, Douek P. Comparison of image quality between spectral photon-counting CT and dual-layer CT for the evaluation of lung nodules: a phantom study. *Eur Radiol*. 2021
44. Pia Porretta A, **Rotzinger DC**, Pruvot E, Pavon AG. Arrhythmic mitral valve prolapse: an iconic case with first documentation on a cardiac CT scan. *Eur Heart J Cardiovasc Imaging*. 2021
45. Ponti A, Saltiel S, **Rotzinger DC**, Qanadli SD. Insights into endovascular management of superior vena cava obstructions. *Front Cardiovasc Med*. 2021

46. Qanadli SD, Gudmundsson L, Gullo G, Ponti A, Saltiel S, Jouannic AM, Faouzi M, **Rotzinger DC**. Virtually Augmented Self-Hypnosis applied to endovascular interventions (VA-HYPO): Randomized Controlled Trial Protocol. PlosOne accepted pending minor revisions

b. Conference papers

1. **D. Rotzinger**, P. Rau, C. Federau, J.-B. Zerlauth, J.-B. Ledoux, P. Omoumi, F. Becce. Diffusion-weighted MRI of the spine: is it helpful to differentiate infectious spondylodiscitis from Modic type 1 vertebral endplate abnormalities? In : 101st Annual Congress of the Swiss Society of Radiology, Montreux 2014
2. **D.C. Rotzinger**, R.A. Meuli, P. Maeder, P. Michel. Site and rate of arterial pathology in acute ischemic stroke: a CT-angiography study of 50'000 cervico-cerebral arterial segments. In : Joint Annual Meeting SGI | SNG | SGNR | SGNOR | SHG | SGVN | SlgE, Interlaken, Switzerland, 2014
3. **D. Rotzinger**, P. Rau, C. Federau, J.-B. Zerlauth, J.-B. Ledoux, P. Omoumi, F. Becce. Diffusion-weighted MRI of the spine: Is it helpful to differentiate vertebral endplate abnormalities caused by infectious spondylodiscitis or Modic type 1 changes? In : ARRS, American Roengen Ray Society 2015 annual meeting, Toronto.
4. L. Veunac, **D. Rotzinger**, S. Breault, A.-M. Jouannic, C. Beigelman, S. D. Qanadli. CT pulmonary artery obstruction index predicts mortality in pulmonary embolism patients without cardiopulmonary comorbidities. In: Swiss Congress of Radiology (SCR), Basel, Switzerland, June 4-6, 2015
5. D. Romascano, D.-E. Meskaldji, G. Bonnier, S. Simioni and **D. Rotzinger** et al. Cerebellar Connectomics Provide New Biomarkers in Early Multiple Sclerosis. In : 22nd annual meeting of the International Society for Magnetic Resonance in Medicine (ISMRM), Milan, Italy, May 10-16, 2014.
6. Bonnier G, Roche A, Romanasco D, Simioni S, Meskaldji D, **Rotzinger D**, Lin Y-C, Menegaz G, Schlupe M, Du Pasquier R, Sumpf TJ, Frahm J, Thiran J-P, Krueger G, Granziera C. Multi-contrast MRI improves the clinical-radiological correlation in early multiple sclerosis and minimally impaired patients. In: 22nd annual meeting of the International Society for Magnetic Resonance in Medicine (ISMRM), Milan, Italy, May 10-16, 2014
7. Bonnier, Guillaume; Roche, Alexis; Romascano, David; Simioni, Samanta; Meskaldji, Djalel Eddine; **Rotzinger, David**; Lin, Ying-Chia; Menegaz, Gloria; Schlupe, Myriam; Du Pasquier, Renaud. Multiple Sclerosis Lesion Fingerprint Using Multicontrast MRI. In: 22nd annual meeting of the International Society for Magnetic Resonance in Medicine (ISMRM), Milan, Italy, May 10-16, 2014

8. **D. Rotzinger**, P. Mosimann, R. A. Meuli, P. Maeder, P. Michel; Lausanne/CH. Site and rate of arterial anomalies in acute ischemic stroke: A CT-angiography study of 50'807 cervico-cerebral arterial segments. In: Swiss Congress of Radiology, Davos, Switzerland, May 19-21, 2016
9. **Rotzinger DC**, Racine D, Alfudhili K, Keller N, Verdun FR, Beigelman-Aubry C, Becce F. Effects of the ASiR-V algorithm on objective and subjective image quality in chest MDCT. In: European Congress of Radiology, Vienna, Austria, March 1-5, 2017
10. **D. Rotzinger**, P. Mosimann, R. A. Meuli, P. Maeder, P. Michel; Lausanne/CH. Site and rate of arterial anomalies in acute ischemic stroke: A CT-angiography study of 50'807 cervico-cerebral arterial segments. In: European Congress of Radiology, Vienna, Austria, March 1-5, 2017
11. **D. Rotzinger**, P. Mosimann, R. A. Meuli, P. Maeder, P. Michel; Lausanne/CH. Site and rate of arterial occlusive disease in acute ischemic stroke: a CT-angiography study of 50'807 cervico-cerebral arterial segments. In: ARRS (American Roentgen Ray Society) annual meeting, New Orleans, USA, April 30 – May 5 2017
12. Ott J, Verdun F, Omoumi P, **Rotzinger D**, Becce F; Lausanne/CH. Effects of Reconstruction Planes on CT Image Quality When Using Iterative Reconstruction Techniques. In: ARRS (American Roentgen Ray Society) annual meeting, New Orleans, USA, April 30 – May 5 2017
13. **Rotzinger D**, Racine D, Alfudhili K, Keller N, Verdun F, Beigelman-Aubry C, Becce F. Objective and subjective image quality in chest MDCT: impact of the ASiR-V algorithm. In: SCR (Swiss Congress of Radiology), Bern, Switzerland, June 8-10 2017
14. **Rotzinger DC**, Knebel JF, Kamel EM, Jouannic AM, Qanadli SD. Risk stratification in Acute Pulmonary Embolism: effects of Arterial Obstruction Index, Cardiopulmonary Comorbidities and Age. In: SCR (Swiss Congress of Radiology), Bern, Switzerland, June 8-10, 2017
15. **Rotzinger DC**, Knebel JF, Kamel EM, Jouannic AM, Qanadli SD. Risk stratification in Acute Pulmonary Embolism: Impact of Arterial Obstruction Index, Cardiopulmonary Comorbidities and Age. In: JFR (Journées Francophones de Radiologie), Paris, France, October 13-16, 2017
16. **Rotzinger DC**, Dunet V, Ilic V, Hugli O, Meuli RA, Schmidt S. Computed Tomography Angiography for Pulmonary Embolism in Pregnancy: Diagnostic Yield and Alternate Diagnoses. In: SCR (Swiss Congress of Radiology), Lausanne, Switzerland, May 10-12, 2018
17. **Rotzinger DC**, Si-Mohamed SA, Matzuzzi M, Bussel L, Hanquier L, Douek P. First-pass myocardial perfusion using dual-layer detector CT in healthy subjects: impact of spectral reconstructions. In: joint meeting of ESTI and ESCR (European Society of Thoracic Imaging and European Society of Cardiovascular Radiology), Geneva, Switzerland, May 24-26, 2018

18. **Rotzinger DC**, Dunet V, Ilic V, Hugli O, Meuli RA, Schmidt S. Computed Tomography Angiography for suspected Pulmonary Embolism in Pregnancy: Diagnostic Yield and Alternate Diagnoses. In: Journées Francophones de Radiologie Diagnostique et Interventionnelle (JFR), Paris, France, October 12-15, 2018.
19. Si-Mohamed S, Dion M, Dupuis N, Rotzinger D, Douek P, Bussel L. Apport diagnostique des images virtuellement sans contraste pour l'hématome aortique intra-mural. In: Journées Francophones de Radiologie Diagnostique et Interventionnelle (JFR), Paris, France, October 12-15, 2018.
20. **Rotzinger DC**, Si-Mohamed S, Douek PC, Bussel L. "Dark Blood" Dual-Energy CT Imaging Using a Dedicated Material Decomposition Method. In: The Radiological Society of North America's (RSNA) 104th Scientific Assembly and Annual Meeting, Chicago, USA, November 25-30, 2018.
21. Si-Mohamed SA, Dupuis N, **Rotzinger DC**, Boccalini S, Yagil Y, Coulon P, Shapira N, Douek P, Bussel L. Virtual non contrast imaging of aortic intramural hematoma for replacing the non contrast CT imaging. In: European Congress of Radiology, Vienna, Austria, February 27 - March 3, 2019.
22. **Rotzinger DC**, Si-Mohamed S, Douek PC, Bussel L. New dual-energy CT angiography method to generate "dark blood" images. In: European Congress of Radiology, Vienna, Austria, February 27 - March 3, 2019.
23. Douek P, **Rotzinger DC**, Meuli R, Dunet V, Schmidt S. Impact of added CT venography performed in combination with CT pulmonary angiography on the detection of deep venous thrombosis and relevant occult CT findings. In: European Congress of Radiology, Vienna, Austria, February 27 - March 3, 2019.
24. Boccalini S, Si-Mohammed SA, Matzuzzi M, Plaine B, **Rotzinger DC**, Hanquier L, Bussel L, Revel D, Douek P. Characteristics of first-pass myocardial iodine distribution as assessed by dual layer CT with different injection protocols. In: European Congress of Radiology, Vienna, Austria, February 27 - March 3, 2019.
25. Beigelman-Aubry C, Villard N, Brauner M, Du Pasquier C, Lazor R, **Rotzinger D**, Hajri R, Gidoïn S. Pneumopathies infiltratives diffuses: pièges et astuces en CT. In: Journées Francophones de Radiologie Diagnostique et Interventionnelle, Paris, France, October 10 – 14, 2019.
26. **Rotzinger DC**, Si-Mohamed S, Bussel L, Bouin M, Meuli RA, Douek PC. Prospective noninferiority study of low iodine dose dual-layer spectral detector coronary CT angiography. In: ESCR (European Society of Cardiovascular Radiology) annual meeting, Antwerp, Belgium, October 24-26, 2019.

27. Darçot E, Delacose J, Dunet V, Dournes G, **Rotzinger D**, Noirez L, Vremaroiu P, Simons J, Long O, Rohner C, Ledoux JB, Stuber M, Lovis A, Beigelman-Aubry C. Evaluation of Lung MR sequences with High Frequency Non-Invasive Ventilation at 3T. In: Radiology Research Interdisciplinary Meeting, CHUV, November 8, 2019
28. **Rotzinger D**, Dunet V, Hugli O, Meuli RA, Schmidt D. Pulmonary Embolism during Pregnancy: A 17-Year Single-Center Retrospective MDCT Pulmonary Angiography Study. In: The Radiological Society of North America's (RSNA) 105th Scientific Assembly and Annual Meeting, Chicago, USA, December 1-6, 2019.
29. **Rotzinger DC**, Si-Mohamed SA, Bousel L, Meuli RA, Douek PC. A prospective randomized non-inferiority study of low iodine dual-energy coronary CT-angiography. In: European Congress of Radiology, virtual meeting, July 15 – 19, 2020.
30. **Rotzinger DC**, Si-Mohamed S, Yerly J, Becce F, Bousel L, Meuli RA, Douek PC. Reduced-iodine-Dose Dual-Energy Coronary CT Angiography Compared with Conventional CT: Non-Inferiority Study. In: ARRS (American Roentgen Ray Society) annual meeting, online event, April 18 – 22, 2021.
31. **Rotzinger DC**, Racine D, Becce F, Lahoud E, Erhard K, Si-Mohamed S, Greffier J, Meuli RA, Douek PC. Model observer assessment of photon-counting-detector coronary CT angiography and comparison with energy-integrating-detector CT. In: European Congress of Radiology, Vienna, Austria, March 3-7, 2021.
32. **Rotzinger DC**, Si-Mohamed SA, Yerly J, Becce F, Qanadli SD, Meuli RA, Douek PC. Reduced-iodine-dose dual-energy coronary CT angiography compared with conventional CT: a non-inferiority study. In: Swiss Congress of Radiology, Online event, 2021
33. **Rotzinger DC**, Racine D, Becce F, Erhard K, Lahoud E, Si-Mohamed SA, Greffier J, Meuli RA, Douek PC. Task-based evaluation of photon-counting-detector coronary CT angiography and comparison with energy-integrating-detector CT. In: Swiss Congress of Radiology, Online event, 2021
34. Racine D, Alvès B, Monnin P, **Rotzinger DC**, Viry A, Becce F. Impact Of Multiplanar Reformations On CT Image Quality With Model-based Iterative And Deep Learning Reconstructions: A Task-based Phantom Study. In: The Radiological Society of North America's (RSNA) Scientific Assembly and Annual Meeting, Chicago, USA, November 28 – December 2, 2021.
35. Huber FA, Becce F, Zadory M, **Rotzinger D**, Froehlich JM, Schmidt B, Jürgens M, Eurler A, Alkadhi H, Guggenberger R. Crystal characterization and differentiation by spectral photon-counting CT: Initial results with the first clinical scanner of its generation. In: The Radiological Society of North America's (RSNA) Scientific Assembly and Annual Meeting, Chicago, USA, November 28 – December 2, 2021

36. **Rotzinger DC**, Van Der Wal AC, Grabherr S, Qanadli SD, Michaud K. Coronary CT angiography for the assessment of atherosclerotic plaque inflammation: post-mortem proof of concept with histological validation. In: the Association for European Cardiovascular Pathology 9th Biennial Meeting, Cambridge, UK, September 16 – 18, 2021

c. Invited talks

- Rotzinger D. Advanced image reconstruction in CT: moving with the times. GE lunch Symposium, Virtual Event, 2020
- Beigelman C, Brun AL, Brauner M, Noirez L, Schwitter J, Lenoir A, Rotzinger D. Emergencies in thoracic oncology. European Society of Radiology Highlight weeks, Cardiovascular / Chest, September 29-30, 2020 virtual meeting.
- Rotzinger DC. CT angiography prior to TAVI. Cardiologist group of the Canton de Vaud, Lausanne 2019
- Rotzinger DC. Reporting Coronary CT angiography. Lyon University Hospital, 2018
- Rotzinger DC. Functional imaging with CT – 5 clinical cases using GSI: beyond morphology. GE Revolution user meeting, Oslo 2018
- Rotzinger DC. Revolution CT: first experience at CHUV with clinical cases. Lausanne 2015